STRUCTURAL CHEMISTRY AND HETEROSTRUCTURES OF LEAD HALIDE PEROVSKITE SEMICONDUCTORS

by

MATTHEW P. HAUTZINGER

A dissertation submitted in partial fulfillment of

the requirements for the degree of

DOCTOR OF PHILOSOPHY

(CHEMISTRY)

at the

UNIVERSITY OF WISCONSIN–MADISON

2021

Date of final oral examination: June 14th, 2021

The dissertation is approved by the following members of the Final Oral Committee:

Song Jin, Professor – Chemistry
John C. Wright, Professor – Chemistry
Kyoung-Shin Choi, Professor – Chemistry
Dawei Feng, Assistant Professor – Materials Science and Engineering

Preface

Structural Chemistry and Heterostructures of Lead Halide Perovskite Semiconductors

Matthew P. Hautzinger

Under the supervision of Professor Song Jin

University of Wisconsin-Madison

The ability to tune atomic composition and arrangement in crystalline materials provides pathways to observe the impact on properties. In semiconductors, examples of these properties include the electronic band structure, conductivity, and vibrational modes. Harnessing the understanding of materials properties as they relate to structure has contributed to the advancement of solid-state electronics. Continued progress in this field of materials chemistry will be key to developing and improving materials for the next generation of sustainable energy, among other societal challenges.

In the past decade, research into halide perovskites has exploded in interest because of their use in highly efficient solar cells. My graduate research is focused on: (1) the discovery of new halide perovskite materials with unique crystal structures or architectures for better understanding of their structure; (2) the investigation of fundamental physical properties and how they relate to the halide perovskite structure.

Chapter 1 reviews the chemistry of the A-site cation in 3D and 2D halide perovskites. First, I summarized the various methods of describing the perovskite structure, such as the tilting and symmetry. This is followed by a comprehensive review of the 3D halide perovskite compounds

reported in literature and the A-site cations utilized to form them. The symmetry, bonding, and tilting in the structures of these 3D halide perovskites is related to the A-site cation choice. The relationship between the 3D halide perovskite and optical properties is described. Next is a description of 2D halide perovskite compounds and the wide range of A-site cations used in these structures. The choice of A-site cation in the 2D structure is related to the bonding in the structures, the optical properties, semiconductor behavior, and non-linear properties. This chapter concludes with a discussion of future directions of research I believe will be enabled by tuning the A-site cation in halide perovskites.

In chapters 2-4, I describe the structure and properties of new 2D Ruddlesden-Popper (RP) perovskites $(A')_m(A)Pb_nX_{3n+1}$ [A = monovalent cation; X = I, Br; A' = aryl- or alkyl- ammonium (m = 2) or diammonium (m = 1)]. First, I explored the use of N,N-dimethylphenylene-p-diammonium (DPDA) as a spacer dication in a 2D perovskite, $(DPDA)PbX_4$ (X = Br, I). This was unexpected at the time, as few dications had been used to host stable 2D perovskites. We believe that the asymmetry of the DPDA dication was the key to the ability to form a 2D perovskite instead of non-perovskite structures. The bonding parameters of the structure were then correlated with the optical properties, suggesting that more ideal Pb-I-Pb bonds favored lower energy absorbance onset. Temperature dependent photoluminescence measured by our collaborator Prof. Jun Dai was used to observe white light emission from these compounds at low temperatures.

I then continued to explore new perovskite structures with my collaborator and mentor, Dr. Yongping Fu. We aimed to explore the A-site cation chemistry of lead halide perovskites. At the time, the A-site cation had been limited to Cs, methylammonium (MA), and formamidinium (FA) in lead halide perovskites single crystal structures. To further explore the cation chemistry, we

pursued utilizing large A-site cations in 2D RP perovskites. We grew single crystals of $(HA)_2(GA)Pb_2I_7$ (HA = *n*-hexylammonium, GA = guanidinium) by an elevated temperature crystallization. The crystal structure of $(HA)_2(GA)Pb_2I_7$ and $(HA)_2(MA)Pb_2I_7$ was solved via single crystal X-ray diffraction. When comparing these two structures, we found the Pb-I bonds are elongated and the PbI_6^{4-} octahedra are distorted in the GA containing compound. By investigating the optical properties, we found that $(HA)_2(GA)Pb_2I_7$ has blue shifted absorbance features, lower intensity photoluminescence (PL), and faster transient PL decay compared to $(HA)_2(MA)Pb_2I_7$. To understand the cause of these properties, our collaborators performed temperature dependent Raman and PL spectroscopy. The Raman spectroscopy proved a useful tool for determining the incorporation of the GA cation in the perovskite cage, as the Pb-I vibrational modes were shifted relative to non-perovskite phases $(GA)PbI_3$ and $(GA)_2PbI_4$. The temperature dependent PL results suggested stronger electron-phonon coupling in $(HA)_2(GA)Pb_2I_7$ compared to $(HA)_2(MA)Pb_2I_7$. This was attributed to the increase in the distortion and bonding of the Pb-I perovskite framework of $(HA)_2(GA)Pb_2I_7$ and is the likely cause of the decreased PL intensity and faster PL decay.

To further investigate the impact of the A-site cation inside of the perovskite A-site cavity, I synthesized colloidal $(HA)_2(A)Pb_2I_7$ RP perovskite nanoplates (NPLs) with A = Cs, MA, FA, dimethylammonium (DMA), ethylammonium (EA), guanidinium (GA), and acetamidinium (AA) in the A-site cavity. The colloidal NPLs solutions provided a convenient platform to investigate this wide range of materials and properties. Absorbance and PL measurements of the material were compared with the structure to show a clear parabolic trend of the band edge energy versus the A-site cation size. This was related to the proposed octahedra tilting (for small Cs cation) and Pb-I bond stretching (from the large A-site cations DMA, EA, GA, AA) raising the band edge energy,

while the moderately sized MA and FA cations occupied the bottom of the parabola, with the lowest band energy. Furthermore, PL quantum yield (PLQY) measurements were used to quantitatively show that the RP perovskite NPLs with large A-site cations (DMA, EA, GA, AA) had decreased PLQY relative to those RP perovskite NPLs with common A-site cations (Cs, MA, GA). This was corroborated with the time-resolved PL measurements of the RP perovskite NPLs, which demonstrated that RP NPL structures with the large A-site cation had faster transient PL decay than those with the common A-site cations. These observations suggest that the structure of RP perovskite containing large A-site cations inhibits the desirable long carrier lifetime typical of halide perovskites. Furthermore, the effects of the A-site cation stretching the Pb-I lattice was discussed in terms of the negative chemical pressure inside of the A-site cavity induced by the large A-site cations. This negative chemical pressure induces the stretching of the Pb-I lattice, resulting in the increased band edge energy, which completes the trend observed in external pressure studies on halide perovskites (i.e., diamond anvil cell studies), where external pressure reduction shortens the Pb-I bond length and lowers the band edge energy. These works have enabled a better understanding of the role of the A' and A-site cation chemistry in halide perovskites and will be valuable in the future pursuit of novel material properties enabled by tuning the halide perovskite structure.

In addition to structural chemistry, I investigated the growth of 2D/3D heterostructures of halide perovskites. Heterostructures of semiconductor materials are valuable for manipulating charge carriers in a device. However, solution-processed, and notoriously facile lead halide perovskites are difficult to grow into heterostructures. To enable the growth of 2D/3D perovskite heterostructures, I developed a chemical vapor deposition approach to grow thin-films of 2D $(BA)_2PbX_4$ (BA = *n*-butylammonium; X = I, Br). This deposition method was then used grow 2D

$(BA)_2PbX_4$ on top of 3D perovskite single crystal substrates of $(FA_{0.75}MA_{0.25})PbI_3$ and $(MA)PbBr_3$. Characterization of the heterostructures showed 2D perovskite films covering the surface of the 3D single crystals. Electrical characterization of the $(BA)_2PbI_4/(FA_{0.75}MA_{0.25})PbI_3$ heterostructure showed photocurrent under illumination at 0 V bias, however, there was inconsistent photocurrent in the I-V measurements. $(BA)_2PbBr_4/(MA)PbBr_3$ heterostructures exhibits diode like behavior in the I-V measurements, but no photocurrent. In addition, the $(BA)_2PbI_4/(FA_{0.75}MA_{0.25})PbI_3$ heterostructure showed a shift in the PL peak energy under increasing excitation energy, which is typical of a type II aligned system. Furthermore, time-resolved PL measurements of both $(BA)_2PbI_4/(FA_{0.75}MA_{0.25})PbI_3$ and $(BA)_2PbBr_4/(MA)PbBr_3$ showed a change in the rise time of the transient PL, which is indicative of a type I aligned system. These results suggest there are competing carrier processes in the heterostructure, and future experiments will be required to elucidate them.

Acknowledgements

First, I would like to thank my advisor, Professor Song Jin. Without his guidance, this thesis would not be up to my own standards. My time working with Song has helped me grow as a scientist; we have had many long and exciting discussions along the way. I would likely to specifically thank you for your patience with me during my "growing pains" as a researcher. This has instilled the confidence I need to go forward in science, and I am grateful.

Second, I would like to extend my appreciation to my committee members Professor Kyoung-Shin Choi and Professor John Wright. Kyoung-Shin challenged me during my exams, and I thoroughly enjoyed discussing science with her. John was not only a committee member, but also a great collaborator. I walked into his office quite a few times to discuss new results or ideas. Even though I am sure he was busy, he made time to discuss whatever piece of data I had printed out and did it with a big smile. For this dissertation, I would like to thank Professor Dawei Feng, for his time and interest.

My thanks and appreciation also go my collaborators who made contributions to the results presented in this dissertation. Dr. Ilia Guzei has been a crucial resource for me during my time at UW-Madison. Working through and discussing challenging experimental works with Ilia has helped me grow as a scientist. I would also like to thank the X-ray crystallography assistants who I had the pleasure of working with, Michael Aristov and Amelia Wheaton. Thank you to Dr. Donald Savage who taught me various X-ray diffraction techniques and talked me through experiments. I would like to thank Dr. Weihao Zheng, Ziyu Luo, and Professor Anlian Pan from Hunan University for graciously hosting me in my visit to Hunan University in China. The experience of visiting China and true global scientific collaboration is not something I will forget.

I would also like to thank the solar group, for their thoughtful discussions during and outside of meetings. Natalia Spitha, Dr. Daniel Kohler, David Layayette II, Jason Scheeler, Kyle Czech, Blaise Thompson and Kayla Lloyd all worked closely with me. I would like to thank Dr. Darien Morrow in particular, who was a great friend and collaborator in the solar group. Darien was always willing to donate his time to discussion with me. I want to extend special thanks to Alexis Pigg, for being a great REU student and working with me. I also want to thank, Dr. Meiying Leng, Ming-yu Kuo, Feifan Wang, Prof. Xiaoyang Zhu, Jun Dai, Yujin Ji, and Prof. Youyong Li for carrying out many experiments for/with me and providing insightful discussions.

I would like to thank all the members who have been a part of the Jin group during my time at UW-Madison. My mentor, Dr. Yongping Fu taught me about cultivating ideas. We have discussed countless science topics together and his insight during the early years of my PhD was invaluable. Dr. Jie Chen was an excellent co-worker and friend. By sitting next to Jie at the beginning of my PhD journey, I got a jump start on research. During my first two years, Dr. Melinda Shearer was a valuable resource to discuss with and learn from. Yuzhou Zhao, Dr. Nitish Mathur, Dr. Lianna Dang, and Dr. Wenjie Li were great for comradery in and outside of the office. I would like to thank the fellow Jin group members I had the pleasure of working with daily, including Dr. Matt Stolt, Dr. Lichen Xu, Dr. Chih-Jung Chen, Dr. Hui-Chun Fu, David Roberts, Chris Roy, Dominic Ross, Emily Reasoner, Katelyn Michael, Rui Wang, Kristel Forlano, and Erika Jackson. In the Jin group, I had the pleasure of learning from and working with numerous visiting scholars which I am thankful to, including Huawei Liu, Dr. Fengmei Wang, Dr. Ying Yang, and Yifan Dong. A very special thank you to Jin group members who started during my year, Dongxu Pan, Hongyuan Sheng, Tim Tiamberg, Stephanie & Brandon Lamb; starting graduate school together creates a special connection between each other and I am grateful for the support

from all of you. Finally, thanks to Willa Mihalyi-Koch for being a great mentee. Working with you helped me grow as a mentor.

I would like to thank the members of the department who made my degree possible. Specifically, the path coordinators Sue Martin and Olivia West, who were both so kind and helpful to me throughout my degree.

I would like to thank friends from Southern Illinois University who made this degree possible as well. Thanks to Professor Kyle Plunkett who answered quite a few phone calls during my PhD and was a great supportive friend. Thanks to Professor Mark Bausch for the encouraging emails and support throughout my degree. Gavin Sowa and Drake Anthony were great companions during my time at SIU, and their encouragement and friendship has lasted through my PhD.

One of the most important support groups I had during my time at UW, was my friends in the department. Zach Jones was my roommate the entirety of grad school. Zach helped me show up on time during our first year and take time off from working during our last year. Our soirees at our various humble apartments will be some of my most fond memories. In addition, I want to thank my cohort Melissa Cendejas, Rebecca Fernandez (honorary roommate), Ann Lindberg, Andjela Radmilovic, and Young-Sun Lee who started graduate school with me and faced the same challenges. You were my support group throughout graduate school, and I could not have done it with you. In the department I had numerous other friends who helped me by serving as guides and role models. In particular, I would like to thank Dr. Aris Vasilopoulos, Dr. Margaret Lumley, Dr. Sarah Specht, Dr. Camile Bishop, Dr. Eric Cueny, and Paige Kinsley who helped me navigate graduate school.

Finally, I would like to thank my friends outside of the department. Cody Fowkes and Jackie Cromer were great friends who helped me through my achievements and challenges. My partner, Kelly Shen has been the most supportive and positive person I have ever met, and I look forward to our future together. Eric Engelson, Trevor Timm, and Seth Murzyn were great travel partners, providing much needed relief during my breaks. I would like to thank my bike riding friends, Billy Calkins, Alex Aviles, Mitch Pilon, Jacob Fraint, Jeff Fitzgerald, Kian Wagner, Matt Hamann, Ben Specht, Brett Fitz, Brett Stepanik, and Conor Polydorf. Your friendship provided an outlet for me to enjoy life outside of academics. My excitement for Thursday night rides motivated me to get the day's work done faster.

Matthew Hautzinger, 06/07/2021

Table of Contents

List of Figures

List of Tables

Chapter 1. The Influences of the A-site Cations in 3D and 2D Halide Perovskites on Crystal Structure and Properties*

1.1 Abstract

The ability to tune the structure of a material allows for the systematic investigation of the relationship between its structure and properties, which creates opportunities to enhance or explore new applications. Halide and 2D layered perovskites are highly tunable compounds making them excellent structures to explore for structure-property relationships, new material properties, and new applications. Here we summarize the effects of one tunable component, the A-site cation in the 3D AMX_3 and 2D $(A')_2(A)_{n-1}M_nX_{3n+1}$ halide perovskite structures. By compiling a comprehensive review of 3D and 2D perovskite structures, we discuss how the A-site cation templates the inorganic metal-halide perovskite framework, resulting in changes in the crystal structure symmetry as well as bonding parameters. Furthermore, the correlations between the effect of the A-site cation on the halide perovskite structure and the resulting semiconductor properties, such as band gap, carrier lifetime, and non-linear properties, are discussed. In addition, we highlight large A-site cations that induce structural distortions required for non-linear properties such as ferroelectricity. Future perspectives discussed include utilizing versatile A-site cations to stabilize new perovskite structures as well as exploring future directions including ferroelectricity and Rashba-splitting.

* in collaboration with W. Mihalyi-Koch, and S. Jin.

1.2 Introduction

There has been a surge of interest in halide perovskite, in large part due to their use in solution-processed high-efficiency photovoltaics (PVs),[1, 2] with power conversion efficiencies achieved greater than 25%.[3] Beyond PVs, halide perovskites have also been explored for a variety of semiconductor applications including light emission,[4, 5] field effect transistors,[6] and spintronic devices.[7] Investigation into growing halide perovskites in thin films,[8] nanostructures, [13] and nanocrystals (NCs) has enabled these applications.[9] Alongside these application based investigations has been research into the understanding of the solid-state chemistry of halide perovskites including how compositional tuning results in various structures and properties. The three-dimensional (3D) halide perovskite structure, AMX_3 (A = $CH_3NH_3^+$ (MA), $HC(NH_2)_2^+$ (FA), Cs^+; M = Pb^{2+}, Sn^{2+}, Ge^{2+}; and X = Cl^-, Br^-, I^-) is a corner sharing network of MX_6^{4-} octahedra with an A-site cation occupying the 12-coordinate cavity formed by eight octahedra (Figure 1.1a,b).[10] 3D perovskites are highly tunable with a variety of combinations of metal-halide and their solid-solutions accessible. By incorporating bulky ammonium cations, the 3D corner sharing network can be broken up into perovskite variants such as 2D layered perovskites known as Ruddlesden-Popper (RP)[11, 12] or Dion-Jacobson (DJ)[13] phases with the formula $(A')_m(A)_{n-1}M_nX_{3n+1}$ (A' = alky- or aryl-ammonium cation for m = 2 RP, or diammonium cation for m = 1 DJ) (Figure 1.1c,d). RP and DJ perovskites form when bulky A' ammonium spacer cations are added to intercede the layers of corner sharing metal halide octahedra. The number of inorganic layers (n) is controlled by the ratio of A-site cations to metal cations present during growth. Similar to 3D perovskites, 2D RP perovskites have been used in PVs[14, 15] and light emission applications.[16,

[17] 2D RP perovskites can be seen as advantageous due to their enhanced environmental stability[14] as well as higher composition tunability than 3D perovskites.[18]

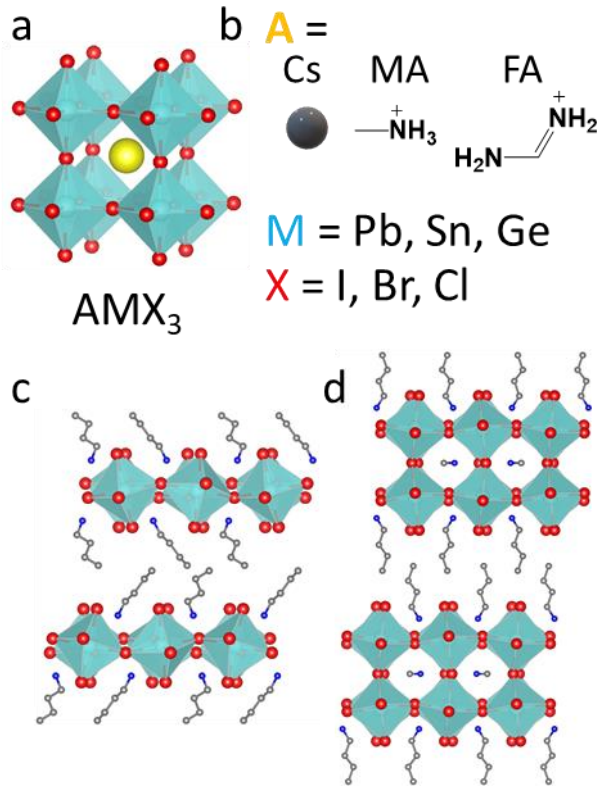

Figure 1.1. Common halide perovskite structures and A-site cations. (a) 3D AMX3 structure with corner sharing metal halide octahedra. (b) The common A-site cations structures, metals (M), and halides (X) in halide perovskites. Structures of 2D Ruddlesden-Popper (RP) perovskite (A')2(A)n-1MnX3n+1 with (c) (n = 1) and (d) (n = 2).

Solid-state chemistry research into 3D and 2D halide perovskite structures has been focused on expanding the structural tunability by understanding how the various A-site and spacer cations affect the resulting semiconducting properties, structure types, and environmental stability. The structure of 3D and RP perovskites is a complex interplay of the cations, metal, and halide ions. The compositions dictate the crystal symmetry, distortion of the perovskite framework, and

even ability to form a stable perovskite. By changing the compositions and resulting structural features, the band gap, stability, carrier behavior can be tuned. Furthermore, recent advances in controlling the A-site cation and spacer cation of RP perovskites have enabled second-harmonic generation (SHG),[19] low temperature ferroelectric phases,[20] and optical spin control.[21] These advancements have opened up perovskites to new or improved applications. While recent reviews have surveyed and discussed the spacer cation of RP perovskites,[18, 22, 23] the A-site cations in both 3D and 2D perovskites have not been discussed outside of thin-film engineering reviews.[8, 24] In this review, we will examine the role of the A-site cation in templating the inorganic framework in both 3D and 2D perovskites through a comprehensive summary of the crystal structures including the symmetry of the compounds, tilting of octahedra, and distortions. Select works on cation orientation, stabilization of structures and alloying of A-site cations will be discussed in the context of structural chemistry. We will also discuss the effect of A-site cations on semiconducting properties as well as additional properties that have been enabled by the recent expansion of the A-site cation library, including SHG and ferroelectricity. Some future perspectives are provided on tailoring the A-site cation to stabilize perovskite structures, achieve NL properties in 2D perovskites, and explore favorable structures for spin-orbitronics. Learning from these recent advances will help guide future research into perovskites.

Box 1. Description of tolerance factor, octahedral tilting, and distortions in halide perovskites

To understand the role of A-site cations in perovskite structures, models based on bonding and ion size have been developed.[25-29] Relative to the traditional, highly ionic oxide perovskites, M-X bonds in halide perovskites are more covalent.[27, 29] However, the empirical Goldschmidt

tolerance factor (α), originally used for oxide perovskites, is still applied to halide perovskites as a rule of thumb. The tolerance factor α (Equation 1.1) is used to show the ionic sizes tolerated in a perovskite structure.

$$\alpha = \frac{r_a + r_x}{\sqrt{2}(r_M + r_x)} \qquad (1.1)$$

where r_i is the radius of the ions in AMX_3, and i = A, M, X. This semi-empirical geometric consideration is useful in predicting which compositions form structurally stable perovskites. In halide perovskites, a tolerance factor range of $\alpha = 0.8 - 1.0$ is favorable (Figure 1.2a). In addition to considering the geometry of the cations and anions, the octahedral factor (μ, Equation 1.2) is used to predict the relative stability of individual metal-halide octahedra.

$$\mu = \frac{r_M}{r_x} \qquad (1.2)$$

Goldschmidt's no-rattling principle dictates that α and μ must be within limits for a stable perovskite to form, as shown in the tolerance factor vs octahedral factor plot in Figure 1.2a.[28]

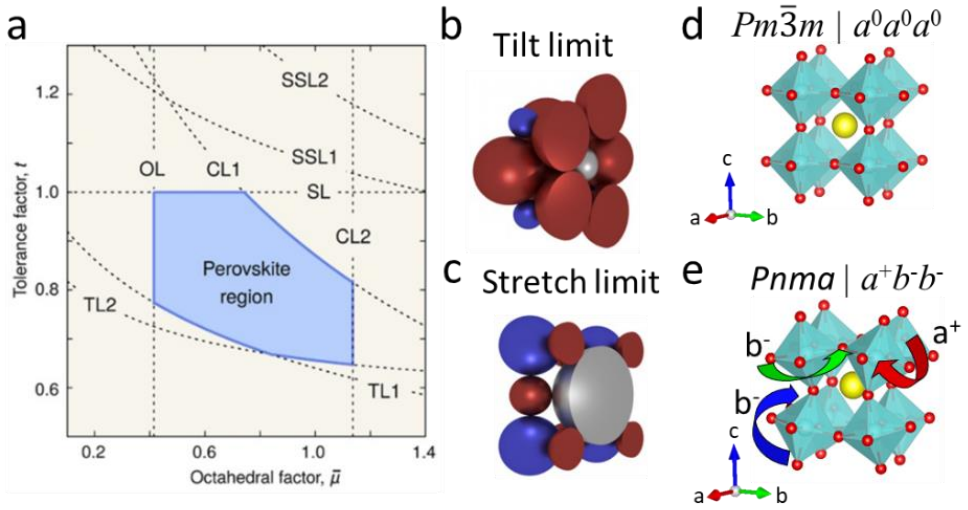

Figure 1.2. Description of stability, tilting, and symmetry in 3D halide perovskite. (a) The tolerance factor (α) and octahedral factor (μ) plotted showing the blue shaded stability region of 3D perovskites as well as lines showing the tilt limit (TL), octahedral limit (OL), chemical limit (CL), and stretch limit (SL). Schematic of perovskite structures at the (b) tilt limit and the (c) stretch limit. Representative diagram (d) of an $a^0a^0a^0$ structure lacking octahedral tilting and an $a^+b^-b^-$ structure (e) with tilting along the a axis (a^+) in a different direction and lesser extent than the b and c axis tilting (b^-).

The size of the A-site cation plays a large role in dictating octahedral tilting.[28] Under the tilt limit, the A-site cation is small, leaving a void for the octahedra to tilt at moderate α and forcing a non-perovskite structure when $\alpha < 0.8$ (Figure 1.2b). In contrast, under the stretch limit where $\alpha > 1$, the A-site cation is too large, forcing the M-X distances to be too high to form stable perovskites (Figure 1.2c). Beyond the A-site cations effects, the octahedral limit describes when the metal is too small to accommodate the anions ($\mu < 0.3$), resulting in tilting or formation of a

different geometry (e.g., M-X adopting a tetrahedral geometry). The symmetry is dictated by the type and degree of tilting. As described by Glazer notation (e.g. $a^0b^+c^-$), octahedra can tilt in the same direction (in-phase), opposite direction (anti-phase), or have no tilt indicated as superscripts +, -, 0, respectively.[30] Furthermore, the octahedra can have the same or unique amplitude of tilt, indicated by *a a a* for the same amplitude or *a b c* for each amplitude of tilt independent along unique crystallographic directions. For example, $a^0a^0a^0$ has no tilting (Figure 1.2d), which fits into the $Pm\bar{3}m$ space group. In contrast, Figure 1.2e shows an $a^+b^-b^-$ structure which has tilting about each axis and fits into the *Pnma* space group.[31]

In addition to tilting, the individual octahedra can be distorted resulting in deviations from ideal X-M-X bond angles. The bond length distortion index (D) describes the elongation of the M-X bond lengths (d_i) relative to ideal M-X bond lengths (d_0) in equation 1.3.[32]

$$D = \frac{1}{6}\sum_{i=1}^{6}\frac{|d_i - d_0|}{d_0} \qquad (1.3)$$

The X-M-X bond angle (θ_i) distortion can be described with the bond angle variance (σ^2).[33]

$$\sigma^2 = \frac{1}{11}\sum_{i=1}^{12}(\theta_i - 90)^2 \qquad (1.4)$$

The combination of D and σ^2 captures the various distortions in an octahedra.

1.3 Effect of A-site cation on the 3D perovskite structure

Three common cations can host 3D halide perovskite structures: MA, FA, and Cs (Figure 1.1b). This range spans the stretch to tilt limit in perovskites with different M-X combinations. These cations and the various combinations of metal and halide form four common crystal

structure types at room temperature (RT) depicted in Figure 1.3. The reported compounds and the tolerance factor, symmetry, bonding parameters, and band gap of each compound are summarized in Table 1.1.

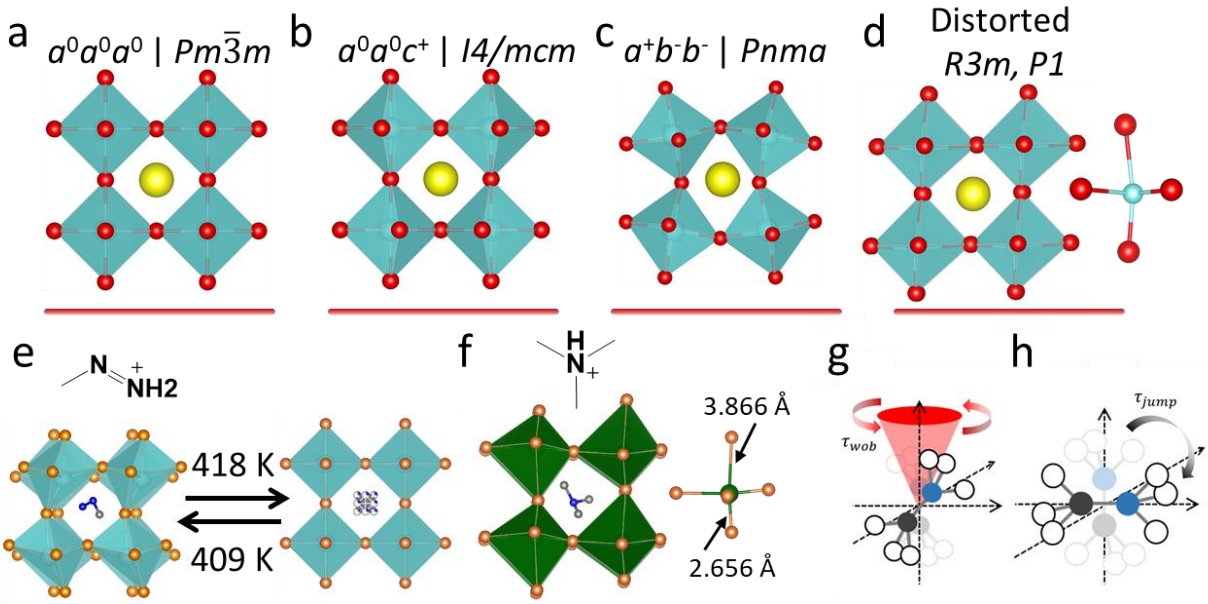

Figure 1.3. The range of halide perovskite structures from ideal to increasingly distorted, exotic A-site cation perovskite structures, and illustration of cation reorientation. (a) The ideal $Pm\bar{3}m$ perovskite structure with no tilting or distortion of the octahedra. (b) Octahedra slightly tilted along one axis due to the smaller ratio of A-cation size to MX_6 (lower α). (c) The tilted perovskite known as the $GdFeO_3$ structure type in which each axis is tilted. (d) A distorted structure with an individual octahedra shown. (e) The methylhydrazinium (MHZ) cation along with the RT non-centrosymmetric $P2_1$ and high temperature $Pm\ \bar{3}\ m$ structures of (MHZ)$PbBr_3$.[34] (f) Trimethylammonium (TMA) cation and the (TMA)$SnBr_3$ structure.[35] The distortions and Sn^{2+} off centering can be clearly seen. Diagram illustrating the (g) wobbling rotations of MA cations and the (h) jump reorientation.[36]

The MA based compounds (MA)PbX_3 (X = Cl, Br)[37-39] and (MA)SnX_3 (X = Br, I)[40, 41] all have favorable tolerance factors (Table 1.1), forming the no tilt $a^0a^0a^0$ $Pm\bar{3}m$ structures (Figure 1.3a) which are examples of ideal, high symmetry perovskite structures. MA cations form two other structures that tilt and distort with Pb and Sn. (MA)PbI_3 has been assigned in the Fmmm,[37] I4/m,[42] I4/mcm,[43-45] and I4cm[10] space groups. Twinning in these crystals presents a challenge in assigning the space group.[37] However, bulk (MA)PbI_3 likely adopts a centrosymmetric *I4/mcm* space group instead of others, as indicated by rotational SHG measurements.[43] (MA)PbI_3 has a slightly tilted structure described as $a^0a^0c^-$ (Figure 1.3b). The slight tilting along a single axis correlates with a α value 0.912 in the middle of other halide perovskites. In contrast, (MA)SnI_3 adopts the $Pm\bar{3}m$ space group ($a^0a^0a^0$) since α is larger (0.954), pushing it closer to a stretch limit and thus having no tilting. The other non-ideal perovskite is (MA)$SnCl_3$ (*P1*, Figure 1.3d),[46] which can be described as a distorted perovskite with large σ^2 and D values (Table 1.1). The lone-pair of the Sn^{2+} ($5s^2$) in combination with the short Cl bonds cause the distortions in the (MA)$SnCl_3$ structure, not predicted by the α and μ.[47]

Table 1.1. Tolerance factor (α), select crystal structure parameters, and band gap for each reported 3D perovskite structure.

Compound	α	Space group	Tilt	D	σ^2	Avg. Bond Length (Å)	Unit Cell Vol. / Z (Å^3)	Band gap (eV)
$CsPbI_3$[48]	0.851	*Pnam*	$a^+b^-b^-$	9.21	2.5422	3.1773	236.83	1.72
$MAPbI_3$[45]	0.912	I4/mcm	$a^0a^0c^+$	0.05	0	3.1522	248.64	1.51
$FAPbI_3$[49]	0.987	$Pm\bar{3}m$	$a^0a^0a^0$	0	0	3.181	256.93	1.41
$CsPbBr_3$[50]	0.862	*Pnma*	$a^+b^-b^-$	0.6	0.5659	2.9699	200.69	2.27
$(MA)PbBr_3$[37]	0.927	$Pm\bar{3}m$	$a^0a^0a^0$	0	0	2.9664	208.82	2.23
$FAPbBr_3$[51]	1.008	$Pm\bar{3}m$	$a^0a^0a^0$	0	0	3.0067	217.45	2.15
$(MHZ)PbBr_3$[34]	1.030	$P2_1$	distorted	16.555	157.6383	3.0424	209.18	2.49
$CsPbCl_3$[50]	0.870	*Pbnm*	$a^+b^-b^-$	2.72	0.4451	2.8309	175.52	2.91
$(MA)PbCl_3$[39]	0.938	$Pm\bar{3}m$	$a^0a^0a^0$	0	0	2.8433	182.80	2.88
$(FA)PbCl_3$[52]	1.023	$Pm\bar{3}m$	$a^0a^0a^0$	0	0	2.8689	188.91	3.00[53]
$(MHZ)PbCl_3$[54]	1.049	$P2_1$	distorted	18.525	167.8357	2.9249	184.80	3.14
$CsSnI_3$[55]	0.890	*Pnam*	$a^+b^-b^-$	2.75	21.9988	3.1143	232.37	1.3
$(MA)SnI_3$[41]	0.954	$Pm\bar{3}m$	$a^0a^0a^0$	0	0	3.1217	243.37	1.21
$(FA)SnI_3$[56]	1.032	$Pm\bar{3}m$	$a^0a^0a^0$	0	0	N/A	251.19	1.41
$CsSnBr_3$[47]	0.905	$Pm\bar{3}m$	$a^0a^0a^0$	0	0	2.9021	195.55	1.9
$(MA)SnBr_3$[40]	0.973	$Pm\bar{3}m$	$a^0a^0a^0$	0	0	2.9537	206.16	2.3
$(FA)SnBr_3$[56]	1.058	$Pm\bar{3}m$	$a^0a^0a^0$	n/a	n/a	n/a	205.90	2.4
$(MP)SnBr_3$[57]	n/a	*Pc*	distorted	107.805	9.3706	3.0462	215.79	2.45
$(TMA)SnBr_3$[35]	n/a	$P2_1$	distorted	170.97	48.4489	3.2144	259.42	n/a
$CsSnCl_3$[58]	0.916	$Pm\bar{3}m$	$a^0a^0a^0$	0	0	2.752	166.74	n/a?
$(MA)SnCl_3$[46]	0.987	*P1*	distorted	92.64	72.2642	2.8286	186.04	n/a?
$(TMA)SnCl_3$[59]	n/a	*Cmc21*	distorted	206.11	36.1172	3.1373	242.34	3.59
$CsGeI_3$[60]	1.027	*R3m*	distorted	83.79	32.1026	3.0044	213.96	1.63
$(MA)GeI_3$[61]	1.055	*R3m*	distorted	108.34	44.8756	3.1093	235.73	2
$(FA)GeI_3$[61]	1.142	*R3m*	distorted	133.82	74.4103	3.1551	242.72	2.35
$CsGeBr_3$[60 40]	1.009	*R3m*	distorted	103.09	19.8318	2.825	178.8	2.38
$CsGeCl_3$[60]	0.985	*R3m*	distorted	136.81	8.6546	2.7202	160.45	3.43

Footnote: MHZ = methylhydrazinium, MP = methylphosphonium, TMA = trimethylammonium.

Formamidinium (FA) forms stable $(FA)PbX_3$ (X = Cl, Br) and $(FA)SnX_3$ (X = Br, I) perovskite structures in the $Pm\bar{3}m$ space group ($a^0a^0a^0$).[51, 52, 56, 62] These structures all form perovskites in spite of having a slightly unfavorable $\alpha > 1$ (Table 1.1), which demonstrates the

breakdown in the utility of α. However, (FA)MI_3 (M = Sn, Pb) has α close to 1 and forms a metastable perovskite phase ($Pm\bar{3}m$, $a^0a^0a^0$) at RT.[49, 63, 64] Under ambient conditions, (FA)MI_3 converts to a non-perovskite phase, indicating the structural instability of these compounds. FA based perovskites are an excellent example of halide perovskites existing at the stretch limit, where the large FA cation causes octahedra in the structure to adopt the $Pm\bar{3}m$, $a^0a^0a^0$ phase with no tilting.

Examining the inorganic halide perovskites, Cs is the primary A-site cation found in crystallographic structures, although solid solutions containing Rb have been reported.[50] At RT, $CsPbX_3$ (X = Cl, Br) forms a tilted structure in the *Pbnm* (no. 62) space group.[50] $CsPbI_3$ crystallizes in the $Pm\bar{3}m$ space group above 583 K which can be quench cooled to a RT metastable perovskite phase in the *Pnam* space group (no. 62).[48] The RT structures of $CsPbX_3$ (X = Cl, Br, I) and $CsSnI_3$ can be considered tilted perovskites with a glazer notation of $a^+b^-b^-$ (Figure 1.3c). This tilting is induced by the small Cs cation occupying the A-site and causing the structures to have $\alpha < 0.9$, thus the structures approach the tilt limit. $CsMI_3$ (M = Sn, Pb) are unstable at RT and without stabilization will convert to a non-perovskite structure.[10, 55] $CsSnX_3$ (X = Cl, Br) have $\alpha > 0.9$ which is larger than their Pb counterparts, and as a result fit into the $Pm\bar{3}m$ non-tilted space group.[47, 58]

Germanium is smaller than Sn and Pb and has pronounced lone pair ($4s^2$) effects. (A)GeI_3 (A = MA, FA)[61] and $CsGeX_3$ X = Cl, Br, I [61, 65] crystallize in the polar *R3m* space group (Figure 1.3d). The GeX_6^{4-} octahedra are trigonally distorted, with three elongated bonds. With increasing A-site cation size, the Ge-I bonds elongate, resulting in a larger unit cell volume and higher D. However, the *R3m* symmetry of Ge-based perovskites is caused by the small Ge with prominent

lone pair effects and does not vary with A-site cation. (A)GeX_3 compounds have higher σ^2 and quadratic elongation than their Pb and Sn counterparts (Table 1.1).

Notably, select cations larger than FA have been incorporated into the 3D halide perovskite structures. Methylhydrazinium (MHZ) has been incorporated into (MHZ)$PbCl_3$[54] and (MHZ)$PbBr_3$[34] which crystallize in the non-centrosymmetric $P2_1$ (no. 4) space group (Figure 1.3e). Upon heating, these compounds undergo a phase change to structures with higher symmetry $Pm\bar{3}m$ (Br, 418 K) and $Pb2_1m$ (no. 26, Cl, 342 K) space groups. Moreover, methylphosphonium (MP) and trimethylammonium (TMA) have been used to form distorted, Sn-based perovskite structures. For example, (MP)$SnBr_3$ crystallizes in the *Pc* space group at RT.[57] (TMA)$SnBr_3$ and (TMA)$SnCl_3$ crystallize in the $P2_1$ (Br) and $Cmc2_1$ (Cl) space groups (Figure 1.3f).[35, 59] TMA has also been used in (TMA)$GeCl_3$ adopting the *Pnma* space group at RT.[66] These low symmetry compounds are best described by the huge distortion the large A-site cation induces in the perovskite structure. All of these large A-site cation 3D halide perovskites have larger D and σ^2 due to the strain imposed on the M-X framework, which must contort to accommodate the oversized cations. This distortion can be seen in Figure 1.3f, where the octahedra has extremely elongated bonds.

1.3.1 A-site cation orientation and motion

Both FA and MA cations are usually highly disordered in the A-site cavity at RT. Solid-state NMR shows the MA cation in (MA)PbX_3 has no fixed position within the A-site cavity.[67] Instead, the NH_3 group reorients inside the cavity, interacting with the different halides in the lattice through hydrogen bonding, while the CH_3 group does not interact with the lattice. These are isotropic reorientations with activation energies on the order of 6-12 KJ/mol.[68] The activation energy of the reorientation decreases in the order of halide (Cl> Br> I), which can be attributed to

the strength of the $NH_3 \cdots X$ hydrogen bonding. Based on 2D vibrational spectroscopy combined with ab-initio molecular dynamics simulations, there are likely two reorientations occurring: a fast, local wobbling-in-a-cone motion (Figure 1.3g) and a slower 90° jump (Figure 1.3h). [36, 69] The fast wobbling occurs on the 0.2 - 0.4 ps time scale, while the jump reorientation is 3 ps. Other reports based on neutron scattering suggest time scales are up to 15 ps.[70] The discrepancy is described in list of reorientation times presented by Gallop *et al*.[36] The FA cation behaves similarly, exhibiting rapidly wobbling within a cone along with reorientation jumps.[71] The rotation about the N-N axis of FA has an energy barrier of 21 meV and occurs on the 8 ps time scale.[72] For further discussion on the cation dynamics halide perovskites, we refer readers to recent reviews.[73, 74] The cation reorientation at rapid time scales is important for the above assigned space groups, as disorder of the MA and FA cations modeled in the crystallographic structures is likely the most accurate assignment reflective of the average (i.e. rotating) A-site cation.

1.3.2 Stabilization and alloying of metastable phases

As mentioned above, select halide perovskite phases such as $(A)PbI_3$ (A= Cs, FA) are unstable as 3D perovskites at RT. However, these perovskites can be stabilized using numerous techniques. One example is surface stabilization, as demonstrated in $CsPbI_3$ and $(FA)PbI_3$ thin-films[75, 76] and NCs.[77-79]. In these low-dimensional thin-film and NC materials, the surface to volume ratio is increased and the enthalpy of the surface outweighs the bulk enthalpy. When ligands such as long chain amines or carboxylic acids are added, the surface can be effectively stabilized, reducing the enthalpy of the entire system. Free energy calculations on $(A)PbI_3$ with and without surface functionalization (Figure 1.4a,b) confirm this stabilization effect. $(A)PbI_3$ (A= Cs, FA) NCs have also been effectively stabilized in the perovskite phase by the utilization of

oleylamine and oleic acid ligands during the growth.[77-79] These strategies are critical to utilizing these materials in devices.

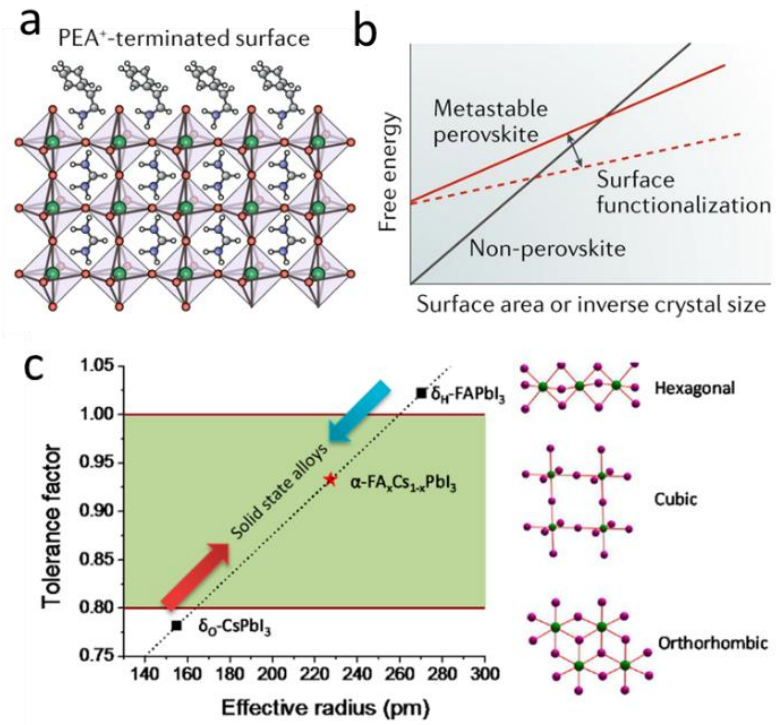

Figure 1.4. Stabilization of metastable perovskite phases via surface functionalization and alloying. (a) Ligand surface chemistry to stabilize the perovskite structure. (b) Calculated free energy of perovskite phases with and without surface functionalization. [75, 80] (c) Tolerance factor versus effective radius for solid-solutions of $(FA_xCs_{1-x})PbI_3$ with drawings of the corresponding crystal structures on the right. [81]

Moreover, alloying A-site cations is another effective strategy to stabilize the perovskite phase as well as enhance the overall stability of the material. One of the first examples of this stabilization was in $Cs_{1-x}FA_xPbI_3$ thin films.[81] By alloying Cs-FA in the structure, the tolerance factor was effectively tuned between the too small Cs and the too large FA structures (Figure 1.4c) and highly stable perovskite materials resulted. In another work alloying FA/Cs, tuning the FA/Cs

ratio in $FA_xCs_{1-x}PbI_3$ changed the tilting and symmetry of the crystal structure, as observed by synchrotron grazing incidence wide angle X-ray scattering.[82, 83] At low Cs content ($x > 0.7$), the $Pm\bar{3}m$ structure is favored. By incorporating mixed FA and Cs ($0.7 > x > 0.2$), a *P4/mbm* structure is formed, with tilting similar to $(MA)PbI_3$. At high Cs concentrations ($x > 0.2$), the structure adopts the tilted *Pbnm* space group. This alloying effect has been demonstrated across other halide perovskite systems as well.[84-86] Furthermore, alloying is an effective method of introducing large or oversized A-site cations into thin-film halide perovskites. Initial work demonstrated guanidinium (GA) incorporation into $(MA_{1-x}GA_x)PbI_3$ thin-films.[87] GA was incorporated up to $x = 0.25$ without byproduct phases appearing in the XRD patterns. As GA content increased, XRD peaks shifted to lower diffraction angles, correlating with the larger GA cation inducing a larger A-site cavity. Interestingly, the perovskite thin films with greater GA content were more stable when used in PVs under operating conditions. Alloying of other large cations, such as dimethylammonium (DMA),[88, 89] and ethylammonium (EA),[90] into thin-films of 3D halide perovskites also showed enhanced stability relative to MA based films. Furthermore, large GA cations have been used in $FA_{1-x}GA_xPbBr_3$ NCs for LEDs, maximized performance at 10% GA incorporation.[91] The mechanism of how the GA cation enhanced the thin-film stability and improve performance is unclear. However, it has been proposed that the stability enhancement may be due to unintended non-perovskite phases forming and passivating the perovskite film, leading to enhanced performance and solar cell stability. [91, 92]

1.3.3 Optical properties related to 3D perovskite structure

The optical properties of halide perovskites are heavily influenced by their compositions. The orbital mixing of M and X in (A)MX_3 comprises the band structure. The series Cl>Br>I and Ge>Pb>Sn and are ordered from largest to smallest bandgap energy (E_g).[10, 61, 93] The A-site cation indirectly affects the E_g by templating the bonding of the M-X framework. Tilted structures such as $CsPbI_3$ have a larger E_g (1.72 eV) relative to the non-tilted structure (FA)PbI_3 (1.41eV).[94, 95] This effect is the result of a shift in the overlap of the M and X orbitals.[96, 97] Based on DFT, the change in symmetry does not dramatically affect the band dispersion, only the band gap.[53]

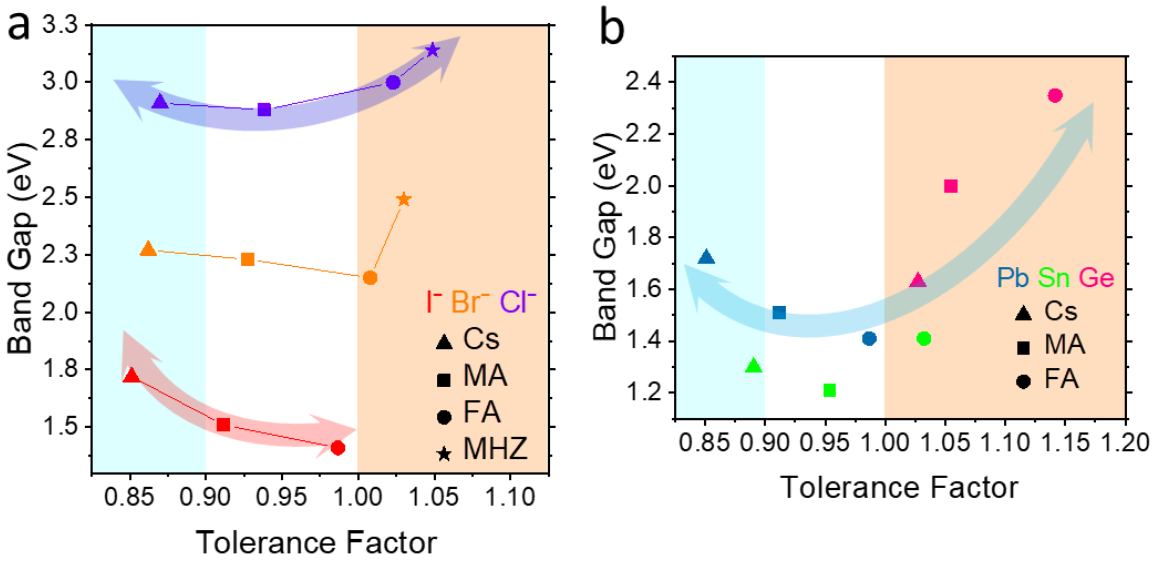

Figure 1.5. Relationship of band gap to tolerance factor in 3D perovskites. (a) Band gap versus tolerance factor of (A)PbX_3 showing the band gap decrease with larger tolerance factor for each halide series until reaching a stretching limit (~$\alpha > 1$), where the band gap increases. (b) Band gap vs. tolerance factor for (A)MI_3 with a similar downward sloping trend for ~$\alpha < 0.9$, followed by increasing band gap at ~$\alpha > 1$ (shaded for clarity).

The E_g of alloyed $(Cs_{1-x}Rb_x)PbX_3$ (X= Cl, Br) and $(FA_{1-x}MA_X)PbI_3$ has been shown to decrease linearly as tolerance factor increases (average A-site cation size gets larger).[50, 98] Across the compounds in Table 1, we see the same general trend of structures with smaller unit cells (those with Cl or Ge) having a larger E_g than structures with larger unit cells. By narrowing the parameters to a single metal (constant r_M) and comparing the E_g of $(A)PbX_3$ versus the tolerance factor, we can see a general negative slope for the X = Br, I structures from $CsPbX_3$ to $(FA)PbX_3$ for the respective halide series (Figure 1.5a). However, the $(A)PbCl_3$ series breaks this trend with $(MA)PbCl_3$ displaying the smallest E_g. The larger $(FA)PbCl_3$ structure has a higher E_g due to the decreased M-X overlap as a result of the elongated Pb-Cl bonds. The even larger $(MHZ)PbCl_3$ has the largest E_g, due to even more elongated bonds and distortion in the octahedra, which is true for $(MHZ)PbBr_3$ as well. When plotting the band gap versus tolerance factor of $(A)MI_3$ (constant r_I), we see a similar trend (Figure 1.5b). The perovskite structures with moderate tolerance factor (0.9-1.0) have the smallest E_g, while the E_g is increased below and above this range. For $\approx \alpha < 0.9$ (small A-site cation for the structure), tilting will raise the E_g and have a negative slope. At $\approx \alpha > 1$ (too big A-site cation for the structure), the bonds are elongated causing an increase in E_g and positive slope. In moderate range ($0.9 < \alpha < 1.0$) the curve is flat/unclear trend. This trend is consistent with RP perovskites as discussed later.

While the role of A-site cations in tuning the structure and band gap is apparent, the role the A-site cations play in charge carrier behavior is less clear. The effect of crystal structure on charge carrier behavior is difficult to elucidate because extrinsic conditions, such as sample quality, can dramatically affect the carrier behavior.[42] Studies comparing the $(A)PbBr_3$ phases, which are not subject to degradation influences as much as $(A)PbI_3$, suggest there is little effect of the A-site

cation on the carrier properties, at least with common cations Cs, MA, FA. By utilizing (A)$PbBr_3$ where A = Cs, MA, stable films and solar cells can be made. In these solar cells, there is little change in V_{oc}, J_{sc}, and PCE, suggesting that Cs is comparable to MA cations.[99] Investigating deeper into the underlying properties that influence carrier behavior, it is suggested that large polaron formation in halide perovskites prevents charge scattering and promotes slow recombination rates of charge carriers. It is a contributing factor to the high performance of halide perovskite solar cells. From spectroscopy and computational investigations, it appears that the polaron formation is independent of A-site cation.[100, 101] While these results suggest that individual A-site cations do not improve carrier lifetimes which is desirable for devices, alloying of A-site cations does appear to help in solar cells. Numerous reports show that mixed cation solar cells are superior to the single cations in performance.[102, 103] Some have suggested the grain passivation is improved from the extra A-site cations acting like an additive.[24, 104-107] But what is clear is for improved PV and LED performance, mixed cations thin-films with their superior carrier mobilities are best.

1.4 RP Perovskite structures with an expanded A-site cation range

Ruddlesden-popper (RP) perovskites can accommodate a larger range of A-site cation sizes than 3D halide perovskites. In RP perovskites, the layers of the inorganic M-X framework are interceded by stabilizing and flexible long chain ammonium cations (A') which allow for large A-site cations to be incorporated, analogous to utilizing surface ligand chemistry to stabilize (FA)PbI_3 and $CsPbI_3$. A variety of large A-site cations (Figure 1.6a) can be incorporated into $(A')_2(A)_{n-1}Pb_nI_{3n+1}$ that do not form perovskite structures in the absence of the A' spacer cations.[108, 109]

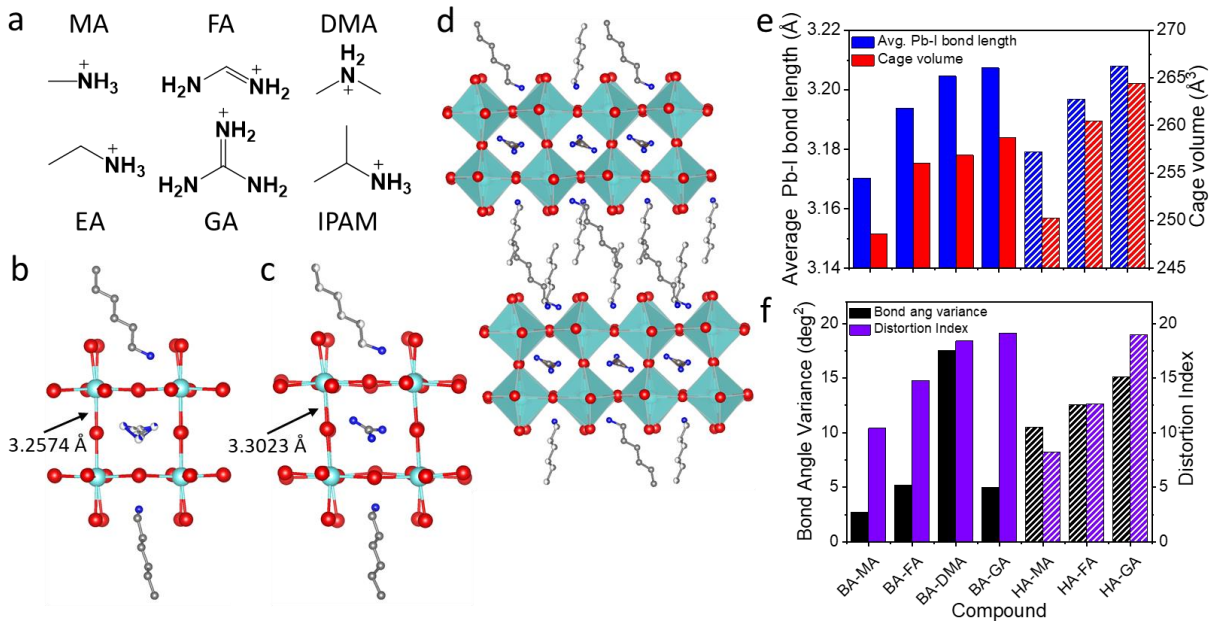

Figure 1.6. Large A-site cation structures, RP crystal structures, and bonding parameters in RP perovskites with varying A-site cations. (a) Structures and labels of the of A-site cations. Crystal packing diagram of the A-site cavities for (b) $(HA)_2(MA)Pb_2I_7$ and (c) $(HA)_2(GA)Pb_2I_7$ showing the elongation of the Pb-I bonds.[110] (d) Extended crystal packing of $(HA)_2(GA)Pb_2I_7$. (e) The average Pb-I bond length and cage volume and (f) average bond angle variance (σ^2) and distortion index (D) of BA and HA based RP perovskites. Labels are abbreviated (e.g., BA-MA = $(BA)_2(MA)Pb_2I_7$). Solid bars are BA and shaded bars are HA.

The symmetry of RP perovskites results from a complex interplay between the A-site cation, spacer cation, octahedra, and layer stacking. One parameter to consider is the A-site cavity volume (also known as the perovskite cage) defined by the cuboid made up of the three Pb-Pb distances in the *a b c* directions. The choice of spacer cation influences the structure to a small extent, as demonstrated by the difference in σ^2, D, and bond length for $(BA)_2(MA)Pb_2I_7$ and $(HA)_2(MA)Pb_2I_7$ (BA = *n*-butylammonium, HA = *n*-hexylammonium) (Table 1.2). Therefore, to

directly compare the effects of the A-cation on the A-site cavity volume, it is more useful to compare the differences between structures with the same spacer cations. We choose to focus on the Pb-based RP perovskites, as robust changes in the A-site cation have not been investigated in the Sn or Ge RP perovskites.

Table 1.2 List of RP perovskite compounds and their parameters including tolerance factor (α), distortion index (D), bond angle variance (σ^2) and band energies.

Compound	α	**Space Group**	**Avg. *D***	**Avg. σ^2**	**Avg. Bond Length (Å)**	**Cage Volume (Å^3)**	**Band gap (eV)**	**Abs. Peak (eV)**
$(BA)_2(MA)Pb_2I_7$[11]	0.911	*Cmcm*	10.4	2.7	3.17025	248.6	2.16	
$(BA)_2(FA)Pb_2I_7$	0.987	*Cmcm*	14.8	5.2	3.1938	256.0	2.18	
$(BA)_2(DMA)Pb_2I_7$[111]	1.026	*Ccmb*	18.4	17.5	3.20455	256.9	2.22	
$(BA)_2(GA)Pb_2I_7$[111]	1.041	*Cmcm*	19.1	5	3.2074	258.7	2.2	
$(HA)_2(MA)Pb_2I_7$[110]	0.911	*C2/c*	8.2	10.51	3.1792	250.26		2.08
$(HA)(FA)Pb_2I_7$[112]	0.987	*Pnma*	12.62	12.57	3.1968	260.47	2.02	
$(HA)(GA)Pb_2I_7$[110]	1.041	*P-1*	18.96	15.11	3.20805	264.44		2.13
$(BA)_2(EA)_2Pb_3I_{10}$[113]	1.03	*Cmc21*	22.35	12.07	3.213	267.2		2.145
$(BA)_2(MA)_2Pb_3I_{10}$[11]	0.911	*C2cb*	16.98	4.4	3.163	255.1		2.023
$(BA)_2(Cs)Pb_2Br_7$[114]	0.862	*Cmc21*	5.48	10.54	2.9856	204.65	2.7	
$(BA)_2(MA)Pb_2Br_7$	0.927	*Cmc21*	10.7	20.1	2.9944	207.3	2.55	
$(BA)_2(FA)Pb_2Br_7$	1.008	*Cmc21*	14.53	10.43	3.0026	218.42	2.24	
$(IBA)_2(EA)Pb_2Br_7$	1.055	*Cc*	24	26.73	3.0172	223.32	n/a	n/a
$(BA)_2(MA)_2Pb_3Br_{10}$	0.927	*Cmc21*	12.74	9.55	2.9871	211.16	2.45	
$(EA)_4Pb_3Br_{10}$[115]	1.055	*C2cb*	41.68	64.46	3.0372	223.31	2.75	
$(EA)_4Pb_3Cl_{10}$[35, 115]	1.072	*$A2_1ma$*	41.09	46.78	2.9074	198.15	3.45	

For the iodide containing RP structures, the GA cation has been incorporated into $(A')(GA)Pb_2I_7$ with A' = BA,[116] *n*-pentylammonium (PA), HA.[110] In these structures, the volume of the A-site cavity is dramatically increased relative to $(A')(MA)Pb_2I_7$ (Table 1.2). The crystal

packing diagrams in Figure 1.6b,c show the change in Pb-I bond distance of $(HA)_2(A)Pb_2I_7$ with A = MA and GA. The clear increases in Pb-I bond length and resulting A-site cavity volume are a result of the larger GA cation. Furthermore, the large GA cation distorts the PbI_6^{4-} octahedra, resulting in a larger σ^2 and D relative to $(A')(MA)Pb_2I_7$ structures. Similarly, other compounds with larger cations, such as $(A')(FA)Pb_2I_7$ (A' = BA, HA[112]) and $(A')_2(DMA)Pb_2I_7$ (A' = BA,[111] PA[117]), exhibit elongated Pb-I bonds and larger distortion relative to MA cations, though to a lesser extent than GA. Figure 1.6d,e shows the trend of increasing average Pb-I bond length, A-site cavity (cage) volume, σ^2, and D with increasing A-site cation size.

The n = 3 iodide RP perovskite structures follow the same trend, as the Pb-I bonds in $(BA)_2(EA)_2Pb_3I_{10}$ (space group *Cmc2₁*, shown in Figure 1.7ab)[113] are elongated and induce a larger A-site cavity compared to $(BA)_2(MA)_2Pb_3I_{10}$ (Table 1.2). In these n = 3 structures, the Pb-I bonding changes depending on whether the octahedra is in the inner layer or the two-outer layers of PbI_6^{4-} octahedra. The inner layer has significantly more distorted octahedra, as it is templated by two EA cations on both sides with large steric interactions (Figure 1.7a). Whereas the outer layer is templated by one EA cation and a more flexible BA cation interaction, leading to less distorted octahedra. To investigate the effect of the larger cation on the structure, $(BA)_2(EA_xMA_{1-x})_2Pb_3I_{10}$ was grown into SCs with varying MA-EA ratios. As the EA content is increased, the Pb-I bond length, cage volume, σ^2, and quadratic elongation (a parameter analogous to distortion index) increases as shown in Figure 1.7c,d.

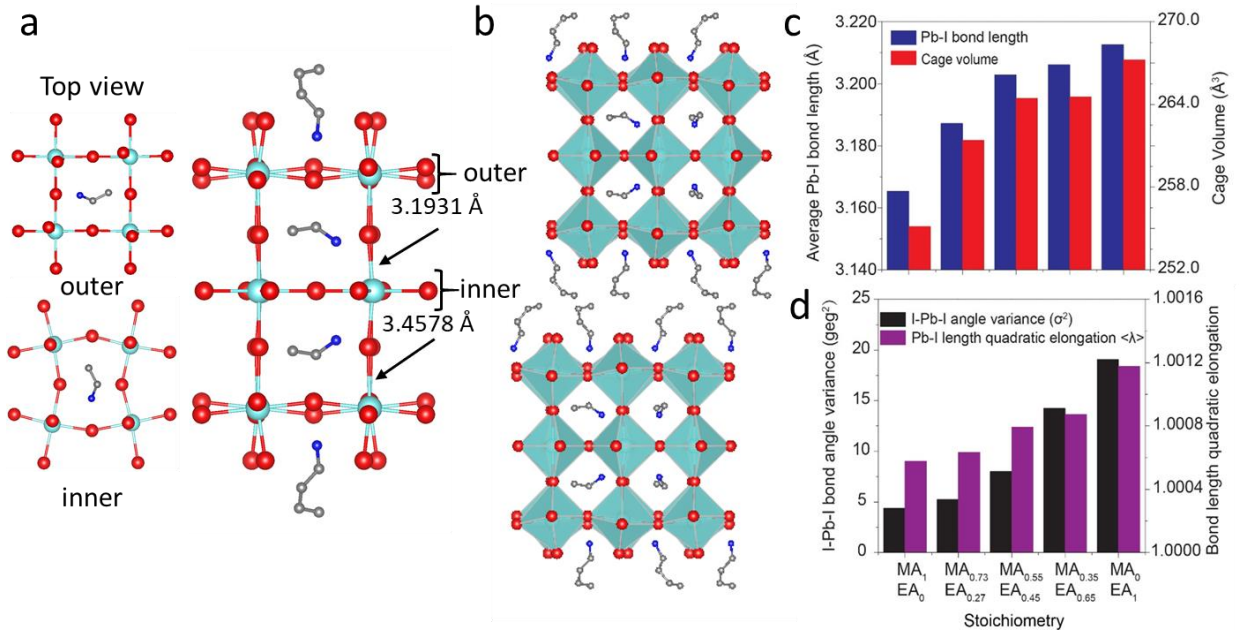

Figure 1.7. $(BA)_2(EA)_2Pb_3I_{10}$ RP perovskite crystal structure and bonding parameters of $(BA)_2(MA_{1-x}EA_x)_2Pb_3I_{10}$. (a) Crystal packing diagram of $(BA)_2(EA)_2Pb_3I_{10}$ with the outer and inner layers shown as well as the elongated and varying Pb-I bond lengths (b) Crystal packing of the extended network of $(BA)_2(EA)_2Pb_3I_{10}$. The average bond Pb-I bond length and cage volume (c) and average σ^2 and quadratic elongation (d) in the MA-EA alloys of $(BA)_2(MA_{1-x}EA_x)_2Pb_3I_{10}$ SCs.

Similar to the iodide system, the bromide RP structures feature increasing D, σ^2, bond lengths, and cage volume as the A-site cation size increases (Table 1.2). $(BA)_2(A)Pb_2Br_7$ (A= Cs,[114] MA,[118] FA[119]) form in the *Cmc2₁* space group at RT. Furthermore, iso-butylammonium (IBA) has been used as the spacer cation in $(IBA)_2(EA)Pb_2Br_7$ which crystallizes in the Cc space group, completing a wide range of A cations in (A')$(A)Pb_2B7$ single crystals.[120] Multiple $(A')(EA)_2Pb_3Br_{10}$ structures have been demonstrated with the A' spacer cation varying from EA,[115, 121] BA,[122] isobutylammonium (IBA),[120] and 4-aminomethyl-1-cyclohexanecarboxylate.[123]

The structure $(EA)_4Pb_3Br_{10}$ forms layered compounds where the EA cation serves as both the A-site cation as well as the spacer cation. Similarly, $(EA)_4Pb_3Cl_{10}$ adopts the *Cmc2₁* [103] space group with elongated Pb-Cl bond lengths and a high distortion index.

1.4.1 Optical properties of 2D perovskite with large A-site cations

Similar to 3D perovskites, the choice of cation in RP perovskites influences the bonding of the inorganic framework and as a result, the band gap and optical properties. In our recent work, we tuned the A-site cation from Cs to acetamidinium in nanoplates of $(HA)_2(A)Pb_2I_7$ RP perovskites to show the effect of the A-cation on the optical properties.[124] Figure 1.8a shows the absorbance/PL energy vs. A-site cation size/α, which clearly shows that RP perovskites with large A-site cations (EA, DMA, GA, AA) have higher energy absorption and PL relative to MA and FA based RP perovskites. This trend is the result of the bond elongation in the stretched large cation containing structures. However, the absorption/PL energy is also higher for the smaller $(HA)_2CsPb_2I_7$, likely due to the tilting in Cs based compounds.[114] Therefore, we see a parabolic or "V-shaped" trend in band gap versus cation size/α (Figure 1.8a). Trends in n = 2 bromide RPs show band gaps decrease with the tolerance factor for A= Cs>MA>FA (left axis of Figure 1.8b), correlating extremely well with 3D perovskites (right axis of Figure 1.8b). While an EA n = 2 bromide compound is yet to be optically characterized, characterization of n = 3 bromide structures suggest that EA would induce a higher band gap than MA in $(BA)_2(A)Pb_2Br_7$ structures, predicting a parabolic trend of band gap versus tolerance factor, much like the RP iodides. This combination of evidence points to similar A-cation effects in both 3D and 2D perovskites and the parabolic or V-shape trend being a real phenomenon.

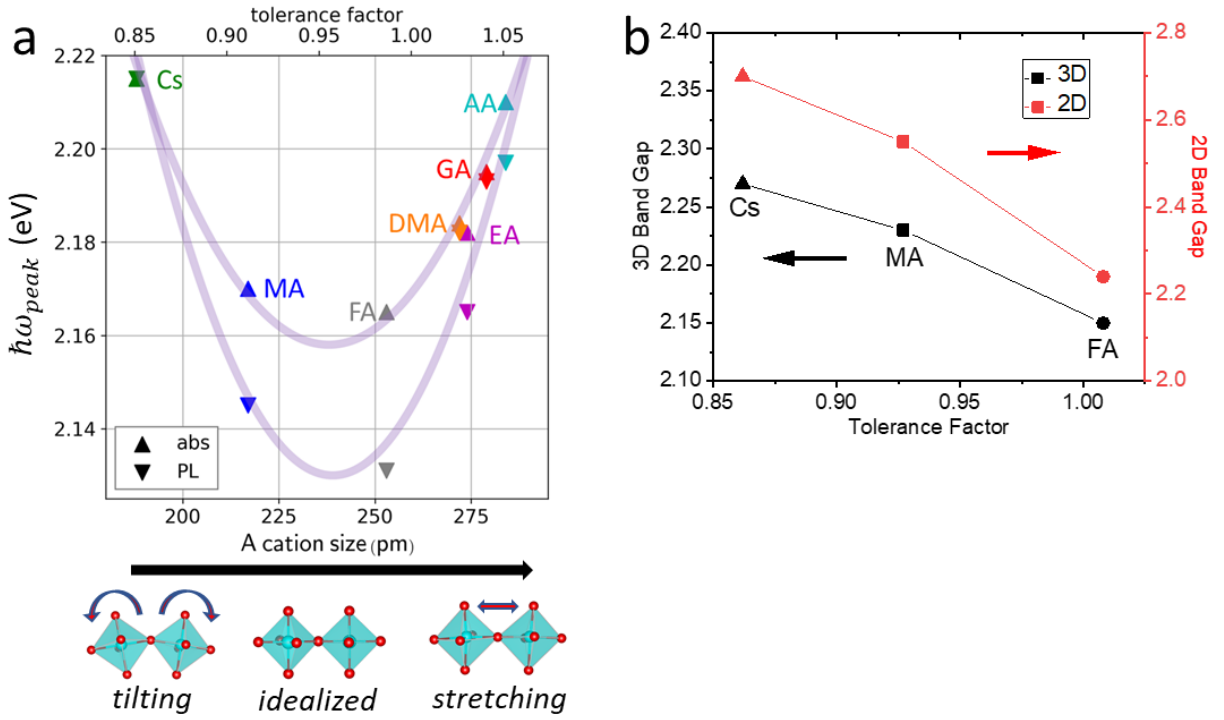

Figure 1.8. Band gap versus cation size/tolerance factor in RP perovskites. (a) absorbance (abs) and PL energy of $(HA)_2(A)Pb_2I_7$ vs. A-site cation size (bottom axis) and tolerance factor (top axis). The schematic structural diagrams below show the proposed tilting and stretching that induces the increase in band gap. (b) Band gap of $(BA)_2(A)Pb_2Br_7$ (left axis) and $(A)PbBr_3$ vs. tolerance factor.

The band gap dependence on the A-site size can be discussed in the context of the chemical pressure of halide perovskites. Small A-site cations induce strong positive chemical pressure, leading to the same M-X bond shortening / tilting as seen in perovskite structures under external pressure.[37] If the A-site cation is large, there is a strong negative chemical pressure inside the A-site cavity, similar to if a material was stretched or "negative pressure" was exerted on it, which results in the elongated bonds shown in Table 1.2. Figure 1.9a shows absorbance energy versus A-site cation size of 2D perovskites with large cations at ambient conditions together with the band

gap evolution of 3D perovskites under external pressure. In 3D perovskites, absorbance decreases under applied pressure due to the shortened Pb-X bonds. In 2D perovskites, the negative chemical pressure induced by large cations results in increased absorbance, effectively providing a clear picture of the effect of both positive and negative pressure. The effect of external pressure has also been investigated on 2D $(HA)_2(GA)Pb_2I_7$ perovskites (Figure 1.9b).[125] At 0 GPa, the structure is a "stretched" by the large GA cation causing a large absorbance energy. When the external pressure is increased, the absorbance energy decreases immediately, as the applied pressure is counteracting the negative chemical pressure induced by the large A-site cation. Around 5 GPa the trend reverses, which is expected from tilting and has been demonstrated in other 2D RP perovskites as well.[126] Alloying is another mechanism that is less explored in 2D perovskite to change band gap. Figure 1.9c shows the alloying of $(BA)_2(MA_xEA_{1-x})_2Pb_3I_{10}$. The structure's absorbance energy changes in a linear fashion from the pure MA structure (x = 0), with the lowest absorbance energy, to the pure EA structure (x =1), with the highest absorbance energy.

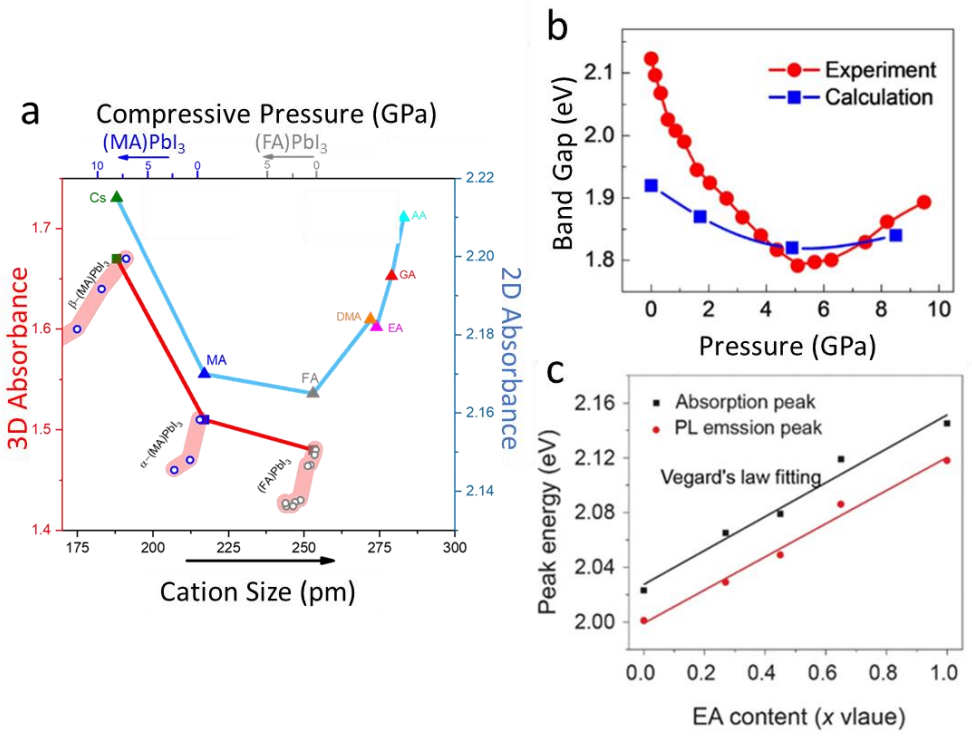

Figure 1.9. External and chemical pressure effects on the optical properties of 2D RP and 3D halide perovskites. Absorbance energy of (a) 3D (left) and 2D (right) perovskites with varying A-site cation sizes and varying external pressure (3D, top axis). (b) External pressure of the compound $(HA)_2(GA)Pb_2I_7$.

A-site cations also influence the carrier decay properties in RP perovskites. RP perovskites with A-site cations larger than FA exhibit decreased PL intensity and lifetime. Figure 1.10a shows this general trend with the decrease in PL intensity of $(BA)_2(MA_xEA_{1-x})_2Pb_3I_{10}$ as the amount of the large EA cation increases. Figure 1.10b shows shorter time-resolved PL (TRPL) lifetime for large GA and DMA cations relative to MA and FA in $(BA)_2(A)Pb_2I_7$.[111] All TRPL shows the same trend from multiple reports: large A-site cations are detrimental to carrier lifetime, suggesting undesirable non-radiative recombination is prominent in these materials. To better understand what induces this shorter carrier lifetime, we discuss an important result from investigating

$(HA)_2(GA)Pb_2I_7$ under external pressure.[125] Figure 1.10c shows the red-tail of the PL in $(HA)_2(GA)Pb_2I_7$, which can be attributed to trap-assisted recombination. When external pressure is applied to $(HA)_2(GA)Pb_2I_7$, the red tail decreases and the PL peak becomes more symmetric while the PL intensity increases (Figure 1.10d). Extrinsic traps such as interstitials or vacancies could exist in this material; however, this evidence points to the traps being related to the intrinsic crystal structure, which is modulated directly by the increasing external pressure. Temperature dependent PL provides further evidence for intrinsic features causing short lived carriers (Figure 1.10e). The PL peak width narrows in both $(HA)_2(A)Pb_2I_7$ (A = MA, GA) compounds with decreasing temperature, as expected with the decreasing contribution from phonons at low T. Fitting of the PL peak width vs. temperature data in Figure 1.10f reveals $(HA)_2(GA)Pb_2I_7$ has a larger inhomogeneous broadening term (Γ_0) and larger electron-phonon coupling strength (γ_{LO}) than $(HA)_2(MA)Pb_2I_7$. The combination of these features suggests the intrinsic structural distortions affect the vibrational modes of the lattice in a way that is detrimental to the carrier lifetime.[127] Other observations include lower Raman resonance energies of the inorganic lattice for structures with large cations DMA and GA compared to MA and broader transient absorption features of large cation compounds, attributed to a wider energetic distribution of electronic states.[111] The culmination of these results suggests that the distortions induced by large A-site cations detrimentally impact the carrier lifetimes via vibrational mode coupling. A-site cations

with suitable sizes that do not induce highly distorted structures are more conducive for excellent photophysical properties of 2D (and 3D) halide perovskites.

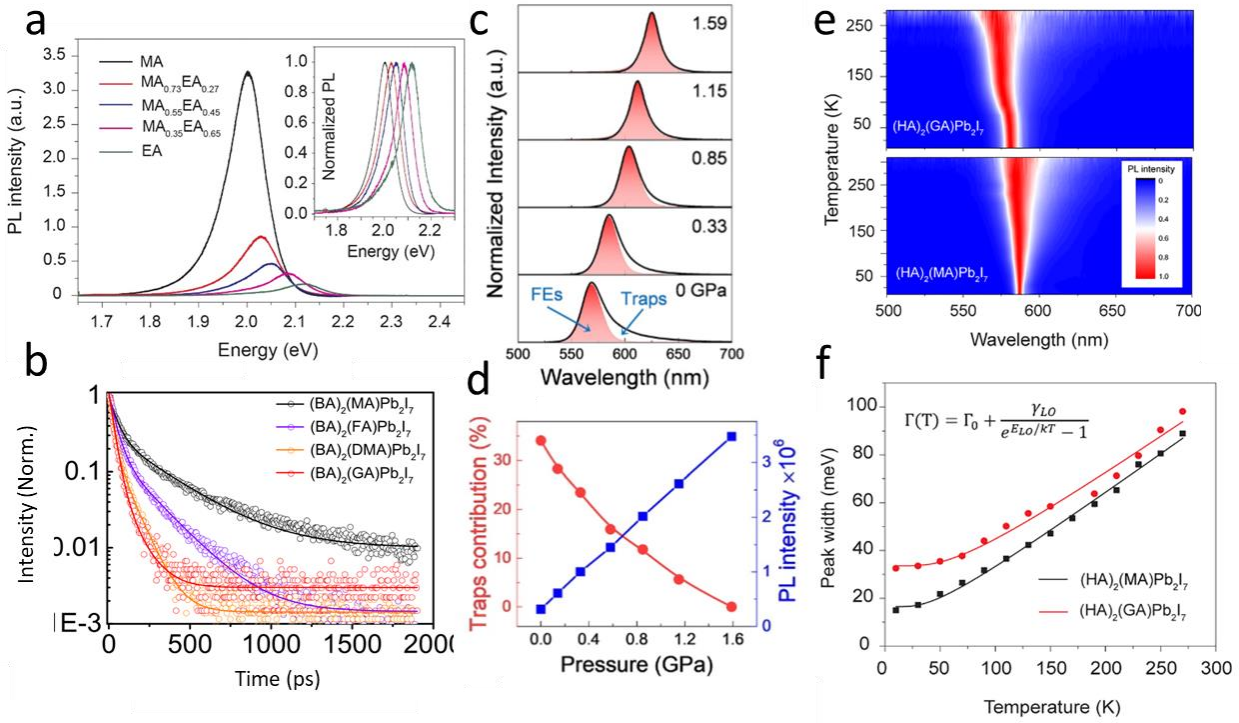

Figure 1.10. Optical properties of RP perovskites with large A-site cations showing carrier behavior. (a) PL intensity of $(BA)_2(MA_xEA_{1-x})_2Pb_3I_{10}$. (b) Time-resolved PL in $(BA)_2(A)Pb_2I_7$ (A = MA, FA, DMA, GA) showing the decrease in lifetime with larger A-site cation. (c) PL of $(HA)_2(GA)Pb_2I_7$ showing the red tail decreasing as pressure increases. (d) Trap contribution and PL intensity vs. external pressure applied on $(HA)_2(GA)Pb_2I_7$. (e) Temperature dependent PL of $(HA)_2(A)Pb_2I_7$ (A = GA, MA) showing line narrowing with temperature. (f) Fittings of the T dependent PL showing increased electron-phonon coupling in $(HA)_2(GA)Pb_2I_7$.

1.4.2 Non-linear properties of RP perovskites

Several RP perovskites have non-centrosymmetric crystal structures and are candidates for non-linear (NL) properties including second-harmonic generation (SHG) and ferroelectricity.

Non-centrosymmetric RP structures with $n \geq 2$ are a result of the interplay between the spacer cation and A-site cation templating the inorganic framework while $n = 1$ structures only have the spacer cation (A') templating the structure to induce inversion asymmetry. Here we focus on utilizing the A-site cation to modulate the NL properties, which is limited to RP structures with $n \geq 2$.

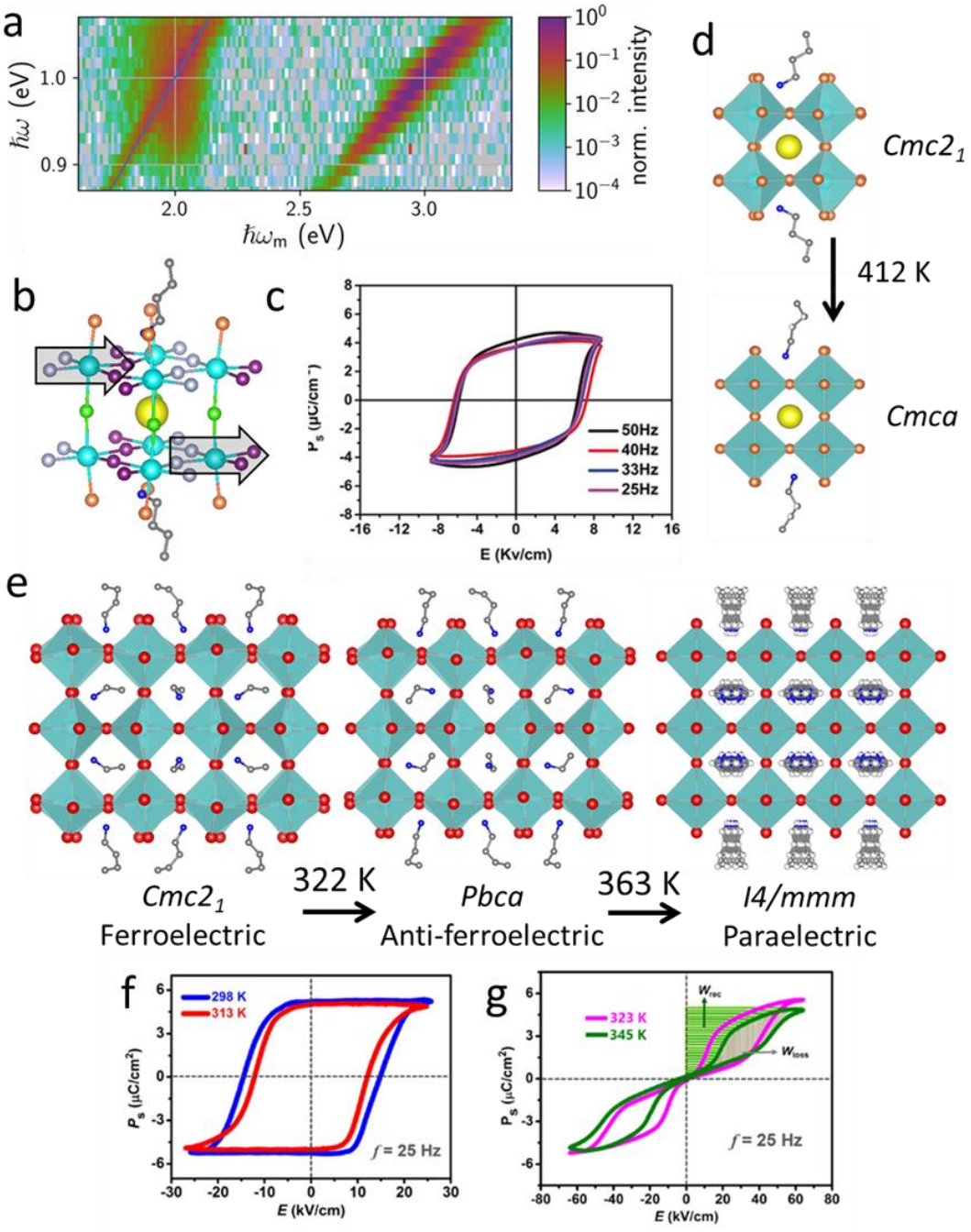

Figure 1.11. Non-linear properties of RP perovskites. (a) Multidimensional harmonic generation of $(BA)_2(EA)_3Pb_2I_{10}$ where the blue line shows SHG.[19] (b) Structure of $(BA)_2(Cs)Pb_2Br_7$ with the

unique bromide positions colored different to show the lack of inversion symmetry.[114] (c) P-E hysteresis loops of $(BA)_2CsPb_2Br_7$ with varying frequency. (d) The phase change of at 412 K from the *Cmc2₁* to the *Cmca* space group of $(BA)_2CsPb_2Br_7$. (e) Structures of $(BA)_2(EA)_2Pb_3I_{10}$ at increasing temperatures.[128] P-E hysteresis loops of $(BA)_2(EA)_2Pb_3I_{10}$ in the (f) ferroelectric phase (*Cmc2₁*) and (g) anti-ferroelectric phase (*Pbca*).

Second harmonic generation (SHG) is the frequency doubling of light from materials that exhibit broken inversion symmetry. This non-linear property has been observed in numerous RP perovskite structures that are inversion asymmetric. The compounds in Table 1.3 all exhibit SHG as predicted from there non-centrosymmetric crystal structures. However, observing SHG can be misleading in halide perovskites which can have large two-photon absorption coefficients[20] as well as strong multi-photon photoluminescence.[19] Figure 1.10a shows the multi-dimensional harmonic generation spectrum from $(BA)_2(EA)_2Pb_3I_{10}$, which helps resolves the SHG signal. The frequency doubles at varying wavelengths shown by the sloped line emission, while the mPL emission does not varying with excitation wavelength. $(BA)_2(MA)_2Pb_3I_{10}$ does not show this SHG, because the large EA cation is required to induce non-centrosymmetry.

Several ferroelectric RP perovskite phases have been identified that are non-centrosymmetric and exhibit spontaneous polarization at room temperature. Overall, significantly more bromide RP perovskites have demonstrated ferroelectric properties than their iodide counterparts. $(BA)_2(A)Pb_2Br_7$ (A = Cs,[114] MA,[118] FA[119]) are all ferroelectric in their RT non-centrosymmetric *Cmc2₁* phase. Figure 1.10b shows $(BA)_2CsPb_2Br_7$ with tilted octahedra and distorted octahedra at RT. The unique bromide positions in the crystal structure are color coded, highlighting that adjacent octahedra (across the center Cs atom for reference) are only related

through translational symmetry, not inversion. As drawn, the purple colored and grey colored bromides are on the right side and left side of the octahedra, respectively, representing different bromide positions. Two adjacent octahedra are drawn with an arrow arbitrarily draw showing the isotropy of the structure sites. These cannot be symmetry adapted through inversion symmetry at any point in the crystal structure. As a result, $(BA)_2CsPb_2Br_7$ shows ferroelectric properties demonstrated by P-E hysteresis loops at RT (Figure 1.10c). Furthermore, $(BA)_2CsPb_2Br_7$ undergoes a ferroelectric phase transition at 412 K to a high temperature paraelectric phase with ideal octahedra, adopting a centrosymmetric space group (*Cmca*). All the $(BA)_2(A)Pb_2Br_7$ phases undergo a ferroelectric phase transition to a higher symmetry space group upon heating (*Cmca* for Cs, MA and *Cmcm* for FA), with the detailed space groups, T_c and P_s shown in Table 1.3.

Table 1.3. Non-centrosymmetric and Ferroelectric compounds ($n \geq 2$) curie temperature (T_c), spontaneous polarization (P_s), and space groups.

Compound	T_c (K)	P_s ($\mu C/cm^2$)	*Space Group* (Phase)	
			RT	HT
$(EA)_4Pb_3Cl_{10}$[129]	415	4.5	*Cmc2₁* (Ferroelectric)	*I4/mmm* (Paraelectric)
$(BA)_2(Cs)Pb_2Br_7$[114]	412	4.2	*Cmc2₁* (Ferroelectric)	*Cmca* (Paraelectric)
$(BA)_2(MA)Pb_2Br_7$[118]	352	3.6	*Cmc2₁* (Ferroelectric)	*Cmca* (Paraelectric)
$(BA)_2(FA)Pb_2Br_7$[119]	322	3.8	*Cmc2₁* (Ferroelectric)	*Cmcm* (Paraelectric)
$(IBA)_2(EA)Pb_2Br_7$[120]	326	1.0	*Cc* (Ferroelectric)	*I4/mmm* (Paraelectric)
$(IBA)_2CsPb_2Br_7$ [130]	353	6.3	*Pmnb* (Antiferroelectric)	*Cmca* (Paraelectric)
$(EA)_4Pb_3Br_{10}$	384	3.5	*C2cb* (Ferroelectric)	*I4/mmm* (Paraelectric)
$(BA)_2(MA)_2Pb_3Br_{10}$	315	2.9	*Cmc2₁* (Ferroelectric)	*Cmca* (Paraelectric)
$(BA)_2(EA)_2Pb_3Br_{10}$[122]	380	5.0	*Cmc2₁* (Ferroelectric)	*I4/mmm* (Paraelectric)
$(IBA)_2(EA)_2Pb_3Br_{10}$[120]	370	3.5	*Cmc2₁* (Ferroelectric)	*I4/mmm* (Paraelectric)
(4-aminomethyl-1-cyclohexane carboxylate)$_2(EA)_2Pb_3Br_{10}$[123]	370	2.9	*Pm* (Ferroelectric)	*Pmmn* (Paraelectric)
(isopentylammonium)$_2(EA)_2Pb_3I_{10}$[131]	340	5.2	*Cmc2₁* (Ferroelectric)	*Pmcn* (Antiferroelectric)
				I4/mmm (Paraelectric)
$(BA)_2(EA)_2Pb_3I_{10}$[128]	363	5.6	*Cmc2₁* (Ferroelectric)	*Pbca* (Antiferroelectric)
				I4/mmm (Paraelectric)

Footnote: IBA = isobutylammonium

The phase $(BA)_2(EA)_2Pb_3I_{10}$ crystallizes in the non-centrosymmetric *Cmc2₁* space group which is a direct result of the large EA cation occupying the a-site. The iodide phases appear less

likely to adopt the non-centrosymmetric space groups than the bromide phases, as $(BA)_2(MA)_2Pb_3I_{10}$ is centrosymmetric (*C2cb* no. 41) unlike its bromide counterpart. However, even in the iodide phase, the large EA cation induces strong distortions into the structure. This example is an excellent demonstration of how A-site cations can be utilized to tailor properties. $(BA)_2(EA)_2Pb_3I_{10}$ undergoes a phase change at 322 K from a RT ferroelectric phase to a high T anti-ferroelectric phase.[128] The room temperature phase is ferroelectric as shown by the P-E hysteresis (Figure 1.10f). Between 322 and 363 K, the compound is anti-ferroelectric, showing the double P-E hysteresis loops typical of an anti-ferroelectric phase (Figure 1.10g). The primary difference between these two phases is the position of the EA A-site cation. In the anti-ferroelectric phase (*Pbca*), the A-site cation dipoles oppose each other as shown in Figure 1.10e. At even higher temperature (T > 363 K), the A-site cation becomes disordered and the octahedra become oriented (non-tilted) in the centrosymmetric *I4/mmm* phase. The same ferroelectric to anti-ferroelectric to paraelectric phase change is observed in $(isopentylammonium)_2(EA)_2Pb_3I_{10}$.[131] Outside of utilizing the large EA cations to access ferroelectricity in the RP iodide phases, Dion-Jacobson phases have also exhibited ferroelectric properties with the diammonium 4-(aminomethyl)piperdinium spacer cation.[132, 133] These insights, including the ability of A-site cations to induce distortions in structures necessary for ferroelectricity, will guide future exploration and prediction of ferroelectric phases in 2D perovskites.

1.5 Conclusions and future perspectives

Halide perovskites are promising materials for next generation semiconductor applications, owing in part to their structural tunability. The A-site cation provides a way to tune the perovskite crystal structure and bonding, which is consequential to the properties of the material. Using A-site cations

and other compositional changes to access new properties could drive continued progress in the research of halide perovskites and broader metal halide semiconductors. Areas of research that can be aided by the tuning of the A-site cation includes exploring new halide perovskite structures enabled by A-site cations, RP structures with expanded A-site cations for improved non-linear properties, and structure control in halide perovskites that have utility for spin-tronic applications.

Significant research has gone into finding halide perovskites with metals beyond group IV (Pb, Sn, Ge). We believe it is possible that new metals and metal combinations can be discovered in perovskite structures by varying the A-site cations. Two particularly interesting structures are the double halide perovskite $A_2M^IM^{III}X_6$[134] and vacancy ordered double halide perovskite A_2MX_6 (e.g. $A_2M^{IV}\square X_6$ where $\square$ is a vacancy). [135, 136] These unique halide perovskites are currently being explored for their magnetic properties,[137] light-emission,[138] and could have undiscovered applications.[139] Large A-site cations could aid in the formation of double and vacancy ordered double perovskites with X = iodide, which has been difficult to form into these structures.[140] Iodide perovskites are desirable for their larger spin-orbit coupling (SOC) and lower band gaps.[137] In addition, being able to tune the A-site could allow metal cations not previously utilized could be incorporated into these perovskite structures. In the double halide perovskites, a wide range of trivalent metals could be incorporated, such as Ru^{III}, which is being explored for potential quantum spin-liquids.[141] New structures and combinations of compounds could be accessed by using a variety of A-site cations, ranging from the small Rb^+ to the extremely large trimethylammonium. Furthermore, the A-site cations could be used to tune these perovskite structures to produce desired properties. A-site cations have already been investigated to tune the charge transfer bands as well as spin-orbit coupling strength of vacancy ordered halide perovskites.[137]

In addition to using cation chemistry to access new structures, we believe the A-site cation can be used to expand the chemistry of RP perovskites. As discussed above, RP perovskites have shown promise as ferroelectrics. So far, most demonstrations are of ferroelectric compounds are Pb-based, bromide phases. As we discussed, the distortions induced by the A-site cations can give rise to the necessary non-centrosymmetry in the RP perovskite crystal structure. Limited iodide structures have shown ferroelectricity, but the incorporation of large A-site cations could expand their use like $(A')(EA)_2Pb_2I_{10}$ structures were able to, particularly when utilized in a Dion-Jacobson phase.[133] Additionally, tin and germanium compounds have not been demonstrated in RP perovskites with large A-site cations. Based on the knowledge of analogous 3D perovskites, such as the highly distorted $(TMA)SnBr_3$, we believe these large A-cations may lead to highly distorted RP phases. There is a large number of combinations of halides and metals to be investigated in RP structures with large A-site cations, which we believe will create a clearer picture of what drives ferroelectricity and increases the polarization strength.

One of the most exciting future directions that can be aided by A-site cation chemistry is the utilization of halide perovskites for spin-orbitronics. In halide perovskite phases that exhibit large spin-orbit coupling (SOC) and broken inversion symmetry, the Rashba and/or Dresselhaus effects can be observed.[142] These effects induce spin splitting, allowing for spin manipulation in the absence of magnetic fields opening up opportunities for spin-based device applications.[143] Lead and tin exhibit strong SOC, leading to spin splitting effects whenever inversion symmetry is broken in Pb, Sn halide perovskites. The required inversion asymmetry can result from broken inversion within the crystal structure or from local, transient symmetry breaking as demonstrated in 3D halide perovskites.[144, 145] The Rashba effect has also been demonstrated in 2D perovskites.

Experimentally, spin splitting has been shown in $(PEA)_2PbI_4$[146, 147] and $(BA)_2(MA)Pb_2I_7$. [148] However, further investigation is still needed to uncover the relationships between the RP perovskite crystal structure and Rashba splitting strengths. So far, only Yu, et. al. has used calculations to show that Rashba splitting strength correlates to octahedron distortion in 2D RP perovskites (n = 1–6).[149] This correlation suggests an extremely promising quality, since as shown in this review, the choice of A-site cation dictates octahedral tilting and distortion, with large A-site cations inducing strong distortions. Therefore, tuning of the A-site cation is a mechanism for manipulating the distortion parameters and the resulting static spin splitting effects. A promising area of future work is to utilize A-site cation chemistry to target phases of 2D perovskites with strong Rashba splitting for spin-orbitronic applications.

1.6 References

1. Kojima, A.; Teshima, K.; Shirai, Y.; Miyasaka, T., Organometal Halide Perovskites as Visible-Light Sensitizers for Photovoltaic Cells. *J. Am. Chem. Soc.* **2009,** *131* (17), 6050-6051.

2. Lee, M. M.; Teuscher, J.; Miyasaka, T.; Murakami, T. N.; Snaith, H. J., Efficient Hybrid Solar Cells Based on Meso-Superstructured Organometal Halide Perovskites. *Science* **2012,** *338* (6107), 643-647.

3. Yoo, J. J.; Seo, G.; Chua, M. R.; Park, T. G.; Lu, Y.; Rotermund, F.; Kim, Y.-K.; Moon, C. S.; Jeon, N. J.; Correa-Baena, J.-P.; Bulović, V.; Shin, S. S.; Bawendi, M. G.; Seo, J., Efficient perovskite solar cells via improved carrier management. *Nature* **2021,** *590* (7847), 587-593.

4. Quan, L. N.; Rand, B. P.; Friend, R. H.; Mhaisalkar, S. G.; Lee, T.-W.; Sargent, E. H., Perovskites for Next-Generation Optical Sources. *Chem. Rev* **2019,** *119* (12), 7444-7477.

5. Zhu, H.; Fu, Y.; Meng, F.; Wu, X.; Gong, Z.; Ding, Q.; Gustafsson, M. V.; Trinh, M. T.; Jin, S.; Zhu, X. Y., Lead halide perovskite nanowire lasers with low lasing thresholds and high quality factors. *Nat. Mater.* **2015,** *14* (6), 636-642.

6. Chin, X. Y.; Cortecchia, D.; Yin, J.; Bruno, A.; Soci, C., Lead iodide perovskite light-emitting field-effect transistor. *Nat. Commun* **2015,** *6* (1), 7383.

7. Long, G.; Sabatini, R.; Saidaminov, M. I.; Lakhwani, G.; Rasmita, A.; Liu, X.; Sargent, E. H.; Gao, W., Chiral-perovskite optoelectronics. *Nat. Rev. Mater.* **2020,** *5* (6), 423-439.

8. Dunlap-Shohl, W. A.; Zhou, Y.; Padture, N. P.; Mitzi, D. B., Synthetic Approaches for Halide Perovskite Thin Films. *Chem. Rev* **2019,** *119* (5), 3193-3295.

9. Shamsi, J.; Urban, A. S.; Imran, M.; De Trizio, L.; Manna, L., Metal Halide Perovskite Nanocrystals: Synthesis, Post-Synthesis Modifications, and Their Optical Properties. *Chem. Rev* **2019,** *119* (5), 3296-3348.

10. Stoumpos, C. C.; Malliakas, C. D.; Kanatzidis, M. G., Semiconducting Tin and Lead Iodide Perovskites with Organic Cations: Phase Transitions, High Mobilities, and Near-Infrared Photoluminescent Properties. *Inorg. Chem.* **2013,** *52* (15), 9019-9038.

11. Stoumpos, C. C.; Cao, D. H.; Clark, D. J.; Young, J.; Rondinelli, J. M.; Jang, J. I.; Hupp, J. T.; Kanatzidis, M. G., Ruddlesden–Popper Hybrid Lead Iodide Perovskite 2D Homologous Semiconductors. *Chem. Mater* **2016,** *28* (8), 2852-2867.

12. Ruddlesden, S. N.; Popper, P., The compound $Sr_3Ti_2O_7$ and its structure. *Acta Crystallographica* **1958,** *11* (1), 54-55.

13. Mao, L.; Ke, W.; Pedesseau, L.; Wu, Y.; Katan, C.; Even, J.; Wasielewski, M. R.; Stoumpos, C. C.; Kanatzidis, M. G., Hybrid Dion–Jacobson 2D Lead Iodide Perovskites. *J. Am. Chem. Soc.* **2018,** *140* (10), 3775-3783.

14. Smith, I. C.; Hoke, E. T.; Solis-Ibarra, D.; McGehee, M. D.; Karunadasa, H. I., A Layered Hybrid Perovskite Solar-Cell Absorber with Enhanced Moisture Stability. *Angew. Chem. Int. Ed.* **2014,** *53* (42), 11232-11235.

15. Grancini, G.; Roldán-Carmona, C.; Zimmermann, I.; Mosconi, E.; Lee, X.; Martineau, D.; Narbey, S.; Oswald, F.; De Angelis, F.; Graetzel, M.; Nazeeruddin, M. K., One-Year stable perovskite solar cells by 2D/3D interface engineering. *Nat. Commun* **2017,** *8* (1), 15684.

16. Yang, X.; Zhang, X.; Deng, J.; Chu, Z.; Jiang, Q.; Meng, J.; Wang, P.; Zhang, L.; Yin, Z.; You, J., Efficient green light-emitting diodes based on quasi-two-dimensional composition and phase engineered perovskite with surface passivation. *Nat. Commun* **2018,** *9* (1), 570.

17. Na Quan, L.; Ma, D.; Zhao, Y.; Voznyy, O.; Yuan, H.; Bladt, E.; Pan, J.; García de Arquer, F. P.; Sabatini, R.; Piontkowski, Z.; Emwas, A.-H.; Todorović, P.; Quintero-Bermudez, R.; Walters, G.; Fan, J. Z.; Liu, M.; Tan, H.; Saidaminov, M. I.; Gao, L.; Li, Y.; Anjum, D. H.; Wei, N.; Tang, J.; McCamant, D. W.; Roeffaers, M. B. J.; Bals, S.; Hofkens, J.; Bakr, O. M.; Lu, Z.-H.; Sargent, E. H., Edge stabilization in reduced-dimensional perovskites. *Nat. Commun* **2020,** *11* (1), 170.

18. Saparov, B.; Mitzi, D. B., Organic–Inorganic Perovskites: Structural Versatility for Functional Materials Design. *Chem. Rev* **2016,** *116* (7), 4558-4596.

19. Morrow, D. J.; Hautzinger, M. P.; Lafayette, D. P.; Scheeler, J. M.; Dang, L.; Leng, M.; Kohler, D. D.; Wheaton, A. M.; Fu, Y.; Guzei, I. A.; Tang, J.; Jin, S.; Wright, J. C., Disentangling Second Harmonic Generation from Multiphoton Photoluminescence in Halide Perovskites using Multidimensional Harmonic Generation. *J. Phys. Chem. Lett.* **2020,** *11* (16), 6551-6559.

20. Li, L.; Sun, Z.; Wang, P.; Hu, W.; Wang, S.; Ji, C.; Hong, M.; Luo, J., Tailored Engineering of an Unusual $(C_4H_9NH_3)_2(CH_3NH_3)_2Pb_3Br_{10}$ Two-Dimensional Multilayered Perovskite Ferroelectric for a High-Performance Photodetector. *Angew. Chem. Int. Ed.* **2017,** *56* (40), 12150-12154.

21. Jana, M. K.; Song, R.; Liu, H.; Khanal, D. R.; Janke, S. M.; Zhao, R.; Liu, C.; Valy Vardeny, Z.; Blum, V.; Mitzi, D. B., Organic-to-inorganic structural chirality transfer in a 2D hybrid perovskite and impact on Rashba-Dresselhaus spin-orbit coupling. *Nat. Commun* **2020,** *11* (1), 4699.

22. Mao, L.; Stoumpos, C. C.; Kanatzidis, M. G., Two-Dimensional Hybrid Halide Perovskites: Principles and Promises. *J. Am. Chem. Soc.* **2019,** *141* (3), 1171-1190.

23. Li, X.; Hoffman, J. M.; Kanatzidis, M. G., The 2D Halide Perovskite Rulebook: How the Spacer Influences Everything from the Structure to Optoelectronic Device Efficiency. *Chem. Rev* **2021,** *121* (4), 2230-2291.

24. Jena, A. K.; Kulkarni, A.; Miyasaka, T., Halide Perovskite Photovoltaics: Background, Status, and Future Prospects. *Chem. Rev* **2019,** *119* (5), 3036-3103.

25. Goldschmidt, V. M., Die Gesetze der Krystallochemie. *Naturwissenschaften* **1926,** *14* (21), 477-485.

26. Kieslich, G.; Sun, S.; Cheetham, A. K., Solid-state principles applied to organic–inorganic perovskites: new tricks for an old dog. *Chem. Sci* **2014,** *5* (12), 4712-4715.

27. Travis, W.; Glover, E. N. K.; Bronstein, H.; Scanlon, D. O.; Palgrave, R. G., On the application of the tolerance factor to inorganic and hybrid halide perovskites: a revised system. *Chem. Sci* **2016,** *7* (7), 4548-4556.

28. Filip, M. R.; Giustino, F., The geometric blueprint of perovskites. *Proc. Natl. Acad. Sci. U.S.A.* **2018,** *115* (21), 5397-5402.

29. Bartel, C. J.; Sutton, C.; Goldsmith, B. R.; Ouyang, R.; Musgrave, C. B.; Ghiringhelli, L. M.; Scheffler, M., New tolerance factor to predict the stability of perovskite oxides and halides. *Sci. Adv.* **2019,** *5* (2), eaav0693.

30. Glazer, A. M., The classification of tilted octahedra in perovskites. *Acta Crystallographica Section B* **1972,** *28* (11), 3384-3392.

31. Howard, C. J.; Stokes, H. T., Structures and phase transitions in perovskites - a group-theoretical approach. *Acta Crystallographica Section A* **2005,** *61* (1), 93-111.

32. Baur, W. H., The geometry of polyhedral distortions. Predictive relationships for the phosphate group. *Acta Crystallographica Section B* **1974,** *30* (5), 1195-1215.

33. Robinson, K.; Gibbs, G. V.; Ribbe, P. H., Quadratic Elongation: A Quantitative Measure of Distortion in Coordination Polyhedra. *Science* **1971,** *172* (3983), 567-570.

34. Mączka, M. a.; Ptak, M.; Gągor, A.; Stefańska, D.; Zaręba, J. K.; Sieradzki, A., Methylhydrazinium Lead Bromide: Noncentrosymmetric Three-Dimensional Perovskite with Exceptionally Large Framework Distortion and Green Photoluminescence. *Chem. Mater* **2020,** *32* (4), 1667-1673.

35. Geselle, M. F., H., Crystal structure of trimethylammonium tribromostannate(II), $(CH_3)_3NHSnBr_3$ *Zeitschrift für Kristallographie* **1996,** *211* (1), 46-46.

36. Gallop, N. P.; Selig, O.; Giubertoni, G.; Bakker, H. J.; Rezus, Y. L. A.; Frost, J. M.; Jansen, T. L. C.; Lovrincic, R.; Bakulin, A. A., Rotational Cation Dynamics in Metal Halide Perovskites: Effect on Phonons and Material Properties. *J. Phys. Chem. Lett.* **2018,** *9* (20), 5987-5997.

37. Jaffe, A.; Lin, Y.; Beavers, C. M.; Voss, J.; Mao, W. L.; Karunadasa, H. I., High-Pressure Single-Crystal Structures of 3D Lead-Halide Hybrid Perovskites and Pressure Effects on their Electronic and Optical Properties. *ACS Cent. Sci.* **2016,** *2* (4), 201-209.

38. Knop, O.; Wasylishen, R. E.; White, M. A.; Cameron, T. S.; Oort, M. J. M. V., Alkylammonium lead halides. Part 2. $CH_3NH_3PbX_3$ (X = Cl, Br, I) perovskites: cuboctahedral halide cages with isotropic cation reorientation. *Canadian Journal of Chemistry* **1990,** *68* (3), 412-422.

39. Nandi, P.; Giri, C.; Swain, D.; Manju, U.; Topwal, D., Room temperature growth of $CH_3NH_3PbCl_3$ single crystals by solvent evaporation method. *CrystEngComm* **2019,** *21* (4), 656-661.

40. Li, B.; Long, R.; Xia, Y.; Mi, Q., All-Inorganic Perovskite $CsSnBr_3$ as a Thermally Stable, Free-Carrier Semiconductor. *Angew. Chem. Int. Ed.* **2018,** *57* (40), 13154-13158.

41. Takahashi, Y.; Obara, R.; Lin, Z.-Z.; Takahashi, Y.; Naito, T.; Inabe, T.; Ishibashi, S.; Terakura, K., Charge-transport in tin-iodide perovskite $CH_3NH_3SnI_3$: origin of high conductivity. *Dalton Transactions* **2011,** *40* (20), 5563-5568.

42. Saidaminov, M. I.; Abdelhady, A. L.; Murali, B.; Alarousu, E.; Burlakov, V. M.; Peng, W.; Dursun, I.; Wang, L.; He, Y.; Maculan, G.; Goriely, A.; Wu, T.; Mohammed, O. F.; Bakr, O. M., High-quality bulk hybrid perovskite single crystals within minutes by inverse temperature crystallization. *Nat. Commun* **2015,** *6* (1), 7586.

43. Frohna, K.; Deshpande, T.; Harter, J.; Peng, W.; Barker, B. A.; Neaton, J. B.; Louie, S. G.; Bakr, O. M.; Hsieh, D.; Bernardi, M., Inversion symmetry and bulk Rashba effect in methylammonium lead iodide perovskite single crystals. *Nat. Commun* **2018,** *9* (1), 1829.

44. Kawamura, Y.; Mashiyama, H.; Hasebe, K., Structural Study on Cubic–Tetragonal Transition of $CH_3NH_3PbI_3$. *Journal of the Physical Society of Japan* **2002,** *71* (7), 1694-1697.

45. Szafrański, M.; Katrusiak, A., Mechanism of Pressure-Induced Phase Transitions, Amorphization, and Absorption-Edge Shift in Photovoltaic Methylammonium Lead Iodide. *J. Phys. Chem. Lett.* **2016,** *7* (17), 3458-3466.

46. Koji, Y.; Yasuhisa, K.; Keita, U.; Shusaku, G.; Tsutomu, O.; Yoshihiro, F., Phase Transition and Electric Conductivity of $ASnCl_3$ (A = Cs and CH_3NH_3). *Bulletin of the Chemical Society of Japan* **1998,** *71* (1), 127-134.

47. Fabini, D. H.; Laurita, G.; Bechtel, J. S.; Stoumpos, C. C.; Evans, H. A.; Kontos, A. G.; Raptis, Y. S.; Falaras, P.; Van der Ven, A.; Kanatzidis, M. G.; Seshadri, R., Dynamic Stereochemical Activity of the Sn^{2+} Lone Pair in Perovskite $CsSnBr_3$. *J. Am. Chem. Soc.* **2016,** *138* (36), 11820-11832.

48. Sutton, R. J.; Filip, M. R.; Haghighirad, A. A.; Sakai, N.; Wenger, B.; Giustino, F.; Snaith, H. J., Cubic or Orthorhombic? Revealing the Crystal Structure of Metastable Black-Phase $CsPbI_3$ by Theory and Experiment. *ACS Energy Lett.* **2018,** *3* (8), 1787-1794.

49. Zhumekenov, A. A.; Saidaminov, M. I.; Haque, M. A.; Alarousu, E.; Sarmah, S. P.; Murali, B.; Dursun, I.; Miao, X.-H.; Abdelhady, A. L.; Wu, T.; Mohammed, O. F.; Bakr, O. M., Formamidinium Lead Halide Perovskite Crystals with Unprecedented Long Carrier Dynamics and Diffusion Length. *ACS Energy Lett.* **2016,** *1* (1), 32-37.

50. Linaburg, M. R.; McClure, E. T.; Majher, J. D.; Woodward, P. M., $Cs_{1-x}Rb_xPbCl_3$ and $Cs_{1-x}Rb_xPbBr_3$ Solid Solutions: Understanding Octahedral Tilting in Lead Halide Perovskites. *Chem. Mater* **2017,** *29* (8), 3507-3514.

51. Hanusch, F. C.; Wiesenmayer, E.; Mankel, E.; Binek, A.; Angloher, P.; Fraunhofer, C.; Giesbrecht, N.; Feckl, J. M.; Jaegermann, W.; Johrendt, D.; Bein, T.; Docampo, P., Efficient Planar Heterojunction Perovskite Solar Cells Based on Formamidinium Lead Bromide. *J. Phys. Chem. Lett.* **2014,** *5* (16), 2791-2795.

52. Govinda, S.; Kore, B. P.; Swain, D.; Hossain, A.; De, C.; Guru Row, T. N.; Sarma, D. D., Critical Comparison of $FAPbX_3$ and $MAPbX_3$ (X = Br and Cl): How Do They Differ? *J. Phys. Chem. C* **2018,** *122* (25), 13758-13766.

53. Yin, W.-J.; Shi, T.; Yan, Y., Unusual defect physics in $CH_3NH_3PbI_3$ perovskite solar cell absorber. *Appl. Phys. Lett.* **2014,** *104* (6), 063903.

54. Mączka, M.; Gagor, A.; Zaręba, J. K.; Stefanska, D.; Drozd, M.; Balciunas, S.; Šimėnas, M.; Banys, J.; Sieradzki, A., Three-Dimensional Perovskite Methylhydrazinium Lead Chloride with Two Polar Phases and Unusual Second-Harmonic Generation Bistability above Room Temperature. *Chem. Mater* **2020,** *32* (9), 4072-4082.

55. Koji, Y.; Shinya, F.; Hiromi, H.; Takashi, M.; Tsutomu, O.; Sumio, I., Structural Phase Transitions of the Polymorphs of $CsSnI_3$ by Means of Rietveld Analysis of the X-Ray Diffraction. *Chemistry Letters* **1991,** *20* (5), 801-804.

56. Schueller, E. C.; Laurita, G.; Fabini, D. H.; Stoumpos, C. C.; Kanatzidis, M. G.; Seshadri, R., Crystal Structure Evolution and Notable Thermal Expansion in Hybrid Perovskites Formamidinium Tin Iodide and Formamidinium Lead Bromide. *Inorg. Chem.* **2018,** *57* (2), 695-701.

57. Zhang, H.-Y.; Chen, X.-G.; Zhang, Z.-X.; Song, X.-J.; Zhang, T.; Pan, Q.; Zhang, Y.; Xiong, R.-G., Methylphosphonium Tin Bromide: A 3D Perovskite Molecular Ferroelectric Semiconductor. *Adv. Mater.* **2020,** *32* (47), 2005213.

58. Bulanova, G. G., Podleskaya, A.V., Soboleva, L.V., Soklakov, A.I., Investigation into tin-cesium chlorides $CsSnCl_3$ and Cs_2SnCl_6. *Neorganicheskie Materialy* **1972,** *8(11)* (4), 1930-1932.

59. Dang, Y.; Zhong, C.; Zhang, G.; Ju, D.; Wang, L.; Xia, S.; Xia, H.; Tao, X., Crystallographic Investigations into Properties of Acentric Hybrid Perovskite Single Crystals $NH(CH_3)_3SnX_3$ (X = Cl, Br). *Chem. Mater* **2016,** *28* (19), 6968-6974.

60. Lin, Z.-G.; Tang, L.-C.; Chou, C.-P., Characterization and properties of infrared NLO crystals: $AGeX_3$ (A=Rb, Cs; X=Cl, Br). *Journal of Crystal Growth* **2008,** *310* (13), 3224-3229.

61. Stoumpos, C. C.; Frazer, L.; Clark, D. J.; Kim, Y. S.; Rhim, S. H.; Freeman, A. J.; Ketterson, J. B.; Jang, J. I.; Kanatzidis, M. G., Hybrid Germanium Iodide Perovskite Semiconductors: Active Lone Pairs, Structural Distortions, Direct and Indirect Energy Gaps, and Strong Nonlinear Optical Properties. *J. Am. Chem. Soc.* **2015,** *137* (21), 6804-6819.

62. Kontos, A. G.; Manolis, G. K.; Kaltzoglou, A.; Palles, D.; Kamitsos, E. I.; Kanatzidis, M. G.; Falaras, P., Halogen–NH_2^+ Interaction, Temperature-Induced Phase Transition, and Ordering in $(NH_2CHNH_2)PbX_3$ (X = Cl, Br, I) Hybrid Perovskites. *J. Phys. Chem. C* **2020,** *124* (16), 8479-8487.

63. Weller, M. T.; Weber, O. J.; Frost, J. M.; Walsh, A., Cubic Perovskite Structure of Black Formamidinium Lead Iodide, α-$[HC(NH_2)_2]PbI_3$, at 298 K. *J. Phys. Chem. Lett.* **2015,** *6* (16), 3209-3212.

64. Fabini, D. H.; Stoumpos, C. C.; Laurita, G.; Kaltzoglou, A.; Kontos, A. G.; Falaras, P.; Kanatzidis, M. G.; Seshadri, R., Reentrant Structural and Optical Properties and Large Positive

Thermal Expansion in Perovskite Formamidinium Lead Iodide. *Angew. Chem. Int. Ed.* **2016,** *55* (49), 15392-15396.

65. Thiele, G.; Rotter, H. W.; Schmidt, K. D., Kristallstrukturen und Phasentransformationen von Caesiumtrihalogenogermanaten(II) $CsGeX_3$ (X = Cl, Br, I). *zeitschrift für anorganische und allgemeine chemie* **1987,** *545* (2), 148-156.

66. Yamada, K.; Isobe, K.; Okuda, T.; Furukawa, Y., Successive Phase Transitions and High Ionic Conductivity of Trichlorogermanate (II) Salts as Studied by ^{35}C1 NQR and Powder X-Ray Diffraction *Verlag der Zeitschrift für Naturforschung A* **1994,** *49* (1-2), 258-266.

67. Baikie, T.; Barrow, N. S.; Fang, Y.; Keenan, P. J.; Slater, P. R.; Piltz, R. O.; Gutmann, M.; Mhaisalkar, S. G.; White, T. J., A combined single crystal neutron/X-ray diffraction and solid-state nuclear magnetic resonance study of the hybrid perovskites $CH_3NH_3PbX_3$ (X = I, Br and Cl). *J. Mater. Chem. A* **2015,** *3* (17), 9298-9307.

68. Xu, Q.; Eguchi, T.; Nakayama, H.; Nakamura, N.; Kishita, M., Molecular Motions and Phase Transitions in Solid $CH_3NH_3PbX_3$ (X = C1, Br, I) as Studied by NMR and NQR. *Verlag der Zeitschrift für Naturforschung A* **1991,** *46* (3), 240-246.

69. Bakulin, A. A.; Selig, O.; Bakker, H. J.; Rezus, Y. L. A.; Müller, C.; Glaser, T.; Lovrincic, R.; Sun, Z.; Chen, Z.; Walsh, A.; Frost, J. M.; Jansen, T. L. C., Real-Time Observation of Organic Cation Reorientation in Methylammonium Lead Iodide Perovskites. *J. Phys. Chem. Lett.* **2015,** *6* (18), 3663-3669.

70. Leguy, A. M. A.; Frost, J. M.; McMahon, A. P.; Sakai, V. G.; Kockelmann, W.; Law, C.; Li, X.; Foglia, F.; Walsh, A.; O'Regan, B. C.; Nelson, J.; Cabral, J. T.; Barnes, P. R. F., The dynamics of methylammonium ions in hybrid organic–inorganic perovskite solar cells. *Nat. Commun* **2015,** *6* (1), 7124.

71. Taylor, V. C. A.; Tiwari, D.; Duchi, M.; Donaldson, P. M.; Clark, I. P.; Fermin, D. J.; Oliver, T. A. A., Investigating the Role of the Organic Cation in Formamidinium Lead Iodide Perovskite Using Ultrafast Spectroscopy. *J. Phys. Chem. Lett.* **2018,** *9* (4), 895-901.

72. Fabini, D. H.; Siaw, T. A.; Stoumpos, C. C.; Laurita, G.; Olds, D.; Page, K.; Hu, J. G.; Kanatzidis, M. G.; Han, S.; Seshadri, R., Universal Dynamics of Molecular Reorientation in Hybrid Lead Iodide Perovskites. *J. Am. Chem. Soc.* **2017,** *139* (46), 16875-16884.

73. Piveteau, L.; Morad, V.; Kovalenko, M. V., Solid-State NMR and NQR Spectroscopy of Lead-Halide Perovskite Materials. *J. Am. Chem. Soc.* **2020,** *142* (46), 19413-19437.

74. Mozur, E. M.; Neilson, J. R., Cation Dynamics in Hybrid Halide Perovskites. *Annu. Rev. Mater. Res* **2021,** *51* (1), null.

75. Fu, Y.; Wu, T.; Wang, J.; Zhai, J.; Shearer, M. J.; Zhao, Y.; Hamers, R. J.; Kan, E.; Deng, K.; Zhu, X. Y.; Jin, S., Stabilization of the Metastable Lead Iodide Perovskite Phase via Surface Functionalization. *Nano Lett.* **2017,** *17* (7), 4405-4414.

76. Fu, Y.; Rea, M. T.; Chen, J.; Morrow, D. J.; Hautzinger, M. P.; Zhao, Y.; Pan, D.; Manger, L. H.; Wright, J. C.; Goldsmith, R. H.; Jin, S., Selective Stabilization and Photophysical Properties of Metastable Perovskite Polymorphs of $CsPbI_3$ in Thin Films. *Chem. Mater* **2017,** *29* (19), 8385-8394.

77. Protesescu, L.; Yakunin, S.; Bodnarchuk, M. I.; Krieg, F.; Caputo, R.; Hendon, C. H.; Yang, R. X.; Walsh, A.; Kovalenko, M. V., Nanocrystals of Cesium Lead Halide Perovskites ($CsPbX_3$, X = Cl, Br, and I): Novel Optoelectronic Materials Showing Bright Emission with Wide Color Gamut. *Nano Lett.* **2015,** *15* (6), 3692-3696.

78. Protesescu, L.; Yakunin, S.; Kumar, S.; Bär, J.; Bertolotti, F.; Masciocchi, N.; Guagliardi, A.; Grotevent, M.; Shorubalko, I.; Bodnarchuk, M. I.; Shih, C.-J.; Kovalenko, M. V., Dismantling the "Red Wall" of Colloidal Perovskites: Highly Luminescent Formamidinium and Formamidinium–Cesium Lead Iodide Nanocrystals. *ACS Nano* **2017,** *11* (3), 3119-3134.

79. Swarnkar, A.; Marshall, A. R.; Sanehira, E. M.; Chernomordik, B. D.; Moore, D. T.; Christians, J. A.; Chakrabarti, T.; Luther, J. M., Quantum dot–induced phase stabilization of α-$CsPbI_3$ perovskite for high-efficiency photovoltaics. *Science* **2016,** *354* (6308), 92-95.

80. Fu, Y.; Zhu, H.; Chen, J.; Hautzinger, M. P.; Zhu, X. Y.; Jin, S., Metal halide perovskite nanostructures for optoelectronic applications and the study of physical properties. *Nat. Rev. Mater.* **2019,** *4* (3), 169-188.

81. Li, Z.; Yang, M.; Park, J.-S.; Wei, S.-H.; Berry, J. J.; Zhu, K., Stabilizing Perovskite Structures by Tuning Tolerance Factor: Formation of Formamidinium and Cesium Lead Iodide Solid-State Alloys. *Chem. Mater* **2016,** *28* (1), 284-292.

82. Vigil, J. A.; Hazarika, A.; Luther, J. M.; Toney, M. F., $FA_xCs_{1-x}PbI_3$ Nanocrystals: Tuning Crystal Symmetry by A-Site Cation Composition. *ACS Energy Lett.* **2020,** *5* (8), 2475-2482.

83. Hazarika, A.; Zhao, Q.; Gaulding, E. A.; Christians, J. A.; Dou, B.; Marshall, A. R.; Moot, T.; Berry, J. J.; Johnson, J. C.; Luther, J. M., Perovskite Quantum Dot Photovoltaic Materials beyond the Reach of Thin Films: Full-Range Tuning of A-Site Cation Composition. *ACS Nano* **2018,** *12* (10), 10327-10337.

84. Mozur, E. M.; Maughan, A. E.; Cheng, Y.; Huq, A.; Jalarvo, N.; Daemen, L. L.; Neilson, J. R., Orientational Glass Formation in Substituted Hybrid Perovskites. *Chem. Mater* **2017,** *29* (23), 10168-10177.

85. Mozur, E. M.; Hope, M. A.; Trowbridge, J. C.; Halat, D. M.; Daemen, L. L.; Maughan, A. E.; Prisk, T. R.; Grey, C. P.; Neilson, J. R., Cesium Substitution Disrupts Concerted Cation Dynamics in Formamidinium Hybrid Perovskites. *Chem. Mater* **2020,** *32* (14), 6266-6277.

86. Nazarenko, O.; Yakunin, S.; Morad, V.; Cherniukh, I.; Kovalenko, M. V., Single crystals of caesium formamidinium lead halide perovskites: solution growth and gamma dosimetry. *NPG Asia Materials* **2017,** *9* (4), e373-e373.

87. Jodlowski, A. D.; Roldán-Carmona, C.; Grancini, G.; Salado, M.; Ralaiarisoa, M.; Ahmad, S.; Koch, N.; Camacho, L.; de Miguel, G.; Nazeeruddin, M. K., Large guanidinium cation mixed with methylammonium in lead iodide perovskites for 19% efficient solar cells. *Nat. Energy* **2017,** *2* (12), 972-979.

88. Ke, W.; Spanopoulos, I.; Stoumpos, C. C.; Kanatzidis, M. G., Myths and reality of $HPbI_3$ in halide perovskite solar cells. *Nat. Commun* **2018,** *9* (1), 4785.

89. Eperon, G. E.; Stone, K. H.; Mundt, L. E.; Schloemer, T. H.; Habisreutinger, S. N.; Dunfield, S. P.; Schelhas, L. T.; Berry, J. J.; Moore, D. T., The Role of Dimethylammonium in Bandgap Modulation for Stable Halide Perovskites. *ACS Energy Lett.* **2020,** *5* (6), 1856-1864.

90. Hsu, H.-L.; Chang, C.-C.; Chen, C.-P.; Jiang, B.-H.; Jeng, R.-J.; Cheng, C.-H., High-performance and high-durability perovskite photovoltaic devices prepared using ethylammonium iodide as an additive. *J. Mater. Chem. A* **2015,** *3* (17), 9271-9277.

91. Kim, Y.-H.; Kim, S.; Kakekhani, A.; Park, J.; Park, J.; Lee, Y.-H.; Xu, H.; Nagane, S.; Wexler, R. B.; Kim, D.-H.; Jo, S. H.; Martínez-Sarti, L.; Tan, P.; Sadhanala, A.; Park, G.-S.; Kim, Y.-W.; Hu, B.; Bolink, H. J.; Yoo, S.; Friend, R. H.; Rappe, A. M.; Lee, T.-W., Comprehensive defect suppression in perovskite nanocrystals for high-efficiency light-emitting diodes. *Nat. Photonics* **2021,** *15* (2), 148-155.

92. Tong, J.; Song, Z.; Kim, D. H.; Chen, X.; Chen, C.; Palmstrom, A. F.; Ndione, P. F.; Reese, M. O.; Dunfield, S. P.; Reid, O. G.; Liu, J.; Zhang, F.; Harvey, S. P.; Li, Z.; Christensen, S. T.; Teeter, G.; Zhao, D.; Al-Jassim, M. M.; van Hest, M. F. A. M.; Beard, M. C.; Shaheen, S. E.; Berry, J. J.; Yan, Y.; Zhu, K., Carrier lifetimes of >1 μs in Sn-Pb perovskites enable efficient all-perovskite tandem solar cells. *Science* **2019,** *364* (6439), 475-479.

93. Buin, A.; Comin, R.; Xu, J.; Ip, A. H.; Sargent, E. H., Halide-Dependent Electronic Structure of Organolead Perovskite Materials. *Chem. Mater* **2015,** *27* (12), 4405-4412.

94. Yin, W.-J.; Shi, T.; Yan, Y., Unique Properties of Halide Perovskites as Possible Origins of the Superior Solar Cell Performance. *Adv. Mater.* **2014,** *26* (27), 4653-4658.

95. Filip, M. R.; Eperon, G. E.; Snaith, H. J.; Giustino, F., Steric engineering of metal-halide perovskites with tunable optical band gaps. *Nat. Commun* **2014,** *5* (1), 5757.

96. Prasanna, R.; Gold-Parker, A.; Leijtens, T.; Conings, B.; Babayigit, A.; Boyen, H.-G.; Toney, M. F.; McGehee, M. D., Band Gap Tuning via Lattice Contraction and Octahedral Tilting in Perovskite Materials for Photovoltaics. *J. Am. Chem. Soc.* **2017,** *139* (32), 11117-11124.

97. Valadares, F.; Guilhon, I.; Teles, L. K.; Marques, M., Electronic Structure Panorama of Halide Perovskites: Approximated DFT-1/2 Quasiparticle and Relativistic Corrections. *J. Phys. Chem. C* **2020,** *124* (34), 18390-18400.

98. Dai, J.; Fu, Y.; Manger, L. H.; Rea, M. T.; Hwang, L.; Goldsmith, R. H.; Jin, S., Carrier Decay Properties of Mixed Cation Formamidinium–Methylammonium Lead Iodide Perovskite $[HC(NH_2)_2]_{1-x}[CH_3NH_3]_xPbI_3$ Nanorods. *J. Phys. Chem. Lett.* **2016,** *7* (24), 5036-5043.

99. Kulbak, M.; Cahen, D.; Hodes, G., How Important Is the Organic Part of Lead Halide Perovskite Photovoltaic Cells? Efficient $CsPbBr_3$ Cells. *J. Phys. Chem. Lett.* **2015,** *6* (13), 2452-2456.

100. Miyata, K.; Meggiolaro, D.; Trinh, M. T.; Joshi, P. P.; Mosconi, E.; Jones, S. C.; De Angelis, F.; Zhu, X.-Y., Large polarons in lead halide perovskites. *Sci. Adv.* **2017,** *3* (8), e1701217.

101. Bretschneider, S. A.; Ivanov, I.; Wang, H. I.; Miyata, K.; Zhu, X.; Bonn, M., Quantifying Polaron Formation and Charge Carrier Cooling in Lead-Iodide Perovskites. *Adv. Mater.* **2018,** *30* (29), 1707312.

102. Saliba, M.; Matsui, T.; Domanski, K.; Seo, J.-Y.; Ummadisingu, A.; Zakeeruddin, S. M.; Correa-Baena, J.-P.; Tress, W. R.; Abate, A.; Hagfeldt, A.; Grätzel, M., Incorporation of rubidium cations into perovskite solar cells improves photovoltaic performance. *Science* **2016,** *354* (6309), 206-209.

103. Saliba, M.; Matsui, T.; Seo, J.-Y.; Domanski, K.; Correa-Baena, J.-P.; Nazeeruddin, M. K.; Zakeeruddin, S. M.; Tress, W.; Abate, A.; Hagfeldt, A.; Grätzel, M., Cesium-containing triple cation perovskite solar cells: improved stability, reproducibility and high efficiency. *Energy Environ. Sci* **2016,** *9* (6), 1989-1997.

104. Jacobsson, T. J.; Correa-Baena, J.-P.; Halvani Anaraki, E.; Philippe, B.; Stranks, S. D.; Bouduban, M. E. F.; Tress, W.; Schenk, K.; Teuscher, J.; Moser, J.-E.; Rensmo, H.; Hagfeldt, A., Unreacted PbI_2 as a Double-Edged Sword for Enhancing the Performance of Perovskite Solar Cells. *J. Am. Chem. Soc.* **2016,** *138* (32), 10331-10343.

105. Philippe, B.; Saliba, M.; Correa-Baena, J.-P.; Cappel, U. B.; Turren-Cruz, S.-H.; Grätzel, M.; Hagfeldt, A.; Rensmo, H., Chemical Distribution of Multiple Cation (Rb^+, Cs^+, MA^+, and FA^+) Perovskite Materials by Photoelectron Spectroscopy. *Chem. Mater* **2017,** *29* (8), 3589-3596.

106. Kubicki, D. J.; Prochowicz, D.; Hofstetter, A.; Zakeeruddin, S. M.; Grätzel, M.; Emsley, L., Phase Segregation in Cs-, Rb- and K-Doped Mixed-Cation $(MA)_x(FA)_{1-x}PbI_3$ Hybrid Perovskites from Solid-State NMR. *J. Am. Chem. Soc.* **2017,** *139* (40), 14173-14180.

107. Ünlü, F.; Jung, E.; Haddad, J.; Kulkarni, A.; Öz, S.; Choi, H.; Fischer, T.; Chakraborty, S.; Kirchartz, T.; Mathur, S., Understanding the interplay of stability and efficiency in A-site engineered lead halide perovskites. *APL Mater.* **2020,** *8* (7), 070901.

108. García-Fernández, A.; Juarez-Perez, E. J.; Bermúdez-García, J. M.; Llamas-Saiz, A. L.; Artiaga, R.; López-Beceiro, J. J.; Señarís-Rodríguez, M. A.; Sánchez-Andújar, M.; Castro-García, S., Hybrid lead halide $[(CH_3)_2NH_2]PbX_3$ (X = Cl− and Br−) hexagonal perovskites with multiple functional properties. *J. Mater. Chem. C* **2019,** *7* (32), 10008-10018.

109. Daub, M.; Haber, C.; Hillebrecht, H., Synthesis, Crystal Structures, Optical Properties, and Phase Transitions of the Layered Guanidinium-Based Hybrid Perovskites $[C(NH_2)_3]_2MI_4$; M = Sn, Pb. *Eur. J. Inorg. Chem* **2017,** *2017* (7), 1120-1126.

110. Fu, Y.; Hautzinger, M. P.; Luo, Z.; Wang, F.; Pan, D.; Aristov, M. M.; Guzei, I. A.; Pan, A.; Zhu, X.; Jin, S., Incorporating Large A Cations into Lead Iodide Perovskite Cages: Relaxed Goldschmidt Tolerance Factor and Impact on Exciton–Phonon Interaction. *ACS Cent. Sci.* **2019,** *5* (8), 1377-1386.

111. Li, X.; Fu, Y.; Pedesseau, L.; Guo, P.; Cuthriell, S.; Hadar, I.; Even, J.; Katan, C.; Stoumpos, C. C.; Schaller, R. D.; Harel, E.; Kanatzidis, M. G., Negative Pressure Engineering with Large Cage Cations in 2D Halide Perovskites Causes Lattice Softening. *J. Am. Chem. Soc.* **2020,** *142* (26), 11486-11496.

112. Wang, Y.; Liu, X.; Li, L.; Ji, C.; Sun, Z.; Han, S.; Tao, K.; Luo, J., $(C_6H_{13}NH_3)_2(NH_2CHNH_2)Pb_2I_7$: A Two-dimensional Bilayer Inorganic–Organic Hybrid Perovskite Showing Photodetecting Behavior. *Chem. – Asian J.* **2019,** *14* (9), 1530-1534.

113. Fu, Y.; Jiang, X.; Li, X.; Traore, B.; Spanopoulos, I.; Katan, C.; Even, J.; Kanatzidis, M. G.; Harel, E., Cation Engineering in Two-Dimensional Ruddlesden–Popper Lead Iodide Perovskites with Mixed Large A-Site Cations in the Cages. *J. Am. Chem. Soc.* **2020,** *142* (8), 4008-4021.

114. Wu, Z.; Ji, C.; Li, L.; Kong, J.; Sun, Z.; Zhao, S.; Wang, S.; Hong, M.; Luo, J., Alloying n-Butylamine into $CsPbBr_3$ To Give a Two-Dimensional Bilayered Perovskite Ferroelectric Material. *Angew. Chem. Int. Ed.* **2018,** *57* (27), 8140-8143.

115. Mao, L.; Wu, Y.; Stoumpos, C. C.; Traore, B.; Katan, C.; Even, J.; Wasielewski, M. R.; Kanatzidis, M. G., Tunable White-Light Emission in Single-Cation-Templated Three-Layered 2D Perovskites $(CH_3CH_2NH_3)_4Pb_3Br_{10-x}Cl_x$. *J. Am. Chem. Soc.* **2017,** *139* (34), 11956-11963.

116. Xu, Z.; Li, Y.; Liu, X.; Ji, C.; Chen, H.; Li, L.; Han, S.; Hong, M.; Luo, J.; Sun, Z., Highly Sensitive and Ultrafast Responding Array Photodetector Based on a Newly Tailored 2D Lead Iodide Perovskite Crystal. *Adv. Opt. Mater.* **2019,** *7* (11), 1900308.

117. Yang, T.; Li, Y.; Han, S.; Liu, Y.; Xu, Z.; Li, M.; Wang, J.; Ma, Y.; Luo, J.; Sun, Z., Exploiting two-dimensional hybrid perovskites incorporating secondary amines for high-performance array photodetection. *J. Mater. Chem. C* **2020,** *8* (37), 12848-12853.

118. Li, L.; Liu, X.; Li, Y.; Xu, Z.; Wu, Z.; Han, S.; Tao, K.; Hong, M.; Luo, J.; Sun, Z., Two-Dimensional Hybrid Perovskite-Type Ferroelectric for Highly Polarization-Sensitive Shortwave Photodetection. *J. Am. Chem. Soc.* **2019,** *141* (6), 2623-2629.

119. Li, L.; Shang, X.; Wang, S.; Dong, N.; Ji, C.; Chen, X.; Zhao, S.; Wang, J.; Sun, Z.; Hong, M.; Luo, J., Bilayered Hybrid Perovskite Ferroelectric with Giant Two-Photon Absorption. *J. Am. Chem. Soc.* **2018,** *140* (22), 6806-6809.

120. Peng, Y.; Bie, J.; Liu, X.; Li, L.; Chen, S.; Fa, W.; Wang, S.; Sun, Z.; Luo, J., Acquiring High-TC Layered Metal Halide Ferroelectrics via Cage-Confined Ethylamine Rotators. *Angew. Chem. Int. Ed.* **2021,** *60* (6), 2839-2843.

121. Geselle, M.; Fuess, H., Crystal structure of tetrakis(ethylammonium) decachlorotriplumbate(II), $(C_2H_5NH_3)_4Pb_3Cl_{10}$ *Zeitschrift für Kristallographie - New Crystal Structures* **1997,** *212* (1), 241-242.

122. Ji, C.; Wang, S.; Wang, Y.; Chen, H.; Li, L.; Sun, Z.; Sui, Y.; Wang, S.; Luo, J., 2D Hybrid Perovskite Ferroelectric Enables Highly Sensitive X-Ray Detection with Low Driving Voltage. *Adv. Funct. Mater.* **2020,** *30* (5), 1905529.

123. Liu, Y.; Han, S.; Wang, J.; Ma, Y.; Guo, W.; Huang, X.-Y.; Luo, J.-H.; Hong, M.; Sun, Z., Spacer Cation Alloying of a Homoconformational Carboxylate trans Isomer to Boost in-Plane Ferroelectricity in a 2D Hybrid Perovskite. *J. Am. Chem. Soc.* **2021,** *143* (4), 2130-2137.

124. Hautzinger, M. P.; Pan, D.; Pigg, A. K.; Fu, Y.; Morrow, D. J.; Leng, M.; Kuo, M.-Y.; Spitha, N.; Lafayette, D. P.; Kohler, D. D.; Wright, J. C.; Jin, S., Band Edge Tuning of Two-Dimensional Ruddlesden–Popper Perovskites by A Cation Size Revealed through Nanoplates. *ACS Energy Lett.* **2020,** *5* (5), 1430-1437.

125. Guo, S.; Zhao, Y.; Bu, K.; Fu, Y.; Luo, H.; Chen, M.; Hautzinger, M. P.; Wang, Y.; Jin, S.; Yang, W.; Lü, X., Pressure-Suppressed Carrier Trapping Leads to Enhanced Emission in Two-Dimensional Perovskite $(HA)_2(GA)Pb_2I_7$. *Angew. Chem. Int. Ed.* **2020,** *59* (40), 17533-17539.

126. Liu, G.; Gong, J.; Kong, L.; Schaller, R. D.; Hu, Q.; Liu, Z.; Yan, S.; Yang, W.; Stoumpos, C. C.; Kanatzidis, M. G.; Mao, H.-k.; Xu, T., Isothermal pressure-derived metastable states in 2D hybrid perovskites showing enduring bandgap narrowing. *Proc. Natl. Acad. Sci. U.S.A.* **2018,** *115* (32), 8076-8081.

127. Wright, A. D.; Verdi, C.; Milot, R. L.; Eperon, G. E.; Pérez-Osorio, M. A.; Snaith, H. J.; Giustino, F.; Johnston, M. B.; Herz, L. M., Electron–phonon coupling in hybrid lead halide perovskites. *Nat. Commun* **2016,** *7* (1), 11755.

128. Han, S.; Liu, X.; Liu, Y.; Xu, Z.; Li, Y.; Hong, M.; Luo, J.; Sun, Z., High-Temperature Antiferroelectric of Lead Iodide Hybrid Perovskites. *J. Am. Chem. Soc.* **2019,** *141* (32), 12470-12474.

129. Wang, S.; Li, L.; Weng, W.; Ji, C.; Liu, X.; Sun, Z.; Lin, W.; Hong, M.; Luo, J., Trilayered Lead Chloride Perovskite Ferroelectric Affording Self-Powered Visible-Blind Ultraviolet Photodetection with Large Zero-Bias Photocurrent. *J. Am. Chem. Soc.* **2020,** *142* (1), 55-59.

130. Wu, Z.; Liu, X.; Ji, C.; Li, L.; Wang, S.; Peng, Y.; Tao, K.; Sun, Z.; Hong, M.; Luo, J., Discovery of an Above-Room-Temperature Antiferroelectric in Two-Dimensional Hybrid Perovskite. *J. Am. Chem. Soc.* **2019,** *141* (9), 3812-3816.

131. Han, S.; Li, M.; Liu, Y.; Guo, W.; Hong, M.-C.; Sun, Z.; Luo, J., Tailoring of a visible-light-absorbing biaxial ferroelectric towards broadband self-driven photodetection. *Nat. Commun* **2021,** *12* (1), 284.

132. Park, I.-H.; Zhang, Q.; Kwon, K. C.; Zhu, Z.; Yu, W.; Leng, K.; Giovanni, D.; Choi, H. S.; Abdelwahab, I.; Xu, Q.-H.; Sum, T. C.; Loh, K. P., Ferroelectricity and Rashba Effect in a Two-Dimensional Dion-Jacobson Hybrid Organic–Inorganic Perovskite. *J. Am. Chem. Soc.* **2019,** *141* (40), 15972-15976.

133. Park, I.-H.; Kwon, K. C.; Zhu, Z.; Wu, X.; Li, R.; Xu, Q.-H.; Loh, K. P., Self-Powered Photodetector Using Two-Dimensional Ferroelectric Dion–Jacobson Hybrid Perovskites. *J. Am. Chem. Soc.* **2020,** *142* (43), 18592-18598.

134. Slavney, A. H.; Hu, T.; Lindenberg, A. M.; Karunadasa, H. I., A Bismuth-Halide Double Perovskite with Long Carrier Recombination Lifetime for Photovoltaic Applications. *J. Am. Chem. Soc.* **2016,** *138* (7), 2138-2141.

135. Maughan, A. E.; Ganose, A. M.; Almaker, M. A.; Scanlon, D. O.; Neilson, J. R., Tolerance Factor and Cooperative Tilting Effects in Vacancy-Ordered Double Perovskite Halides. *Chem. Mater* **2018,** *30* (11), 3909-3919.

136. Maughan, A. E.; Ganose, A. M.; Bordelon, M. M.; Miller, E. M.; Scanlon, D. O.; Neilson, J. R., Defect Tolerance to Intolerance in the Vacancy-Ordered Double Perovskite Semiconductors Cs_2SnI_6 and Cs_2TeI_6. *J. Am. Chem. Soc.* **2016,** *138* (27), 8453-8464.

137. Vishnoi, P.; Zuo, J. L.; Cooley, J. A.; Kautzsch, L.; Gómez-Torres, A.; Murillo, J.; Fortier, S.; Wilson, S. D.; Seshadri, R.; Cheetham, A. K., Chemical Control of Spin-Orbit

Coupling and Charge Transfer in Vacancy-Ordered Ruthenium(IV) Halide Perovskites. *Angew. Chem. Int. Ed.* **2021,** *60* (10), 5184-5188.

138. Luo, J.; Wang, X.; Li, S.; Liu, J.; Guo, Y.; Niu, G.; Yao, L.; Fu, Y.; Gao, L.; Dong, Q.; Zhao, C.; Leng, M.; Ma, F.; Liang, W.; Wang, L.; Jin, S.; Han, J.; Zhang, L.; Etheridge, J.; Wang, J.; Yan, Y.; Sargent, E. H.; Tang, J., Efficient and stable emission of warm-white light from lead-free halide double perovskites. *Nature* **2018,** *563* (7732), 541-545.

139. Wolf, N. R.; Connor, B. A.; Slavney, A. H.; Karunadasa, H. I., Doubling the Stakes: The Promise of Halide Double Perovskites. *Angew. Chem. Int. Ed. n/a* (n/a).

140. Vishnoi, P.; Seshadri, R.; Cheetham, A. K., Why are Double Perovskite Iodides so Rare? *J. Phys. Chem. C* **2021**.

141. Banerjee, A.; Bridges, C. A.; Yan, J. Q.; Aczel, A. A.; Li, L.; Stone, M. B.; Granroth, G. E.; Lumsden, M. D.; Yiu, Y.; Knolle, J.; Bhattacharjee, S.; Kovrizhin, D. L.; Moessner, R.; Tennant, D. A.; Mandrus, D. G.; Nagler, S. E., Proximate Kitaev quantum spin liquid behaviour in a honeycomb magnet. *Nat. Mater.* **2016,** *15* (7), 733-740.

142. Kepenekian, M.; Robles, R.; Katan, C.; Sapori, D.; Pedesseau, L.; Even, J., Rashba and Dresselhaus Effects in Hybrid Organic-Inorganic Perovskites: From Basics to Devices. *ACS Nano* **2015,** *9* (12), 11557-11567.

143. Kepenekian, M.; Even, J., Rashba and Dresselhaus Couplings in Halide Perovskites: Accomplishments and Opportunities for Spintronics and Spin-Orbitronics. *J. Phys. Chem. Lett.* **2017,** *8* (14), 3362-3370.

144. Niesner, D.; Hauck, M.; Shrestha, S.; Levchuk, I.; Matt, G. J.; Osvet, A.; Batentschuk, M.; Brabec, C.; Weber, H. B.; Fauster, T., Structural fluctuations cause spin-split states in tetragonal (CH 3 NH 3)PbI 3 as evidenced by the circular photogalvanic effect. *Proc. Natl. Acad. Sci. U.S.A.* **2018,** *115* (38), 9509-9514.

145. Etienne, T.; Mosconi, E.; De Angelis, F., Dynamical Origin of the Rashba Effect in Organohalide Lead Perovskites: A Key to Suppressed Carrier Recombination in Perovskite Solar Cells? *J. Phys. Chem. Lett.* **2016,** *7* (9), 1638-1645.

146. Zhai, Y.; Baniya, S.; Zhang, C.; Li, J.; Haney, P.; Sheng, C. X.; Ehrenfreund, E.; Vardeny, Z. V., Giant Rashba splitting in 2D organic-inorganic halide perovskites measured by transient spectroscopies. *Sci. Adv.* **2017,** *3* (7), e1700704.

147. Liu, X.; Chanana, A.; Huynh, U.; Xue, F.; Haney, P.; Blair, S.; Jiang, X.; Vardeny, V. Z., Circular photogalvanic spectroscopy of Rashba splitting in 2D hybrid organic–inorganic perovskite multiple quantum wells. *Nat. Commun* **2020,** *11* (1), 1-8.

148. Todd, S. B.; Riley, D. B.; Binai-Motlagh, A.; Clegg, C.; Ramachandran, A.; March, S. A.; Hoffman, J. M.; Hill, I. G.; Stoumpos, C. C.; Kanatzidis, M. G.; Yu, Z. G.; Hall, K. C.,

Detection of Rashba spin splitting in 2D organic-inorganic perovskite via precessional carrier spin relaxation. *APL Mater.* **2019,** *7* (8).

149. Yu, S.; Na, G.; Luo, S.; Rubel, O.; Zhang, L., Rashba band splitting in two-dimensional Ruddlesden-Popper halide perovskites. *J. Appl. Phys.* **2020,** *128* (17).

Chapter 2. Two-Dimensional Lead Halide Perovskites Templated by a Conjugated Asymmetric Diammonium*

2.1 Abstract

We report novel two-dimensional lead halide perovskite structures templated by a unique conjugated aromatic dication, N,N-dimethylphenylene-p-diammonium (DPDA). The asymmetrically substituted primary and tertiary ammoniums in DPDA facilitates the formation of two-dimensional network (2DN) perovskite structures incorporating a conjugated dication between the PbX_4^{2-} (X = Br, I) layers. These 2DN structures of (DPDA)PbI_4 and (DPDA)$PbBr_4$ were characterized by single crystal X-ray diffraction, showing uniquely low distortions in the Pb-X-Pb bond angle for 2D perovskites. The Pb-I-Pb bond angle is very close to ideal (180°) for a 2DN lead iodide perovskite which can be attributed to the rigid diammonium DPDA's ability to insert into the PbX_6^{2-} octahedral pockets. Optical characterization of (DPDA)PbI_4 shows an excitonic absorption peak at 2.29 eV (541 nm), which is red-shifted compared to similar 2DN lead iodide structures. Temperature dependent photoluminescence of both compounds reveal both a self-trapped exciton and free exciton emission feature. The reduced exciton absorption energy and emission properties are attributed to the dication induced structural order of the inorganic PbX_4^{2-} layers. DFT calculation results suggest mixing of the conjugated organic orbital component in the valence band of these 2DN perovskites. These results demonstrate a rational new strategy to

---

* This chapter was originally published in *Inorg. Chem.*, **2017**, 56, 24, 14991−14998 in collaboration with J. Dai, Y. Ji, Y. Fu, J. Chen, I.A. Guzei, J.C. Wright, Y. Li, and S. Jin

incorporate conjugated organic dications into hybrid perovskites and will spur spectroscopic investigations of these compounds as well as optoelectronic applications.

2.2 Introduction

Hybrid inorganic-organic metal halide perovskite semiconductors have received intense attention in recent years, largely due to their excellent performance in solar cells. The efficiency of perovskite solar cells has climbed to above 20% in the past few years, making them very promising for application in solar energy.[1-3] The potential for commercialization of metal halide perovskites is hindered partly by the structural and moisture instability[4-6] of the three-dimensional (3D) perovskite AMX_3 (A = monovalent cation, M = Pb, Sn, Ge; and X = Cl^-, Br^-, and I^-).[7] Alternatively, low-dimensional perovskite semiconductors have demonstrably improved moisture and crystal structure stability relative to their 3D counterparts, while still maintaining interesting optoelectronic properties.[8-15] In particular, two-dimensional network (2DN) metal halide perovskites, $(RNH_3)_2MX_4$ (RNH_3^+= alkylammonium), display efficient light emission,[16-22] non-linear electronic properties,[23-25] low-intrinsic doping levels,[26] and can be used in stabilizing 3D perovskite solar cells as quasi-2D structures,[27-29] which make these materials highly versatile semiconductors. The moisture stability of 2DN perovskite is often attributed to the hydrophobic nature of the alkylammonium cations (RNH_3^+) in between the inorganic layers of 2DN perovskite structures.[11,29-31] In addition to providing moisture stability, the organic component of 2DN perovskites allows them to be a structural playground, as the geometric restriction of cation choice in the 3D perovskite is lifted.[32-37] These structures form multiple types of 2DN metal halide layers, most often formed from slicing the (001) or (110) plane of a cubic 3D perovskite.[38] These structures are commonly modeled as quantum confined 2D wells with a low dielectric organic in

between.[39-42] The different choices of the organic cations has been shown to cause different bond angles and octahedral distortions in the 2DN layers.[25] An important trend that has been observed is cations that induce less structural distortion in the 2DN layers lead to lower absorption energies in these materials. In addition to absorption energies, unique emission properties can be observed showing broadband emissions that correlate with the structural distortions and the efficiency/appearance of a broad emission feature in addition to the sharp, low stokes shifted free-exciton emission.[33,42] The broad emission is attributed to self-trapped excitons (STEs) that form via excited-state lattice distortions, creating self-induced defects capable of trapping free excitons.[19] The formation of these lattice distortions is highly correlated with longitudinal phonon energies and thus the bonding of the inorganic component of 2DN perovskites.[43]

Recent investigations have been focused on 2DN lead halide perovskites templated using alkylammonium dications with a structural formula (NRN)PbX_4 (NRN = alkyldiammonium).[17,44-47] They form a monolayer of dications in between layers of corner-sharing lead halide octahedra, of both the (001) and (110) orientations. The rigidity of the dication monolayer structures relative to the flexible bilayers of monocations often tends to yield more distorted PbX_6^{4-} octahedra. This unique structural motif of increased octahedral distortion leads to the broadband emission observed in the PL spectra, in both (001) and (110) perovskites.[33,48] However, there is a limit on the rigidity and size of the structures that can be used to form 2D perovskites.[49-52] Phenylene-p-diamine, as well as other similar rigid conjugated aromatic diamines were demonstrated to form one-dimensional networks (1DN) of lead iodide octahedra as shown in Figure 2.1.[49] When considering this, the rigidity of conjugated dication systems appears to be too intense for the lead halide network to assemble into a 2DN perovskite. More recently, Mao et al utilized asymmetrically

methylated N,N-dimethylethylenediamine (DMEN) to form 2DN perovskites,[22] while other reports on similar diamine structures with symmetric methylation such as N,N'-dimethylethylenediamine forms 1DN perovskites.[53] This balance of these compounds forming 2D vs 1D can be attributed to the distance between the ammonium group and the halide plane. The alternating methyl groups in the asymmetric DMEN dications induce the distortions required for structural stability. This idea is consistent with the recent demonstration that ammonium groups that are closer to the halide plane induce greater distortions in the Pb-X-Pb layer.[25]

Figure 2.1. Scheme showing a representative symmetric rigid conjugated diammonium PDA (right) yields 1DN perovskites; in contrast, the similarly rigid, but asymmetrically substituted DPDA (left) leads to 2DN perovskites. This is attributed to the energetically favorable distortions of the PbI_6^{2-} 2DN caused by the asymmetric methyl groups of DPDA.

Inspired by the observation that asymmetric diammonium groups favor 2DN perovskite formation, we targeted new 2DN perovskite structures using a totally rigid, asymmetrically substituted, and commercially available conjugated diamine, N,N-dimethylphenylene-p-diamine (DPDA) (Figure 2.1 left). Two-dimensional network lead halide perovskite structures can be formed with both the iodide and bromide $(DPDA)PbX_4$ (X = Br, I). $(DPDA)PbI_4$ is particularly

interesting as it shows red-shifted absorbance and photoluminescence relative to previous reports of 2DN lead iodide perovskites. The Pb-X-Pb bonding angle is very close to the ideal 180° in this structure and promotes these interesting optical properties. In fact, the structural rigidity of DPDA can lead to the formation of a 1DN chain perovskite, $(DPDA)_2PbI_5 \cdot I$, under a different stoichiometric condition, in addition to the 2DN phase. Temperature dependent photoluminescence (TDPL) was utilized to investigate the light emission properties and to probe the excitonic features in these structures. While $(DPDA)PbBr_4$ shows broad emission as expected at low temperature, the unexpected broad emission of a self-trapped exciton was observed in $(DPDA)PbI_4$. Electronic structure calculations suggest that the conjugated aromatic dication DPDA contributes to the unusual optical properties, not only because the increased overlap of the lead and halides orbitals, but also because the aromatic ring could contribute to the conduction band of the perovskites.

2.3 Materials and Methods

$Pb(CH_3COO)_2 \cdot 3H_2O$ (99.999% trace metals basis), N,N-dimethylene-p-diamine (97%), HI (57 wt % in H_2O, stabilized with H_3PO_4, 99.95%), HBr (48 wt% in H_2O), H_3PO_4 (85 wt% in H_2O), ethanol (99.9%), diethyl ether (99%), were all purchased from Sigma Aldrich and used without further purification.

2.3.1 Synthesis and Crystal growth of $(DPDA)PbX_4$ (X = Br, I)

Lead acetate trihydrate ($Pb(CH_3COO)_2 \cdot 3H_2O$) (2.2 g, 6.8 mmol) was stirred and heated gently in 9 mL of HX and 1 mL of H_3PO_4 until fully dissolved. N,N-dimethylene-p-diamine (DPDA) (920 mg, 6.8 mmol) was dissolved in 5 mL of ethanol. The acid solution was added dropwise over 10 minutes to the DPDA/EtOH solution at -70 °C (to mediate the exothermic acid

base reaction) with rapid stirring. The mixture was then sonicated for 5 min at room temperature to yield a red/orange (HI) or purple (HBr) powder. This precipitate was filtered through a sintered glass frit followed by washing with diethyl ether (5 x 10 mL). The crude precipitate mixture was purified by re-dissolving in 5 mL HX and 1 mL H_3PO_4 and evaporating off half of the solution, followed by leaving the flask unperturbed to cool on the hot plate. The purified crystals were washed with diethyl ether (5 x 10 mL) and dried under vacuum overnight. (Yield 76% for (DPDA)PbI_4, 56% for (DPDA)$PbBr_4$)

To grow large (DPDA)PbX_4 single crystals, crude powders of (DPDA)PbX_4 (X = Br, I) (0.5 g) were dissolved in 5 mL of HX (X = Br, I) and 1 mL of H_3PO_4 and heated at 110 °C until half of the original solution was evaporated off. After cooling to room temperature, the mother liquor was allowed to sit undisturbed at 4 °C for 12 h to yield well-faceted single crystals.

To prepare (DPDA)PbX_4 thin films, crystals of each (DPDA)PbX_4 (0.5 g) (X = Br, I) were dissolved in DMF (1 mL) and the solutions were spin coated onto clean glass slides at 3000 rpm for 30s. Before deposition, the glass slides were rinsed by acetone then isopropanol twice followed by ozone plasma cleaning. PXRD confirms the layered structure in the thin films (Figure A4).

2.3.2 Single Crystal Diffraction

Crystals were selected under oil under ambient conditions and attached to the tip of a MiTeGen MicroMount©. The crystal was mounted in a stream of cold nitrogen at 100(1) K and centered in the X-ray beam by using a video camera. The crystal evaluation and data collection were performed on a Bruker Quazar SMART APEXII diffractometer with Mo Kα (λ = 0.71073 Å) radiation and the diffractometer to crystal distance of 4.96 cm.[62] The initial cell constants were

obtained from three series of ω scans at different starting angles. Each series consisted of 12 frames collected at intervals of 0.5º in a 6º range about ω with the exposure time of (1; 1; 2)* seconds per frame. [* The compounds are referred to in the order of (DPDA)PbI_4; (DPDA)$PbBr_4$; $(DPDA)_2PbI_5 \cdot I$.] The reflections were successfully indexed by an automated indexing routine built in the APEXII program suite. The final cell constants were calculated from a set of (9903; 9833; 9898)* strong reflections from the actual data collection. The data were collected by using the full sphere data collection routine to survey the reciprocal space to the extent of a full sphere to a resolution of (0.67; 0.70; 0.70)* Å. A total of (47409; 46661; 87394)* data were harvested by collecting (5; 6; 6)* sets of frames with 0.5º scans in ω and φ with exposure times of (13; 20; 6)* sec per frame. These highly redundant datasets were corrected for Lorentz and polarization effects. The absorption correction was based on fitting a function to the empirical transmission surface as sampled by multiple equivalent measurements.[63]

2.3.3 Powder X-Ray diffraction

PXRD patterns were collected on as-grown powder samples deposited on glass substrates using a Bruker D8 Advance Powder X-ray Diffractometer with Cu Kα radiation.

2.3.4 Absorption Measurements

Thin-film UV-Vis absorption data were obtained with a Cary-5000 UV-vis-NIR spectrophotometer equipped with an integrating sphere attachment (Agilent) in transmission mode. Bulk powder UV-Vis absorption data were obtained with the same spectrometer in reflectance mode. *Room-temperature photoluminescence (PL)* was collected with an Aramis confocal Raman microscope using a 442 nm laser excitation source.

2.3.5 Temperature dependent photoluminescence (PL)

The sample was loaded in the optical cryogenic chamber (JANIS CCS-900) with a temperature controller (Cryo.Con Model 22C). The temperature was decreased to 15 K first, and then increased to each set temperature point for PL test. The sample in the optical cryogenic chamber was excited by a 325 nm CW laser (KIMMON) with laser spot size of 1 mm in radius and the power of 100 mW, the PL spectra were collected by a spectrometer (Action SP 2500i) coupled with a CCD camera (PIXIS 400BRX).

2.3.6 Computational details (Dmol3)

All spin-unrestricted calculations are implemented in the software Dmol3 based on the expansion of atomic orbitals. The ground state of electronic structure is described within density functional theory (DFT) using the generalized gradient approximation (GGA) with Perdew-Burke-Ernzerhof (PBE) exchange-correlation functional. The weak van der Waals correction proposed by Tkatchenko-Scheffler (TS) is taken into consideration. DFT semi-core pseudopots (DSPP) is used to replace core electrons by a single effective potential and reduce the computational cost. The double numerical plus polarization (DNP) in version 4.4 is chosen as the atomic orbital basis set. The convergence tolerances of energy, maximum force and displacement corresponding to 1.0×10−6 Ha, 0.002 Ha/Å, and 0.005 Å, respectively. A Morkhost-pack mesh of K-points 8×4×2 is sampled to calculate the electronic properties of the perovskites

2.4 Results and Discussion

Powders of (DPDA)PbX_4 (X = Br, I) were obtained by the dropwise addition of lead acetate precursor in concentrated HX to a cold (-70°C) solution of N,N-dimethylphenylene-p-diamine in ethanol to afford a precipitate of (DPDA)PbX_4. Large and high quality single crystals suitable for

single crystal structure determination were grown in concentrated acid solution from the re-dissolved stoichiometric precipitate. Images of the single crystals are shown in Figure 2.2. Flamboyantly twinned crystals of $(DPDA)PbI_4$ were formed from supersaturated solutions, producing large aesthetically pleasing crystals (Figure 2.2F) (see Experimental Section for synthesis details and X-ray structural refinements). A summary of the crystallographic parameters of these new compounds can be found in Table 2.1. The compounds are stable and can be handled in ambient conditions as indicated by no change in the PXRD patterns collected before and after one month of storage (Figure A.1). Thin-film samples were obtained via spin coating DMF solutions of dissolved single crystals.

Table 2.1. Crystal data for $(DPDA)PbI_4$, $(DPDA)PbBr_4$, and $(DPDA)_2PbI_5{\cdot}I$

Compound Name	$(DPDA)PbI_4$	$(DPDA)PbBr_4$	$(DPDA)_2PbI_5{\cdot}I$
Empirical formula	$C_8H_{14}I_4N_2Pb$	$C_8H_{14}Br_4N_2Pb$	$C_{16}H_{28}I_6N_4Pb$
Formula weight	853.03	665.04	1245.01
Crystal system	monoclinic	monoclinic	orthorhombic
Space group	$P2_1/n$	$P2_1/n$	$P2_12_12_1$
a/Å	6.417(2)	6.0681(15)	9.112(2)
b/Å	12.601(3)	11.846(3)	17.456(4)
c/Å	21.734(5)	21.259(5)	18.861(5)
β/°	96.832(7)	95.964(13)	90
Volume/Å^3	1744.9(8)	1519.9(7)	2999.9(13)
Z	4	4	4
ρ_{calc}, g/cm^3	3.247	2.906	2.757
2Θ range /°	3.742 to 61.056	3.852 to 63.952	3.18 to 61.116
Reflections collected	47409	46661	87394
Independent reflections	5334 (R_{int} = 0.0314)	5248 (R_{int} = 0.0315)	9166 (R_{int} = 0.0316)
Data/restraints/parameters	5334/0/140	5248/0/140	9166/0/251
Goodness-of-fit on F^2	1.135	1.013	1.168
Final R_1 indexes [all data]	R_1 = 0.0142	R_1 = 0.0198	R_1 = 0.0116
Final R_2 indexes [all data]	wR_2 = 0.0335	wR_2 = 0.0559	wR_2 = 0.0261

2.4.1 Crystal Structures and Bonding

The new 2DN perovskite structures are formed along the (001) orientation of a perovskite 3D unit cell as presented in Figure 2.2A, B. The 2D network of lead halide octahedra (PbX_6^{4-}) are corner sharing as expected from similar compounds. Both the bromide and iodide compounds crystalize in the monoclinic $P2_1/n$ space group and they are largely isostructural, with minor differences in the bonding. The Pb-X-Pb bond angle is slightly smaller in the bromide (166°/177°) than the iodide analogue (167°/177°) (Figure 2.2C). Even though these bond angles in both compounds are quite close to ideal (180°), there is significant distortion in the octahedra due to bond lengths and X-Pb-X angles normal to the *a*/*b* plane. In (DPDA)$PbBr_4$ the Pb-X bond distances range from 2.8045(8) Å all the way to 3.2033(9) Å (a 14% difference), but the bond distances in (DPDA)PbI_4 are closer in range 3.0158(8) Å to 3.3873(8) Å (a 10% difference). We further characterized the structural distortion using the quadratic elongation ($\langle\lambda\rangle$) and bond angle variance (σ^2) parameters, which were calculated using the Vesta software following the equations A.1, A.2, respectively.[54-56] The bromide has much higher quadratic elongation ($\langle\lambda\rangle = 1.0255$) and bond angle variance ($\sigma^2 = 71.7395$ deg^2) compared to the iodide ($\langle\lambda\rangle = 1.0202$ and $\sigma^2 = 58.7739$ deg^2) as summarized in Table 2.2.

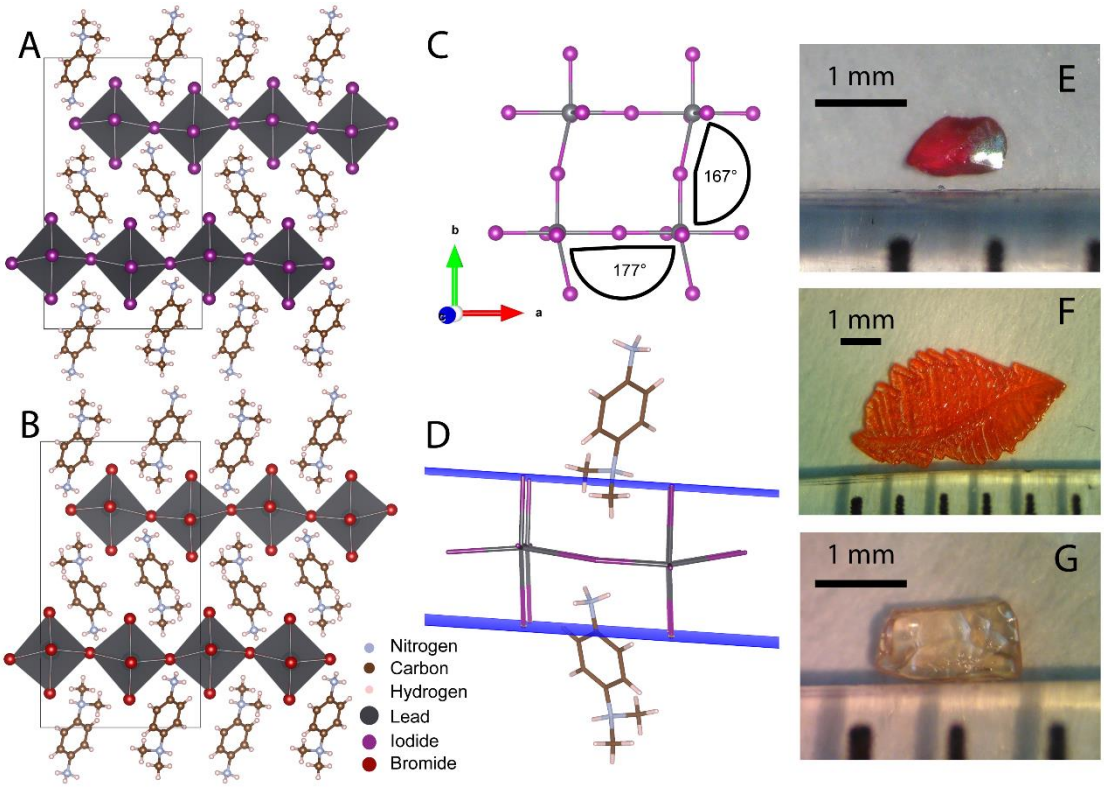

Figure 2.2. Crystal structures of (A) (DPDA)PbI_4 and (B) (DPDA)$PbBr_4$, both crystallized in the $P2_1/n$ space group and are viewed along the a-axis. The solid line boxes delineate the unit cells. (C) In a magnified view along the c-axis, the Pb-I-Pb bond angles are shown on the a/b axis as 167.06°/176.64° for (DPDA)PbI_4. (D) The iodide plane/nitrogen atom distance is shown visually for (DPDA)PbI_4. Photographs of (E) the single crystal selected for diffraction and (F) the heavily twinned crystal of (DPDA)PbI_4 compound, and (G) single crystal of (DPDA)$PbBr_4$.

Table 2.2. The optical characteristics and bonding parameters for the title compounds as well as common 2DN lead halide perovskites previously reported.

Compound	Exciton Abs. Peak Position (eV) (thin-film/bulk)	Narrow Emission Position (nm)	Pb-X-Pb Angles	Quadratic elongation⟨λ⟩	Bond angle Variance σ^2(deg^2)
(DPDA)PbI$_4$	2.37/2.29	537	167.06/ 176.64	1.0202	58.7739
(PEA)PbI$_4$	2.40 /2.35 [57]	525[8]	152.83	1.0011	3.6476
(NBT)PbI$_4$	2.42 [19]/2.35 [28]	517 [19]	149.25	1.0018	6.2464
(DPDA)PbBr$_4$	3.08/2.99	423	165.92/ 176.88	1.0255	71.7395
(DMAPA)PbBr$_4$ [22]	NA/2.96	~440	156.78/ 170.90	1.0119	40.5843
(DMABA)PbBr$_4$ [22]	NA/2.88	~450	162.90/ 167.82	1.0123	42.3259
(N-MPDA)PbBr$_4$ [16]	NA/2.95	~435	162.63/ 164.67	1.0009	3.0321

The Pb-X-Pb bond angles in (DPDA)PbX$_4$ are much closer to the ideal 180° compared to most previously reported 2DN lead halide compounds (Table 2.2). This is indeed quite unique for the (DPDA)PbX$_4$ structures and the DPDA cation promotes such a unique bonding structure. Interestingly, we can see from Figure 2.2A, B that the tertiary ammonium ($RNHMe_2^+$) and the smaller primary ammonium (RNH_3^+) group alternate back and forth to template the lead halide layers. The variation in distance between the ammonium group and the iodide plane is considerably large (Figure 2.2D). The methylated ammonium-plane distance is 0.566(2) Å, and the primary ammonium-plane distance is -1.110(2) Å, i.e., it inserts deeply into the pocket formed by PbI_6^{2-} octahedra (Figure 2.2D). This distance, calculated by the RMS of the halide plane-atom distance, deviates significantly from ammonium - halide plane distances summarized by Du et al., which

range from *ca* -0.7 to 0.7 Å for 2DN lead iodide compounds.[25] The impact of this unusual ammonium plane distance variation is also reflected in the large quadratic elongation and bond angle variance values. Unlike the well investigated 2D lead bromide perovskites, few structural reports are available in the literature for 2DN (001) lead iodide perovskites with dications, but it is reasonable to suspect these structural parameters are due to the uniquely rigid dication. 2DN lead bromide perovskites formed with dications are more commonly reported and we compared similar structures in Table 2.2. The new compound (DPDA)$PbBr_4$ has more ideal Pb-Br-Pb angles, but larger octahedral distortions ($\langle\lambda\rangle$ and σ^2), compared to previous dication structures.

The DPDA dication is so structurally rigid, it can also result in a 1DN chain perovskite phase, $(DPDA)_2PbI_5{\cdot}I$, when different reagent stoichiometry is used. The structural parameters are presented in Table 2.1 and the crystal structure is presented in the Append A Figure A.2. The demonstrated formation of 2DN perovskites, in addition to the formation of a 1DN perovskite is quite unique. This shows the DPDA dication is at the boundary of what can be tolerated in 2DN perovskites. Upon heating, the 1DN crystal turns from its native yellow color to a deep red color corresponding to the 2DN structure of (DPDA)PbI_4 (Figure A.2). This was briefly investigated using PXRD (Figure A.2) which demonstrated partial degradation to form the 2DN (DPDA)PbI_4, i.e., predominant pattern of 2DN with smaller 1DN peaks present.

2.4.2 Optical Properties

UV-Vis absorption spectroscopy was collected for both (DPDA)PbX_4 compounds. The excitonic features are observed quite clearly in both compounds in thin films (Figure 2.4A, B) and bulk powder samples (Figure 2.A.3). The excitonic peak of (DPDA)PbI_4, in both bulk powder (2.29 eV) and thin film (2.37 eV), is significantly red-shifted relative to previously reported 2DN

lead iodide compounds (Table 2.2). This is expected based on the correlation between bond angle and absorption onset. The more ideal Pb-I-Pb angles allow for increased orbital overlap in the lead and iodide's LUMO leading to a lower energy conduction band, as shown in the literature.[58] Both phenylethylamine (PEA) and n-butylamine (NBT) have been used in quasi-2D perovskites, where layers of 3D perovskite intercede between 2D layers. It is not unreasonable to expect a lower energy absorbing 2D perovskite layer could improve the performance of quasi-2D perovskite solar cells. Previous reports indicated the octahedral distortion parameters also affect the exciton absorbance peak,[25] but the relatively large distortion seen in (DPDA)PbI_4 does not appear to have as significant of an effect as bond angle does on the exciton absorbance peak. Interestingly, the bromide compound (DPDA)$PbBr_4$ does not appear to follow the trend of lower energy features associated with more ideal angles as closely. (DPDA)$PbBr_4$ has a highly ideal Pb-Br-Pb angle compared to previous compounds, and correspondingly has a reasonably low energy exciton absorption. However, the more pronounced octahedral distortions that are present in (DPDA)$PbBr_4$ could be of greater significance, which would explain the increased absorption energies. There appears to be a balance between octahedral distortions and Pb-X-Pb bond angles that contribute to the optical absorbance features.

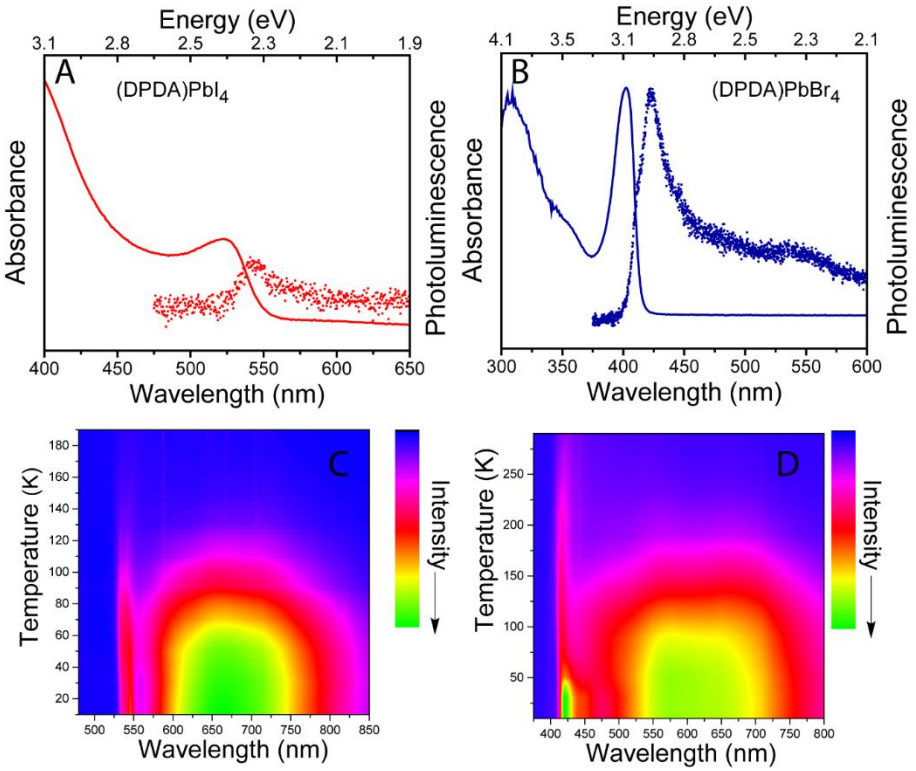

Figure 2.3. Absorbance and photoluminescence spectra of (A) (DPDA)PbI_4 and (B) (DPDA)$PbBr_4$. Both spectra show an excitonic absorption peak followed by broad bulk absorbance. At room temperature, the emission is weakly shifted relative to the excitonic absorbance peak, indicating free-exciton emission. Temperature dependent PL spectra of (C) (DPDA)PbI_4 and (D) (DPDA)$PbBr_4$ highlighting the broad emission observed at low temperature.

The photoluminescence spectra (PL) of both compounds show a broad red shouldered PL peak with a low stoke shifts. This is indicative of the commonly observed free excitons in 2DN perovskite compounds. Furthermore, temperature dependent PL results show that low temperature emission changed significantly (Figure 2.4C, D). We performed this experiment with the aim of extracting exciton binding energy from the changing intensity of the free exciton emission of

(DPDA)PbI_4 (narrow peak). However, in addition to an expected increase in the intensity of the free exciton peak, a very broad new emission feature was observed as temperature decreased. This has been observed in the well characterized 2DN lead bromide compounds, and is attributed to low-temperature self-trapped exciton emission.[33] However, this broad and significantly red-shifted feature has not been reported previously in 2DN lead iodide perovskites. Previous reports show a strong correlation between the distortion parameters and this broad emission,[33] thus it is not surprising that (DPDA)PbI_4 with its relatively high octahedral distortions shows this broad emission feature at low temperature. This self-trapped emission has been previously attributed to the formation of a X^-_2 dimer[59] or even X_3^- trimer[19], where X is a halide. This mechanism is quite likely in this material, but additional experiments are needed to confirm it. Interestingly, after the onset of the broad emission in (DPDA)PbI_4, the PL spectra show the emergence of a new peak at ~545 nm from 70 K to 15 K. This is possibly due the existence of a low-temperature phase. The broadband emission does not show a significant change in features over this potential structural phase transition, which is possibly because that the formation of the X_2^-/X_3^- species responsible for self-trapping of the exciton is independent of the exact unit cell crystal structure.[19,59]

2.4.3 Electronic Structure Calculations

We performed preliminary investigation into the potential contribution of the DPDA dication's orbitals to the electronic structures using density functional theory (DFT) calculations. Most discussions on the electronic contribution of the cations in 2DN perovskite materials are greatly overshadowed by the more dominant effects of lead halide bonding and distortions. The DFT projected partial density of states (PDOS), however, revealed that this conjugated diammonium cation may play a role on the electronic structure of 2DN perovskites, as shown in

Figure 2.4. As expected in a lead halide perovskite, the iodide forms the major contribution to valence band maximum (VBM, HOMO) of (DPDA)PbI_4, and the conduction band minimum (CBM, LUMO) is made up of lead/iodide mixing. However, (DPDA)$PbBr_4$ deviates from this motif, where the CBM (LUMO) has significant contributions from the conjugated aromatic DPDA dication. Notably, both compounds show contributions of DPDA in the near edge conduction band. These results suggest that the interesting properties of the conjugated dications may contribute to the electronic structure of the 2DN perovskites, but more experiments such as transient-absorbance spectroscopy or more complex multidimensional spectroscopy should be investigated to draw firm conclusions.[60,61]

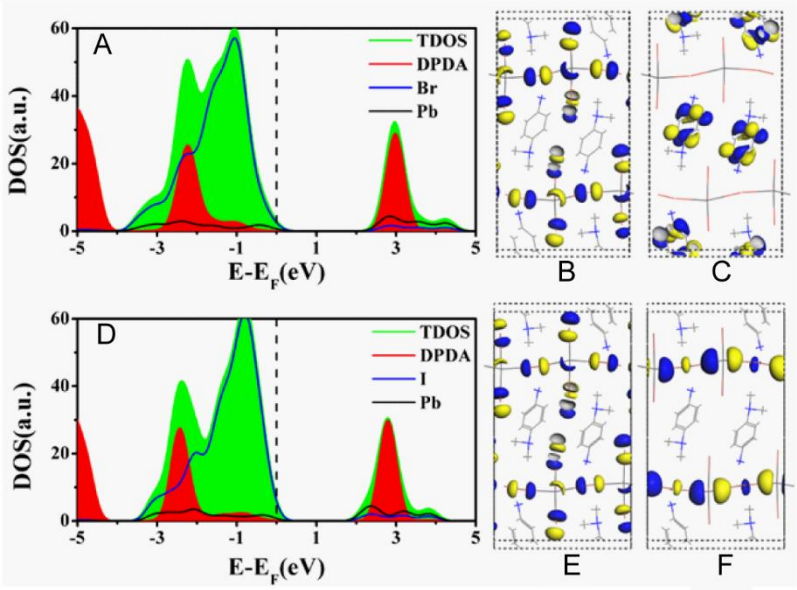

Figure 2.4. The projected partial density of state (PDOS), the highest occupied molecular orbital (HOMO) and the lowest unoccupied molecular orbital (LUMO) of (A, B, and C) (DPDA)$PbBr_4$ and (D, E, and F) (DPDA)PbI_4.

2.5 Conclusions

We report the synthesis, crystal structures, and optical properties of two new 2DN perovskite compounds based on an asymmetrically substituted, rigid, and conjugated diammonium, (DPDA)PbI_4 and (DPDA)PbI_4. The crystal structures display unique bonding features in the lead halide networks, where the Pb-X-Pb bond angles are closer to the ideal 180° than most previous 2DN perovskites. This is promoted by the high rigidity of the DPDA dication and the ability of this asymmetric diammonium to insert into the PbX_6^{2-} octahedral pockets. Such a rigid compound is at the limits of what can be formed into 2DN perovskites as demonstrated by its bond angles and the possibility to form both 1DN and 2DN perovskites. These unusual structural features also give rise to interesting optical properties, namely the red-shifted excitonic absorption feature relative to previous compounds, and a broadband emission observed at low temperatures unique for 2DN lead iodide perovskites. This report should spur investigations into these interesting 2DN perovskite compounds based on other rigid conjugated dications, and more in depth spectroscopic characterization, as well as a potentially better choice for more efficient quasi-2D perovskite solar cells.

2.6 References

(1) Lee, M. M.; Teuscher, J.; Miyasaka, T.; Murakami, T. N.; Snaith, H. J. Efficient Hybrid Solar Cells Based on Meso-Superstructured Organometal Halide Perovskites. *Science* **2012**, *338*, 643.

(2) Kojima, A.; Teshima, K.; Shirai, Y.; Miyasaka, T. Organometal Halide Perovskites as Visible-Light Sensitizers for Photovoltaic Cells. *J. Am. Chem. Soc.* **2009**, *131*, 6050.

(3) Saliba, M.; Matsui, T.; Domanski, K.; Seo, J.-Y.; Ummadisingu, A.; Zakeeruddin, S. M.; Correa-Baena, J.-P.; Tress, W. R.; Abate, A.; Hagfeldt, A.; Grätzel, M. Incorporation of rubidium cations into perovskite solar cells improves photovoltaic performance. *Science* **2016**, *354*, 206.

(4) Juarez-Perez, E. J.; Hawash, Z.; Raga, S. R.; Ono, L. K.; Qi, Y. Thermal degradation of $CH_3NH_3PbI_3$ perovskite into NH_3 and CH_3I gases observed by coupled thermogravimetry-mass spectrometry analysis. *Energy. Environ. Sci.* **2016**, *9*, 3406.

(5) Misra, R. K.; Aharon, S.; Li, B.; Mogilyansky, D.; Visoly-Fisher, I.; Etgar, L.; Katz, E. A. Temperature- and Component-Dependent Degradation of Perovskite Photovoltaic Materials under Concentrated Sunlight. *J. Phys. Chem. Lett.* **2015**, *6*, 326.

(6) Niu, G.; Li, W.; Meng, F.; Wang, L.; Dong, H.; Qiu, Y. Study on the stability of CH3NH3PbI3 films and the effect of post-modification by aluminum oxide in all-solid-state hybrid solar cells. *J. Mater. Chem. A* **2014**, *2*, 705.

(7) Stoumpos, C. C.; Malliakas, C. D.; Kanatzidis, M. G. Semiconducting Tin and Lead Iodide Perovskites with Organic Cations: Phase Transitions, High Mobilities, and Near-Infrared Photoluminescent Properties. *Inorg. Chem.* **2013**, *52*, 9019.

(8) Mitzi, D. B. Synthesis, Crystal Structure, and Optical and Thermal Properties of $(C_4H_9NH_3)_2MI_4$ (M = Ge, Sn, Pb). *Chem. Mater.* **1996**, *8*, 791.

(9) Li, T.; Dunlap-Shohl, W. A.; Han, Q.; Mitzi, D. B. Melt Processing of Hybrid Organic–Inorganic Lead Iodide Layered Perovskites. *Chem. Mater.* **2017**, *29*, 6200.

(10) Saidaminov, M. I.; Mohammed, O. F.; Bakr, O. M. Low-Dimensional-Networked Metal Halide Perovskites: The Next Big Thing. *ACS Energy Lett.* **2017**, *2*, 889.

(11) Grancini, G.; Roldan-Carmona, C.; Zimmermann, I.; Mosconi, E.; Lee, X.; Martineau, D.; Narbey, S.; Oswald, F.; De Angelis, F.; Graetzel, M.; Nazeeruddin, M. K. One-Year stable perovskite solar cells by 2D/3D interface engineering. *Nat. Commun.* **2017**, *8*, 15684.

(12) Dou, L.; Wong, A. B.; Yu, Y.; Lai, M.; Kornienko, N.; Eaton, S. W.; Fu, A.; Bischak, C. G.; Ma, J.; Ding, T.; Ginsberg, N. S.; Wang, L.-W.; Alivisatos, A. P.; Yang, P. Atomically thin two-dimensional organic-inorganic hybrid perovskites. *Science* **2015**, *349*, 1518.

(13) Mitzi, D. B.; Chondroudis, K.; Kagan, C. R. Organic-inorganic electronics. *IBM J. Res. Dev.* **2001**, *45*, 29.

(14) Knutson, J. L.; Martin, J. D.; Mitzi, D. B. Tuning the Band Gap in Hybrid Tin Iodide Perovskite Semiconductors Using Structural Templating. *Inorg. Chem.* **2005**, *44*, 4699.

(15) Kagan, C. R.; Mitzi, D. B.; Dimitrakopoulos, C. D. Organic-Inorganic Hybrid Materials as Semiconducting Channels in Thin-Film Field-Effect Transistors. *Science* **1999**, *286*, 945.

(16) Dohner, E. R.; Jaffe, A.; Bradshaw, L. R.; Karunadasa, H. I. Intrinsic white-light emission from layered hybrid perovskites. *J. Am. Chem. Soc.* **2014**, *136*, 13154.

(17) Dohner, E. R.; Hoke, E. T.; Karunadasa, H. I. Self-assembly of broadband white-light emitters. *J. Am. Chem. Soc.* **2014**, *136*, 1718.

(18) Wang, G. E.; Xu, G.; Wang, M. S.; Cai, L. Z.; Li, W. H.; Guo, G. C. Semiconductive 3-D haloplumbate framework hybrids with high color rendering index white-light emission. *Chem. Sci.* **2015**, *6*, 7222.

(19) Cortecchia, D.; Neutzner, S.; Srimath Kandada, A. R.; Mosconi, E.; Meggiolaro, D.; De Angelis, F.; Soci, C.; Petrozza, A. Broadband Emission in Two-Dimensional Hybrid Perovskites: The Role of Structural Deformation. *J. Am. Chem. Soc.* **2017**, *139*, 39.

(20) Ma, D.; Fu, Y.; Dang, L.; Zhai, J.; Guzei, I. A.; Jin, S. Single-crystal microplates of two-dimensional organic–inorganic lead halide layered perovskites for optoelectronics. *Nano Res.* **2017**, *10*, 2117.

(21) Liang, D.; Peng, Y.; Fu, Y.; Shearer, M. J.; Zhang, J.; Zhai, J.; Zhang, Y.; Hamers, R. J.; Andrew, T. L.; Jin, S. Color-Pure Violet-Light-Emitting Diodes Based on Layered Lead Halide Perovskite Nanoplates. *ACS Nano* **2016**, *10*, 6897.

(22) Mao, L.; Wu, Y.; Stoumpos, C. C.; Traore, B.; Katan, C.; Even, J.; Wasielewski, M. R.; Kanatzidis, M. G. Tunable White-Light Emission in Single-Cation-Templated Three-Layered 2D Perovskites $(CH_3CH_2NH_3)_4Pb_3Br_{10-x}Cl_x$. *J. Am. Chem. Soc.* **2017**, 139, 11956.

(23) Liao, W. Q.; Zhang, Y.; Hu, C. L.; Mao, J. G.; Ye, H. Y.; Li, P. F.; Huang, S. D.; Xiong, R. G. A lead-halide perovskite molecular ferroelectric semiconductor. *Nat. Commun.* **2015**, *6*, 7338.

(24) Gao, H.; Yuan, G.-J.; Lu, Y.-N.; Zhao, S.-P.; Ren, X.-M. Inorganic–organic hybrid compound with face-sharing iodoplumbate chains showing novel dielectric relaxation. *Inorg. Chem. Comm.* **2013**, *32*, 18.

(25) Du, K. Z.; Tu, Q.; Zhang, X.; Han, Q.; Liu, J.; Zauscher, S.; Mitzi, D. B. Two-Dimensional Lead(II) Halide-Based Hybrid Perovskites Templated by Acene Alkylamines: Crystal Structures, Optical Properties, and Piezoelectricity. *Inorg. Chem.* **2017**, *56*, 9291.

(26) Peng, W.; Yin, J.; Ho, K.-T.; Ouellette, O.; De Bastiani, M.; Murali, B.; El Tall, O.; Shen, C.; Miao, X.; Pan, J.; Alarousu, E.; He, J.-H.; Ooi, B. S.; Mohammed, O. F.; Sargent, E.; Bakr, O.

M. Ultralow Self-Doping in Two-dimensional Hybrid Perovskite Single Crystals. *Nano Lett.* **2017**, *17*, 4759.

(27) Cao, D. H.; Stoumpos, C. C.; Farha, O. K.; Hupp, J. T.; Kanatzidis, M. G. 2D Homologous Perovskites as Light-Absorbing Materials for Solar Cell Applications. *J. Am. Chem. Soc.* **2015**, *137*, 7843.

(28) Tsai, H.; Nie, W.; Blancon, J. C.; Stoumpos, C. C.; Asadpour, R.; Harutyunyan, B.; Neukirch, A. J.; Verduzco, R.; Crochet, J. J.; Tretiak, S.; Pedesseau, L.; Even, J.; Alam, M. A.; Gupta, G.; Lou, J.; Ajayan, P. M.; Bedzyk, M. J.; Kanatzidis, M. G. High-efficiency two-dimensional Ruddlesden-Popper perovskite solar cells. *Nature* **2016**, *536*, 312.

(29) Smith, I. C.; Hoke, E. T.; Solis-Ibarra, D.; McGehee, M. D.; Karunadasa, H. I. A layered hybrid perovskite solar-cell absorber with enhanced moisture stability. *Angew. Chem. Int. Ed.* **2014**, *53*, 11232.

(30) Fu, Y.; Wu, T.; Wang, J.; Zhai, J.; Shearer, M. J.; Zhao, Y.; Hamers, R. J.; Kan, E.; Deng, K.; Zhu, X. Y.; Jin, S. Stabilization of the Metastable Lead Iodide Perovskite Phase via Surface Functionalization. *Nano Lett.* **2017**, *17*, 4405.

(31) Quan, L. N.; Yuan, M.; Comin, R.; Voznyy, O.; Beauregard, E. M.; Hoogland, S.; Buin, A.; Kirmani, A. R.; Zhao, K.; Amassian, A.; Kim, D. H.; Sargent, E. H. Ligand-Stabilized Reduced-Dimensionality Perovskites. *J. Am. Chem. Soc.* **2016**, *138*, 2649.

(32) Solis-Ibarra, D.; Karunadasa, H. I. Reversible and irreversible chemisorption in nonporous-crystalline hybrids. *Angew. Chem. Int. Ed.* **2014**, *53*, 1039.

(33) Smith, M. D.; Jaffe, A.; Dohner, E. R.; Lindenberg, A. M.; Karunadasa, H. I. Structural origins of broadband emission from layered Pb–Br hybrid perovskites. *Chem. Sci.* **2017**, *8*, 4497.

(34) Kamminga, M. E.; Fang, H.-H.; Filip, M. R.; Giustino, F.; Baas, J.; Blake, G. R.; Loi, M. A.; Palstra, T. T. M. Confinement Effects in Low-Dimensional Lead Iodide Perovskite Hybrids. *Chem. Mater.* **2016**, *28*, 4554.

(35) Billing, D. G.; Lemmerer, A. Synthesis, characterization and phase transitions in the inorganic-organic layered perovskite-type hybrids $[(C_nH_{2n+1}NH_3)_2PbI_4]$, n = 4, 5 and 6. *Acta Crystallogr. B* **2007**, *63*, 735.

(36) Mitzi, D. B. Templating and structural engineering in organic-inorganic perovskites. *J. Chem. Soc., Dalton Trans.* **2001**, *1*, 1.

(37) Chondroudis, K.; Mitzi, D. B. Electroluminescence from an Organic−Inorganic Perovskite Incorporating a Quaterthiophene Dye within Lead Halide Perovskite Layers. *Chem. Mater.* **1999**, *11*, 3028.

(38) Saparov, B.; Mitzi, D. B. Organic–Inorganic Perovskites: Structural Versatility for Functional Materials Design. *Chem. Rev.* **2016**, *116*, 4558.

(39) Hong, X.; Ishihara, T.; Nurmikko, A. V. Dielectric confinement effect on excitons inPbI4-based layered semiconductors. *Phys. Rev. B* **1992**, *45*, 6961.

(40) Blancon, J. C.; Tsai, H.; Nie, W.; Stoumpos, C. C.; Pedesseau, L.; Katan, C.; Kepenekian, M.; Soe, C. M. M.; Appavoo, K.; Sfeir, M. Y.; Tretiak, S.; Ajayan, P. M.; Kanatzidis, M. G.; Even, J.; Crochet, J. J.; Mohite, A. D. Extremely efficient internal exciton dissociation through edge states in layered 2D perovskites. *Science* **2017**, *355*, 1288.

(41) Braun, M.; Tuffentsammer, W.; Wachtel, H.; Wolf, H. C. Tailoring of energy levels in lead chloride based layered perovskites and energy transfer between the organic and inorganic planes. *Chem. Phys. Lett.* **1999**, *303*, 157.

(42) Wu, K.; Bera, A.; Ma, C.; Du, Y.; Yang, Y.; Li, L.; Wu, T. Temperature-dependent excitonic photoluminescence of hybrid organometal halide perovskite films. *Phys. Chem. Chem. Phys.* **2014**, *16*, 22476.

(43) Thirumal, K.; Chong, W. K.; Xie, W.; Ganguly, R.; Muduli, S. K.; Sherburne, M.; Asta, M.; Mhaisalkar, S.; Sum, T. C.; Soo, H. S.; Mathews, N. Morphology-Independent Stable White-Light Emission from Self-Assembled Two-Dimensional Perovskites Driven by Strong Exciton–Phonon Coupling to the Organic Framework. *Chem. Mater.* **2017**, *29*, 3947.

(44) Li, Y. Y.; Lin, C. K.; Zheng, G. L.; Cheng, Z. Y.; You, H.; Wang, W. D.; Lin, J. Novel 〈 110 〉 -Oriented Organic−Inorganic Perovskite Compound Stabilized by N-(3-Aminopropyl)imidazole with Improved Optical Properties. *Chem. Mater.* **2006**, *18*, 3463.

(45) Mao, L.; Wu, Y.; Stoumpos, C. C.; Wasielewski, M. R.; Kanatzidis, M. G. White-Light Emission and Structural Distortion in New Corrugated Two-Dimensional Lead Bromide Perovskites. *J. Am. Chem. Soc.* **2017**.

(46) Dobrzycki, L.; Woźniak, K. Inorganic–organic hybrid salts of diaminobenzenes and related cations. *Cryst. Eng. Comm.* **2008**, *10*, 577.

(47) Rayner, M. K.; Billing, D. G. Poly[1,4-bis-(ammonio-meth-yl)cyclo-hexane [di-mu-bromido-dibromido-plumbate(II)]]. *Acta Crystallogr Sect E Struct Rep Online* **2010**, *66*, m658.

(48) Yangui, A.; Garrot, D.; Lauret, J. S.; Lusson, A.; Bouchez, G.; Deleporte, E.; Pillet, S.; Bendeif, E. E.; Castro, M.; Triki, S.; Abid, Y.; Boukheddaden, K. Optical Investigation of Broadband White-Light Emission in Self-Assembled Organic–Inorganic Perovskite $(C_6H_{11}NH_3)_2PbBr_4$. *J. Phys. Chem. C* **2015**, *119*, 23638.

(49) Wang, G.-E.; Wang, M.-S.; Jiang, X.-M.; Liu, Z.-F.; Lin, R.-G.; Cai, L.-Z.; Guo, G.-C.; Huang, J.-S. Crystal structures and optical properties of 1-D iodoplumbates templated by in situ synthesized p-phenylenediamine derivatives. *Inorg. Chem. Comm.* **2011**, *14*, 1957.

(50) Wang, C.-H.; Ma, C.-J.; Huang, Z.-P.; Zai, Y.-X.; Yang, Q.; Li, L.; Liang, Y.; Niu, Y.-Y. Bis(imidazole) Cation Templates and Subtle Effect: Syntheses and Characterization of Three New Pb(II) Halide Supramolecular Polymers. *J. Cluster Sci.* **2014**, *26*, 1027.

(51) Zhu, X.-H.; Mercier, N.; Frère, P.; Blanchard, P.; Roncali, J.; Allain, M.; Pasquier, C.; Riou, A. Effect of Mono- versus Di-ammonium Cation of 2,2‘-Bithiophene Derivatives on the Structure of Organic−Inorganic Hybrid Materials Based on Iodo Metallates. *Inorg. Chem.* **2003**, *42*, 5330.

(52) Mokhnache, O.; Boughzala, H. Crystal structure of a new hybrid compound based on an iodido-plumbate(II) anionic motif. *Acta Crystallogr E Crystallogr Commun* **2016**, *72*, 56.

(53) Yuan, Z.; Zhou, C.; Tian, Y.; Shu, Y.; Messier, J.; Wang, J. C.; van de Burgt, L. J.; Kountouriotis, K.; Xin, Y.; Holt, E.; Schanze, K.; Clark, R.; Siegrist, T.; Ma, B. One-dimensional organic lead halide perovskites with efficient bluish white-light emission. *Nat. Commun.* **2017**, *8*, 14051.

(54) Momma, K.; Izumi, F. VESTA 3 for three-dimensional visualization of crystal, volumetric and morphology data. *J. Appl. Crystallogr.* **2011**, *44*, 1272.

(55) Robinson, K.; Gibbs, G. V.; Ribbe, P. H. Quadratic Elongation: A Quantitative Measure of Distortion in Coordination Polyhedra. *Science* **1971**, *172*, 567.

(56) Brese, N. E.; O'Keeffe, M. Bond-valence parameters for solids. *Acta Crystallogr. Sect. E* **1991**, *47*, 192.

(57) Ishihara, T. Optical properties of PbI-based perovskite structures. *J. Lumin.* **1994**, *60*, 269.

(58) Amat, A.; Mosconi, E.; Ronca, E.; Quarti, C.; Umari, P.; Nazeeruddin, M. K.; Grätzel, M.; De Angelis, F. Cation-Induced Band-Gap Tuning in Organohalide Perovskites: Interplay of Spin–Orbit Coupling and Octahedra Tilting. *Nano Lett.* **2014**, *14*, 3608.

(59) Williams, R. T.; Song, K. S. The self-trapped exciton. *J. Phys. Chem. Solids* **1990**, *51*, 679.

(60) Pakoulev, A. V.; Block, S. B.; Yurs, L. A.; Mathew, N. A.; Kornau, K. M.; Wright, J. C. Multiply Resonant Coherent Multidimensional Spectroscopy: Implications for Materials Science. *J. Phys. Chem. Lett.* **2010**, *1*, 822.

(61) Manger, L. H.; Rowley, M. B.; Fu, Y.; Foote, A. K.; Rea, M. T.; Wood, S. L.; Jin, S.; Wright, J. C.; Goldsmith, R. H. Global Analysis of Perovskite Photophysics Reveals Importance of Geminate Pathways. *J. Phys. Chem. C* **2017**, *121*, 1062.

(62) Bruker-AXS (2016). $APEX_3$. Version 2016.5-0. Madison, W., USA.

(63) Krause, L., Herbst-Irmer, R., Sheldrick, G. M., Stalke, D. *J. Appl. Cryst.* **2015**, *48*, 3.

Chapter 3. Incorporating Large A-Cations into Lead Iodide Perovskite Cages: Relaxed Goldschmidt Tolerance Factor and Impact on Exciton-Phonon Interaction*

3.1 Abstract

The stability and formation of a perovskite structure is dictated by the Goldschmidt tolerance factor as a general geometric guideline. The tolerance factor has limited the choice of cations (A) in 3D lead iodide perovskites ($APbI_3$), an intriguing class of semiconductors for high-performance photovoltaics and optoelectronics. Here, we show the tolerance factor requirement is relaxed in 2D Ruddlesden-Popper (RP) perovskites, enabling the incorporation of a variety of larger cations beyond the methylammonium (MA), formamidinium, and caesium ions in the lead iodide perovskite cages for the first time. This is unequivocally confirmed with the single crystal X-ray structure of newly synthesized guanidinium (GA) based $(n\text{-}C_6H_{13}NH_3)_2(GA)Pb_2I_7$, which exhibits significantly enlarged and distorted perovskite cage containing sterically constrained GA cation. Structural comparison with $(n\text{-}C_6H_{13}NH_3)_2(MA)Pb_2I_7$ reveals that the structural stabilization originates from the mitigation of strain accumulation and self-adjustable strain-balancing in 2D RP structures. Furthermore, spectroscopic studies show a large A cation significantly influences carrier dynamics and exciton−phonon interactions through modulating the inorganic sublattice. These results enrich the diverse families of perovskite materials, provide new

* This chapter was originally published in *ACS Cent. Sci.,* **2019**, 5, 8, 1377-1386 in collaboration with Y. Fu, Z. Luo, F. Wang, M.M. Aristov, D. Pan, I.A. Guzei, A. Pan, X-Y. Zhu, and S. Jin

insights into the mechanistic role of A-cations on their physical properties, and have implications to solar device studies using engineered perovskite thin films incorporating such large organic cations.

3.2 Introduction

Three-dimensional (3D) lead iodide perovskites with a chemical formula of $APbI_3$, where A is a small monovalent cation, are a new class of semiconductors for high-performance photovoltaics and optoelectronics.[1-3] The typical crystal structure consists of a 3D framework of corner-sharing PbI_6 octahedra with the A cation occupying the 12 coordinate center site of each cuboid formed by eight PbI_6 octahedra (see Figure 3.1a for crystal structure), referred to here as the "perovskite cage". Despite the structural versatility,[4-5] the choice of A-cations in perovskite cages is limited by the geometric considerations of the empirical Goldschmidt tolerance factor (t),

$$t = (r_A + r_I)/[\sqrt{2}(r_{Pb} + r_I)],$$

in which r_A, r_{Pb}, and r_I are the effective radii of A, Pb^{2+}, and I^- ions, respectively.[6-7] Empirically, a t value between 0.8 and 1.0 is favorable for halide perovskite structures, but larger (> 1) or smaller (< 0.8) t values result in non-perovskite structures that adapt different types of connectivity of the PbI_6 octahedra. Thus far, only three cations [methylammonium ($CH_3NH_3^+$, MA), formamidinium ($[CH(NH_2)_2]^+$, FA), and caesium ion (Cs^+)] have been demonstrated to support a 3D halide perovskite structure (Figure 3.2b). However, both Cs^+ and FA cations barely support the A-site cavity in the case of iodides, resulting in metastable 3D perovskites of $CsPbI_3$ and $FAPbI_3$. The thermodynamically stable phases at room temperature are a "yellow" non-perovskite phase lacking a 3D perovskite framework. Organic cations such as ethylammonium (EA, $CH_3CH_2NH_3^+$) and

guanidinium (GA, $[C(NH_2)_3]^+$) with radii larger than that of FA are considered too large to enter the lead iodide perovskite cage,[6-8] as the increased elongation of the cage destabilizes the perovskite framework. In fact, all previous structural studies of GA-containing halide perovskites invariably showed that the GA cations do not occupy the A-sites in the perovskite cages.[8-11]

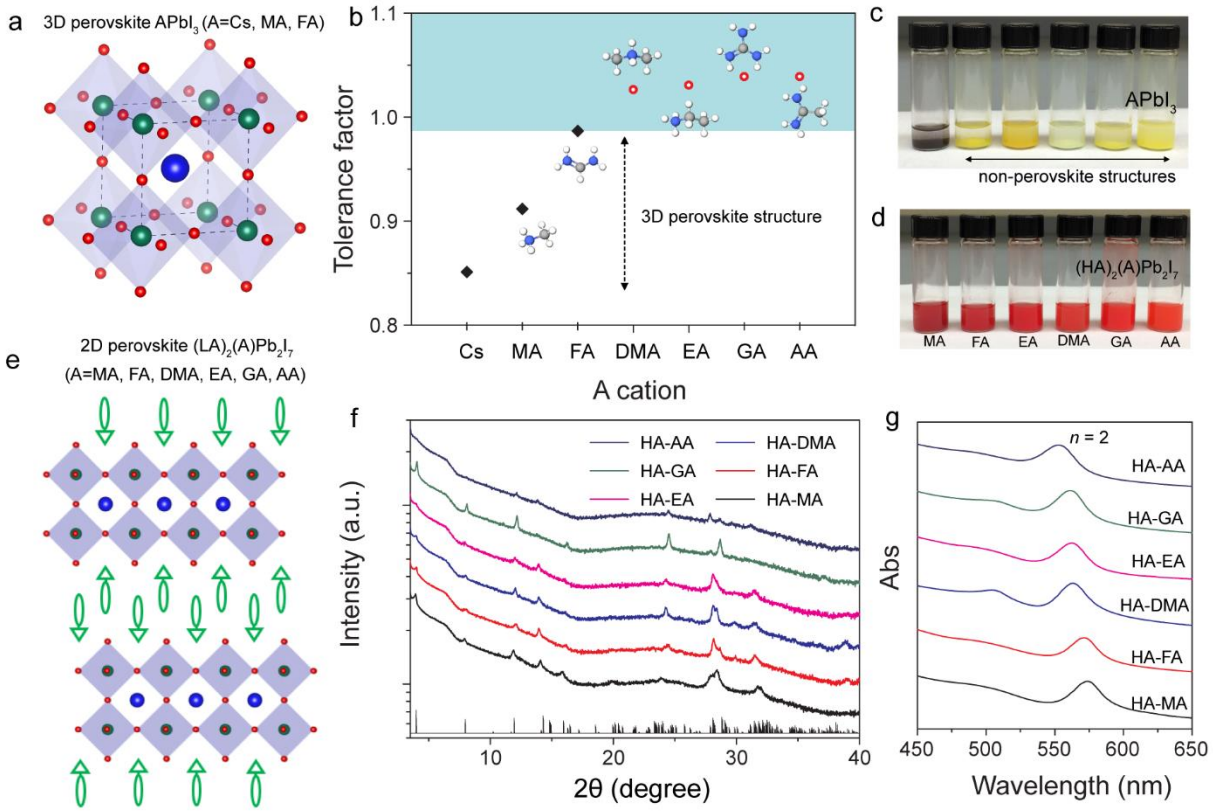

Figure 3.1. Crystal structures of $APbI_3$ and 2D RP perovskites of $(HA)_2(A)Pb_2I_7$. (a) The schematic crystal structure of 3D lead iodide perovskites $APbI_3$, A = Cs, MA, or FA. (b) Goldschmidt tolerance factor of $APbI_3$ perovskite with different A cations. The inset images depict the molecular structures of A cations. Large organic cations, such as dimethylammonium (DMA), ethylammonium (EA), guanidinium (GA), and acetamidinium (AA), do not support a 3D perovskite structure. (c) Photographs of yellow non-perovskite structures of $APbI_3$ with various A cations. (d) Photographs of red 2D RP perovskites of $(HA)_2(A)Pb_2I_7$ with various A cations. (e)

The schematic crystal structure of 2D RP perovskites of $(HA)_2(A)Pb_2I_7$, where HA is *n*-hexylammonium and A = MA, FA, DMA, EA, GA, and AA. (f) PXRD patterns of the $(HA)_2(A)Pb_2I_7$ crystalline powder products prepared by antisolvent growth of $APbI_3$ with excessive *n*-hexylammonium iodide, in comparison with the standard PXRD of $(HA)_2(MA)Pb_2I_7$. (g) Absorption spectra of the suspension solutions of $(HA)_2(A)Pb_2I_7$ with various cations.

Halide perovskites generally exhibit intrinsic lattice softness and structural disorders, which lead to fundamentally different chemistry and physics from the rigid crystalline structures of conventional semiconductors and oxide perovskites.[12] Fundamental insights into structure-property relationships hold the key to understand the mechanistic origins of halide perovskite's remarkable carrier properties, such as long carrier lifetimes and carrier diffusion lengths. These insights can also drive the design and discovery of new functional materials. There have been several theories on how the polar nature and dynamic behaviors of organic A cations can contribute to charge separation, long carrier lifetime, ferroelectricity, and the dynamic Rashba effect.[13-15] Recent studies have proposed that local structural fluctuation of the lead halide sublattice (and coupled to cation motions) may play a dominant role in determining these properties.[16-18] Experimental study of these hypotheses has proven challenging, largely because of the limited options for A cations occupying the cages. Recent progress has shown that a fine-tuning of the Goldschmidt tolerance factor by using mixed cation can further boost solar conversion efficiency and stability of perovskite solar cells.[19-21] However, the impacts on crystal lattice and optoelectronic properties of larger A cations inside the perovskite cage has not been examined.

In addition to 3D perovskites, when long-chain organo-ammonium ligands (LA) are introduced into the structure, 2D Ruddlesden-Popper (RP) perovskite can be formed. The RP structures with

the chemical formula of $(LA)_2(A)_{n-1}Pb_nI_{3n+1}$ (n is an integer), can be described as 2D quantum well analogues of 3D $APbI_3$ perovskites with a well thickness of n layers of lead iodide sheets.[22-24] RP perovskites with a $n \geq 2$ accommodate A cations in the perovskite cage in a similar manner as 3D perovskites. Owing to increased chemical stability, RP lead iodide perovskites have been demonstrated as promising alternatives to the 3D perovskites in photovoltaics and light emitting diodes,[25-26] but again the choices of A cations have been limited to MA, FA, and Cs cations so far[27] (in fact, most of the reported crystal structures have MA as the A-site cations).

Here, we show the Goldschmidt tolerance factor requirement is relaxed in 2D RP perovskites, enabling the incorporation of a series of large cations in the lead iodide perovskite cages. We have obtained the single crystal structure of $(HA)_2(GA)Pb_2I_7$ (HA = *n*-hexylammonium) to unequivocally confirm the occupancy of the large GA cation in the A-site of the lead iodide perovskite cage for the first time. By comparing the crystal structures of $(HA)_2(GA)Pb_2I_7$ and $(HA)_2(MA)Pb_2I_7$, we found that this structural stabilization of an oversized A-cation originates from the mitigation of strain accumulation and the capability of self-adjustable strain-balancing in 2D RP crystal structures. Low-frequency Raman spectroscopy studies revealed the large GA cation significantly influenced the exciton-phonon interactions, which is further correlated with the changes in the photoluminescence and carrier lifetime of $(HA)_2(GA)Pb_2I_7$ relative to $(HA)_2(MA)Pb_2I_7$. These more diverse and previously unavailable perovskite materials with large cations reveal the critical role of the A cations in modifying the lattice dynamics and carrier properties, which have important implications for understanding the exceptional carrier properties in halide perovskites.

3.3 Materials and Methods

3.3.1 Synthesis and Single-Crystal Growth of Various Samples

All chemicals and regents were purchased from Sigma-Aldrich and used as received, except for *n*-hexylammonium iodide (HAI) and AI (A = methylammonium (MA), formamidinium (FA), ethylammonium (EA), guanidinium (GA), acetamidinium (AA)) which were purchased from Dysol.

Safety Statement. Exposure to lead halides can cause acute and chronic lead poisoning. A respirator is recommended while handling powders of lead halides. For lead halides solvated in DMF, PPE compatible with DMF (i.e. butyl rubber gloves) should be used.

Antisolvent growth of non-perovskites of $APbI_3$ and 2D RP perovskites of $(HA)_2(A)Pb_2I_7$. The various non-perovskite compounds of $APbI_3$ were synthesized by adding chloroform into a solution of $APbI_3$, which was made by dissolving stoichiometric PbI_2 and the respective AI in dimethylformamide (DMF). The precipitated yellow powders were collected by centrifugation at 10 k rpm for 1 min and then dried at 60 °C in an oven. The various 2D RP perovskites of $(HA)_2(A)Pb_2I_7$ were synthesized by adding chloroform into a solution of $APbI_3$ with additional excessive HAI in dimethylformamide (DMF). Experimental parameters, such as the concentration and added volume of each component, are summarized in Table B.1. The precipitated red powders were collected by centrifugation at 10 k rpm for 1 min, and then washed with chloroform several times before dried at 60 °C in an oven. The suspended solutions of various $(HA)_2(A)Pb_2I_7$ were prepared by adding 10 μL of $APbI_3$ solution with HAI into ~2 mL chloroform. Experimental

parameters, such as the concentration and volume of each chemical, for obtaining precursor solutions are summarized in Table B.2.

Growth of $(HA)_2(MA)Pb_2I_7$ and $(HA)_2(MA)Pb_2I_7$ single crystals To grow $(HA)_2(GA)Pb_2I_7$ single crystals, powders of PbI_2 (922 mg, 2.00 mmol) and GAI (187 mg, 1.00 mmol) were dissolved in 2.0 mL of HI solution (57 wt % in H_2O) and 0.2 mL of H_3PO_2 in a vial. In a separate vial, *n*-hexylamine (700 μL, 5.33 mmol) was slowly added into 6 mL of HI solution and 0.2 mL of H_3PO_2 to form an HAI solution. The HAI solution (0.6 mL) was then added into the solution of PbI_2 and GAI. The solution was heated to 150 °C on a hot plate to completely dissolve all the solids. The mother liquour was then transferred into another vial in an oven and held at a constant temperature of 70 °C. Flake-like red-coloured single crystals of $(HA)_2(GA)Pb_2I_7$ were produced within a few hours. To grow $(HA)_2(MA)Pb_2I_7$ single crystals, powders of PbI_2 (922 mg, 2.00 mmol) and MAI (159 mg, 1.00 mmol) were dissolved in 2.0 mL of HI solution (57 wt % in H_2O) and 0.2 mL of H_3PO_2 in a vial. HAI solution (1.0 mL) was then added into the solution of PbI_2 and MAI. The solution was heated to 150 °C on a hot plate to completely dissolve all the solids. The mother liquour was allowed to sit undisturbed at room temperature for several hours to yield flake-like red-coloured single crystals.

3.3.2 Single Crystal X-ray Structure Determination

Single Crystal Diffraction Data Collection of $(HA)_2(GA)Pb_2I_7$ and $(HA)_2(MA)Pb_2I_7$. Red crystals with approximate dimensions of 0.12 × 0.04 × 0.04 mm^3 [$(HA)_2(GA)Pb_2I_7$] and 0.003 × 0.03 × 0.04 mm^3 [$(HA)_2(MA)Pb_2I_7$] were selected under oil under ambient conditions and attached to the tip of a MiTeGen MicroMount©. Note that compounds are referred to in the order of $(HA)_2GAPb_2I_7$, $(HA)_2MAPb_2I_7$ for the rest of the description. The crystal was mounted in a stream

of cold nitrogen at 100(1) K and centered in the X-ray beam by using a video camera. The crystal evaluation and data collection were performed on a Bruker Quazar SMART APEXII diffractometer with Mo K_α (λ = 0.71073 Å) radiation and the diffractometer to crystal distance of (6.00; 4.96 cm). The initial cell constants were obtained from three series of ω scans at different starting angles. Each series consisted of 12 frames collected at intervals of 0.5º in a 6º range about ω with the exposure time of 10 seconds per frame. The reflections were successfully indexed by an automated indexing routine built in the APEXII program suite. The final cell constants were calculated from a set of (4599; 9941) strong reflections from the actual data collection. The data were collected by using the full sphere data collection routine to survey the reciprocal space to the extent of a full sphere to a resolution of (0.80; 0.77 Å). A total of (40129; 61721) data were harvested by collecting (6; 10) sets of frames with (0.4º; 0.5 º) scans in ω and φ with exposure times of (20; 11) sec per frame. These highly redundant datasets were corrected for Lorentz and polarization effects. The absorption correction was based on fitting a function to the empirical transmission surface as sampled by multiple equivalent measurements.

Single Crystal Diffraction Data Collection of (GA)PbI$_3$. A colorless crystal with approximate dimensions 0.046 ×0.046 ×1.00 mm^3 was selected under oil under ambient conditions and attached to the tip of a MiTeGen MicroMount©. The crystal was mounted in a stream of cold nitrogen at 100(1) K and centered in the X-ray beam by using a video camera. The crystal evaluation and data collection were performed on a Bruker Quazar SMART APEXII diffractometer with Mo K_α (λ = 0.71073 Å) radiation and the diffractometer to crystal distance of 4.96 cm. The initial cell constants were obtained from three series of ω scans at different starting angles. Each series consisted of 12 frames collected at intervals of 0.5º in a 6º range about ω with the exposure time of 1 second per

frame. The reflections were successfully indexed by an automated indexing routine built in the APEX3 program suite. The final cell constants were calculated from a set of 9885 strong reflections from the actual data collection. The data were collected by using the full sphere data collection routine to survey the reciprocal space to the extent of a full sphere to a resolution of 0.66 Å. A total of 31655 data were harvested by collecting 10 sets of frames with 0.3/0.5º scans in ω and φ with exposure times of 1/6 sec per frame. These highly redundant datasets were corrected for Lorentz and polarization effects. The absorption correction was based on fitting a function to the empirical transmission surface as sampled by multiple equivalent measurements. A structural figure with probability ellipsoids of $GAPbI_3$ is shown in Figure B.6.

Structure Solution and Refinement of *$(HA)_2(GA)Pb_2I_7$:* The systematic absences in the diffraction data were consistent for the space groups $P\bar{1}$ and $P1$. The *E*-statistics strongly suggested the centrosymmetric space group $P\bar{1}$ that yielded chemically reasonable and computationally stable results of refinement. A successful solution by the direct methods provided most non-hydrogen atoms from the *E*-map. The remaining non-hydrogen atoms were located in an alternating series of least-squares cycles and difference Fourier maps. All non-hydrogen atoms were refined with anisotropic displacement coefficients. All hydrogen atoms were included in the structure factor calculation at idealized positions and were allowed to ride on the neighboring atoms with relative isotropic displacement coefficients. In the N5 hexan-1-aminium, the carbon atoms are equally disordered over two positions. The disordered components were refined with restraints and constraints. The crystal selected for the single-crystal X-ray diffraction experiment proved to be a two-component non-merohedral twin with a 30.15(12) % second component contribution. The twin domains are related by a 179.9° rotation about direct axis [010]. The final

least-squares refinement of 298 parameters against 28779 data resulted in residuals *R* (based on F^2 for $I \geq 2\sigma$) and *wR* (based on F^2 for all data) of 0.0315 and 0.0928, respectively. Evaluation of the CIF using the CheckCIF routine at *www.checkcif.iucr.org* yielded one B alert. The missing reflection 101 was affected by the beam stop. However, its presence does not noticeably affect the refinement. A structural figure with probability ellipsoids of $(HA)_2(GA)Pb_2I_7$ is shown in Figure B.7.

Structure Solution and Refinement of *$(HA)_2(MA)Pb_2I_7$*: The systematic absences in the diffraction data were consistent for the space groups *C*2/*c* and *Cc*. The *E*-statistics strongly suggested the centrosymmetric space group *C*2/*c* that yielded chemically reasonable and computationally stable results of refinement. A successful solution by the direct methods provided most non-hydrogen atoms from the *E*-map. The remaining non-hydrogen atoms, unless specified otherwise, were located in an alternating series of least-squares cycles and difference Fourier maps. All non-hydrogen atoms, unless otherwise noted, were refined with anisotropic displacement coefficients. All hydrogen atoms were included in the structure factor calculation at idealized positions and were allowed to ride on the neighboring atoms with relative isotropic displacement coefficients. The asymmetric unit contains ½ of $Pb_2I_7^{3-}$, one hexylammonium, and ½ methyl ammonium. Atom I3 of this $Pb_2I_7^{3-}$ dimer resides on a crystallographic two-fold axis. The methylammonium is disordered over two positions near a crystallographic two-fold axis and thus there are four positions shared by this cation. The relative occupancies of these four positions are 30.2(6), 19.8(6), 30.2(6), and 19.8(6), but only two of these are symmetry-independent. The methylammoniums were refined with distant restraints and anisotropic displacement parameter constraints. It is not possible to decisively distinguish between the nitrogen and carbon atoms in

the methylammonium. The final least-squares refinement of 125 parameters against 3931 data resulted in residuals *R* (based on F^2 for $I \geq 2\sigma$) and *wR* (based on F^2 for all data) of 0.0211 and 0.0509, respectively. The final difference Fourier map contained several residual electron density peaks (ca. 2.36 e/Å^3). These peaks were located in the vicinity of the heaviest atoms and were considered noise. A structural figure with probability ellipsoids of $(HA)_2(MA)Pb_2I_7$ is shown in Figure B.8.

Structure Solution and Refinement of *(GA)PbI$_3$*: The systematic absences in the diffraction data were uniquely consistent for the space group $P2_1/n$ that yielded chemically reasonable and computationally stable results of refinement. A successful solution by the direct methods provided most non-hydrogen atoms from the *E*-map. The remaining non-hydrogen atoms were located in an alternating series of least-squares cycles and difference Fourier maps. All non-hydrogen atoms were refined with anisotropic displacement coefficients. All hydrogen atoms were included in the structure factor calculation at idealized positions and were allowed to ride on the neighboring atoms with relative isotropic displacement coefficients. The final least-squares refinement of 73 parameters against 2393 data resulted in residuals *R* (based on F^2 for $I \geq 2\sigma$) and *wR* (based on F^2 for all data) of 0.0233 and 0.0523, respectively. The final difference Fourier map was featureless.

Crystal structure data of $(HA)_2(GA)Pb_2I_7$ and $(HA)_2(MA)Pb_2I_7$, and *GAPbI$_3$* have been deposited at the Cambridge Crystallographic Data Centre (CCDC) under reference numbers 1888368, 1886888, and 1886889, respectively. These data can be obtained free of charge from the website (https://www.ccdc.cam.ac.uk/structures/).

3.3.3 Other Structural and Spectroscopic Characterizations

The PXRD patterns were collected on as-prepared samples on glass substrates using a Bruker D8 Advance Powder X-ray Diffractometer with Cu Kα radiation. The optical images of the single crystals were obtained on an Olympus BX51M optical microscope.

Absorption and PL measurements. Bulk powder UV−vis absorption data were obtained with a Cary-5000 UV−vis−NIR spectrophotometer equipped with an integrating sphere attachment (Agilent) in reflectance mode. The UV−vis absorption data of suspended solutions were collected using a JASCO V-550 spectrometer.

The steady-state photoluminescence of $(HA)_2(GA)Pb_2I_7$ and $(HA)_2(MA)Pb_2I_7$ single crystals were collected with an Aramis Confocal Raman Microscope using a 442 nm laser source. The temperature dependent PL spectra of $(HA)_2(GA)Pb_2I_7$ and $(HA)_2(MA)Pb_2I_7$ single crystals were measured with a 488 nm CW laser at different temperature from 10 K to 290 K in a Microscope Cryostat System (Link Physics C01-001-122). Time-resolved PL decay kinetics of $(HA)_2(GA)Pb_2I_7$ and $(HA)_2(MA)Pb_2I_7$ single crystals were collected using a streak camera (Hamamatsu C10910) with a confocal microscope (WITec, alpha-300), and with a excitation light of Ti:Sapphire laser pulses at 400 nm (repetition rate of 80 MHz, pulse width of 80 fs). The 400 nm excitation light was generated by the second harmonic of an 800 nm laser from a mode-locked oscillator (Tsunami 3941-X1BB, Spectra-Physics) after a BBO crystal. The laser beam was focused onto the sample surface by an objective lens (50×, Zeiss, 0.75 NA) with a spot diameter of 3 μm, and the PL emission was collected by the same objective lens. The laser power was calibrated with a power meter (PM100D from THORLABS).

Raman measurements. The Raman spectra of $(HA)_2(GA)Pb_2I_7$ and $(GA)_2PbI_4$ single crystals (shown in Figure S3) were collected with an Aramis Confocal Raman Microscope using a 633 nm laser source. The low-frequency Raman spectra of $(HA)_2(GA)Pb_2I_7$ and $(HA)_2(MA)Pb_2I_7$ single crystals were collected on a home-built microscopic Raman setup with a 1064 nm YAG laser. A volume Brag grating (VBG) beamsplitter filter (BPF, OptiGrate, Inc.) was used to purify the incident laser wavelength and guided the laser towards the sample in a cryostat (Oxford Instruments Microstat HiRes2) under vacuum of 10^{-6} to 10^{-5} Torr. A 40× objective with a numerical aperture of 0.6 (S Plan Fluor, Nikon) was applied to focus the beam and collect the scattered light. Three ultra-narrow band BVG notch filters attenuated the Rayleigh line each with O. D. > 3.0, then the light containing large enough portion of Raman signal was sent into a 4-f spectrometer with 600 grooves/mm diffraction grating through a special filter (resolution of 0.8 cm^{-1}). The signal was read out by an InGaAs CCD camera (Pylon IR 1024, Princeton Instruments) with liquid nitrogen cooling. Each spectrum was acquired after the sample was stabilized at the target temperature for 10 min.

3.4 Results

3.4.1 Synthesis of 2D RP lead iodide perovskites with large A-cations

We first describe how 2D RP lead iodide perovskites offer more structural flexibility for the incorporation of large A cations relative to their 3D perovskite counterparts. Among various organic cations, only the MA cation can support a stable 3D perovskite structure of $APbI_3$ at room temperature (Figure 3.1b). Large organic cations, such as dimethylammonium (DMA, $CH_3NH_2^+CH_3$,), ethylammonium (EA, $CH_3CH_2NH_3^+$), guanidinium (GA, $[C(NH_2)_3]^+$), and

acetamidinium (AA, $[CH_3C(NH_2)_2]^+$), exclusively form non-perovskite compounds with lead iodide. Typical antisolvent growth of $APbI_3$ with these large A cations yield yellow precipitates (Figure 3.1c). The corresponding PXRD patterns confirm the non-perovskite structures with either edge-shared double chain or face-shared one-dimensional chain of PbI_3^- (illustrated in Figure B.1). FA cations are considered at the edge of the tolerable size, as demonstrated by $FAPbI_3$ adopting a thermodynamically stable non-perovskite structure at room temperature in addition to a metastable 3D perovskite lattice.[28] Interestingly, nanostructuring and surface functionalization have been shown to stabilize the 3D perovskite polymorph of $FAPbI_3$ (or $CsPbI_3$) due to the effects of surface energy relative to bulk energy.[28-30]

Inspired by the surface ligand induced phase stabilization of metastable $FAPbI_3$, we discovered that the perovskite lattices of $APbI_3$ with large A cations contained in the perovskite cage can be stabilized in a reduced dimensionality, i.e. 2D RP perovskites of $(LA)_2(A)_{n-1}Pb_nI_{3n+1}$ (see Figure 3.1e for a schematic crystal structure for the case of $n = 2$). When *n*-hexylammonium iodide (HAI) is introduced into the precursor solutions of $APbI_3$ (see details in section 3.3 Materials and Methods), antisolvent growth yields red-colored precipitates (Figure 3.1d), in striking contrast to their yellow non-perovskite counterparts (Figure 3.1c). The corresponding PXRD patterns (Figure 3.1f) show a set of diffraction peaks similar to the PXRD pattern observed for $(HA)_2(MA)Pb_2I_7$, confirming the formation of 2D RP perovskites of $(LA)_2(A)Pb_2I_7$. Additionally, the absorption spectra from suspended solutions show a dominant excitonic peak located at ~560 nm (Figure 3.1g), as expected from quantum confined $(LA)_2(A)Pb_2I_7$.[31] The excitonic absorbance peak slightly blue shifts as the size of the A-site cation increases. Furthermore, when *n*-hexylammonium iodide is replaced with *n*-butylammonium (BA) iodide, similar results were obtained (Figure B.2),

which shows the generality of the Goldschmidt tolerance factor relaxation in 2D RP structures with different long chain alkylammonium cations. It appears the n = 2 perovskites are the most easily accessible structures, but for the case of the smaller EA cation, the PXRD pattern suggests the formation of higher n perovskite structures is possible (Figure B.2).

3.4.2 Single crystal structure of $(HA)_2(GA)Pb_2I_7$

To unequivocally confirm the capture of the large A cation in the perovskite cage, we grew single crystals of $(HA)_2(GA)Pb_2I_7$ and solved the crystal structures via single-crystal XRD analysis (Table 3.1, see details in section 3.3 Materials and Methods). We choose GA as a representative large cation, because there have been significant research interests in and many attempts at incorporating GA into perovskite lattice for improving solar devices.[19, 32] However, rigorous crystallographic evidence of the successful incorporation of GA in the perovskite cage has not been demonstrated thus far. Instead, several crystal structures, such as $(GA)_2PbI_4$,[8] $(FA)(GA)PbI_4$,[11] $(Cs,GA)(Cs)Pb_2Br_7$,[9] and $(GA)(MA)_nPbI_{3n+1}$,[10] have repeatedly shown the GA cations occupy the interlayer space between the 2D lead halide sublattice, i.e., GA serves as the "LA cation" in these 2D RP perovskites. Moreover, GA is particularly interesting because it is the only non-polar organic cation among the organic cations listed above.[33] This may benefit future fundamental studies regarding the role of polarity of A cations in optoelectronic and ferroelectric properties.

Table 3.1. Complete Crystal data and structure Refinement of $(HA)_2(MA)Pb_2I_7$ and $(HA)_2(GA)Pb_2I_7$ at 100K

Compound name	$(HA)_2(MA)Pb_2I_7$	$(HA)_2(GA)Pb_2I_7$
Empirical formula	$(C_6H_{13}NH_3)_2(CH_3NH_3)Pb_2I_7$	$(C_6H_{13}NH_3)_2[C(NH_2)_3]Pb_2I_7$

Formula weight	665.04	1567.16
Crystal system	monoclinic	triclinic
Space group	*C*2/*c*	*P-1*
a/Å; α/°	45.146(16); 90	8.8195(14); 79.965(13)
b/Å; β/°	8.814(3); 100.030(5)	9.0300(15); 87.341(9)
c/Å; γ/°	8.695(3); 90	21.699(4); 89.986(10)
Volume/Å^3	3407(2)	1699.8(5)
Z	4	2
ρ_{calc}, g/cm^3	3.000	3.062
Reflections collected	61721	28779
Independent reflections	3931 [R_{int} = 0.0456, R_{sigma} = 0.0170]	28779 [R_{int} = 0.0390, R_{sigma} = 0.0463]
Goodness-of-fit on F^2	1.061	1.047
Final R indexes [I>=2σ (I)]	R_1 = 0.0211, wR_2 = 0.0497	R_1 = 0.0315, wR_2 = 0.0886
Final R indexes [all data]	R_1 = 0.0241, wR_2 = 0.0509	R_1 = 0.0335, wR_2 = 0.0928
Largest diff. peak/hole / e Å^{-3}	2.36/-1.32	2.40/-1.74

To gain mechanistic insights of the relaxed *t* requirement and to study the structure-property relationship, we also synthesized crystals of $(HA)_2(MA)Pb_2I_7$ to compare with the structure of $(HA)_2(GA)Pb_2I_7$ (see Figure 3.2e for representative optical images). All crystals were grown from concentrated hydroiodic acid using an off-stoichiometry protocol.[22] It is noted that we did not observe any $(HA)_2(GA)_{n-1}Pb_nI_{3n+1}$ structures with $n > 2$ by varying the precursor stoichiometries. Crystallographic data and important structural refinement information for the two compounds are listed in Table 3.1 (full details listed in Table B.3). The crystal structures (Figure 3.2a and 3.2b) consist of two layers of corner-sharing PbI_6 octahedra ($n = 2$) with bilayer of HA cations separating the inorganic slabs, and the GA or MA cations filling in the perovskite cages.

One significant feature of $(HA)_2(GA)Pb_2I_7$ is that the occupancy of GA in the perovskite cage significantly elongates the Pb-I bond distances, swelling the volume of the perovskite cage (see

Figure 3.2c), which is defined by the volume of the cuboid made up by the three Pb-Pb distances in the *a*, *b*, and *c* directions. As shown in Table 3.2 that compares the structural parameters of the two compounds, the volume of the perovskite cage increases by 14.776 $Å^3$ (~5.9 % volume expansion) for $(HA)_2(GA)Pb_2I_7$ compared to $(HA)_2(MA)Pb_2I_7$. Moreover, we find that the volume of the cage for $(HA)_2(GA)Pb_2I_7$ is larger than all previously reported 2D RP perovskites with n = 2 (Table B.4). This exceptionally large cage volume indicates large tensile strain on the inorganic sublattice, which is further confirmed by the higher octahedral distortion parameters of bond angle variance (σ^2) and quadratic elongation ($\langle\lambda\rangle$) in $(HA)_2(GA)Pb_2I_7$ relative to $(HA)_2(MA)Pb_2I_7$ (Table 3.2, see Equation B.1 and B.2 for calculations).[34-35] Because the inorganic framework is templated by both the A-site cation and HA cation, different conformation of HA cations can also influence the Pb-I network distortion. One may expect that strain will accumulate as successive 2D slabs of GA cages are stacked, leading to the eventual destabilization of a 3D perovskite structure.

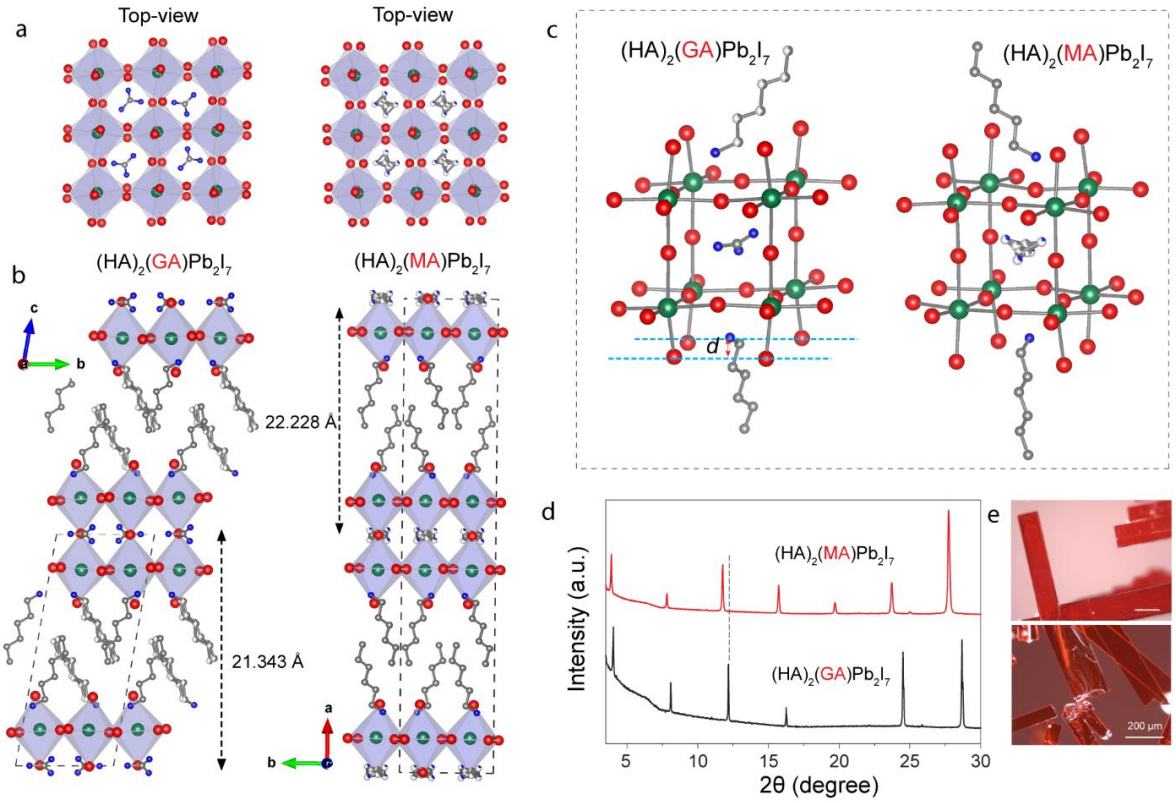

Figure 3.2. The crystal structure of $(HA)_2(GA)Pb_2I_7$ in comparison with $(HA)_2(MA)Pb_2I_7$. (a) Top-view of the crystal structures of $(HA)_2(GA)Pb_2I_7$ and $(HA)_2(MA)Pb_2I_7$. (b) Side-view of the crystal structures of $(HA)_2(GA)Pb_2I_7$ along *a* direction and $(HA)_2(MA)Pb_2I_7$ along *c* direction. (c) Comparison of the perovskite cages of $(HA)_2(GA)Pb_2I_7$ and $(HA)_2(MA)Pb_2I_7$. Also illustrated is the definition of the distance of the N atom in HA from the iodide plane. (d) PXRD and (e) optical images of single-crystal flakes of $(HA)_2(MA)Pb_2I_7$ (top) and $(HA)_2(GA)Pb_2I_7$ (bottom). The diffraction peaks of $(HA)_2(GA)Pb_2I_7$ appear at higher angles than those of $(HA)_2(MA)Pb_2I_7$, indicating even smaller interlayer distance in the former.

Table 3.2. Comparison of the structural and bonding parameters between $(HA)_2(MA)Pb_2I_7$ and $(HA)_2(GA)Pb_2I_7$.

structural parameters	$(HA)_2(MA)Pb_2I_7$	$(HA)_2(GA)Pb_2I_7$	difference (GA-MA)
volume of cage ($Å^3$)	250.2589	264.446	14.187
a,*b* axis Pb-plane to Pb-plane distance (avg) (Å)	6.1905	6.3112	0.1207
c-axis Pb-plane to Pb-plane distance (cage) (Å)	6.5150	6.6412	0.1262
c-axis Pb-plane to Pb-plane distance (ligand bilayer) (Å)	15.713	14.702	-1.011
ammonium - iodide plane distance *d* (avg) (Å)	0.75	0.834	0.084
Pb-I-Pb angle (a, b) (°)	155.73	162.02	6.29
Pb-I-Pb angle (c) (°)	179.228	178.87	-0.358
bond angle variance (σ^2, deg^2)	10.5161	15.1104	4.5943
quadratic elongation ($\langle\lambda\rangle$)	1.0031	1.0046	0.0015

3.4.3 Relaxing the Goldschmidt tolerance factor

We believe the issue of strain accumulation due to large A cations in 3D perovskites is circumvented in 2D RP perovskites with reduced dimensionality. Strain relaxation readily occurs at the top and bottom of PbI_6 octahedra due to less geometric constraint. This is aided by the structural flexibility of the HA cation bilayers outside the cage that can accommodate the PbI_6 octahedral distortions. Strain dissipation into the interlayer space thus leads to different molecular conformations of the HA cations in $(HA)_2(MA)Pb_2I_7$ and $(HA)_2(GA)Pb_2I_7$ (Figure 3.2b). As a result, $(HA)_2(GA)Pb_2I_7$ exhibits an even smaller interlayer distance despite having a larger

perovskite cage than $(HA)_2(MA)Pb_2I_7$ (Table 3.2). On the other hand, the interlayer HA cations act as strain compensation layers by applying opposite strain from the GA cages to balance the global strain of the overall structure. Specifically, the tensile strain in the GA cage is balanced by compressive strain applied from the bilayers of HA cations. Compressive molecular packings of the interlayer HA in the $(HA)_2(GA)Pb_2I_7$ is supported by the surprisingly smaller interlayer spacing and unit cell volume of the $(HA)_2(GA)Pb_2I_7$ (see Figure 3.2d and Table 3.2) relative to the $(HA)_2(MA)Pb_2I_7$ (considered as a strain-free structure), despite the fact that $(HA)_2(GA)Pb_2I_7$ has a larger perovskite cage.

Moreover, to compensate for the strained GA cage, the HA ammonium head inserts deeper into the octahedral pocket, as characterized by the increased distance between the N atom and the iodide plane (*d*) in the $(HA)_2(GA)Pb_2I_7$ relative to the $(HA)_2(MA)Pb_2I_7$ (illustrated in Figure 3.2c and values shown Table 3.2). The interaction between the N and I atoms is through hydrogen bond N-H-I. These structural features show that the increased structural flexibility of 2D RP perovskites relative to their 3D counterparts reduces cumulative strain and balances the strain in a self-adjustable manner, thus facilitates the incorporation of large A cations and relaxes the tolerance factor requirement. In addition to these 2D lead iodide perovskites with DMA, EA, GA and AA cations reported herein, there are examples of 2D RP lead chloride or bromide perovskites[36-37] $(EA)_2(EA_2)Pb_3X_{10}$ (X = Br or Cl) and 2D RP tin iodide perovskite[38] $(IPA)_2(IPA)Sn_2I_7$ (IPA = isopropylammonium) that exhibit a relaxed tolerance factor. This indicates the relaxed tolerance factor is likely a universal property of the 2D RP perovskite structure, which is understandable based on the lattice strain mitigation in 2D RP perovskite structures that is not possible in 3D perovskite structures.

The GA cation has a symmetric planar structure forcing the perovskite cage to elongate diagonally to accommodate this cation. Therefore, one may expect the molecular motions of GA to be sterically hindered in the cage. Indeed, the configuration of the GA cation in the perovskite cage is fixed while the MA cations can adopt several disordered configurations (Figure 3.2c) in the $(HA)_2(MA)Pb_2I_7$. The MA cation is disordered over two positions about a crystallographic two-fold axis with relative occupancies of 30.2% and 19.8% (determined from the crystal structure refinements at 100 K), and thus generating four partially occupied positions (Figure 3.2a and 3.2c). We note that carbon and nitrogen atoms in the MA cation could not be definitively identified. We consider this dynamic disorder of MA cation as a reflection of the structural flexibility of the inorganic cage in $(HA)_2(MA)Pb_2I_7$. We further compared the Raman vibration modes of the GA cation occupying the cage of $(HA)_2(GA)Pb_2I_7$, with those of the GA cation occupying the interlayer gallery of $(GA)_2PbI_4$ (Figure B.3). Raman peaks at ~505 and 1010 cm^{-1} are respectively assigned to the angle deformations and stretching vibrations of the CN_3 group.[8] The stretching mode of cage-GA is blue-shifted by 4 cm^{-1} than that of GA in the gallery. Moreover, the bending vibration of cage-GA is significantly suppressed, which is demonstrated by the much lower relative intensity ($I_{bending}/I_{stretching}$, 0.65 versus 2.08). These results confirm a large degree of steric hindrance experienced by the GA cation in the cage.

3.4.4 Impacts of A cations on physical properties

Having established the structural information from single-crystal XRD analysis, we turn to studying the impacts of varying the A cation on the physical properties, such as optical bandgaps, and carrier and phonon properties. UV-Vis diffuse reflectance spectroscopy was collected for $(HA)_2(GA)Pb_2I_7$ in comparison with $(HA)_2(MA)Pb_2I_7$. The corresponding absorption spectra

(Figure 3.3a) converted by the Kubelka-Munk function show an excitonic absorption feature of $(HA)_2(GA)Pb_2I_7$ located at 582 nm (2.13 eV), which is blue shifted from that of $(HA)_2(MA)Pb_2I_7$ at 596 nm (2.08 eV). This blue shift can be attributed to the expansion of the GA cage with increased Pb-I bond lengths. Room temperature PL emission peaks (Figure 3.3b) are at 577 and 582 nm (2.15 and 2.13 eV) for $(HA)_2(GA)Pb_2I_7$ and $(HA)_2(MA)Pb_2I_7$, respectively. Under continuous laser illumination (λ = 532 nm), $(HA)_2(GA)Pb_2I_7$ showed less decrease in PL intensity, indicating the 2D perovskite incorporating the larger GA cation may have enhanced photostability relative to that incorporating MA cation (Figure B.9). Strikingly, the PL emission intensity of $(HA)_2(MA)Pb_2I_7$ is about one order of magnitude higher than that of $(HA)_2(GA)Pb_2I_7$, suggesting more pronounced non-radiative recombination in the $(HA)_2(GA)Pb_2I_7$. These results suggest that the A cations can influence the optical properties by modulating the distortion of the Pb-I inorganic sublattices, which dictates the electronic band structures.

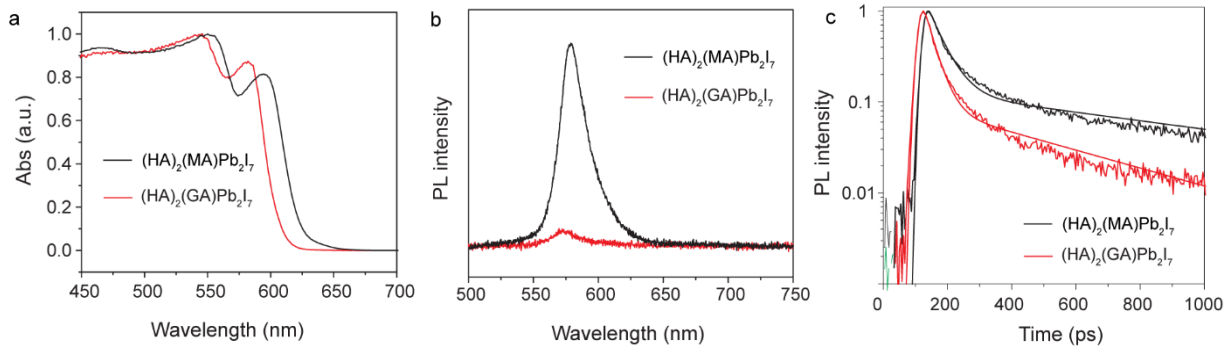

Figure 3.3. Comparison of the optical properties of (HA)2(GA)Pb2I7 and (HA)2(MA)Pb2I7. (a) absorption spectra, (b) steady-state PL, and (c) time-resolved PL of (HA)2(GA)Pb2I7 and (HA)2(MA)Pb2I7 single-crystals.

To further probe the carrier dynamics, we performed time-resolved PL (TRPL) measurements on the single crystals of both compounds under the same excitation power density. Representative pseudocolor plots of the TRPL spectra (Figure B.4) reveal a fast band-edge emission at early time (< 100 ps) and a slower band-edge emission at longer time (> 100 ps). Long-lived PL emission up to 2 ns is observed in $(HA)_2(MA)Pb_2I_7$, but PL emission diminish after ~500 ps in $(HA)_2(GA)Pb_2I_7$. The corresponding PL decay curves (Figure 3.3c) are quantitatively fitted using a bi-exponential function [$PL(t) = A_1 \exp\left(-\frac{t}{\tau_1}\right) + A_2 \exp\left(-\frac{t}{\tau_2}\right)$] to yield a fast decay lifetime of τ_1 = 31 and 46 ps, and a slow decay lifetime of τ_2 = 440 and 927 ps for $(HA)_2(GA)Pb_2I_7$ and $(HA)_2(MA)Pb_2I_7$, respectively. Statistical analysis of the TRPL spectra from multiple samples shows the average lifetime ($A_1\tau_1 + A_2\tau_2$) of $(HA)_2(MA)Pb_2I_7$ is two times longer than that of $(HA)_2(GA)Pb_2I_7$ (Table B.5), which corroborates the stronger PL emission observed.

Phonons that interact with charge carriers and excitons govern many important physical properties, such as carrier mobility, and PL linewidth broadening with temperature, and phonon mediated nonradiative recombination. Studies on 3D lead halide perovskites suggested that charge carriers in perovskite materials are coupled to low-frequency optical phonons (< 100 cm^{-1}) that mainly involve vibrational modes of the inorganic framework.[16, 39-42] A recent report correlated the nonradiative recombination rate in 2D n = 1 RP perovskites with the exciton-phonon coupling strength and molecular rigidity of the long chain organic cations (LA).[43]

To probe the low frequency phonons, we collected Raman spectra of the $(HA)_2(GA)Pb_2I_7$ and $(HA)_2(MA)Pb_2I_7$ single crystals in a broad range of the temperatures from 77 to 300 K (Figure B.5). Representative spectra at three temperatures are highlighted in Figure 3.4a and 3.4b. Broad

Raman peaks at ~ 50 cm^{-1} regions can be assigned to the collective framework modes and local Pb-I vibrations, while the modes of organic cations reside at > 200 cm^{-1} regions (such as those for the GA cation shown in Figure B.3). In a previous study on $MAPbBr_3$, the low frequency Raman spectra show dramatic changes as the temperature is increased from 77 K to 295 K.[39] In the more crystalline and ordered low temperature orthorhombic phase of $MAPbBr_3$, phonon modes attributed to the inorganic framework were well resolved. As the crystal enters the tetragonal phase at intermediate temperatures and the cubic phase at room temperature, the Raman spectra are characterized by a broad and featureless central peak characteristic of extensive dynamic disorder.[39] In contrast, low-frequency Raman spectra of both $(HA)_2(GA)Pb_2I_7$ and $(HA)_2(MA)Pb_2I_7$ show little change with temperature in the 77-295 K window, suggesting that there are no transitions of crystalline phases. Comparing these two 2D perovskite materials, both the phonon peaks and the diffuse background are broader in $(HA)_2(MA)Pb_2I_7$ than those in $(HA)_2(GA)Pb_2I_7$ at each temperature. This can be attributed to the small size of the MA cation, which allows significant free space for a wider range of inorganic cage motion, and thus more phonon disorder. The inorganic cage motions of $(HA)_2(GA)Pb_2I_7$ might be constrained due to the

synergistic steric hindrance of the large GA cation in the perovskite cage and more compressed interlayer HA cations.

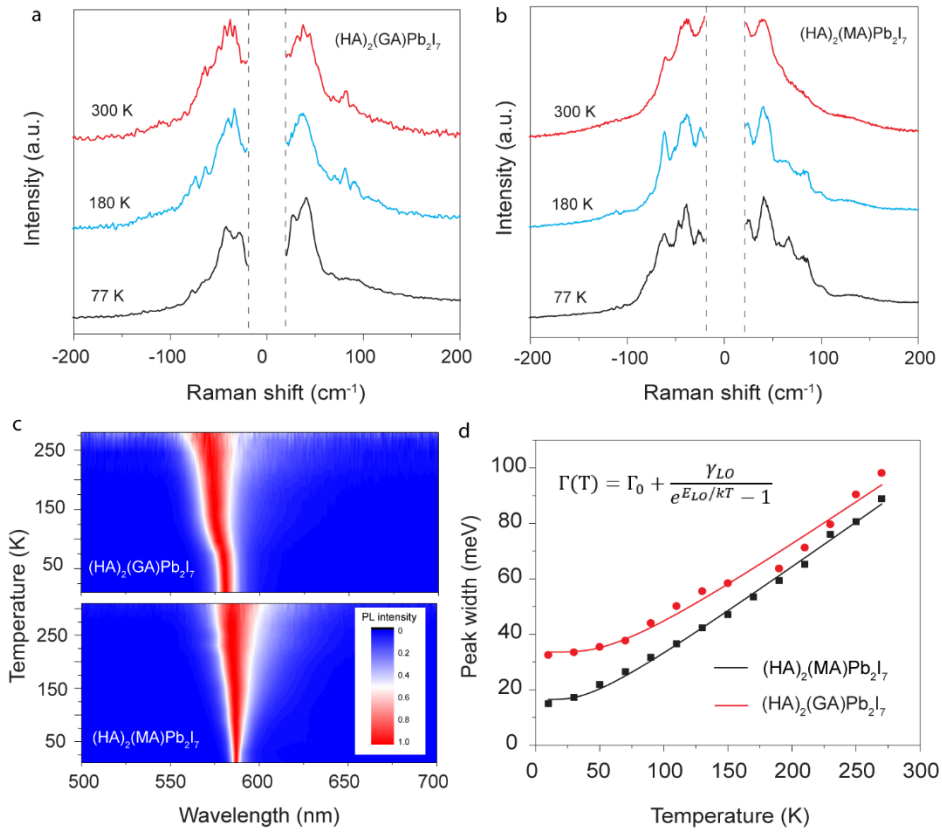

Figure 3.4. Comparison of phonon properties of $(HA)_2(GA)Pb_2I_7$ and $(HA)_2(MA)Pb_2I_7$. (a,b) Low-frequency Raman spectra of $(HA)_2(GA)Pb_2I_7$ and $(HA)_2(MA)Pb_2I_7$ single crystals at three temperatures. (c) 2D pseudo-color plots of temperature-dependent PL spectra of $(HA)_2(GA)Pb_2I_7$ and $(HA)_2(MA)Pb_2I_7$ single crystals. (d) The corresponding PL emission linewidths as a function of temperature together with their fits.

To further compare the exciton-phonon interactions of these two compounds, we performed temperature-dependent PL studies (Figure 3.4c). The lack of drastic change of PL peak position for both compounds further confirms the absence of phase transition in this temperature range, consistent with the Raman results discussed above. The PL linewidth at low temperature (i.e. 10

K) is primarily due to inhomogeneous broadening. However, as temperature increases, phonon scattering leads to significantly observable broadening. Figure 3.4d shows the extracted emission linewidths as a function of temperature for the two compounds, which are fitted according to following equation:[44]

$$\Gamma(T) = \Gamma_0 + \Gamma_{LO} = \Gamma_0 + \frac{\gamma_{LO}}{e^{E_{LO}/kT} - 1}$$

The first term, Γ_0, is the inhomogeneous broadening term and the linewidth at 0 K. The second term describes the homogeneous broadening due to the longitudinal optical (LO) phonon scattering via Fröhlich interaction, where γ_{LO} is coupling strength and E_{LO} represents a dominant phonon or an average phonon energy. Note, we ignore the negligible homogeneous broadening that results from acoustic phonon scattering with exciton.[44-45] The fits yield Γ_0 = 34 meV, γ_{LO} = 58 meV, and E_{LO} = 15.7 meV for $(HA)_2(GA)Pb_2I_7$; Γ_0 = 16.4 meV, γ_{LO} = 40 meV, and E_{LO} = 10.6 meV for $(HA)_2(MA)Pb_2I_7$. The inhomogeneous linewidth is larger in $(HA)_2(GA)Pb_2I_7$ than in $(HA)_2(MA)Pb_2I_7$, which can be attributed to the larger structural distortion of the inorganic sublattice as has been described above (Table 3.2). The coupling strengths and phonon energies are similar to those values previously reported for $MAPbI_3$ (40 meV, 11.5 meV),[44] $(HA)_2PbI_4$ (17 meV, 56 meV), and $(BA)_2PbI_4$ (10.9 meV, 34 meV).[46] $(HA)_2(GA)Pb_2I_7$ exhibits a different coupling phonon energy (E_{LO}) from $(HA)_2(MA)Pb_2I_7$, as expected from the change of inorganic sublattice. The larger inhomogeneous broadening in $(HA)_2(GA)Pb_2I_7$ than that in $(HA)_2(MA)Pb_2I_7$ points to more structural disorder and/or defect density in the former. The structural defects may serve as centers for exciton trapping and nonradiative recombination, thus leading to lower PLQY and shorter PL lifetime in $(HA)_2(GA)Pb_2I_7$ in comparison to $(HA)_2(MA)Pb_2I_7$. All of these

demonstrate that the A site cation can have dramatic effects on the exciton-phonon interactions and carrier properties of halide perovskites, which was not previously elucidated due to the limited choices of the three common cations (Cs^+, MA, FA).

3.5 Discussion

Although potential technological applications of these new 2D perovskites remain to be explored, our results not only have enabled new insights into the structure-bandgap relationship in perovskite materials, but also will spur spectroscopic studies to understand mechanistic origins of their varying optoelectronic properties. One of the most significant structural features due to the incorporation of large A-site cations is the perovskite cage expansion (see Table 3.2 above), which induces a significantly blue-shifted bandgap and modifies the phonon properties of inorganic sublattice. In general, the electronic structures of valence band maxima and conduction band minima are dominated by the orbital overlap between lead and halide atoms. Therefore, the bandgap is correlated with the orbital overlap associated with the deformation of inorganic framework.[47] In the three available 3D perovskites $APbI_3$ ($A = Cs^+$, MA^+, FA^+), the redshift of bandgap from Cs^+ to MA^+ and then to FA^+ can be attributed to the decreasing octahedral tilt angle with increasing cation size (while maintaining Pb-I bond length), which increases the orbital overlap.[48-49] However, the bandgap blueshift from MA to GA in our 2D perovskites comes from a different structural origin, i.e. the significantly increased Pb-I bond length due to the incorporation of the large GA cation in the cage, which decreases the orbital overlap of lead and iodine atoms. In addition, $(HA)_2(GA)Pb_2I_7$ exhibits a smaller octahedral tilt angle than $(HA)_2(MA)Pb_2I_7$ (Table 3.2), further highlighting the dominant role that the increased bond length plays in the bandgap blueshift.

The discovery of these new 2D perovskites with unique A-site cations may further spur fundamental studies to understand the relationship between the structure and optoelectronic properties. Mechanistic studies have proposed that the favorable optoelectronic properties of perovskite materials are associated with structural fluctuations of the organic and inorganic sublattices,[50-52] such as the large dynamic disorder of the inorganic framework and fast reorientation of the polar organic cations in the cage. Comparative studies on the three available 3D perovskites $APbI_3$ ($A = Cs^+$, MA^+, FA^+) have examined the role of A-site cations on the photophysical properties.[16, 53-55] However, providing a clear picture of the relationship remains challenging due to the limited three data points as well as the complex interplay between motions of the inorganic and organic sublattices.[14-15] In this regard, the series of new 2D perovskites incorporating various organic cations with different size and polarity reported herein provide a new platform for understanding the lattice disorder of inorganic sublattice,[40, 56-58] cation dynamics,[59-62] and their mutual interactions, thus could reveal a more quantitative and comprehensive structure-property relationship. This is the first crystallographic report demonstrating the occupation of the 2D perovskite A-sites with large GA cations, and thus the structural features and basic optical properties of this compound are discussed. Further in-depth investigations of the impact of such expanded perovskite cages on other physical properties, such as charge-carrier transport, ion migration,[63] spin−orbital coupling,[64-67] and defects[68-69] will guide the tuning of the properties and functionalities of perovskite materials.

Lastly, even though the large GA cation cannot support 3D perovskite structures alone, the above results are highly relevant to the many thin film composition engineering and solar device studies using such large A cations.[19, 32, 70-72] Specifically, studies that attempted to introduce the

large GA cation into thin films of 3D perovskites for solar cell devices have demonstrated longer carrier lifetime, improved material stability, and increased energy conversion efficiency.[19, 32, 70-72] However, the mechanistic origin of the enhanced performance has been debated. Multiple reports claim the superior photophysical performance of thin-films with GA incorporation is attributed to grain boundary passivation.[32, 73] In contrast, others have suggested incorporation of GA cation in the perovskite cage lead to enhanced solar cell performance.[70] The new crystal structure of the 2D perovskite incorporating GA as the A-cation reported herein, $(HA)_2(GA)Pb_2I_7$, suggests that it is *possible* for large A cations, such as DMA, EA, GA, and AA, to occupy the perovskite cages, provided there are means to dissipate the strain. Cation alloying with a small percentage of large A cations could occur in those thin films. However, the incorporation of the large GA cation in the perovskite cages could deteriorate the photophysical properties, as shown in this work by comparing $(HA)_2(GA)Pb_2I_7$ and $(HA)_2(MA)Pb_2I_7$. These results hence suggest that the observed enhanced photophysical properties in thin films is likely due to large A-cations potentially passivating grain boundaries. Using this 2D perovskite structure $(HA)_2(A)Pb_2I_7$, the role each of the individual large A-cations play in the perovskite photophysical properties could be studied in-depth in the future.

3.6 Conclusions

In summary, we show that the decreased structural rigidity of 2D RP lead iodide perovskites can facilitate an expanded volume of the perovskite A-site cavity. This enables the incorporation of larger organic cations into the perovskite cages that are not able to form stable 3D perovskite structures. This can be considered a relaxation of the Goldschmidt tolerance factor which enables a significantly expanded library of 2D RP lead iodide perovskites with exotic larger A cations that

may exhibit unique properties and new applications. The successful incorporation of GA cation in the perovskite cage is unambiguously confirmed through the crystal structure determination of $(HA)_2(GA)Pb_2I_7$, which is used as a model system. Comparison of the structural parameters of $(HA)_2(GA)Pb_2I_7$ with $(HA)_2(MA)PbI_7$ reveals the flexible long-chain ammonium cations (i.e. HA) facilitates the perovskite cage expansion while maintaining the structural integrity, and the structural stabilization originates from strain balance in alternate tensile (inorganic sublattice with GA in the cage) and compressively strained layers (interlayer HA cations). Moreover, such large A cation significantly increases the distortion of inorganic perovskite sublattice, and subsequently optoelectronic properties, carrier dynamics, and exciton−phonon interactions. These results not only enrich the diverse structural chemistry of halide perovskite materials that may lead to new applications, but also highlight the critical role A-cations plays in the remarkable physical properties of perovskite materials and have important implications to solar device studies using engineered perovskite thin films incorporating such large organic cations.

3.7 References

1. Kojima, A.; Teshima, K.; Shirai, Y.; Miyasaka, T., Organometal Halide Perovskites as Visible-Light Sensitizers for Photovoltaic Cells. *J. Am. Chem. Soc.* **2009,** *131* (17), 6050-6051.

2. Lee, M. M.; Teuscher, J.; Miyasaka, T.; Murakami, T. N.; Snaith, H. J., Efficient Hybrid Solar Cells Based on Meso-Superstructured Organometal Halide Perovskites. *Science* **2012,** *338* (6107), 643-647.

3. Fu, Y.; Zhu, H.; Chen, J.; Hautzinger, M. P.; Zhu, X. Y.; Jin, S., Metal halide perovskite nanostructures for optoelectronic applications and the study of physical properties. *Nature Reviews Materials* **2019,** *4* (3), 169-188.

4. Saparov, B.; Mitzi, D. B., Organic–Inorganic Perovskites: Structural Versatility for Functional Materials Design. *Chem. Rev.* **2016,** *116* (7), 4558-4596.

5. Smith, M. D.; Karunadasa, H. I., White-Light Emission from Layered Halide Perovskites. *Accounts of Chemical Research* **2018,** *51* (3), 619-627.

6. Kieslich, G.; Sun, S.; Cheetham, A. K., Solid-State Principles Applied to Organic-Inorganic Perovskites: New Tricks for An Old Dog. *Chem. Sci.* **2014,** *5* (12), 4712-4715.

7. Travis, W.; Glover, E. N. K.; Bronstein, H.; Scanlon, D. O.; Palgrave, R. G., On the Application of the Tolerance Factor to Inorganic and Hybrid Halide Perovskites: A Revised System. *Chem. Sci.* **2016,** *7* (7), 4548-4556.

8. Michael, D.; Christoph, H.; Harald, H., Synthesis, Crystal Structures, Optical Properties, and Phase Transitions of the Layered Guanidinium ‐Based Hybrid Perovskites $[C(NH_2)_3]_2MI_4$; M = Sn, Pb. *Eur. J. Inorg. Chem.* **2017,** *2017* (7), 1120-1126.

9. Nazarenko, O.; Kotyrba, M. R.; Wörle, M.; Cuervo-Reyes, E.; Yakunin, S.; Kovalenko, M. V., Luminescent and Photoconductive Layered Lead Halide Perovskite Compounds Comprising Mixtures of Cesium and Guanidinium Cations. *Inorg. Chem.* **2017,** *56* (19), 11552-11564.

10. Soe, C. M. M.; Stoumpos, C. C.; Kepenekian, M.; Traoré, B.; Tsai, H.; Nie, W.; Wang, B.; Katan, C.; Seshadri, R.; Mohite, A. D.; Even, J.; Marks, T. J.; Kanatzidis, M. G., New Type of 2D Perovskites with Alternating Cations in the Interlayer Space, $[C(NH_2)_3](CH_3NH_3)_nPb_nI_{3n+1}$: Structure, Properties, and Photovoltaic Performance. *J. Am. Chem. Soc.* **2017,** *139* (45), 16297-16309.

11. Nazarenko, O.; Kotyrba, M. R.; Yakunin, S.; Aebli, M.; Rainò, G.; Benin, B. M.; Wörle, M.; Kovalenko, M. V., Guanidinium-Formamidinium Lead Iodide: A Layered Perovskite-Related Compound with Red Luminescence at Room Temperature. *J. Am. Chem. Soc.* **2018,** *140* (11), 3850-3853.

12. Miyata, K.; Atallah, T. L.; Zhu, X.-Y., Lead Halide Perovskites: Crystal-Liquid Duality, Phonon Glass Electron Crystals, and Large Polaron Formation. *Sci. Adv.* **2017,** *3* (10), e1701469.

13. Egger, D. A.; Bera, A.; Cahen, D.; Hodes, G.; Kirchartz, T.; Kronik, L.; Lovrincic, R.; Rappe, A. M.; Reichman, D. R.; Yaffe, O., What Remains Unexplained about the Properties of Halide Perovskites? *Adv. Mater.* **2018,** *30* (20), 1800691.

14. Gallop, N. P.; Selig, O.; Giubertoni, G.; Bakker, H. J.; Rezus, Y. L. A.; Frost, J. M.; Jansen, T. L. C.; Lovrincic, R.; Bakulin, A. A., Rotational Cation Dynamics in Metal Halide Perovskites: Effect on Phonons and Material Properties. *J. Phys. Chem. Lett.* **2018,** *9* (20), 5987-5997.

15. Herz, L. M., How Lattice Dynamics Moderate the Electronic Properties of Metal-Halide Perovskites. *J. Phys. Chem. Lett.* **2018,** *9* (23), 6853-6863.

16. Miyata, K.; Meggiolaro, D.; Trinh, M. T.; Joshi, P. P.; Mosconi, E.; Jones, S. C.; De Angelis, F.; Zhu, X.-Y., Large Polarons in Lead Halide Perovskites. *Sci. Adv.* **2017,** *3* (8), e1701217.

17. Yaffe, O.; Guo, Y.; Tan, L. Z.; Egger, D. A.; Hull, T.; Stoumpos, C. C.; Zheng, F.; Heinz, T. F.; Kronik, L.; Kanatzidis, M. G.; Owen, J. S.; Rappe, A. M.; Pimenta, M. A.; Brus, L. E., Local Polar Fluctuations in Lead Halide Perovskite Crystals. *Phys. Rev. Lett.* **2017,** *118* (13), 136001.

18. Guo, P.; Mannodi-Kanakkithodi, A.; Gong, J.; Xia, Y.; Stoumpos, C. C.; Cao, D. H.; Diroll, B. T.; Ketterson, J. B.; Wiederrecht, G. P.; Xu, T.; Chan, M. K. Y.; Kanatzidis, M. G.; Schaller, R. D., Infrared-Pump Electronic-Probe of Methylammonium Lead Iodide Reveals Electronically Decoupled Organic and Inorganic Sublattices. *Nat. Commun.* **2019,** *10* (1), 482.

19. Jodlowski, A. D.; Roldán-Carmona, C.; Grancini, G.; Salado, M.; Ralaiarisoa, M.; Ahmad, S.; Koch, N.; Camacho, L.; de Miguel, G.; Nazeeruddin, M. K., Large Guanidinium Cation Mixed with Methylammonium in Lead Iodide Perovskites for 19% Efficient Solar Cells. *Nat. Energy* **2017,** *2* (12), 972-979.

20. Ke, W.; Spanopoulos, I.; Stoumpos, C. C.; Kanatzidis, M. G., Myths and Reality of HPbI3 in Halide Perovskite Solar Cells. *Nat. Commun.* **2018,** *9* (1), 4785.

21. Saliba, M.; Matsui, T.; Domanski, K.; Seo, J.-Y.; Ummadisingu, A.; Zakeeruddin, S. M.; Correa-Baena, J.-P.; Tress, W. R.; Abate, A.; Hagfeldt, A.; Grätzel, M., Incorporation of Rubidium Cations into Perovskite Solar Cells Improves Photovoltaic Performance. *Science* **2016,** *354* (6309), 206-209.

22. Stoumpos, C. C.; Cao, D. H.; Clark, D. J.; Young, J.; Rondinelli, J. M.; Jang, J. I.; Hupp, J. T.; Kanatzidis, M. G., Ruddlesden–Popper Hybrid Lead Iodide Perovskite 2D Homologous Semiconductors. *Chem. Mater* **2016,** *28* (8), 2852-2867.

23. Stoumpos, C. C.; Soe, C. M. M.; Tsai, H.; Nie, W.; Blancon, J.-C.; Cao, D. H.; Liu, F.; Traoré, B.; Katan, C.; Even, J.; Mohite, A. D.; Kanatzidis, M. G., High Members of the 2D Ruddlesden-Popper Halide Perovskites: Synthesis, Optical Properties, and Solar Cells of $[CH_3(CH_2)_3NH_3]_2(CH_3NH_3)_4Pb_5I_{16}$. *Chem* **2017,** *2* (3), 427-440.

24. Mao, L.; Ke, W.; Pedesseau, L.; Wu, Y.; Katan, C.; Even, J.; Wasielewski, M. R.; Stoumpos, C. C.; Kanatzidis, M. G., Hybrid Dion–Jacobson 2D Lead Iodide Perovskites. *J. Am. Chem. Soc.* **2018,** *140* (10), 3775-3783.

25. Smith, I. C.; Hoke, E. T.; Solis‐Ibarra, D.; McGehee, M. D.; Karunadasa, H. I., A Layered Hybrid Perovskite Solar‐Cell Absorber with Enhanced Moisture Stability. *Angewandte Chemie* **2014,** *126* (42), 11414-11417.

26. Wang, N.; Cheng, L.; Ge, R.; Zhang, S.; Miao, Y.; Zou, W.; Yi, C.; Sun, Y.; Cao, Y.; Yang, R.; Wei, Y.; Guo, Q.; Ke, Y.; Yu, M.; Jin, Y.; Liu, Y.; Ding, Q.; Di, D.; Yang, L.; Xing, G.; Tian, H.; Jin, C.; Gao, F.; Friend, R. H.; Wang, J.; Huang, W., Perovskite Light-Emitting Diodes Based on Solution-Processed Self-Organized Multiple Quantum Wells. *Nat. Photonics* **2016,** *10*, 699.

27. Mao, L.; Stoumpos, C. C.; Kanatzidis, M. G., Two-Dimensional Hybrid Halide Perovskites: Principles and Promises. *J. Am. Chem. Soc.* **2018,** *141* (3), 1171-1190.

28. Fu, Y.; Wu, T.; Wang, J.; Zhai, J.; Shearer, M. J.; Zhao, Y.; Hamers, R. J.; Kan, E.; Deng, K.; Zhu, X. Y.; Jin, S., Stabilization of the Metastable Lead Iodide Perovskite Phase via Surface Functionalization. *Nano Lett.* **2017,** *17* (7), 4405-4414.

29. Fu, Y.; Rea, M. T.; Chen, J.; Morrow, D.; Hautzinger, M. P.; Zhao, Y.; Pan, D.; Manger, L. H.; Wright, J. C.; Goldsmith, R. H.; Jin, S., Selective Stabilization and Photophysical Properties of Metastable Perovskite Polymorphs of CsPbI3 in Thin Films. *Chem. Mater.* **2017,** *29* (19), 8385–8394.

30. Swarnkar, A.; Marshall, A. R.; Sanehira, E. M.; Chernomordik, B. D.; Moore, D. T.; Christians, J. A.; Chakrabarti, T.; Luther, J. M., Quantum Dot–Induced Phase Stabilization of α-$CsPbI_3$ Perovskite for High-Efficiency Photovoltaics. *Science* **2016,** *354* (6308), 92-95.

31. Weidman, M. C.; Seitz, M.; Stranks, S. D.; Tisdale, W. A., Highly Tunable Colloidal Perovskite Nanoplatelets through Variable Cation, Metal, and Halide Composition. *ACS Nano* **2016,** *10* (8), 7830-7839.

32. De Marco, N.; Zhou, H.; Chen, Q.; Sun, P.; Liu, Z.; Meng, L.; Yao, E.-P.; Liu, Y.; Schiffer, A.; Yang, Y., Guanidinium: A Route to Enhanced Carrier Lifetime and Open-Circuit Voltage in Hybrid Perovskite Solar Cells. *Nano Lett.* **2016,** *16* (2), 1009-1016.

33. Giorgi, G.; Fujisawa, J.-I.; Segawa, H.; Yamashita, K., Organic–Inorganic Hybrid Lead Iodide Perovskite Featuring Zero Dipole Moment Guanidinium Cations: A Theoretical Analysis. *J. Phys. Chem. C* **2015,** *119* (9), 4694-4701.

34. Du, K.-z.; Tu, Q.; Zhang, X.; Han, Q.; Liu, J.; Zauscher, S.; Mitzi, D. B., Two-Dimensional Lead(II) Halide-Based Hybrid Perovskites Templated by Acene Alkylamines: Crystal Structures, Optical Properties, and Piezoelectricity. *Inorg. Chem.* **2017,** *56* (15), 9291-9302.

35. Hautzinger, M. P.; Dai, J.; Ji, Y.; Fu, Y.; Chen, J.; Guzei, I. A.; Wright, J. C.; Li, Y.; Jin, S., Two-Dimensional Lead Halide Perovskites Templated by a Conjugated Asymmetric Diammonium. *Inorg. Chem.* **2017,** *56* (24), 14991-14998.

36. Geselle, M.; Fuess, H., Crystal Structure of Tetrakis(ethylammonium) Decachlorotriplumbate(II), $(C_2H_5NH_3)_4Pb_3Cl_{10}$. In *Zeitschrift für Kristallographie - New Crystal Structures*, 1997; Vol. 212, p 241.

37. Mao, L.; Wu, Y.; Stoumpos, C. C.; Traore, B.; Katan, C.; Even, J.; Wasielewski, M. R.; Kanatzidis, M. G., Tunable White-Light Emission in Single-Cation-Templated Three-Layered 2D Perovskites $(CH_3CH_2NH_3)_4Pb_3Br_{10-x}Cl_x$. *J. Am. Chem. Soc.* **2017,** *139* (34), 11956-11963.

38. Stoumpos, C. C.; Mao, L.; Malliakas, C. D.; Kanatzidis, M. G., Structure–Band Gap Relationships in Hexagonal Polytypes and Low-Dimensional Structures of Hybrid Tin Iodide Perovskites. *Inorg. Chem.* **2017,** *56* (1), 56-73.

39. Guo, Y.; Yaffe, O.; Paley, D. W.; Beecher, A. N.; Hull, T. D.; Szpak, G.; Owen, J. S.; Brus, L. E.; Pimenta, M. A., Interplay Between Organic Cations and Inorganic Framework and Incommensurability in Hybrid Lead-Halide Perovskite $CH_3NH_3PbBr_3$. *Phys. Rev. Mater.* **2017,** *1* (4), 042401.

40. Sendner, M.; Nayak, P. K.; Egger, D. A.; Beck, S.; Müller, C.; Epding, B.; Kowalsky, W.; Kronik, L.; Snaith, H. J.; Pucci, A.; Lovrinčić, R., Optical Phonons in Methylammonium Lead Halide Perovskites and Implications for Charge Transport. *Mater. Horizons* **2016,** *3* (6), 613-620.

41. Batignani, G.; Fumero, G.; Srimath Kandada, A. R.; Cerullo, G.; Gandini, M.; Ferrante, C.; Petrozza, A.; Scopigno, T., Probing Femtosecond Lattice Displacement Upon Photo-Carrier Generation in Lead Halide Perovskite. *Nat. Commun.* **2018,** *9* (1), 1971.

42. Park, M.; Neukirch, A. J.; Reyes-Lillo, S. E.; Lai, M.; Ellis, S. R.; Dietze, D.; Neaton, J. B.; Yang, P.; Tretiak, S.; Mathies, R. A., Excited-State Vibrational Dynamics Toward the Polaron in Methylammonium Lead Iodide Perovskite. *Nat. Commun.* **2018,** *9* (1), 2525.

43. Gong, X.; Voznyy, O.; Jain, A.; Liu, W.; Sabatini, R.; Piontkowski, Z.; Walters, G.; Bappi, G.; Nokhrin, S.; Bushuyev, O.; Yuan, M.; Comin, R.; McCamant, D.; Kelley, S. O.; Sargent, E. H., Electron–Phonon Interaction in Efficient Perovskite Blue Emitters. *Nat. Mater.* **2018,** *17* (6), 550-556.

44. Wright, A. D.; Verdi, C.; Milot, R. L.; Eperon, G. E.; Pérez-Osorio, M. A.; Snaith, H. J.; Giustino, F.; Johnston, M. B.; Herz, L. M., Electron–Phonon Coupling in Hybrid Lead Halide Perovskites. *Nat. Commun.* **2016,** *7*, 11755.

45. Guo, Z.; Wu, X.; Zhu, T.; Zhu, X.; Huang, L., Electron–Phonon Scattering in Atomically Thin 2D Perovskites. *ACS Nano* **2016,** *10* (11), 9992-9998.

46. Ni, L.; Huynh, U.; Cheminal, A.; Thomas, T. H.; Shivanna, R.; Hinrichsen, T. F.; Ahmad, S.; Sadhanala, A.; Rao, A., Real-Time Observation of Exciton–Phonon Coupling Dynamics in Self-Assembled Hybrid Perovskite Quantum Wells. *ACS Nano* **2017,** *11* (11), 10834-10843.

47. Knutson, J. L.; Martin, J. D.; Mitzi, D. B., Tuning the Band Gap in Hybrid Tin Iodide Perovskite Semiconductors Using Structural Templating. *Inorg. Chem.* **2005,** *44* (13), 4699-4705.

48. Filip, M. R.; Eperon, G. E.; Snaith, H. J.; Giustino, F., Steric Engineering of Metal-Halide Perovskites with Tunable Optical Band Gaps. *Nat. Commun.* **2014,** *5*, 5757.

49. Stoumpos, C. C.; Malliakas, C. D.; Kanatzidis, M. G., Semiconducting Tin and Lead Iodide Perovskites with Organic Cations: Phase Transitions, High Mobilities, and Near-Infrared Photoluminescent Properties. *Inorg. Chem.* **2013,** *52* (15), 9019-9038.

50. Katan, C.; Mohite, A. D.; Even, J., Entropy in Halide Perovskites. *Nat. Mater.* **2018,** *17* (5), 377-379.

51. Miyata, K.; Zhu, X. Y., Ferroelectric Large Polarons. *Nat. Mater.* **2018,** *17* (5), 379-381.

52. Stranks, S. D.; Plochocka, P., The Influence of the Rashba Effect. *Nat. Mater.* **2018,** *17* (5), 381-382.

53. Yang, J.; Wen, X.; Xia, H.; Sheng, R.; Ma, Q.; Kim, J.; Tapping, P.; Harada, T.; Kee, T. W.; Huang, F.; Cheng, Y.-B.; Green, M.; Ho-Baillie, A.; Huang, S.; Shrestha, S.; Patterson, R.; Conibeer, G., Acoustic-Optical Phonon Up-Conversion and Hot-Phonon Bottleneck in Lead-Halide Perovskites. *Nat. Commun.* **2017,** *8*, 14120.

54. Fu, Y.; Zhu, H.; Stoumpos, C. C.; Ding, Q.; Wang, J.; Kanatzidis, M. G.; Zhu, X.; Jin, S., Broad Wavelength Tunable Robust Lasing from Single-Crystal Nanowires of Cesium Lead Halide Perovskites (CsPbX3, X = Cl, Br, I). *ACS Nano* **2016,** *10* (8), 7963-7972.

55. Madjet, M. E.; Berdiyorov, G. R.; El-Mellouhi, F.; Alharbi, F. H.; Akimov, A. V.; Kais, S., Cation Effect on Hot Carrier Cooling in Halide Perovskite Materials. *J. Phys. Chem. Lett.* **2017,** *8* (18), 4439-4445.

56. Leguy, A. M. A.; Goñi, A. R.; Frost, J. M.; Skelton, J.; Brivio, F.; Rodríguez-Martínez, X.; Weber, O. J.; Pallipurath, A.; Alonso, M. I.; Campoy-Quiles, M.; Weller, M. T.; Nelson, J.; Walsh, A.; Barnes, P. R. F., Dynamic Disorder, Phonon Lifetimes, and the Assignment of Modes to the Vibrational Spectra of Methylammonium Lead Halide Perovskites. *Phys. Chem. Chem. Phys.* **2016,** *18* (39), 27051-27066.

57. Brivio, F.; Frost, J. M.; Skelton, J. M.; Jackson, A. J.; Weber, O. J.; Weller, M. T.; Goñi, A. R.; Leguy, A. M. A.; Barnes, P. R. F.; Walsh, A., Lattice Dynamics and Vibrational Spectra of the

Orthorhombic, Tetragonal, and Cubic Phases of Methylammonium Lead Iodide. *Phys. Rev. B* **2015,** *92* (14), 144308.

58. Marronnier, A.; Roma, G.; Boyer-Richard, S.; Pedesseau, L.; Jancu, J.-M.; Bonnassieux, Y.; Katan, C.; Stoumpos, C. C.; Kanatzidis, M. G.; Even, J., Anharmonicity and Disorder in the Black Phases of Cesium Lead Iodide Used for Stable Inorganic Perovskite Solar Cells. *ACS Nano* **2018,** *12* (4), 3477-3486.

59. Fabini, D. H.; Siaw, T. A.; Stoumpos, C. C.; Laurita, G.; Olds, D.; Page, K.; Hu, J. G.; Kanatzidis, M. G.; Han, S.; Seshadri, R., Universal Dynamics of Molecular Reorientation in Hybrid Lead Iodide Perovskites. *J. Am. Chem. Soc.* **2017,** *139* (46), 16875-16884.

60. Wu, X.; Tan, L. Z.; Shen, X.; Hu, T.; Miyata, K.; Trinh, M. T.; Li, R.; Coffee, R.; Liu, S.; Egger, D. A.; Makasyuk, I.; Zheng, Q.; Fry, A.; Robinson, J. S.; Smith, M. D.; Guzelturk, B.; Karunadasa, H. I.; Wang, X.; Zhu, X.; Kronik, L.; Rappe, A. M.; Lindenberg, A. M., Light-Induced Picosecond Rotational Disordering of the Inorganic Sublattice in Hybrid Perovskites. *Sci. Adv.* **2017,** *3* (7), e1602388.

61. Taylor, V. C. A.; Tiwari, D.; Duchi, M.; Donaldson, P. M.; Clark, I. P.; Fermin, D. J.; Oliver, T. A. A., Investigating the Role of the Organic Cation in Formamidinium Lead Iodide Perovskite Using Ultrafast Spectroscopy. *J. Phys. Chem. Lett.* **2018,** *9* (4), 895-901.

62. Motta, C.; El-Mellouhi, F.; Kais, S.; Tabet, N.; Alharbi, F.; Sanvito, S., Revealing the Role of Organic Cations in Hybrid Halide Perovskite $CH_3NH_3PbI_3$. *Nat. Commun.* **2015,** *6*, 7026.

63. Xiao, X.; Dai, J.; Fang, Y.; Zhao, J.; Zheng, X.; Tang, S.; Rudd, P. N.; Zeng, X. C.; Huang, J., Suppressed Ion Migration along the In-Plane Direction in Layered Perovskites. *ACS Energy Lett.* **2018,** *3* (3), 684-688.

64. Even, J.; Pedesseau, L.; Jancu, J.-M.; Katan, C., Importance of Spin–Orbit Coupling in Hybrid Organic/Inorganic Perovskites for Photovoltaic Applications. *J. Phys. Chem. Lett.* **2013,** *4* (17), 2999-3005.

65. Zhai, Y.; Baniya, S.; Zhang, C.; Li, J.; Haney, P.; Sheng, C.-X.; Ehrenfreund, E.; Vardeny, Z. V., Giant Rashba Splitting in 2D Organic-Inorganic Halide Perovskites Measured by Transient Spectroscopies. *Sci. Adv.* **2017,** *3* (7), e1700704.

66. Chen, X.; Lu, H.; Li, Z.; Zhai, Y.; Ndione, P. F.; Berry, J. J.; Zhu, K.; Yang, Y.; Beard, M. C., Impact of Layer Thickness on the Charge Carrier and Spin Coherence Lifetime in Two-Dimensional Layered Perovskite Single Crystals. *ACS Energy Lett.* **2018,** *3* (9), 2273-2279.

67. Etienne, T.; Mosconi, E.; De Angelis, F., Dynamical Origin of the Rashba Effect in Organohalide Lead Perovskites: A Key to Suppressed Carrier Recombination in Perovskite Solar Cells? *J. Phys. Chem. Lett.* **2016,** *7* (9), 1638-1645.

68. Peng, W.; Yin, J.; Ho, K.-T.; Ouellette, O.; De Bastiani, M.; Murali, B.; El Tall, O.; Shen, C.; Miao, X.; Pan, J.; Alarousu, E.; He, J.-H.; Ooi, B. S.; Mohammed, O. F.; Sargent, E.; Bakr, O. M., Ultralow Self-Doping in Two-dimensional Hybrid Perovskite Single Crystals. *Nano Lett.* **2017,** *17* (8), 4759-4767.

69. Shi, E.; Deng, S.; Yuan, B.; Gao, Y.; Akriti; Yuan, L.; Davis, C. S.; Zemlyanov, D.; Yu, Y.; Huang, L.; Dou, L., Extrinsic and Dynamic Edge States of Two-Dimensional Lead Halide Perovskites. *ACS Nano* **2019,** *13* (2), 1635-1644.

70. Kubicki, D. J.; Prochowicz, D.; Hofstetter, A.; Saski, M.; Yadav, P.; Bi, D.; Pellet, N.; Lewiński, J.; Zakeeruddin, S. M.; Grätzel, M.; Emsley, L., Formation of Stable Mixed Guanidinium–Methylammonium Phases with Exceptionally Long Carrier Lifetimes for High-Efficiency Lead Iodide-Based Perovskite Photovoltaics. *J. Am. Chem. Soc.* **2018,** *140* (9), 3345-3351.

71. Hou, X.; Hu, Y.; Liu, H.; Mei, A.; Li, X.; Duan, M.; Zhang, G.; Rong, Y.; Han, H., Effect of Guanidinium on Mesoscopic Perovskite Solar Cells. *J. Mater. Chem. A* **2017,** *5* (1), 73-78.

72. Luo, D.; Yang, W.; Wang, Z.; Sadhanala, A.; Hu, Q.; Su, R.; Shivanna, R.; Trindade, G. F.; Watts, J. F.; Xu, Z.; Liu, T.; Chen, K.; Ye, F.; Wu, P.; Zhao, L.; Wu, J.; Tu, Y.; Zhang, Y.; Yang, X.; Zhang, W.; Friend, R. H.; Gong, Q.; Snaith, H. J.; Zhu, R., Enhanced Photovoltage for Inverted Planar Heterojunction Perovskite Solar Cells. *Science* **2018,** *360* (6396), 1442-1446.

73. Tong, J.; Song, Z.; Kim, D. H.; Chen, X.; Chen, C.; Palmstrom, A. F.; Ndione, P. F.; Reese, M. O.; Dunfield, S. P.; Reid, O. G.; Liu, J.; Zhang, F.; Harvey, S. P.; Li, Z.; Christensen, S. T.; Teeter, G.; Zhao, D.; Al-Jassim, M. M.; van Hest, M. F. A. M.; Beard, M. C.; Shaheen, S. E.; Berry, J. J.; Yan, Y.; Zhu, K., Carrier Lifetimes of >1 μs in Sn-Pb Perovskites Enable Efficient All-Perovskite Tandem Solar Cells. *Science* **2019,** *364* (6439), 475-479.

Chapter 4. Band Edge Tuning of 2D Ruddlesden-Popper Perovskites by A Cation Size Revealed through Nanoplates*

4.1 Abstract

Current understanding of the effects of various A site cations on the photophysical properties of halide perovskites ($APbI_3$) is limited by the compositional tunability. Here we report the synthesis and characterization of colloidal nanoplates of a series of 2D Ruddlesden-Popper (RP) perovskites $(HA)_2(A)Pb_2I_7$ (HA = *n*-hexylammonium) with seven small and large A site cations to reveal the size effects of such A cations. Absorbance and photoluminescence (PL) measurements show a clear parabolic trend of the optical band gap vs. the A cation size, with methylammonium and formamidinium near the bottom. This band gap shifting is attributed to the changing chemical pressure inside of the A site cavity templating the Pb-I framework. PL quantum yield and time resolved PL measurements show the effect of A cation size on the PL efficiencies and carrier lifetimes. This fundamental investigation can inform the choices of A site cations that can be incorporated into halide perovskite materials for optoelectronic applications.

4.2 Introduction

Halide perovskites have been the subject of intense investigation in the past decade for their remarkable performance in solar cells,[1] LEDs,[2] and exciting fundamental semiconductor properties.[3] The structure of three dimensional (3D) perovskites ABX_3 (A= methylammonium

---

* This chapter was originally published for *ACS Energy Lett.* **2020**, 5, 5, 1430-1437 in collaboration with D. Pan, A.K. Pigg, Y. Fu, D.J. Morrow, M. Leng, M. Kuo, N. Spitha, D.P. Lafayette II, D.D. Kohler, J.C. Wright, S. Jin

(MA), formamidinium (FA), Cs^+; B = Pb, Sn, Ge; X = Cl, Br, I)[4] has been investigated for its diverse chemical structures.[5] However, the number of possible compositions of 3D $APbI_3$ perovskites is limited by the allowed A site cations. The Goldschmidt tolerance factor,[6] $t = (r_A + r_I)/[\sqrt{2}(r_{Pb} + r_I)]$, in which r_A, r_{Pb}, and r_I are the effective radii of the A site cation, Pb^{2+}, and I^- ions, respectively, provides a rough geometric guideline[7] to which cations can occupy the 12-fold coordinated cavities between the $[PbI_6]^{4-}$ octahedra. Based on this equation, only three cations, MA, FA, and Cs, yield tolerance factors in the favorable range of t = 0.8-1.0 for 3D $APbI_3$ perovskite formation. This predictive tolerance range has been empirically confirmed by the formation of 3D perovskite structures with these cations (Figure 4.1). Conversely, large cations such as ethylammonium (EA), dimethylammonium (DMA), guanidinium (GA), and acetamidinium (AA) fall out of the a favorable tolerance factor range for $APbI_3$ perovskites[8] and have been shown to form non-perovskite phases (Figure 4.1).[9] A chemical explanation for this empirical tolerance factor is that when the A site cations are small, there is too much negative chemical pressure in the A site cavity, resulting in the formation of tilted perovskites (orthorhombic $GdFeO_3$ type) or non-perovskite structures.[10] Conversely, when the A site cations are too large, the positive chemical pressure exerted on the inorganic Pb-I framework is too high, stretching the perovskite beyond its viable Pb-I bond lengths and forming non-perovskite structures.[9] This limited range of tunability has made it difficult to study the effects of the A site composition.

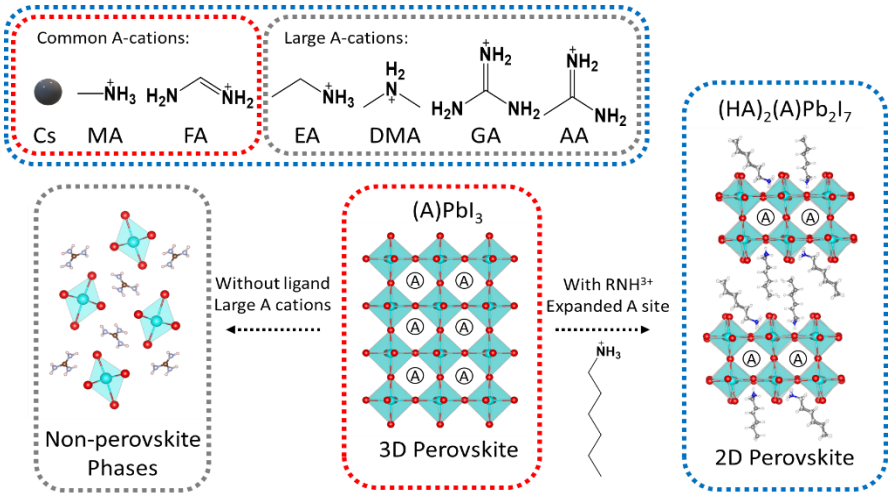

Figure 4.1. The 2D layered perovskite crystal structures allow for large cations to occupy the A site cavity of a halide perovskite. Only the common A site cations listed: Cs, MA and FA, can be hosted in the 3D perovskite structures. When a large A site cation is used, non-perovskite phases are formed. However, when added in addition to a long chain RNH_3^+ ligand such as hexylammonium (HA), a 2D perovskite with the large A cations occupying the perovskite cavity is formed.

However, there are significant efforts in alloying of the A site of halide perovskites for enhanced stability and solar cell performance.[11-13] One approach has been to alloy the commonly used A site cations, MA, FA, and Cs, with exotic A cation candidates that cannot host a perovskite lattice on their own.[14-18] These reports suggest that the addition of unique A site cations in halide perovskite thin films enhances the efficiency of solar cells by increasing the open-circuit voltage. However, it is unclear what role such unconventional A site cations play in enhancing these thin film systems, namely, crystal structure changes, improvement of film morphology, or passivation of grain boundaries. Investigating perovskite structures with large cations in the A site is one method in uncovering the role of these cations in the complex perovskites materials system.

Colloidal nanocrystals (NCs) of 2D perovskites[19-21] have been recently developed to explore various optoelectronic applications including luminescent solar concentrators[22] and light emitting diodes. [23-26] 2D perovskites can be described as $(RNH_3)_2(A)_{n-1}Pb_nX_{3n+1}$, where RNH_3 is a long chain ammonium cation that intercedes the inorganic perovskite framework and acts as a spacer cation (Figure 4.1). Besides the promising applications of NCs, in a pragmatic outlook, perovskite NCs are also well suited for fundamental studies due to their ease of synthesis as well as facile manipulation in solution as a stable colloidal suspension.[27-30] Thus, NCs have been successfully utilized to study the fundamental properties of 2D perovskite materials spanning a range of compositions including A= MA, FA, Cs and X = Cl, Br, I, as well as various interlayer spacer cations (RNH_3^+).[21, 31] The tunability of these structures results in a wide range of possible color emissions, which is useful in light emitting applications.[32-33] Colloidal NCs have even enabled 2D perovskite compositions not yet demonstrated in bulk materials, such as $(RNH_3)_2Cs_{n-1}Pb_nI_{3n+1}$.[21]

Here we further expand and investigate the perovskite A site cations systematically by incorporating seven A cations: Cs, MA, FA, EA, DMA, GA, and AA, in colloidal nanoplates (NPLs) of $(HA)_2(A)Pb_2I_7$ (Figure 4.1). This composition is the simplest RP perovskite (n = 2) that contain an A site cation. This builds upon our previous study on the single crystal structure of $(HA)_2(GA)Pb_2I_7$[34] as well as other recent studies showing incorporation of large A site cations is possible when templated by a 2D perovskite.[35-38] This compositional tunability allows us to study the effect of a large variety of A site cations on the photophysical properties of RP perovskites. We use UV-Vis absorbance spectroscopy, steady-state photoluminescence (PL) spectroscopy, PL quantum yield (PLQY) measurements, and time resolved PL (TRPL) to demonstrate optical band gap tuning via composition, as well as effects on other photophysical properties. The results are

discussed in relation to the size dependent chemical pressure effects as well as the relevance to semiconductor performance.

4.3 Materials and Methods

All chemicals were used without further purification. Cesium iodide (Sigma-Aldrich, 99.999%), methylammonium iodide (MAI, Greatcellsolar), formamidinium iodide (FAI, Sigma-Aldrich, ≥98%), dimethylammonium iodide (DMAI, Sigma-Aldrich, 98%), ethylammonium iodide (EAI, Sigma-Aldrich, 98%), guanidinium iodide (GAI, Sigma-Aldrich, ≥99%), acetamidinium iodide (AAI, Greatcellsolar), *n*-hexylammonium iodide (HAI, Greatcellsolar), lead (II) iodide (TCI, 99.99%). Oleic acid (technical grade, 90%), oleylamine (technical grade, 70%), N,N-dimethylformamide (DMF) (ACS reagent, ≥99.5%), toluene (ACS reagent, ≥99.5%) were all purchased from Sigma-Aldrich. All experiments were carried out on the as-synthesized nanoplates without further purification unless otherwise noted.

4.3.1 Synthesis of the nanoplates

All nanoplate (NPL) synthesis was done in ambient conditions. Stock precursor solutions of PbI_2, HAI, and the various A cation iodide salts were prepared by dissolving precursor salts in DMF. The salt precursor solutions were mixed in the following ratio: 75 μL HAI solution (2.0 M), 50 μL PbI_2 solution (0.50 M), 25 μL AI solution (0.50 M, A = Cs, MA, FA, DMA, EA, GA, AA). To this mixture was added 5 μL oleic acid and 5 μL oleylamine to form the NPL precursor solution. The NPL precursor solution was then added to 5.0 mL of toluene while stirring at room temperature. By allowing the mixture to stir for ~ 5 m, the NPL growth was complete, and exclusively $n=2$ $(HA)_2(A)Pb_2I_7$ was formed as demonstrated by a single PL peak**.**

When less HAI solution (i.e. stoichiometric, 12.5 μL of 2.0 M HAI) was added, the synthesis produced significant amounts of product that appeared to be n=3 RP perovskites as revealed by an emerging PL peak around 600 nm. Conversely, excessive HAI addition (100 μL of 2.0 M HAI) resulted in a PL peak at 515 nm, which can be attributed to n=1 2D perovskites (i.e. $(HA)_2PbI_4$). An example is shown in Figure C.5. The amount of HAI was optimized (75 μL of 2.0 M HAI) to produce pure n = 2 $(HA)_2(A)Pb_2I_7$ NPLs.

For the NMR studies of the composition ratios between HA/A, oleylamine and oleic acid were omitted from the synthesis, producing a fine powder representative of the RP perovskite compounds for the purposes of confirming the compositions.

4.3.2 Powder X-ray diffraction (PXRD)

The NPL solution was centrifuged at 5000 rpm for 5 min at 10 °C to yield a bright red precipitate. The supernatant was completely discarded and the resulting powder was scraped onto a silicon wafer covered with 300 nm native oxide as a low background substrate. PXRD patterns were collected using a Bruker D8 Advance equipped with a Cu Kα X-ray tube collimated with a 0.6 mm slit and a Lynxeye detector with a 0.2-mm nickel foil filter and a knife-edge attachment to attenuate low angle scattering. Scans were collected from 2θ = 3.5 to 15 °, with an increment of ~0.01023°, and collection time of 3 s per step.

4.3.4 Imaging

The scanning electron microscopy (SEM) images were collected on a LEO SUPRA 55 VP field-emission scanning electron microscope operated at 3 kV on NPL samples drop casted on silicon substrates covered with native oxide. TEM was performed on FEI Tecnai 12 TEM at 120

kV accelerating voltage with NPL samples drop casted on pure carbon film (200 mesh copper) TEM grids.

4.3.5 H-NMR

Spectra were recorded on a Bruker Avance III 400 spectrometer (^{1}H 400.1 MHz) on various RP perovskite samples dissolved in DMSO-d_6. The chemical shifts are reported in parts per million (ppm) and referenced to residual DMSO-d_6 at 2.55 ppm (^{1}H).

4.3.6 UV-Vis spectroscopy

UV-vis absorption spectra were recorded for NPL suspensions in toluene at room temperature using a Cary 50 spectrophotometer at a scan rate of 300 nm/min and resolution of 0.5 nm.

4.3.7 Steady-state photoluminescence spectroscopy

Steady-state photoluminescence spectra were obtained for NPL suspensions in toluene at room temperature using a Hitachi F4500 fluorescence spectrophotometer at a scan rate of 240 nm/min, a PMT voltage of 950 V and response of 0.5 s. The excitation wavelength was 470 nm. For the PLQY experiments, emission and excitation slit widths were maintained at 2.5 nm.

4.3.8 Time-resolved photoluminescence (TRPL)

TRPL was collected on NPL suspensions in toluene using a home-built system. Specifically, excitation pulses of 400 nm were created by the second harmonic generation of a Ti:Sapphire oscillator (Coherent Vitesse 800-2) output. Second harmonic generation was achieved by focusing the fundamental into a 500 μm Type-I phase matched BBO (Eksma Optics BBO-603H). All excitations were widefield in nature and focused with a 10X plan apochromatic objective lens (Olympus) and an excitation fluence as noted in the spectra. A Becker & Hickel

SPC-130 time correlated single photon counting module equipped with an IDQ-50-ULN avalanche photodiode was used. The instrument response function (IRF) was 55 ps FWHM and is shown in Figure C.8. The spectral fitting equations and details are discussed later in the Supporting Information.

4.4 Results and Discussion

4.4.1 Synthesis and characterization of NPLs

Colloidal nanoparticles of $(HA)_2(A)Pb_2I_7$ were synthesized via a ligand-assisted reprecipitation method[21,39] as described in detail in the section 4.3.1. In brief, halide perovskite precursors PbI_2, HAI, and A cation iodide salts with added ligands oleic acid and oleylamine in DMF were added to toluene, to rapidly yield bright red colloidal suspensions of $(HA)_2(A)Pb_2I_7$ NPLs. Powder X-ray diffraction confirmed the phase purity of the NPL products (Figure 4.2a). A strong diffraction peak at around $2\theta \approx 4°$ for each compound is in agreement with the calculated patterns for $(HA)_2(GA)Pb_2I_7$ [(001) plane] and $(HA)_2(MA)Pb_2I_7$ [(200) plane],[34] confirming the formation of the *n*=2 phase $(HA)_2(A)Pb_2I_7$. In the case of $(HA)_2(AA)Pb_2I_7$ and $(HA)_2(EA)Pb_2I_7$, these compounds were less stable (Figure C.1), and a minor impurity peak from $(HA)_2PbI_4$ at $2\theta \approx 5.6°$ was also observed. The first diffraction peak position varies between $2\theta \approx 3.82°$ and 4.02° for different cations, but there is no clear trend between the relative XRD peak position of each compound and the corresponding A site cation size (Table 4.1). This can be attributed to the fact that the 2D perovskite unit cell dimensions (and interlayer distance) are determined by the combination of Pb-I bonding distances and the interlayer distance dictated by the *n*-hexylammonium, as discussed thoroughly in our previous work.[34] Table C.1 in Appendix C further shows the lack of trend between selected unit cell dimensions and the A-site cation size for reported crystal structures of RP perovskites with different A cations. To further confirm the compositions

of the $(HA)_2(A)Pb_2I_7$ products, we performed quantitative ^1H NMR (see Appendix C, Figure C.2,3 for NMR Spectra). These results showed the cation ratio of HA:A is roughly 2:1 (Table C.2), in agreement with the proposed composition. TEM and SEM micrographs of various samples show NPLs with the lateral size of 100-400 nm for each compound (Figure 4.2b,c and more images in Figure C.4).

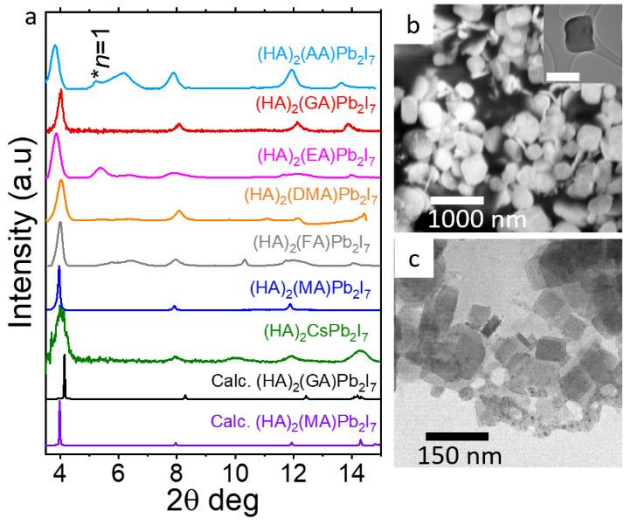

Figure 4.2. Materials characterization of various $(HA)(A)Pb_2I_7$ nanoplates. (a) PXRD patterns of the samples in comparison with the calculated PXRD patterns of $(HA)_2(GA)Pb_2I_7$ and $(HA)_2(MA)Pb_2I_7$. (b) Representative SEM image of $(HA)_2(GA)Pb_2I_7$ NPLs (inset: TEM image of a single nanoplate, scale bar = 200 nm) and (c) TEM image of $(HA)_2(MA)Pb_2I_7$ NPLs.

Table 4.1. Structural parameters and absorbance and PL peak positions for each $(HA)_2(A)Pb_2I_7$ compound.

Compound	Cation Size (pm)	Tolerance Factor	First XRD Peak (°)	Plane Spacing (Å)	Absorbance peak (eV)	PL Peak (eV)
$(HA)_2(AA)Pb_2I_7$	284	1.05	3.82	23.1	2.215	2.197
$(HA)_2(GA)Pb_2I_7$	279	1.04	4.02	21.9	2.170	2.193
$(HA)_2(EA)Pb_2I_7$	274	1.03	4.02	21.9	2.165	2.165
$(HA)_2(DMA)Pb_2I_7$	272	1.03	3.86	22.9	2.184	2.182
$(HA)_2(FA)Pb_2I_7$	253	0.99	3.98	22.2	2.182	2.131
$(HA)_2(MA)Pb_2I_7$	217	0.91	3.95	22.3	2.195	2.145
$(HA)_2CsPb_2I_7$	188	0.89	3.99	22.1	2.210	2.215

4.4.2 Optical Properties

Absorbance (abs) and PL spectra of these colloidal NPL samples in toluene were collected. (Figure 4.3). The absorbance spectra each show a well-defined excitonic feature centered between 560 and 580 nm (Table 4.1). Unlike many classical nanocrystals or quantum dots, these nanoplates are quantum confined due to their layered RP perovskite crystal structures, and their physical dimensions are not in the regime that could lead to quantum confinement. The 2D crystal structure forming natural quantum wells leads to various degree of quantum confinement, which provides a clear distinction of the *n*-value of the 2D perovskite phases in the absorbance and PL spectra.[40] The absorbance and PL spectra of $(HA)_2PbI_4$ (n=1) (Figure 4.3a, lower right panel) show clearly blue shifted peaks relative to the n=2 phases. Other isolated discrete PL peaks appear when

different precursor stoichiometry was used for the synthesis (an example for DMA is shown in Figure C.5), which has been shown to be the emission from other higher *n*-value RP perovskite phases in previous reports.[21] When the optimized stoichiometry is used in the synthesis, only PL from the n=2 RP perovskite phase is observed.

We found a clear shift in the first absorption peaks (as well as the PL peaks) with the A site cation size, which is highlighted in the stacked absorbance spectra in Figure 4.3b. Plotting the absorbance and PL peak position vs. the cation size reveals a clear parabolic trend (Figure 4.3c). The two most common A cations, MA and FA, are at the bottom of this parabolic curve. The larger A cations EA, DMA, GA, and AA have blue shifted absorbance/PL peaks relative to FA and MA. The smallest cation, Cs, also shows blue shifted absorbance/PL peak relative to FA and MA. We believe this is due to the templating effects the A site cations have on the stretching and tilting of the Pb-I framework.[41-42] With larger A site cation, the A site cavity stretches and distorts, forcing the Pb-I bonding out of equilibrium.[34] On the other hand, the smaller Cs cation does not fully support the cavity, resulting in the tilting of the PbI_6 octahedra (see Figure 4.3C bottom). This parabolic curve might suggest that a mixture of FA and MA cations (perhaps with a slightly larger fraction of FA) appear to be the "most ideal" A cation for a lead iodide perovskite cage (with respect to the optical band gap), which appears to be supported by photophysical studies on mixed $(FA_xMA_{1-x})PbI_3$.[43]

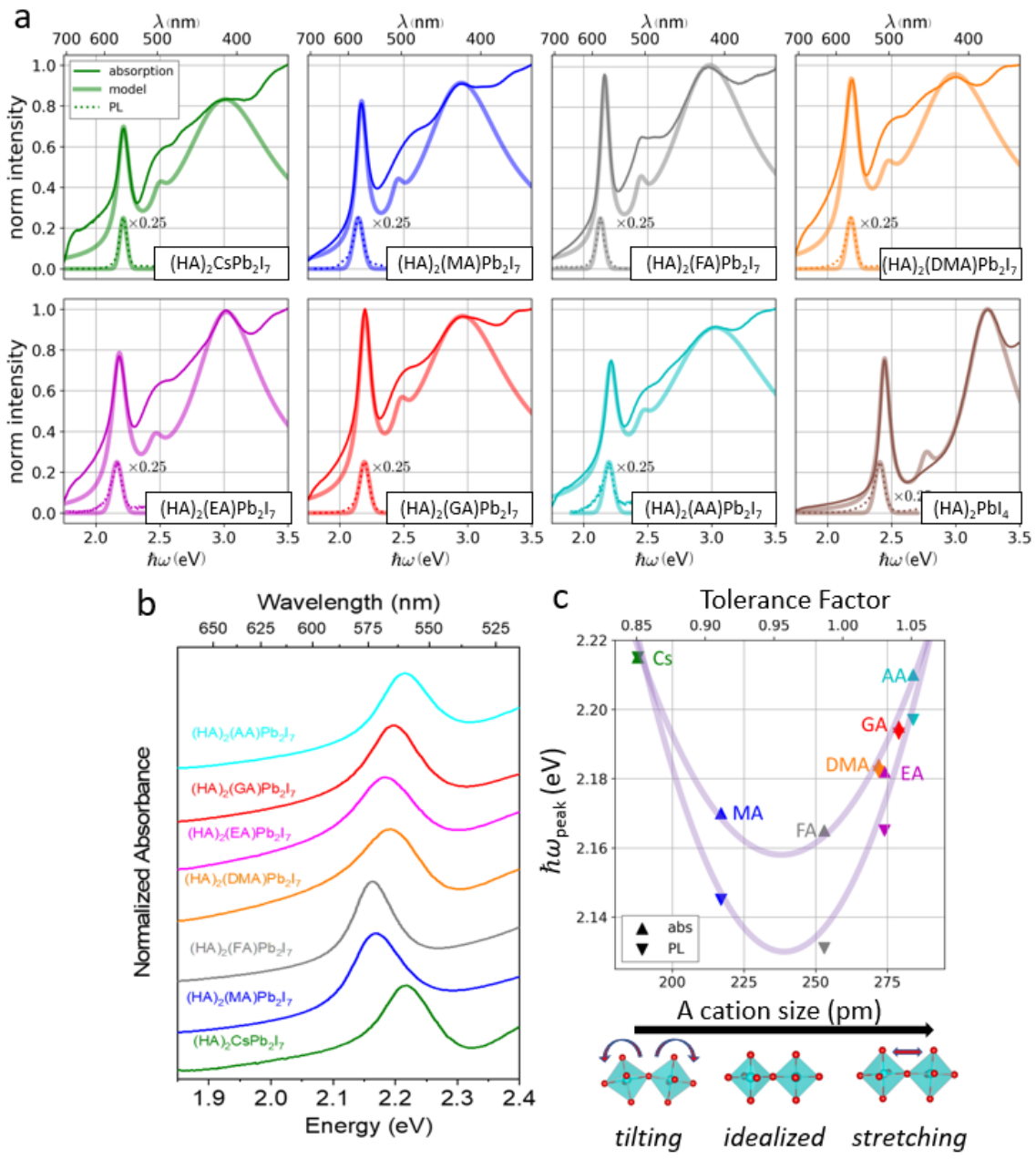

Figure 4.3. (a) Absorbance and photoluminescence spectra (λ_{ex} =470 nm) of the various $(HA)_2(A)Pb_2I_7$ NPLs and $(HA)_2PbI_4$ NPLs. Fittings of the absorbance spectra with a 2D Elliot model and Gaussian line fits of the PL were used to determine peak positions (see the Supporting Information for details). (b) Stacked absorbance spectra highlighting the changes in peak position

with A site cation composition. (c) Plot of absorbance and PL peak positions vs. A site cation size showing a clear parabolic trend.

Furthermore, we carried out time-resolved PL (TRPL) measurements to compare the PL lifetimes of these NPLs in a self-consistent manner. $(HA)_2(A)Pb_2I_7$ with A = Cs, MA, and FA have observably longer decay traces relative to EA, DMA, GA, and AA. Two examples of $(HA)_2(FA)Pb_2I_7$ and $(HA)_2(GA)Pb_2I_7$ NPLs are shown in Figure 4.4a and the full data are shown in Figure C.6. The TRPL decays were fit with a bi-exponential decay model (equation C.2), showing shorter lifetimes for both τ_1 and τ_2 for $(HA)_2(A)Pb_2I_7$ with large A cations (Figure 4.4b), i.e. the carrier lifetimes are longer in the 2D perovskites with Cs, MA, and FA cations when compared to those with larger A cations (EA, DMA, GA, and AA). The lifetimes τ_1 and τ_2 of the biexponential fitting can be described as the defect trapping (Shockley-Read-Hall recombination) and exciton or free carrier recombination, respectively.[44] Furthermore, the PLQY of each compound was measured using the comparative method (Figure C.7).[45] The perovskites with common A site cations (Cs, MA, and FA), have higher PLQY relative to those with the large A cations (EA, DMA, GA, and AA) (Figure 4.4b). The suppressed PLQY as well as the shorter radiative lifetimes of large A site cation perovskites suggests non-radiative recombination channels[46] are more prevalent in $(HA)_2(A)Pb_2I_7$ compounds with larger A site cation relative to MA, FA, and Cs. The lower PLQY and shorter charge carrier lifetimes are likely a result of higher defect concentrations in the compounds with large A site cations. As the synthesis and corresponding surface chemistry of each of the nanoplate sample was held constant, the higher defect concentrations may be caused by structural distortions, which have been shown to reduce PLQY and charge carrier lifetimes by providing a driving force for defect formation.[38] The

introduction of large cations into the perovskite A site cavity elongates the Pb-I bonds and distorts the Pb-I networks (see Table C.1), possibly leading to higher defect concentrations. Such structural distortion effect is perhaps also analogous to strain effect in perovskite lattices.[47-48] In addition, charge carrier-phonon coupling has been suggested to be important to the carrier dynamics in halide perovskites.[49] Our previous work has shown that the electron-phonon interaction (as well as phonon energies) is significantly changed in 2D perovskites with a large GA cation in the A-site cavity, due to the stretching of the Pb-I lattice.[34] The induced change in phonon energies was correlated with fast non-radiative decay lowering the PLQY in a previous work.[49]

a

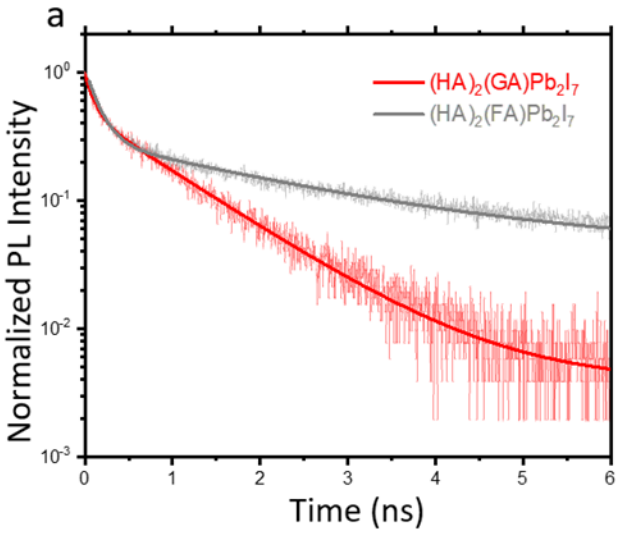

b

Compound	τ_1 (ns)	τ_2 (ns)	PLQY (%)
$(HA)(AA)Pb_2I_7$	0.112	0.944	0.52%
$(HA)_2(GA)Pb_2I_7$	0.108	0.972	2.37%
$(HA)_2(EA)Pb_2I_7$	0.100	1.15	0.42%
$(HA)_2(DMA)Pb_2I_7$	0.080	0.952	0.99%
$(HA)_2(FA)Pb_2I_7$	0.153	2.41	4.04%
$(HA)_2(MA)Pb_2I_7$	0.131	2.94	7.17%
$(HA)_2(Cs)Pb_2I_7$	0.122	2.42	11.5%

Figure 4.4. TRPL plots and summary of NPLs PLQY and lifetimes. (a) TRPL decay and fitting of two selected compounds $(HA)_2(GA)Pb_2I_7$ and $(HA)_2(FA)Pb_2I_7$ showing the general trend of shorter lifetimes of 2D perovskites with large A site cations compared to those with smaller cations. Complete data are shown in Figure C.6. (b) Summary of the TRPL fitting results and PLQY experiments for each compound. Complete fitting results are shown in Table C.3.

4.4.3 Discussion of A-site chemical pressure

These systematic measurements of colloidal NPLs of a complete series of $(HA)_2(A)Pb_2I_7$ allow us to examine the impact the A site cation size has on the optical properties of perovskites. Alloying the A site in perovskite NCs has been shown to allow some tuning of the optical band gap,[27, 50] however not to this extent. Interestingly, the size dependence trend of the absorbance of 2D perovskites (Figure 4.5a blue line) follows the same trend displayed by the three available 3D perovskites $APbI_3$ structures (A = Cs, MA, FA) (Figure 4.5a red line). $CsPbI_3$ has the highest bandgap of the three $APbI_3$ perovskites structures, which is attributed to the tilting observed in the Pb-I framework (Figure 4.5c). The band gap of $MAPbI_3$ is slightly higher than $FAPbI_3$. The 2D perovskites $(HA)_2(A)Pb_2I_7$, follow this same trend (of course blue shifted due to quantum confinement in 2D perovskites), with $(HA)_2CsPb_2I_7$ having the highest energy absorbance, and $(HA)_2(MA)Pb_2I_7$ being slightly higher in energy than $(HA)_2(FA)PbI_7$. The fact that 2D $(HA)_2(A)Pb_2I_7$ perovskites follow the same structural trends in the inorganic framework as the 3D perovskites offers insights for those hypothetical 3D perovskites that are not structurally stable.

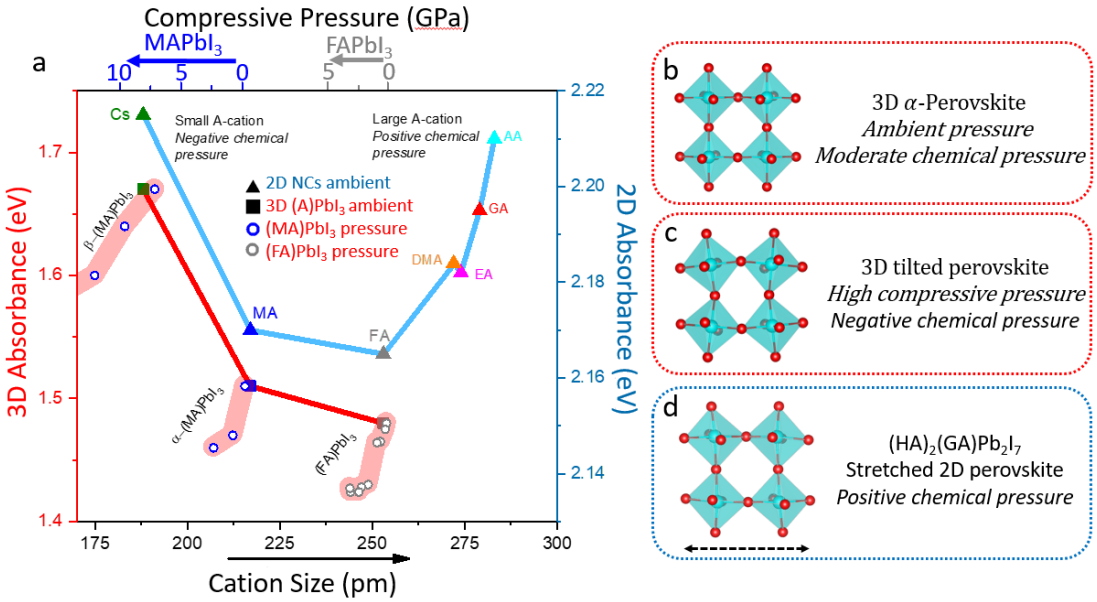

Figure 4.5. Dependence of optical band gap energy on the A site cation size for the 3D and 2D perovskites. (a) Dependence of optical band gap energy on the A site cation size for the 3D perovskite (left axis, red line) and 2D perovskites (right axis, blue line) demonstrating that the effect of the A site cation size is consistent between 2D and 3D perovskites with the available cations (MA, FA, Cs). The pressure data points for 3D perovskites show the effect of applied compressive pressure on the perovskite cage, resulting in a red shifted band gap (top axis shows the pressure scale). This redshift is opposite to what is observed for 2D perovskites with the large A site cation with increased chemical pressure in the A site cavity. (b-d) Schematic illustration of the inorganic frameworks of (b) 3D $MAPbI_3$ at ambient conditions, showing moderate chemical pressure inside the cage with moderate bond distances and low tilting, (c) under high compressive pressure (β-$MAPbI_3$ phase) or under negative chemical pressure conditions ($CsPbI_3$) with significant tilting, (d) under increased positive chemical pressure ($(HA)_2(GA)Pb_2I_7$ framework

shown), showing the increased stretching of the perovskite cage. Compressive pressure as well as absorbance results in (a) are from ref [51] and [52] for $MAPbI_3$ and $FAPbI_3$, respectively.

We believe this clear trend of optical band gap tuning reveals the impact of the A site cation size on the inorganic framework of the perovskite lattice and is indicative of the chemical pressure inside the perovskite A site cavity.[53] Recent research on the effects of high external pressure on halide perovskites[54] has revealed that, in 3D lead iodide perovskites with MA and FA cations, as compressive external pressure increases, the optical band gap is increasingly red-shifted (Figure 4.5a, the circles in the lower half of the panel).[51-52] This is correlated with decreased Pb-I distances observed via PXRD, which lead to lower band gap energies. Even though the presence of multiple pressure-induced phase transitions in 3D perovskites makes such trends non-continuous, an overall red-shifting trend is present with increasing compressive pressure. While high pressure studies show the red shifting of bandgap due to decreasing Pb-I bond distances, there is no mechanism for stretching the bond distances from external pressure. When expanding the A site cation series to larger A cations, stretching of the Pb-I bonds can be achieved by the increased positive chemical pressure inside the A site cavity. This positive chemical pressure is manifested in the blue shift in the absorbance/PL energy of the 2D perovskites seen here, opposite to the red shift caused by external compressive pressure observed in the 3D perovskites, as clearly shown in Figure 4.5a. The Pb-I bond stretching (Figure 4.5d) induced by large A site cations was confirmed previously by the crystal structure of $(HA)_2(GA)Pb_2I_7$ [34] and tabulated in Table C.1. Moreover, recent work on the structures of $(BA)_2(EA_xMA_{1-x})_2Pb_3I_7$ (BA = *n*-butylammonium), where MA is systematically substituted by EA in the perovskite cages, shows the same trend of Pb-I bond stretching and blue shifting of the optical bandgap in a systematic fashion.[38] The elongation of the

Pb-I bonds decreases the amount of Pb $6s^2$ and I 5p antibonding combinations, leading to a destabilization of the valence band thus increasing the band gap.[41, 55] Similarly, blue shifted optical bandgap and tilting have been discussed in 3D $CsPbI_3$.[10] The tilting observed in Cs based compounds has the same effect of decreasing Pb $6s^2$ and I 5p overlap, raising the bandgap. This entire series of common and large A site cations provide a new method of modulating the perovskite lattice and optical band gaps via positive chemical pressure, that is opposite of the effects observed in high pressure studies. We can also draw analogy to the classic studies that modulate the size of the A site in $LaMnO_3$ perovskites by changing rare earth and alkaline earth composition in the A site.[53, 58] In those studies, with decreasing average size of the A site, an increases in the magnetoresistance of the perovskite oxide compounds was observed.

In addition to optical band gap tuning, these 2D perovskites can provide insights into the recent works on alloying exotic large cations in 3D perovskite films to improve solar cells. For example, it was reported that the incorporation of large GA cation into thin films of proposed compositions $(MA_xGA_{1-x})PbI_3$ led to enhanced solar cell performance, attributed to a larger open circuit voltage of the devices.[14-17] Solid-state NMR studies suggested incorporation of GA cation in the cage and rapid reorientation of GA cation, which leads to charge carrier stabilization through electron-rotor interaction.[15] It should be noted that GA in particular has been demonstrated to form various 2D perovskite like structures, where GA is the interlayer cation.[59-61] Consequently, a 2D perovskite analogue of GA perovskite has been observed to form at the grain boundaries in thin-films when GA-thiocyanate was mixed with $(FASnI_3)_{0.6}(MAPbI_3)_{0.4}$,[62] which highlights the complexity of these mixed A site cation systems. Our results suggest that the incorporation of large A site cations could decrease PLQY as well as suppress carrier lifetimes relative to perovskites with smaller

cations Cs, MA, and FA, both of which are detrimental to solar cell performance. Our results further suggest that A site alloying is not responsible for the improved performance, but instead the passivation of grain boundaries from large A cation compounds could be the more likely reason for the improved solar performance of perovskite thin-films with large A cation incorporation. We would like to note, that while our model system is an effective method of introducing these large and exotic cations into the perovskite A site, the carrier dynamics of exciton and free carrier recombination deviate from 3D perovskites, making it an imperfect model system.

4.5 Conclusions

In summary, we report the synthesis of colloidal nanoplates of a series of 2D $(HA)_2(A)Pb_2I_7$ perovskites with A site cations expanded from the commonly reported Cs, MA, FA to the larger DMA, EA, GA, AA cations. This allows a systematic study on the impact of A cation size on photophysical properties, showing blue shifted absorbance and photoluminescence, reduced PLQY and TRPL lifetimes for 2D perovskites containing large cations. There is a clear parabolic trend of the optical band gap vs. A site cation size that can be correlated with the chemical pressure tuning of the A site cavity. The decreased PLQY and TRPL lifetimes suggest that the improved performance of the solar cells using perovskite thin films containing large A cations is likely not due to A site alloying, but rather grain boundary passivation in thin films. This fundamental investigation of 2D perovskites using nanoplates as model systems provides new insights on the impact of the A site cation on all halide perovskites and inform the choice of A cations to be incorporated into perovskites for optoelectronic applications.

4.6 References

1. Lee, M. M.; Teuscher, J.; Miyasaka, T.; Murakami, T. N.; Snaith, H. J., Efficient Hybrid Solar Cells Based on Meso-Superstructured Organometal Halide Perovskites. *Science* **2012,** *338* (6107), 643-647.

2. Yuan, M.; Quan, L. N.; Comin, R.; Walters, G.; Sabatini, R.; Voznyy, O.; Hoogland, S.; Zhao, Y.; Beauregard, E. M.; Kanjanaboos, P.; Lu, Z.; Kim, D. H.; Sargent, E. H., Perovskite energy funnels for efficient light-emitting diodes. *Nature Nanotechnology* **2016,** *11*, 872-877.

3. Fu, Y.; Zhu, H.; Chen, J.; Hautzinger, M. P.; Zhu, X. Y.; Jin, S., Metal halide perovskite nanostructures for optoelectronic applications and the study of physical properties. *Nature Reviews Materials* **2019,** *4* (3), 169-188.

4. Stoumpos, C. C.; Malliakas, C. D.; Kanatzidis, M. G., Semiconducting Tin and Lead Iodide Perovskites with Organic Cations: Phase Transitions, High Mobilities, and Near-Infrared Photoluminescent Properties. *Inorg. Chem.* **2013,** *52* (15), 9019-9038.

5. Quan, L. N.; Rand, B. P.; Friend, R. H.; Mhaisalkar, S. G.; Lee, T.-W.; Sargent, E. H., Perovskites for Next-Generation Optical Sources. *Chem. Rev* **2019,** *119* (12), 7444-7477.

6. Goldschmidt, V. M., Die Gesetze der Krystallochemie. *Naturwissenschaften* **1926,** *14* (21), 477-485.

7. Travis, W.; Glover, E. N. K.; Bronstein, H.; Scanlon, D. O.; Palgrave, R. G., On the application of the tolerance factor to inorganic and hybrid halide perovskites: a revised system. *Chem. Sci* **2016,** *7* (7), 4548-4556.

8. Kieslich, G.; Sun, S.; Cheetham, A. K., Solid-state principles applied to organic-inorganic perovskites: new tricks for an old dog. *Chem. Sci* **2014,** *5* (12), 4712-4715.

9. Stoumpos, C. C.; Mao, L.; Malliakas, C. D.; Kanatzidis, M. G., Structure–Band Gap Relationships in Hexagonal Polytypes and Low-Dimensional Structures of Hybrid Tin Iodide Perovskites. *Inorg. Chem.* **2017,** *56* (1), 56-73.

10. Sutton, R. J.; Filip, M. R.; Haghighirad, A. A.; Sakai, N.; Wenger, B.; Giustino, F.; Snaith, H. J., Cubic or Orthorhombic? Revealing the Crystal Structure of Metastable Black-Phase $CsPbI_3$ by Theory and Experiment. *ACS Energy Lett.* **2018,** *3* (8), 1787-1794.

11. Saliba, M.; Matsui, T.; Domanski, K.; Seo, J.-Y.; Ummadisingu, A.; Zakeeruddin, S. M.; Correa-Baena, J.-P.; Tress, W. R.; Abate, A.; Hagfeldt, A.; Grätzel, M., Incorporation of rubidium cations into perovskite solar cells improves photovoltaic performance. *Science* **2016,** *354* (6309), 206-209.

12. Li, Z.; Yang, M.; Park, J.-S.; Wei, S.-H.; Berry, J. J.; Zhu, K., Stabilizing Perovskite Structures by Tuning Tolerance Factor: Formation of Formamidinium and Cesium Lead Iodide Solid-State Alloys. *Chem. Mater* **2016,** *28* (1), 284-292.

13. Saliba, M.; Matsui, T.; Seo, J.-Y.; Domanski, K.; Correa-Baena, J.-P.; Nazeeruddin, M. K.; Zakeeruddin, S. M.; Tress, W.; Abate, A.; Hagfeldt, A.; Grätzel, M., Cesium-containing triple cation perovskite solar cells: improved stability, reproducibility and high efficiency. *Energy Environ. Sci* **2016,** *9* (6), 1989-1997.

14. Jodlowski, A. D.; Roldán-Carmona, C.; Grancini, G.; Salado, M.; Ralaiarisoa, M.; Ahmad, S.; Koch, N.; Camacho, L.; de Miguel, G.; Nazeeruddin, M. K., Large guanidinium cation mixed with methylammonium in lead iodide perovskites for 19% efficient solar cells. *Nat. Energy* **2017,** *2* (12), 972-979.

15. Kubicki, D. J.; Prochowicz, D.; Hofstetter, A.; Saski, M.; Yadav, P.; Bi, D.; Pellet, N.; Lewiński, J.; Zakeeruddin, S. M.; Grätzel, M.; Emsley, L., Formation of Stable Mixed Guanidinium–Methylammonium Phases with Exceptionally Long Carrier Lifetimes for High-Efficiency Lead Iodide-Based Perovskite Photovoltaics. *J. Am. Chem. Soc* **2018,** *140* (9), 3345-3351.

16. De Marco, N.; Zhou, H.; Chen, Q.; Sun, P.; Liu, Z.; Meng, L.; Yao, E.-P.; Liu, Y.; Schiffer, A.; Yang, Y., Guanidinium: A Route to Enhanced Carrier Lifetime and Open-Circuit Voltage in Hybrid Perovskite Solar Cells. *Nano Letters* **2016,** *16* (2), 1009-1016.

17. Stoddard, R. J.; Rajagopal, A.; Palmer, R. L.; Braly, I. L.; Jen, A. K. Y.; Hillhouse, H. W., Enhancing Defect Tolerance and Phase Stability of High-Bandgap Perovskites via Guanidinium Alloying. *ACS Energy Lett.* **2018,** *3* (6), 1261-1268.

18. Ke, W.; Spanopoulos, I.; Stoumpos, C. C.; Kanatzidis, M. G., Myths and reality of $HPbI_3$ in halide perovskite solar cells. *Nat. Commun* **2018,** *9* (1), 4785.

19. Weidman, M. C.; Goodman, A. J.; Tisdale, W. A., Colloidal Halide Perovskite Nanoplatelets: An Exciting New Class of Semiconductor Nanomaterials. *Chem. Mater* **2017,** *29* (12), 5019-5030.

20. Akkerman, Q. A.; Motti, S. G.; Srimath Kandada, A. R.; Mosconi, E.; D'Innocenzo, V.; Bertoni, G.; Marras, S.; Kamino, B. A.; Miranda, L.; De Angelis, F.; Petrozza, A.; Prato, M.; Manna, L., Solution Synthesis Approach to Colloidal Cesium Lead Halide Perovskite Nanoplatelets with Monolayer-Level Thickness Control. *J. Am. Chem. Soc* **2016,** *138* (3), 1010-1016.

21. Weidman, M. C.; Seitz, M.; Stranks, S. D.; Tisdale, W. A., Highly Tunable Colloidal Perovskite Nanoplatelets through Variable Cation, Metal, and Halide Composition. *ACS Nano* **2016,** *10* (8), 7830-7839.

22. Wei, M.; de Arquer, F. P. G.; Walters, G.; Yang, Z.; Quan, L. N.; Kim, Y.; Sabatini, R.; Quintero-Bermudez, R.; Gao, L.; Fan, J. Z.; Fan, F.; Gold-Parker, A.; Toney, M. F.; Sargent, E. H., Ultrafast narrowband exciton routing within layered perovskite nanoplatelets enables low-loss luminescent solar concentrators. *Nat. Energy* **2019,** *4* (3), 197-205.

23. Kumar, S.; Jagielski, J.; Yakunin, S.; Rice, P.; Chiu, Y.-C.; Wang, M.; Nedelcu, G.; Kim, Y.; Lin, S.; Santos, E. J. G.; Kovalenko, M. V.; Shih, C.-J., Efficient Blue Electroluminescence Using Quantum-Confined Two-Dimensional Perovskites. *ACS Nano* **2016,** *10* (10), 9720-9729.

24. Zhang, X.; Wang, C.; Zhang, Y.; Zhang, X.; Wang, S.; Lu, M.; Cui, H.; Kershaw, S. V.; Yu, W. W.; Rogach, A. L., Bright Orange Electroluminescence from Lead-Free Two-Dimensional Perovskites. *ACS Energy Lett.* **2019,** *4* (1), 242-248.

25. Congreve, D. N.; Weidman, M. C.; Seitz, M.; Paritmongkol, W.; Dahod, N. S.; Tisdale, W. A., Tunable Light-Emitting Diodes Utilizing Quantum-Confined Layered Perovskite Emitters. *ACS Photonics* **2017,** *4* (3), 476-481.

26. Hoye, R. L. Z.; Lai, M.-L.; Anaya, M.; Tong, Y.; Gałkowski, K.; Doherty, T.; Li, W.; Huq, T. N.; Mackowski, S.; Polavarapu, L.; Feldmann, J.; MacManus-Driscoll, J. L.; Friend, R. H.; Urban, A. S.; Stranks, S. D., Identifying and Reducing Interfacial Losses to Enhance Color-Pure Electroluminescence in Blue-Emitting Perovskite Nanoplatelet Light-Emitting Diodes. *ACS Energy Lett.* **2019,** *4* (5), 1181-1188.

27. Huang, H.; Bodnarchuk, M. I.; Kershaw, S. V.; Kovalenko, M. V.; Rogach, A. L., Lead Halide Perovskite Nanocrystals in the Research Spotlight: Stability and Defect Tolerance. *ACS Energy Lett.* **2017,** *2* (9), 2071-2083.

28. Akkerman, Q. A.; Rainò, G.; Kovalenko, M. V.; Manna, L., Genesis, challenges and opportunities for colloidal lead halide perovskite nanocrystals. *Nature Materials* **2018,** *17* (5), 394-405.

29. Becker, M. A.; Vaxenburg, R.; Nedelcu, G.; Sercel, P. C.; Shabaev, A.; Mehl, M. J.; Michopoulos, J. G.; Lambrakos, S. G.; Bernstein, N.; Lyons, J. L.; Stöferle, T.; Mahrt, R. F.; Kovalenko, M. V.; Norris, D. J.; Rainò, G.; Efros, A. L., Bright triplet excitons in caesium lead halide perovskites. *Nature* **2018,** *553* (7687), 189-193.

30. Wheeler, L. M.; Sanehira, E. M.; Marshall, A. R.; Schulz, P.; Suri, M.; Anderson, N. C.; Christians, J. A.; Nordlund, D.; Sokaras, D.; Kroll, T.; Harvey, S. P.; Berry, J. J.; Lin, L. Y.; Luther, J. M., Targeted Ligand-Exchange Chemistry on Cesium Lead Halide Perovskite Quantum Dots for High-Efficiency Photovoltaics. *J. Am. Chem. Soc* **2018,** *140* (33), 10504-10513.

31. Tyagi, P.; Arveson, S. M.; Tisdale, W. A., Colloidal Organohalide Perovskite Nanoplatelets Exhibiting Quantum Confinement. *J. Phys. Chem. Lett* **2015,** *6* (10), 1911-1916.

32. Ha, S. K.; Mauck, C. M.; Tisdale, W. A., Toward Stable Deep-Blue Luminescent Colloidal Lead Halide Perovskite Nanoplatelets: Systematic Photostability Investigation. *Chem. Mater* **2019,** *31* (7), 2486-2496.

33. Lin, J.-T.; Liao, C.-C.; Hsu, C.-S.; Chen, D.-G.; Chen, H.-M.; Tsai, M.-K.; Chou, P.-T.; Chiu, C.-W., Harnessing Dielectric Confinement on Tin Perovskites to Achieve Emission Quantum Yield up to 21%. *J. Am. Chem. Soc* **2019,** *141* (26), 10324-10330.

34. Fu, Y.; Hautzinger, M. P.; Luo, Z.; Wang, F.; Pan, D.; Aristov, M. M.; Guzei, I. A.; Pan, A.; Zhu, X.; Jin, S., Incorporating Large A Cations into Lead Iodide Perovskite Cages:Relaxed Goldschmidt Tolerance Factor and Impact on Exciton−Phonon Interaction. *ACS Cent. Sci.* **2019,** (5), 1377-1386.

35. Mao, L.; Wu, Y.; Stoumpos, C. C.; Traore, B.; Katan, C.; Even, J.; Wasielewski, M. R.; Kanatzidis, M. G., Tunable White-Light Emission in Single-Cation-Templated Three-Layered 2D Perovskites $(CH_3CH_2NH_3)_4Pb_3Br_{10-x}Cl_x$. *J. Am. Chem. Soc* **2017,** *139* (34), 11956-11963.

36. Han, S.; Liu, X.; Liu, Y.; Xu, Z.; Li, Y.; Hong, M.; Luo, J.; Sun, Z., High-Temperature Antiferroelectric of Lead Iodide Hybrid Perovskites. *J. Am. Chem. Soc* **2019,** *141* (32), 12470-12474.

37. Wang, S.; Liu, X.; Li, L.; Ji, C.; Sun, Z.; Wu, Z.; Hong, M.; Luo, J., An Unprecedented Biaxial Trilayered Hybrid Perovskite Ferroelectric with Directionally Tunable Photovoltaic Effects. *J. Am. Chem. Soc* **2019,** *141* (19), 7693-7697.

38. Fu, Y.; Jiang, X.; Li, X.; Traore, B.; Spanopoulos, I.; Katan, C.; Even, J.; Kanatzidis, M. G.; Harel, E., Cation Engineering in Two-Dimensional Ruddlesden–Popper Lead Iodide Perovskites with Mixed Large A-Site Cations in the Cages. *J. Am. Chem. Soc* **2020,** *142* (8), 4008-4021.

39. Sun, S.; Yuan, D.; Xu, Y.; Wang, A.; Deng, Z., Ligand-Mediated Synthesis of Shape-Controlled Cesium Lead Halide Perovskite Nanocrystals via Reprecipitation Process at Room Temperature. *ACS Nano* **2016,** *10* (3), 3648-3657.

40. Wheeler, L. M.; Anderson, N. C.; Bliss, T. S.; Hautzinger, M. P.; Neale, N. R., Dynamic Evolution of 2D Layers within Perovskite Nanocrystals via Salt Pair Extraction and Reinsertion. *J. Phys. Chem. C* **2018,** *122* (25), 14029-14038.

41. Prasanna, R.; Gold-Parker, A.; Leijtens, T.; Conings, B.; Babayigit, A.; Boyen, H.-G.; Toney, M. F.; McGehee, M. D., Band Gap Tuning via Lattice Contraction and Octahedral Tilting in Perovskite Materials for Photovoltaics. *J. Am. Chem. Soc* **2017,** *139* (32), 11117-11124.

42. Mitzi, D. B., Templating and structural engineering in organic-inorganic perovskites. *J. Chem. Soc., Dalton Trans.* **2001,** (1), 1-12.

43. Dai, J.; Fu, Y.; Manger, L. H.; Rea, M. T.; Hwang, L.; Goldsmith, R. H.; Jin, S., Carrier Decay Properties of Mixed Cation Formamidinium–Methylammonium Lead Iodide Perovskite [HC(NH2)2]1–x[CH3NH3]xPbI3 Nanorods. *J. Phys. Chem. Lett* **2016,** *7* (24), 5036-5043.

44. Chen, X.; Lu, H.; Li, Z.; Zhai, Y.; Ndione, P. F.; Berry, J. J.; Zhu, K.; Yang, Y.; Beard, M. C., Impact of Layer Thickness on the Charge Carrier and Spin Coherence Lifetime in Two-Dimensional Layered Perovskite Single Crystals. *ACS Energy Lett.* **2018,** *3* (9), 2273-2279.

45. Brouwer, A., *Standards for photoluminescence quantum yield measurements in solution (IUPAC Technical Report)**. 2011; Vol. 83, p 2213-2228.

46. Stranks, S. D., Nonradiative Losses in Metal Halide Perovskites. *ACS Energy Lett.* **2017,** *2* (7), 1515-1525.

47. Jiang, J.; Sun, X.; Chen, X.; Wang, B.; Chen, Z.; Hu, Y.; Guo, Y.; Zhang, L.; Ma, Y.; Gao, L.; Zheng, F.; Jin, L.; Chen, M.; Ma, Z.; Zhou, Y.; Padture, N. P.; Beach, K.; Terrones, H.; Shi, Y.; Gall, D.; Lu, T.-M.; Wertz, E.; Feng, J.; Shi, J., Carrier lifetime enhancement in halide perovskite via remote epitaxy. *Nat. Commun* **2019,** *10* (1), 4145.

48. Jones, T. W.; Osherov, A.; Alsari, M.; Sponseller, M.; Duck, B. C.; Jung, Y.-K.; Settens, C.; Niroui, F.; Brenes, R.; Stan, C. V.; Li, Y.; Abdi-Jalebi, M.; Tamura, N.; Macdonald, J. E.; Burghammer, M.; Friend, R. H.; Bulović, V.; Walsh, A.; Wilson, G. J.; Lilliu, S.; Stranks, S. D., Lattice strain causes non-radiative losses in halide perovskites. *Energy Environ. Sci* **2019,** *12* (2), 596-606.

49. Gong, X.; Voznyy, O.; Jain, A.; Liu, W.; Sabatini, R.; Piontkowski, Z.; Walters, G.; Bappi, G.; Nokhrin, S.; Bushuyev, O.; Yuan, M.; Comin, R.; McCamant, D.; Kelley, S. O.; Sargent, E. H., Electron–phonon interaction in efficient perovskite blue emitters. *Nature Materials* **2018,** *17* (6), 550-556.

50. Suri, M.; Hazarika, A.; Larson, B. W.; Zhao, Q.; Vallés-Pelarda, M.; Siegler, T. D.; Abney, M. K.; Ferguson, A. J.; Korgel, B. A.; Luther, J. M., Enhanced Open-Circuit Voltage of Wide-Bandgap Perovskite Photovoltaics by Using Alloyed (FA1–xCsx)Pb(I1–xBrx)3 Quantum Dots. *ACS Energy Lett.* **2019,** *4* (8), 1954-1960.

51. Jaffe, A.; Lin, Y.; Beavers, C. M.; Voss, J.; Mao, W. L.; Karunadasa, H. I., High-Pressure Single-Crystal Structures of 3D Lead-Halide Hybrid Perovskites and Pressure Effects on their Electronic and Optical Properties. *ACS Cent. Sci.* **2016,** *2* (4), 201-209.

52. Liu, G.; Kong, L.; Gong, J.; Yang, W.; Mao, H.-k.; Hu, Q.; Liu, Z.; Schaller, R. D.; Zhang, D.; Xu, T., Pressure-Induced Bandgap Optimization in Lead-Based Perovskites with Prolonged Carrier Lifetime and Ambient Retainability. *Adv. Funct. Mater* **2017,** *27* (3), 1604208.

53. Hwang, H. Y.; Cheong, S. W.; Radaelli, P. G.; Marezio, M.; Batlogg, B., Lattice Effects on the Magnetoresistance in Doped $LaMnO_3$. *Physical Review Letters* **1995,** *75* (5), 914-917.

54. Liu, G.; Kong, L.; Yang, W.; Mao, H.-k., Pressure engineering of photovoltaic perovskites. *Mater. Today* **2019,** *27*, 91-106.

55. Lee, J.-H.; Bristowe, N. C.; Lee, J. H.; Lee, S.-H.; Bristowe, P. D.; Cheetham, A. K.; Jang, H. M., Resolving the Physical Origin of Octahedral Tilting in Halide Perovskites. *Chem. Mater* **2016,** *28* (12), 4259-4266.

56. Rodriguez-Martinez, L. M.; Attfield, J. P., Cation disorder and size effects in magnetoresistive manganese oxide perovskites. *Physical Review B* **1996,** *54* (22), 15622-R15625.

57. Michael, D.; Christoph, H.; Harald, H., Synthesis, Crystal Structures, Optical Properties, and Phase Transitions of the Layered Guanidinium-Based Hybrid Perovskites $[C(NH_2)_3]_2MI_4$; M = Sn, Pb. *Eur. J. Inorg. Chem* **2017,** *2017* (7), 1120-1126.

58. Soe, C. M. M.; Stoumpos, C. C.; Kepenekian, M.; Traoré, B.; Tsai, H.; Nie, W.; Wang, B.; Katan, C.; Seshadri, R.; Mohite, A. D.; Even, J.; Marks, T. J.; Kanatzidis, M. G., New Type of 2D Perovskites with Alternating Cations in the Interlayer Space, (C(NH2)3)(CH3NH3)nPbnI3n+1: Structure, Properties, and Photovoltaic Performance. *J. Am. Chem. Soc* **2017,** *139* (45), 16297-16309.

59. Nazarenko, O.; Kotyrba, M. R.; Yakunin, S.; Aebli, M.; Rainò, G.; Benin, B. M.; Wörle, M.; Kovalenko, M. V., Guanidinium-Formamidinium Lead Iodide: A Layered Perovskite-Related Compound with Red Luminescence at Room Temperature. *J. Am. Chem. Soc* **2018,** *140* (11), 3850-3853.

60. Tong, J.; Song, Z.; Kim, D. H.; Chen, X.; Chen, C.; Palmstrom, A. F.; Ndione, P. F.; Reese, M. O.; Dunfield, S. P.; Reid, O. G.; Liu, J.; Zhang, F.; Harvey, S. P.; Li, Z.; Christensen, S. T.; Teeter, G.; Zhao, D.; Al-Jassim, M. M.; van Hest, M. F. A. M.; Beard, M. C.; Shaheen, S. E.; Berry, J. J.; Yan, Y.; Zhu, K., Carrier lifetimes of >1 μs in Sn-Pb perovskites enable efficient all-perovskite tandem solar cells. *Science* **2019,** *364* (6439), 475-479.

Chapter 5. Vapor phase grown 2D/3D halide perovskite heterostructures exhibiting charge separation*

5.1 Abstract

Halide perovskites have been intensively investigated as solution-processed high-performance optoelectronics. However, this solution processing limits the controlled fabrication of halide perovskite heterostructures comparable to traditional inorganic semiconductors. Here, we develop chemical vapor deposition of 2D halide perovskites $(BA)_2PbX_4$ (X = Br, I; BA = *n*-butylammonium) thin films onto 3D perovskite $(A)PbX_3$ (A = methylammonium (MA), formamidinium (FA)) single crystals to form 2D/3D perovskite heterostructures that are made of high-quality phase pure materials with clear 2D/3D interfaces that are superior to previously obtained perovskite heterostructures. Electrical characterization of the 2D/3D perovskite heterostructures reveals diode like behaviors and the iodide heterostructure $(BA)_2PbI_4/(FA_{0.75}MA_{0.25})PbI_3$ shows photocurrent at zero bias. Furthermore, excitation power dependent photoluminescence (PL) of the iodide heterostructure shows shifting in the 2D perovskite PL energy. These results suggest there is charge-carrier separation at the interface of the 2D/3D iodide heterostructure. However, time resolved photoluminescence of the heterostructure suggests a competing energy transfer process occurs, pointing to complex behaviors. In addition to the new growth method for 2D/3D perovskite heterostructures, this work provides new insights on the competing charge and energy transfer occurring at the 2D/3D interface.

---

* In collaboration with D. Lafayette II, J. Feng, Z. Luo, W. Zheng, M. Kuo, N. Spitha, A. Pan, J. C. Wright, and S. Jin

5.2 Introduction

Lead halide perovskites have received intense investigation over the past decade due to their remarkable photophysical properties and use in high efficiency photovoltaics (PVs) and light emitting diodes (LEDs).[1-3] Three-dimensional (3D) lead halide perovskites are highly tunable compounds based on the formula $(A)PbX_3$ (A = Cs, methylammonium (MA), formamidinium (FA); X = Cl, Br, I).[4] Adding to the structural tunability are two-dimensional (2D) layered Ruddlesden-Popper (RP) perovskites, in which long chain ammonium (LA) spacer cations intercede inorganic perovskite slabs of MX_6^{4-} octahedra to form $(RNH_3)_2(A)_{n-1}M_nX_{3n+1}$ structures.[5, 6] 2D RP perovskites are quantum confined materials that display enhanced environmental stability[7] and interesting optical properties such strong photoluminescence,[8] white-light emission,[9] and non-linear properties.[10, 11] Furthermore, two-dimensional/three-dimensional (2D/3D) perovskite heterostructures have been utilized in photovoltaics (PVs) to combine the stability of 2D perovskites with the high carrier mobility of 3D perovskites for efficient and stable PVs[12-16] and LEDs.[17, 18] However, it is difficult to control and elucidate the heterostructures compositions in these devices, as often the 2D and 3D perovskites are mixed into a multidimensional junction, with various n-values and unclear interfaces.[19-21] While commonly employed solution syntheses have been successful in making 2D/3D perovskite heterostructures for efficient PVs and LEDs, better understanding of the heterostructures and new applications[22, 23] could be enabled by improving the growth techniques for 2D/3D perovskite heterostructures.

Recently, 2D RP perovskite nanosheets of varying *n* value were synthesized, transferred and stacked to deterministically fabricate heterostructures of RP perovskites.[24] In addition, other works demonstrated the solution growth of $(PEA)_2PbBr_4$ microplates (PEA = phenylethylammonium) onto single crystal thin films of $CsPbBr_3$ allowed more controlled

formation of 2D/3D perovskite heterostructures[25] due to the low solubility of $CsPbBr_3$ in the growth solution of 2D perovskites. However, only the $(PEA)_2PbBr_4/CsPbBr_3$ heterostructures could be grown this way, the 2D/3D iodide heterostructures are inaccessible due to the instability of $CsPbI_3$ perovskite phase. To expand beyond the limiting solution growth of halide perovskites, significant research has gone into the vapor phase deposition of halide perovskites, including the direct vapor phase growth of all-inorganic $CsPbX_3$ thin films and nanostructures,[26-28] as well as 2D hybrid perovskite flakes.[29-31] Furthermore, vapor phase conversion processes have been successfully utilized to make halide perovskites, such as growing PbI_2 thin-films or single crystal microplates followed by conversion to perovskite phase by treatment with organoammonium halide vapor.[32-35] Vapor phase growths have been successfully utilized to grow halide perovskite thin films used in solar cells.[36, 37] These successes suggest that vapor phase growth could be used to enable 2D/3D perovskite heterostructures with composition control not previously realized.

Furthermore, the understanding on how 2D/3D perovskite heterostructures behave is compounded by the poorly defined heterostructures.[38] Some reports suggest that charge carriers can separate at the 2D/3D interface[39, 40] (beneficial for PVs) while other reports suggest energy transfer/funneling processes occur (beneficial for LEDs).[41, 42] Different explanations for these two apparently contradictory phenomena have been suggested. For example, this competing behavior could be the result of compositional changes at the 2D/3D interface, which has been shown to cause changes in the relative band positions. Another report showed that in mixed n – value $(BA)_2(MA)_{n-1}Pb_nI_{3n+1}$ (BA = *n*-butylammonium) films the same interface has both energy transfer and electron transfer (carrier separation) at different time scales, with the energy transfer occurring at sub nanosecond time scales, which can be extrapolated to highlight the complexity of 2D/3D heterostructures.[43] Our recent work on $(PEA)_2PbBr_4/CsPbBr_3$ heterostructures suggested via

kinetic modeling of time-resolved photoluminescence (TRPL) that these energy transfer and carrier separation process could be competing processes in the same material.[25] More work is needed to fully understand what occurs at the 2D/3D perovskite interface with more controlled interface, especially the lower bandgap iodide heterostructures that are more pertinent for solar cells.

In this report, we used chemical vapor deposition (CVD) to grow 2D perovskite $(BA)_2PbX_4$ (X = I, Br) thin films onto single crystal (SC) 3D perovskite $(FA_{0.75}MA_{0.25})PbI_3$ and $(MA)PbBr_3$ substrates to form large area 2D/3D perovskite heterostructures. X-ray diffraction, microscopy, and steady state optical measurements confirmed the formation of heterostructures of $(BA)_2PbI_4/(FA_{0.75}MA_{0.25})PbI_3$ and $(BA)_2PbBr_4/(MA)PbBr_3$, which are referred to as 2D/3D iodide and 2D/3D bromide heterostructures, respectively. Electrical measurements across the 2D/3D interface demonstrate diode like behaviors in both 2D/3D iodide and bromide heterostructures. Interestingly, only the iodide heterostructure shows observable photocurrent at 0 V bias, which suggests charge separation at the 2D/3D perovskite interface. Power dependent photoluminescence (PL) shows blue shifting of the 2D perovskite PL peak in the heterostructure with increasing excitation intensity. Time-resolved PL (TRPL) shows a change in the rise time between the 3D and 2D components.

5.3 Materials and Methods

All chemicals and regents were used as received unless otherwise noted. Lead (II) bromide ($PbBr_2$), *n*-butylammonium bromide, *n*-butylammonium iodide, γ -butyrolactone, and N,N-dimethylformamide, were purchased from sigma Aldrich. Methylammonium bromide, methylammonium iodide, and formamidinium iodide was purchased from Greatcellsolar. Lead (II)

iodide was purchased from TCI chemicals. Pelco® conductive colloidal silver paste (Prod# 16032), and Pelco® SEM-Gold/Silver Thinner/Extender (Prod# 16021) were purchased from Ted Pella.

5.3.1 CVD growth of $(BA)_2PbX_4$

The CVD growth of $(BA)_2PbBr_4$ was carried out in a home-built chemical vapor deposition (CVD) setup equipped with mass flow controllers and pressure control. The (BA)Br precursor in a ceramic boat (3 cm in length) and $PbBr_2$ in a ceramic boat (3 cm in length) were loaded into a fused silica tube (inner diameter 2.1 cm). The (BA)Br boat was initially placed outside of the hot zone and the $PbBr_2$ boat was 6-9 cm downstream from the center of the tube furnace (Lindberg Blue). The CVD tube was put under vacuum (~ 4 mTorr) and heated to 300 °C for 5 min. Subsequently, the (BA)Br boat was pushed into position 17-14 cm upstream from the center of the furnace, where the temperature was approximately 115 °C. The deposition was allowed to proceed for 5 min with a Ar gas flow of 90 sccm, then the furnace was opened and allowed to cool to room temperature naturally. Films of $(BA)_2PbBr_4$ were deposited onto a piece of Si wafer, glass microscope slide, or single crystal substrate placed ≈18.5 cm downstream from the center of the furnace. The same method was used for the growth of $(BA)_2PbI_4$ films, except the furnace temperature was reduced to 275 °C.

5.3.2 Single crystal growth

$(MA)PbBr_3$ SCs. A 0.8 M solution of $(MA)PbBr_3$ (molarity based on a Pb basis) was prepared in DMF by sonicating the precursor salts in the DMF at room temperature for < 5 m. A closed vial with 5 mL of the solution was heated at 90 °C in an oil bath for 3 h. Millimeter scale crystals were then removed from the still hot solution and dried under vacuum filtration.

$(FA_{0.75}MA_{0.25})PbI_3$ SCs. A 1.3 M solution $(FA_{0.75}MA_{0.25})PbI_3$ (molarity based on a Pb basis) was prepared in γ-butrylactone by heating the precursor salts in DMF at 60 °C for < 30 m. A closed vial with 5 mL of the solution was then heated at 130 °C in an oil bath for up to 3 h. Millimeter scale crystals were then removed from the still hot solution and dried under vacuum filtration.

5.3.3 Structural characterizations

XRD patterns of the $(BA)_2PbX_4$ films, $(MA)PbBr_3$ crystals, and $(FA_{0.75}MA_{0.25})PbI_3$ crystals were collected using a Bruker D8 Advance X-ray diffractometer equipped with a Cu K$\alpha\alpha$ X-ray tube. XRD patterns of the heterostructure were collected using a Bruker D8 Discovery X-ray diffractometer equipped with a Vantec 500 area detector. The measurements were performed with an incident beam angle of 1° θ and the detector at 19° θ. The scanning electron microscopy (SEM) images were collected on a LEO SUPRA 55 VP field-emission scanning electron microscope.

5.3.4 Electrical Characterization

The device for electrical measurements was directly fabricated on a sample of 2D/3D halide heterostructure that was partially masked with a piece of copper foil during CVD growth of 2D perovskite. After the growth, the mask was removed, and conductive colloidal silver paste was carefully deposited onto the 2D/3D area and the 3D crystal area of the sample. The I-V curve and photocurrent measurements of the 2D/3D heterostructures were performed using a Cascade Microtech RF-1 probe station. Voltage was applied through a National Instruments DAQ BNC-2090 terminal block and the currents were amplified using a DL Instruments Model 1211 current pre-amplifier and measured using computer controlled National Instruments DAC card. The sample was illuminated with a Techniquip fiber optic illuminator (FOI-150).

5.3.5 Spectroscopic characterization

Time-resolved photoluminescence (TRPL) and excitation intensity dependent steady state PL was collected on the $(BA)_2PbI_4/(FA_{0.75}MA_{0.25})PbI_3$ heterostructures using a home-built system. Specifically, excitation pulses of 400 nm were created by the second harmonic generation of a Ti:Sapphire oscillator (Coherent Vitesse 800-2) output. Second harmonic generation was achieved by focusing the fundamental into a 500 μm Type-I phase matched BBO (Eksma Optics BBO-603H). All excitations were focused with a 20X plan apochromatic objective lens (Olympus). A Becker S4 & Hickel SPC-130 time correlated single photon counting module equipped with an IDQ-50-ULN avalanche photodiode was used. The instrument response function (IRF) was 55 ps FWHM.

Time-resolved photoluminescence (TRPL) and steady state PL of the $(BA)_2PbBr_4/(MA)PbBr_3$ heterostructure was collected by using a confocal WITec microscope (alpha-300) equipped with a streak camera (C10910, Hamamatsu) detector. The excitation source was a Ti:sapphire with 400 nm output generated from the 800 nm laser from a mode-locked oscillator (Tsunami 3941-X1BB, Spectra-Physics) after a barium metaborate (BBO) crystal with 80 fs pulse width and 80 MHz repetition.

5.4 Results and Discussion

We first developed the chemical vapor deposition (CVD) of 2D $(BA)_2PbI_4$ perovskite with a two-precursor boat system (Figure 5.1a). To successfully deposit 2D perovskite via CVD, the (BA)I precursor was kept upstream at ≈115 °C separate from the inorganic PbI_2 precursor at ≈300 °C in order to accommodate the more volatile (BA)I by ensuring it is evaporating at a similar rate to the PbI_2. A similar procedure was used for $(BA)_2PbBr_4$ growth (see Materials and Methods for full details). SEM images of the $(BA)_2PbX_4$ thin films deposited on silicon substrates show smooth, uniform and pinhole-free films (Figure 5.1b,c). X-ray diffraction (XRD) of the films confirms these are phase pure materials of the layered $(BA)_2PbX_4$, well matched to their calculated XRD patterns (Figure 5.1d,e).

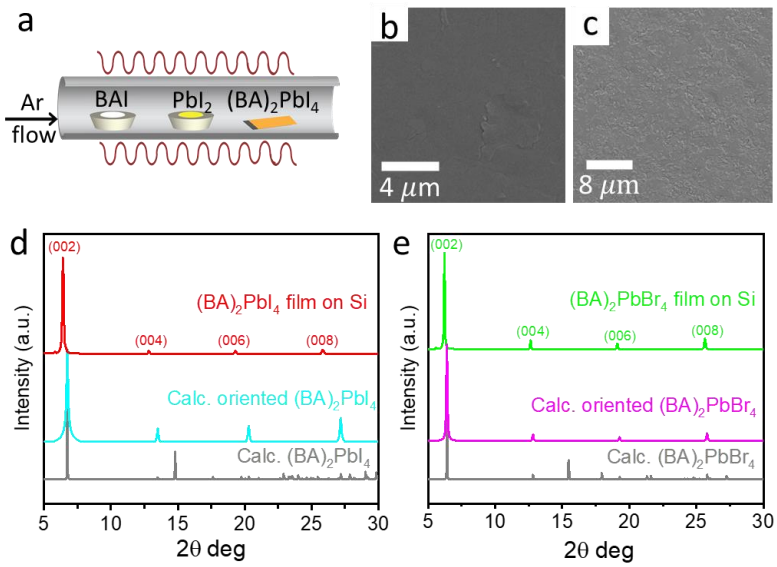

Figure 5.1. Vapor phase deposition of 2D halide perovskites. (a) Schematic showing the CVD flow reactor setup for the deposition. SEM of the (b) $(BA)_2PbI_4$ and (c) $(BA)_2PbBr_4$ films on Si wafer. XRD of the (d) $(BA)_2PbI_4$ and (e) $(BA)_2PbBr_4$ films grown onto Si wafer. The observed XRD patterns agree well with the patterns calculated with the 2D structure orientated with the c-plane parallel to the substrate.

Once the deposition method of 2D perovskites was established, we aimed to grow 2D perovskite on top of 3D perovskite single crystals (SCs) as shown in the schematic in Figure 5.2a. Large SCs of $(FA_{0.75}MA_{0.25})PbI_3$ and $(MA)PbBr_3$ were grown from solutions by inverse temperature crystallization as described in the Materials and Methods section.[44] SEM images (Figure 5.2b,c) show that the surface of the SCs was smooth and crack free. The insets show optical images of the millimeter-scale SCs, making them suitable substrates for the CVD deposition. Powder XRD of these crystals ground into powders confirms the perovskite phases (Figure D.1a,b). The mixed FA-MA composition in $(FA_{0.75}MA_{0.25})PbI_3$ was used because $(MA)PbI_3$ decomposes at relatively low temperatures and $(FA)PbI_3$ perovskite phase is unstable at ambient conditions. In contrast, $(FA_{0.75}MA_{0.25})PbI_3$ is stable up to 315 °C as confirmed by TGA data in Figure D.1c.

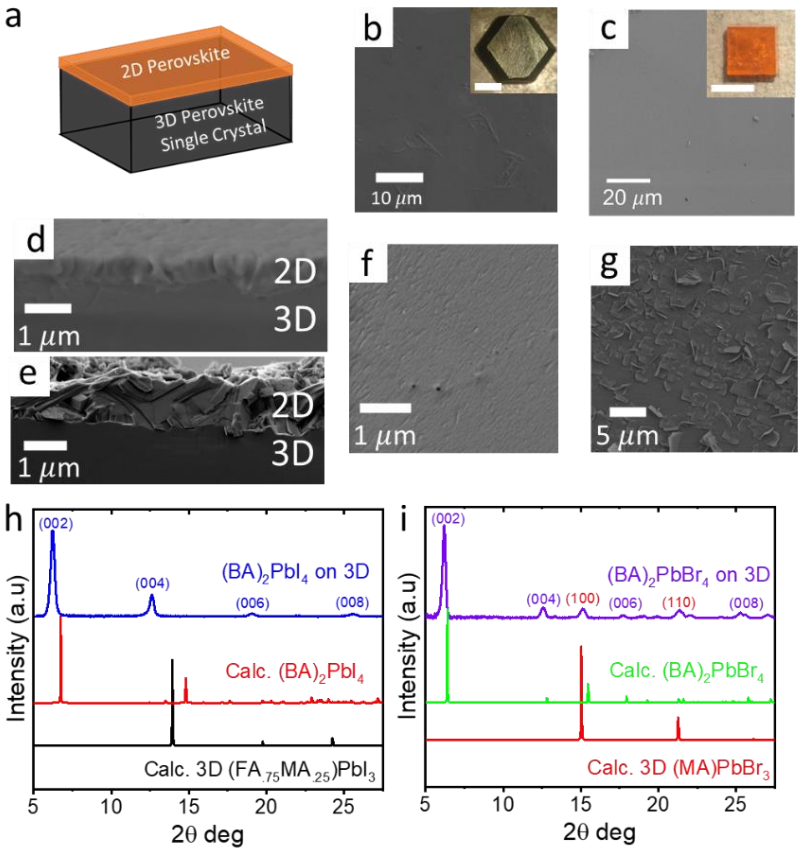

Figure 5.2. Structural characterization of 2D/3D perovskite heterostructures. (a) Schematic showing the $(BA)_2PbX_4$ film (2D perovskite) on top of a 3D perovskite $(A)PbX_3$ single crystal (SC). SEM images of (b) large $(FA_{0.75}MA_{0.25})PbI_3$ and (c) $(MA)PbBr_3$ SC substrate surface. Insets are optical images of the SCs (inset scale bars are 2 mm). SEM cross section images of (d) $(BA)_2PbI_4$ and (e) $(BA)_2PbBr_4$ films on respective 3D perovskite SCs. Top-down SEM images of the 2D perovskite films in the (f) 2D/3D iodide and (g) 2D/3D bromide perovskite heterostructures. (h,i) XRD of the 2D/3D heterostructures compared to calculated patterns of 2D and 3D perovskites.

With the 3D perovskite single crystal substrates, 2D perovskite thin films were grown on top via the already described CVD method. Figure 5.2d,e show SEM cross-section images of the heterostructures with a clear interface between the 2D and 3D perovskites. The 2D perovskite layer is ≈400 nm thick in the iodide and ≈1 μm thick in the bromide. Top-view SEM image shows the

surface of 2D $(BA)_2PbI_4$ grown on top of the 3D perovskite appears roughened with small features of the film (Figure 5.2f). The $(BA)_2PbBr_4$ film has some plate-like microstructures forming on the surface (Figure 5.2b). XRD of the heterostructures shows the characteristic low angle periodic diffraction peaks characteristic of 2D perovskites (00*l*) diffraction planes (Figure 5.2h,i). These characterizations establish large scale 2D/3D perovskite heterostructures, with well-defined interfaces suitable for investigating the 2D/3D perovskite interface.

We then performed electrical and photoconductivity measurements to understand how the 2D/3D halide perovskite heterostructures behave. For fabricating the devices illustrated in Figure 5.3a, the 3D perovskite SC was partially masked prior to the 2D perovskite CVD growth followed by depositing silver paste contacts onto the bare 3D perovskite (masked region) and 2D perovskite. This enables the interface of the heterostructure to be studied under illumination of a white light halogen fiber optic illuminator (see Materials and Methods for details). Measurements show the 2D/3D iodide heterostructure exhibits photocurrent under 0 V bias and illumination (Figure 5.3b). This suggests that charges are separating in the heterostructure with no external driving force (0 V bias). Interestingly, the 2D/3D bromide heterostructure did not show 0 V bias photocurrent (Figure D.2a). Furthermore, I-V measurements show clear diode like behaviors in both heterostructures under illumination (Figure 5.3c,d), but the bromide heterostructure displays a higher onset voltage. With increasing light intensity, the photocurrent is increased. Magnified regions of the I-V curves around 0 V show photocurrent under illumination for the 2D/3D iodide, but not the 2D/3D bromide (Figure 5.3c,d insets). This corresponds well with the 2D/3D bromide having no photocurrent under 0 V bias in the on-off illumination measurements, while the iodide does. As a control experiment, we tested pure 2D and 3D iodide perovskites for potential 0 V bias photocurrent and diode behaviors and did not observe any (Figure D2b,c). Considering these results, it is clear both

iodide and bromide 2D/3D heterostructures behave as a diode, indicating there is type II interfaces in the heterostructures. However, the iodide heterostructure appears to show charge carrier separation at the interface while bromide heterostructure does not.

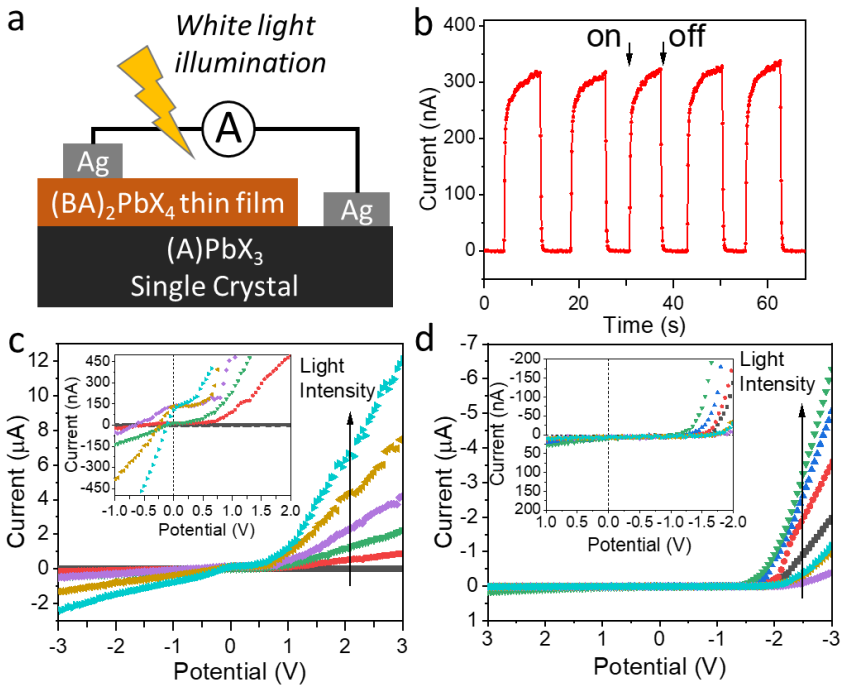

Figure 5.3. Electrical characterization of 2D/3D perovskite heterostructures under illumination. (a) Schematic showing the device architecture for electrical measurements. (b) Photocurrent at 0 V bias for the $(BA)_2PbI_4/(FA_{0.75}MA_{0.25})PbI_3$ heterostructure under 1 Sun illumination. I-V curves under increasing illumination intensity for (c) 2D/3D iodide and (d) 2D/3D bromide heterostructures showing clear diode like behaviors under illumination. The insets show magnified regions around 0 V, highlighting the inconsistent photocurrent in the iodide heterostructure and lack of photocurrent in the bromide heterostructure.

We further investigated the heterostructure behaviors with spectroscopy. Photoluminescence (PL) measurements show PL peaks of the 2D/3D heterostructures at the same wavelength as the pure component 2D and 3D perovskites (Figure 5.4a for iodide, Figure D.3a for bromide). There was some spatial dependence of the steady state PL in 2D/3D iodide

heterostructure, showing some impurity phases (higher *n*-value) in select regions, but this was uncommon (Figure D.3b). In III-V semiconductor heterostructures, it has been shown that charge separation, caused by band bending at the interface, blueshifts the PL energy of a material as excitation power increases.[45-48] By testing 2D/3D iodide heterostructure across as wide a range of laser excitation intensity (P) as possible (i.e. not degrading the sample), we can see there is clear shift in the PL peak energy of the 2D perovskite (ΔE_{PL}, Figure 5.4b). For a type II heterostructure, the PL is predicted to shift as $\Delta E_{PL} \alpha\, P^{1/3}$.[47] The fitting of our results shows the 2D/3D iodide perovskite heterostructure follows $\Delta E_{PL} \alpha\, P^{1/2}$, deviating from the $P^{1/3}$ expected. However, the upper limit of excitation power is limited by the perovskites degradation and others have observed the $P^{1/2}$ power dependence at low fluences.[45] Furthermore, a control experiment performed on pure 2D $(BA)_2PbI_4$ under increasing laser excitation does not show a PL shift (Figure D.4). Excitation power dependence studies could not be performed in the 2D/3D bromide heterostructure due to the limited spectral resolution of the available instrument.

We further probed the behaviors of the 2D/3D interface with time-resolved photoluminescence (TRPL) measurements of the 2D/3D heterostructures. The measurements on 2D/3D iodide structures show there is a clear change in the rise time of the PL (Figure 5.4c). The narrow band gap $(FA_{0.75}MA_{0.25})PbI_3$ 3D perovskite has delayed PL relative to the wider band gap $(BA)_2PbI_4$ 2D perovskite. As seen previously, energy transfer between materials can cause a delayed rise time in the TRPL.[41, 49, 50] A similar delayed emission of the 3D bromide perovskite in 2D/3D bromide perovskite heterostructures is shown in Figure D.5. This change in rise time is more typical of energy transfer between materials, not charge separation as would be seen in a type

II material. Transient reflectance measurements collected on the 2D/3D iodide heterostructure suggest a similar decreased rise time in a sub bandgap bleach feature (Figure D.6).

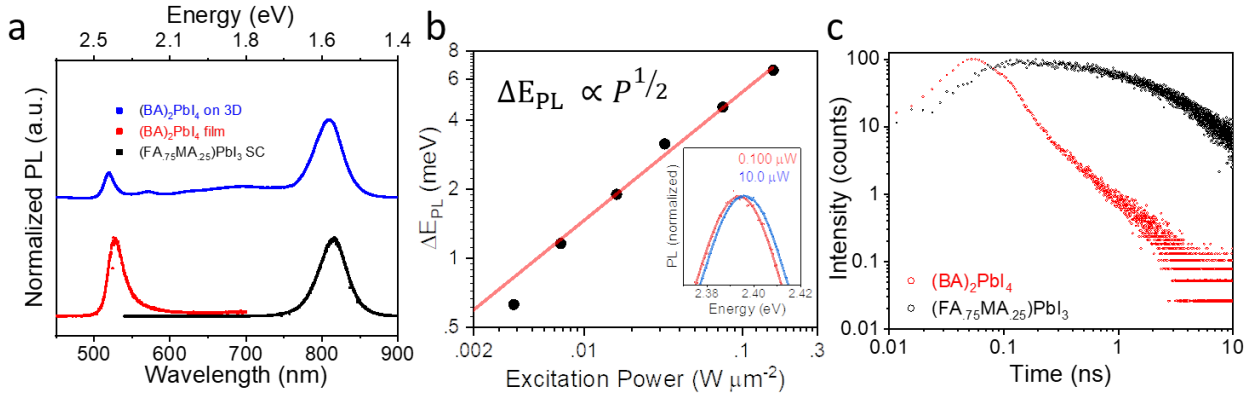

Figure 5.4. Spectroscopic studies of 2D/3D iodide heterostructure $(BA)_2PbI_4$ on $(FA_{0.75}MA_{0.25})PbI_3$. (a) PL spectra of 2D/3D iodide heterostructure, pure $(BA)_2PbI_4$ and pure $(FA_{0.75}MA_{0.25})PbI_3$. (b) Dependence of the PL peak shift of $(BA)_2PbI_4$ in the 2D/3D iodide heterostructure on the excitation power with a fitting shown. Inset shows PL peak on top of each other, highlighting the PL shift. (c) TRPL of 2D/3D iodide heterostructure.

Our results suggest there are competing processes occurring at the 2D/3D perovskite interface. The observation of photocurrent at 0 V bias is evidence that points to carriers separating at the 2D/3D iodide heterostructure interface. In addition, the diode like behaviors in the 2D/3D iodide and bromide heterostructures point to the rectifying type II heterostructure behavior which would suggest a picture illustrated in Figure 5.5a. The lack of photocurrent in 2D/3D bromide heterostructure could be due to the number of carriers present in the material. It's expected that the wider band gap 2D/3D bromide heterostructure would have less carriers under white light illumination that the lower band gap 2D/3D iodide heterostructures,[51] resulting in the lack of measurable photocurrent. It should be noted, another report on similar 2D/3D bromide perovskite heterostructure was able to resolve weak photocurrent between 2-6 nAs at zero bias,[39] behaving similar to our 2D/3D iodide system (though with significantly smaller photocurrent). Furthermore,

excitation power dependent PL energy shift indicates there is a type II alignment at the interface of the 2D/3D iodide heterostructure, pointing again to the schematic in Figure 5.5a. However, the change in rise time of the TRPL in the 2D/3D iodide and bromide suggests energy transfer could occur at the interface, closer to what is illustrated Figure 5.5b. Further control over the materials growth, such as 2D thin-film thickness and improved electrical measurements could help to form a clearer picture.

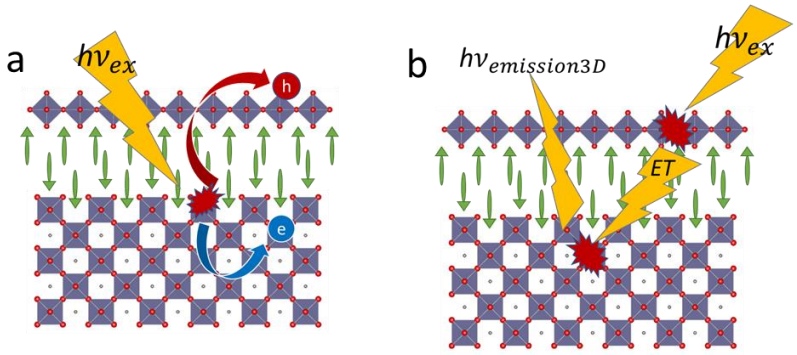

Figure 5.5. Schematic of different potential carrier behaviors in the 2D/3D perovskite heterostructures. (a) Schematic depicting charge carrier separation at the 2D/3D heterostructure interface and (b) depicting energy transfer (ET) at the 2D/3D heterostructure interface.

5.5 Conclusion

Here we demonstrate the CVD growth of 2D halide perovskite $(BA)_2PbX_4$ thin films on top of 3D perovskite single crystal substrates to form heterostructures with more controlled phase pure materials and clear interfaces between the 2D and 3D perovskites. Electrical characterization of both the 2D/3D iodide and bromide heterostructures show diode like behaviors, indicative of a type II aligned system. This is correlated with the 2D/3D iodide heterostructure that displays photocurrent at 0 V bias, suggesting charge carrier separation in the heterostructure. However, the 2D/3D bromide heterostructure does no display photocurrent at 0V. The source of this discrepancy between the 2D/3D iodide and bromide is unclear and requires further experiments to elucidate. Furthermore, the excitation power dependent PL on the 2D/3D iodide heterostructure shows blue

shifting of PL peak, suggesting type II alignment, while change in the rise time of the TPRL of 2D/3D heterostructures suggests a type I heterostructure alignment. These competing processes create a complex situation for the utility of 2D/3D heterostructures. Future research should focus on quantifying these competing effects, to determine whether 2D/3D perovskite heterostructures have more utility in applications reliant on energy transfer, such as LEDs, or if the charge separation process dominates.

5.6 References

1. Correa-Baena, J.-P.; Abate, A.; Saliba, M.; Tress, W.; Jesper Jacobsson, T.; Grätzel, M.; Hagfeldt, A., The rapid evolution of highly efficient perovskite solar cells. *Energy Environ. Sci.* **2017,** *10* (3), 710-727.

2. Sutherland, B. R.; Sargent, E. H., Perovskite photonic sources. *Nat. Photonics* **2016,** *10* (5), 295-302.

3. Fu, Y.; Zhu, H.; Chen, J.; Hautzinger, M. P.; Zhu, X. Y.; Jin, S., Metal halide perovskite nanostructures for optoelectronic applications and the study of physical properties. *Nat. Rev. Mater.* **2019,** *4* (3), 169-188.

4. Stoumpos, C. C.; Malliakas, C. D.; Kanatzidis, M. G., Semiconducting Tin and Lead Iodide Perovskites with Organic Cations: Phase Transitions, High Mobilities, and Near-Infrared Photoluminescent Properties. *Inorg. Chem.* **2013,** *52* (15), 9019-9038.

5. Stoumpos, C. C.; Cao, D. H.; Clark, D. J.; Young, J.; Rondinelli, J. M.; Jang, J. I.; Hupp, J. T.; Kanatzidis, M. G., Ruddlesden–Popper Hybrid Lead Iodide Perovskite 2D Homologous Semiconductors. *Chem. Mater* **2016,** *28* (8), 2852-2867.

6. Li, X.; Hoffman, J. M.; Kanatzidis, M. G., The 2D Halide Perovskite Rulebook: How the Spacer Influences Everything from the Structure to Optoelectronic Device Efficiency. *Chem. Rev* **2021,** *121* (4), 2230-2291.

7. Smith, I. C.; Hoke, E. T.; Solis-Ibarra, D.; McGehee, M. D.; Karunadasa, H. I., A Layered Hybrid Perovskite Solar-Cell Absorber with Enhanced Moisture Stability. *Angew. Chem. Int. Ed.* **2014,** *53* (42), 11232-11235.

8. Quan, L. N.; Rand, B. P.; Friend, R. H.; Mhaisalkar, S. G.; Lee, T.-W.; Sargent, E. H., Perovskites for Next-Generation Optical Sources. *Chem. Rev* **2019,** *119* (12), 7444-7477.

9. Smith, M. D.; Karunadasa, H. I., White-Light Emission from Layered Halide Perovskites. *Acc. Chem. Res.* **2018,** *51* (3), 619-627.

10. Morrow, D. J.; Hautzinger, M. P.; Lafayette, D. P.; Scheeler, J. M.; Dang, L.; Leng, M.; Kohler, D. D.; Wheaton, A. M.; Fu, Y.; Guzei, I. A.; Tang, J.; Jin, S.; Wright, J. C., Disentangling Second Harmonic Generation from Multiphoton Photoluminescence in Halide Perovskites using Multidimensional Harmonic Generation. *J. Phys. Chem. A.* **2020,** *11* (16), 6551-6559.

11. Li, L.; Sun, Z.; Wang, P.; Hu, W.; Wang, S.; Ji, C.; Hong, M.; Luo, J., Tailored Engineering of an Unusual $(C_4H_9NH_3)_2(CH_3NH_3)_2Pb_3Br_{10}$ Two-Dimensional Multilayered Perovskite Ferroelectric for a High-Performance Photodetector. *Angew. Chem. Int. Ed.* **2017,** *56* (40), 12150-12154.

12. Wang, Z.; Lin, Q.; Chmiel, F. P.; Sakai, N.; Herz, L. M.; Snaith, H. J., Efficient ambient-air-stable solar cells with 2D–3D heterostructured butylammonium-caesium-formamidinium lead halide perovskites. *Nat. Energy* **2017,** *2* (9), 17135.

13. Proppe, A. H.; Wei, M.; Chen, B.; Quintero-Bermudez, R.; Kelley, S. O.; Sargent, E. H., Photochemically Cross-Linked Quantum Well Ligands for 2D/3D Perovskite Photovoltaics with Improved Photovoltage and Stability. *J. Am. Chem. Soc.* **2019,** *141* (36), 14180-14189.

14. Li, P.; Zhang, Y.; Liang, C.; Xing, G.; Liu, X.; Li, F.; Liu, X.; Hu, X.; Shao, G.; Song, Y., Phase Pure 2D Perovskite for High-Performance 2D–3D Heterostructured Perovskite Solar Cells. *Adv. Mater.* **2018,** *30* (52), 1805323.

15. Gharibzadeh, S.; Abdollahi Nejand, B.; Jakoby, M.; Abzieher, T.; Hauschild, D.; Moghadamzadeh, S.; Schwenzer, J. A.; Brenner, P.; Schmager, R.; Haghighirad, A. A.; Weinhardt, L.; Lemmer, U.; Richards, B. S.; Howard, I. A.; Paetzold, U. W., Record Open-Circuit Voltage Wide-Bandgap Perovskite Solar Cells Utilizing 2D/3D Perovskite Heterostructure. *Adv. Energy Mater.* **2019,** *9* (21), 1803699.

16. Lin, Y.; Bai, Y.; Fang, Y.; Chen, Z.; Yang, S.; Zheng, X.; Tang, S.; Liu, Y.; Zhao, J.; Huang, J., Enhanced Thermal Stability in Perovskite Solar Cells by Assembling 2D/3D Stacking Structures. *J. Phys. Chem. A.* **2018,** *9* (3), 654-658.

17. Han, T.-H.; Lee, J.-W.; Choi, Y. J.; Choi, C.; Tan, S.; Lee, S.-J.; Zhao, Y.; Huang, Y.; Kim, D.; Yang, Y., Surface-2D/Bulk-3D Heterophased Perovskite Nanograins for Long-Term-Stable Light-Emitting Diodes. *Adv. Mater.* **2020,** *32* (1), 1905674.

18. Chin, X. Y.; Perumal, A.; Bruno, A.; Yantara, N.; Veldhuis, S. A.; Martínez-Sarti, L.; Chandran, B.; Chirvony, V.; Lo, A. S.-Z.; So, J.; Soci, C.; Grätzel, M.; Bolink, H. J.; Mathews, N.; Mhaisalkar, S. G., Self-assembled hierarchical nanostructured perovskites enable highly efficient LEDs via an energy cascade. *Energy Environ. Sci.* **2018,** *11* (7), 1770-1778.

19. Ortiz-Cervantes, C.; Carmona-Monroy, P.; Solis-Ibarra, D., Two-Dimensional Halide Perovskites in Solar Cells: 2D or not 2D? *ChemSusChem* **2019,** *12* (8), 1560-1575.

20. Zhou, N.; Shen, Y.; Li, L.; Tan, S.; Liu, N.; Zheng, G.; Chen, Q.; Zhou, H., Exploration of Crystallization Kinetics in Quasi Two-Dimensional Perovskite and High Performance Solar Cells. *J. Am. Chem. Soc.* **2018,** *140* (1), 459-465.

21. Akriti; Shi, E.; Shiring, S. B.; Yang, J.; Atencio-Martinez, C. L.; Yuan, B.; Hu, X.; Gao, Y.; Finkenauer, B. P.; Pistone, A. J.; Yu, Y.; Liao, P.; Savoie, B. M.; Dou, L., Layer-by-layer anionic diffusion in two-dimensional halide perovskite vertical heterostructures. *Nat. Nanotechnology* **2021,** *16* (5), 584-591.

22. Kim, Y.-H.; Zhai, Y.; Lu, H.; Pan, X.; Xiao, C.; Gaulding, E. A.; Harvey, S. P.; Berry, J. J.; Vardeny, Z. V.; Luther, J. M.; Beard, M. C., Chiral-induced spin selectivity enables a room-temperature spin light-emitting diode. *Science* **2021,** *371* (6534), 1129-1133.

23. Zhang, L.; Zhang, X.; Lu, G., Predictions of moiré excitons in twisted two-dimensional organic–inorganic halide perovskites. *Chem. Sci* **2021,** *12* (17), 6073-6080.

24. Pan, D.; Fu, Y.; Spitha, N.; Zhao, Y.; Roy, C. R.; Morrow, D. J.; Kohler, D. D.; Wright, J. C.; Jin, S., Deterministic fabrication of arbitrary vertical heterostructures of two-dimensional Ruddlesden–Popper halide perovskites. *Nat. Nanotechnology* **2021,** *16* (2), 159-165.

25. Kuo, M.-Y.; Spitha, N.; Hautzinger, M. P.; Hsieh, P.-L.; Li, J.; Pan, D.; Zhao, Y.; Chen, L.-J.; Huang, M. H.; Jin, S.; Hsu, Y.-J.; Wright, J. C., Distinct Carrier Transport Properties Across Horizontally vs Vertically Oriented Heterostructures of 2D/3D Perovskites. *J. Am. Chem. Soc.* **2021,** *143* (13), 4969-4978.

26. Chen, J.; Morrow, D. J.; Fu, Y.; Zheng, W.; Zhao, Y.; Dang, L.; Stolt, M. J.; Kohler, D. D.; Wang, X.; Czech, K. J.; Hautzinger, M. P.; Shen, S.; Guo, L.; Pan, A.; Wright, J. C.; Jin, S., Single-Crystal Thin Films of Cesium Lead Bromide Perovskite Epitaxially Grown on Metal Oxide Perovskite ($SrTiO_3$). *J. Am. Chem. Soc.* **2017,** *139* (38), 13525-13532.

27. Chen, J.; Fu, Y.; Samad, L.; Dang, L.; Zhao, Y.; Shen, S.; Guo, L.; Jin, S., Vapor-Phase Epitaxial Growth of Aligned Nanowire Networks of Cesium Lead Halide Perovskites ($CsPbX_3$, X = Cl, Br, I). *Nano Lett.* **2017,** *17* (1), 460-466.

28. Wang, Y.; Sun, X.; Shivanna, R.; Yang, Y.; Chen, Z.; Guo, Y.; Wang, G.-C.; Wertz, E.; Deschler, F.; Cai, Z.; Zhou, H.; Lu, T.-M.; Shi, J., Photon Transport in One-Dimensional Incommensurately Epitaxial $CsPbX_3$ Arrays. *Nano Lett.* **2016,** *16* (12), 7974-7981.

29. Chen, Z.; Wang, Y.; Sun, X.; Guo, Y.; Hu, Y.; Wertz, E.; Wang, X.; Gao, H.; Lu, T.-M.; Shi, J., Van Der Waals Hybrid Perovskite of High Optical Quality by Chemical Vapor Deposition. *Adv. Opt. Mater.* **2017,** *5* (21), 1700373.

30. Chen, Z.; Wang, Y.; Sun, X.; Xiang, Y.; Hu, Y.; Jiang, J.; Feng, J.; Sun, Y.-Y.; Wang, X.; Wang, G.-C.; Lu, T.-M.; Gao, H.; Wertz, E. A.; Shi, J., Remote Phononic Effects in Epitaxial Ruddlesden–Popper Halide Perovskites. *J. Phys. Chem. A.* **2018,** *9* (23), 6676-6682.

31. Wang, Y.; Shi, Y.; Xin, G.; Lian, J.; Shi, J., Two-Dimensional van der Waals Epitaxy Kinetics in a Three-Dimensional Perovskite Halide. *Cryst. Growth Des.* **2015,** *15* (10), 4741-4749.

32. Yang, T.; Wang, X.; Zheng, B.; Qi, Z.; Ma, C.; Fu, Y.; Fu, Y.; Hautzinger, M. P.; Jiang, Y.; Li, Z.; Fan, P.; Li, F.; Zheng, W.; Luo, Z.; Liu, J.; Yang, B.; Chen, S.; Li, D.; Zhang, L.; Jin, S.; Pan, A., Ultrahigh-Performance Optoelectronics Demonstrated in Ultrathin Perovskite-Based Vertical Semiconductor Heterostructures. *ACS Nano* **2019,** *13* (7), 7996-8003.

33. Erkılıç, U.; Solís-Fernández, P.; Ji, H. G.; Shinokita, K.; Lin, Y.-C.; Maruyama, M.; Suenaga, K.; Okada, S.; Matsuda, K.; Ago, H., Vapor Phase Selective Growth of Two-Dimensional Perovskite/WS_2 Heterostructures for Optoelectronic Applications. *ACS Appl. Mater. Interfaces* **2019,** *11* (43), 40503-40511.

34. Lin, D.; Zhang, T.; Wang, J.; Long, M.; Xie, F.; Chen, J.; Wu, B.; Shi, T.; Yan, K.; Xie, W.; Liu, P.; Xu, J., Stable and scalable 3D-2D planar heterojunction perovskite solar cells via vapor deposition. *Nano Energy* **2019,** *59*, 619-625.

35. La-Placa, M.-G.; Gil-Escrig, L.; Guo, D.; Palazon, F.; Savenije, T. J.; Sessolo, M.; Bolink, H. J., Vacuum-Deposited 2D/3D Perovskite Heterojunctions. *ACS Energy Lett.* **2019,** *4* (12), 2893-2901.

36. Leyden, M. R.; Ono, L. K.; Raga, S. R.; Kato, Y.; Wang, S.; Qi, Y., High performance perovskite solar cells by hybrid chemical vapor deposition. *J. Mater. Chem. A* **2014,** *2* (44), 18742-18745.

37. Leyden, M. R.; Lee, M. V.; Raga, S. R.; Qi, Y., Large formamidinium lead trihalide perovskite solar cells using chemical vapor deposition with high reproducibility and tunable chlorine concentrations. *J. Mater. Chem. A* **2015,** *3* (31), 16097-16103.

38. Zhang, L.; Zhang, X.; Lu, G., Band Alignment in Two-Dimensional Halide Perovskite Heterostructures: Type I or Type II? *J. Phys. Chem. A.* **2020,** *11* (8), 2910-2916.

39. Zhang, X.; Ji, C.; Liu, X.; Wang, S.; Li, L.; Peng, Y.; Yao, Y.; Hong, M.; Luo, J., Solution-Grown Large-Sized Single-Crystalline 2D/3D Perovskite Heterostructure for Self-Powered Photodetection. *Adv. Opt. Mater.* **2020,** *8* (19), 2000311.

40. Liu, J.; Leng, J.; Wu, K.; Zhang, J.; Jin, S., Observation of Internal Photoinduced Electron and Hole Separation in Hybrid Two-Dimentional Perovskite Films. *J. Am. Chem. Soc.* **2017,** *139* (4), 1432-1435.

41. Fu, Y.; Zheng, W.; Wang, X.; Hautzinger, M. P.; Pan, D.; Dang, L.; Wright, J. C.; Pan, A.; Jin, S., Multicolor Heterostructures of Two-Dimensional Layered Halide Perovskites that Show Interlayer Energy Transfer. *J. Am. Chem. Soc.* **2018,** *140* (46), 15675-15683.

42. Yuan, M.; Quan, L. N.; Comin, R.; Walters, G.; Sabatini, R.; Voznyy, O.; Hoogland, S.; Zhao, Y.; Beauregard, E. M.; Kanjanaboos, P.; Lu, Z.; Kim, D. H.; Sargent, E. H., Perovskite energy funnels for efficient light-emitting diodes. *Nat. Nanotechnology* **2016,** *11* (10), 872-877.

43. Zhou, N.; Ouyang, Z.; Hu, J.; Williams, O. F.; Yan, L.; You, W.; Moran, A. M., Distinguishing Energy- and Charge-Transfer Processes in Layered Perovskite Quantum Wells with Two-Dimensional Action Spectroscopies. *J. Phys. Chem. A.* **2020,** *11* (12), 4570-4577.

44. Saidaminov, M. I.; Abdelhady, A. L.; Murali, B.; Alarousu, E.; Burlakov, V. M.; Peng, W.; Dursun, I.; Wang, L.; He, Y.; Maculan, G.; Goriely, A.; Wu, T.; Mohammed, O. F.; Bakr, O. M., High-quality bulk hybrid perovskite single crystals within minutes by inverse temperature crystallization. *Nat. Commun.* **2015,** *6* (1), 7586.

45. Jo, M.; Sato, M.; Miyamura, S.; Sasakura, H.; Kumano, H.; Suemune, I., Origin of the blueshift of photoluminescence in a type-II heterostructure. *Nanoscale Res. Lett.* **2012,** *7* (1), 654.

46. Alonso-Álvarez, D.; Alén, B.; García, J. M.; Ripalda, J. M., Optical investigation of type II GaSb⁄GaAs self-assembled quantum dots. *Appl. Phys. Lett.* **2007,** *91* (26), 263103.

47. Ledentsov, N. N.; Ustinov, V. M.; Shchukin, V. A.; Kop'ev, P. S.; Alferov, Z. I.; Bimberg, D., Quantum dot heterostructures: Fabrication, properties, lasers (Review). *Semiconductors* **1998,** *32* (4), 343-365.

48. Klenovský, P.; Steindl, P.; Geffroy, D., Excitonic structure and pumping power dependent emission blue-shift of type-II quantum dots. *Sci. Rep.* **2017,** *7* (1), 45568.

49. Berney, C.; Danuser, G., FRET or No FRET: A Quantitative Comparison. *Biophys.* **2003,** *84* (6), 3992-4010.

50. Schröder, G. F.; Alexiev, U.; Grubmüller, H., Simulation of Fluorescence Anisotropy Experiments: Probing Protein Dynamics. *Biophys.* **2005,** *89* (6), 3757-3770.

51. Euvrard, J.; Yan, Y.; Mitzi, D. B., Electrical doping in halide perovskites. *Nat. Rev. Mater.* **2021,** *6* (6), 531-54

Appendix A. Supporting Information for Chapter 2 Two-Dimensional Lead Halide Perovskites Templated by a Conjugated Asymmetric Diammonium*

Equations used to calculate Quadratic Elongation ($\langle\lambda\rangle$) and Bond angle variance (σ^2).[1-2]

Equation A.1: Quadratic Elongation ($\langle\lambda\rangle$)

$$\langle\lambda\rangle = \frac{1}{6}\sum_{\{i=1\}}^{6}\left(\frac{d_i}{d_o}\right)^2$$

Where d_i is the Pb-X bond length, d_o is the Pb-X bond length from an ideal octahedron of the same volume, $\langle\lambda\rangle$ is dimensionless.

Equations A.2: Bond angle variance (σ^2)

$$\sigma^2 = \frac{1}{11}\sum_{\{i=1\}}^{12}(\alpha_i - 90)^2$$

Where α_i is the Pb-X-Pb bond angles of the octahedra.

* This chapter was originally published in *Inorg. Chem.*, **2017**, 56, 24, 14991−14998 in collaboration with J. Dai, Y. Ji, Y. Fu, J. Chen, I.A. Guzei, J.C. Wright, Y. Li, and S. Jin

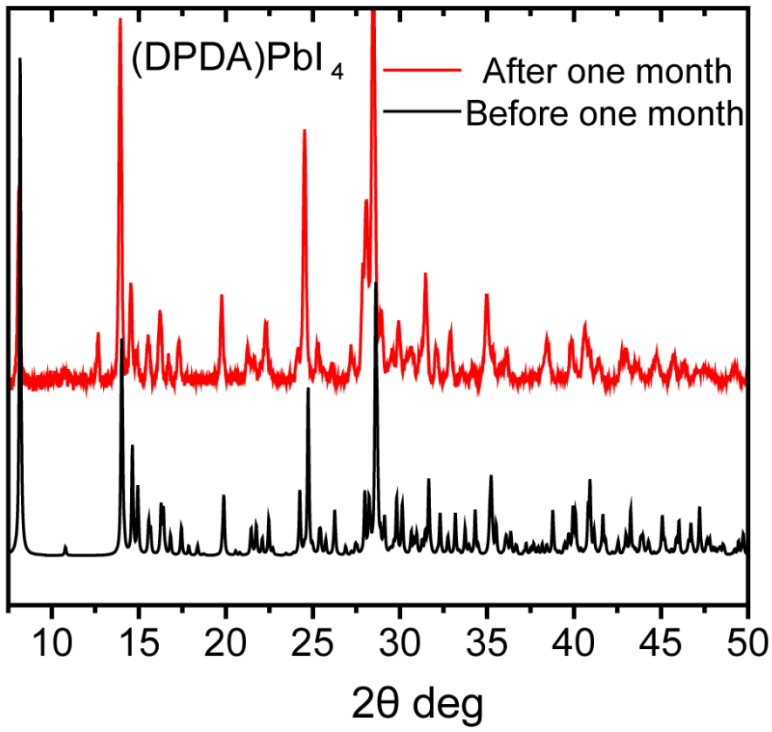

Figure A.1. PXRD patterns of (DPDA)PbI_4 powders (crushed from single crystals) before and after one month of storage in ambient conditions.

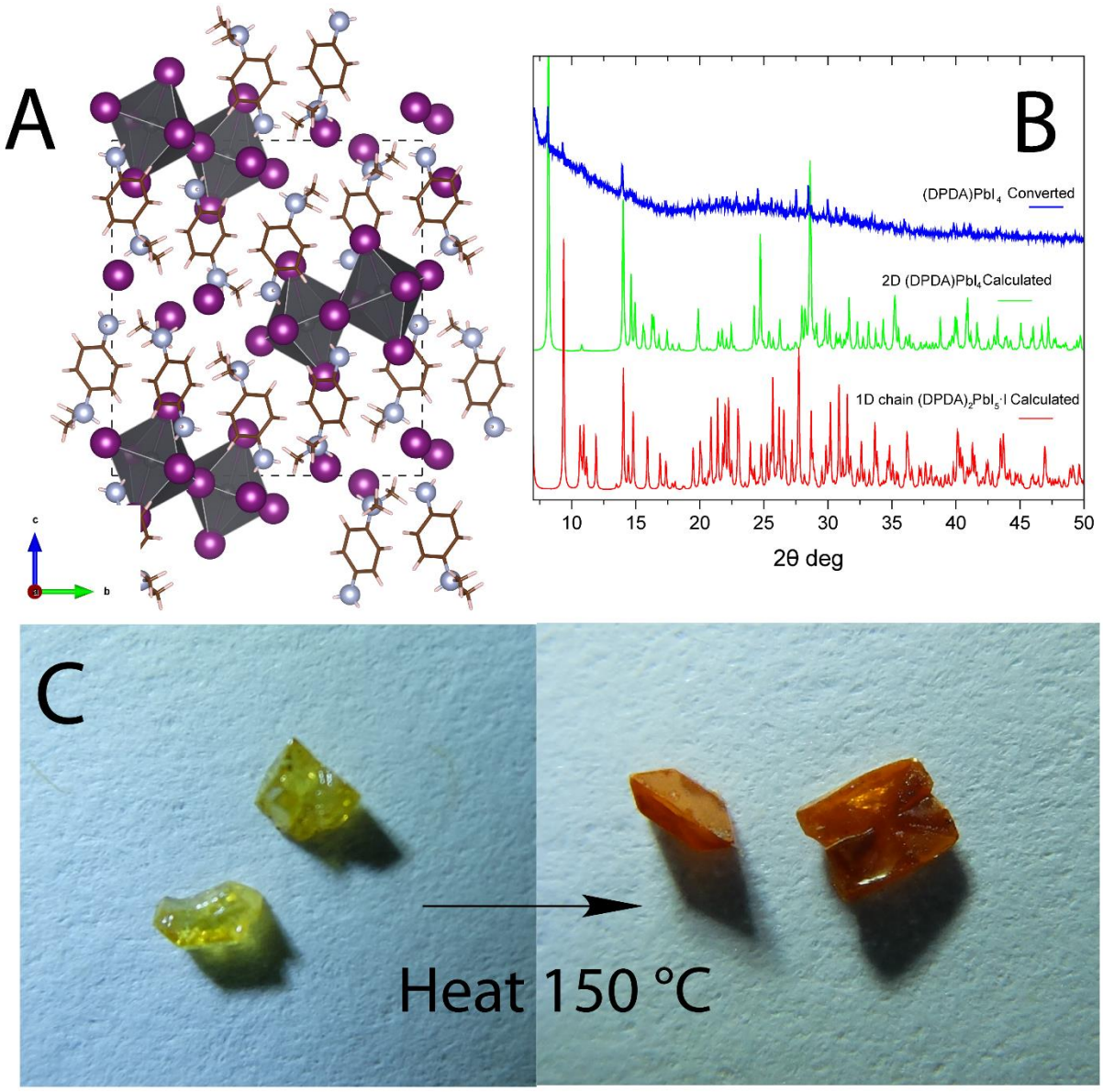

Figure A.2. (A) Crystal structure of $(DPDA)_2PbI_5 \cdot I$ showing 1D corner sharing chains. Upon heating, these crystals turned from yellow to red (C) and showed peaks of the 2DN perovskite in the PXRD pattern (B) indicating partial degradation/conversion to the 2DN layered compound.

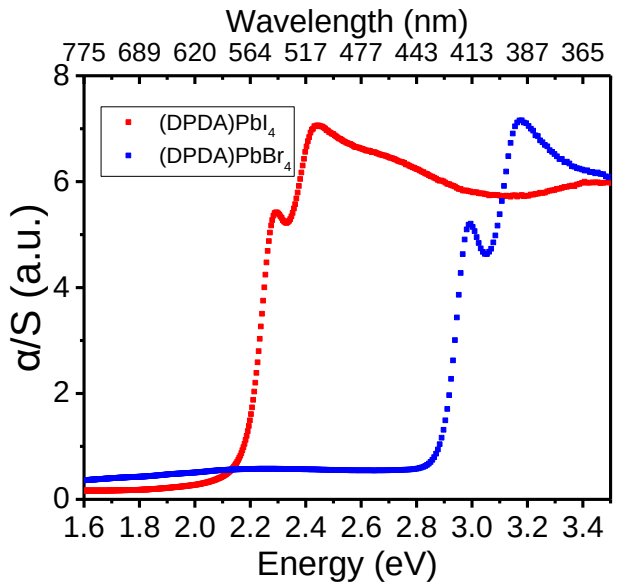

Figure A.3. Reflectance spectroscopy of bulk powders of (DPDA)PbI_4 and (DPDA)$PbBr_4$.

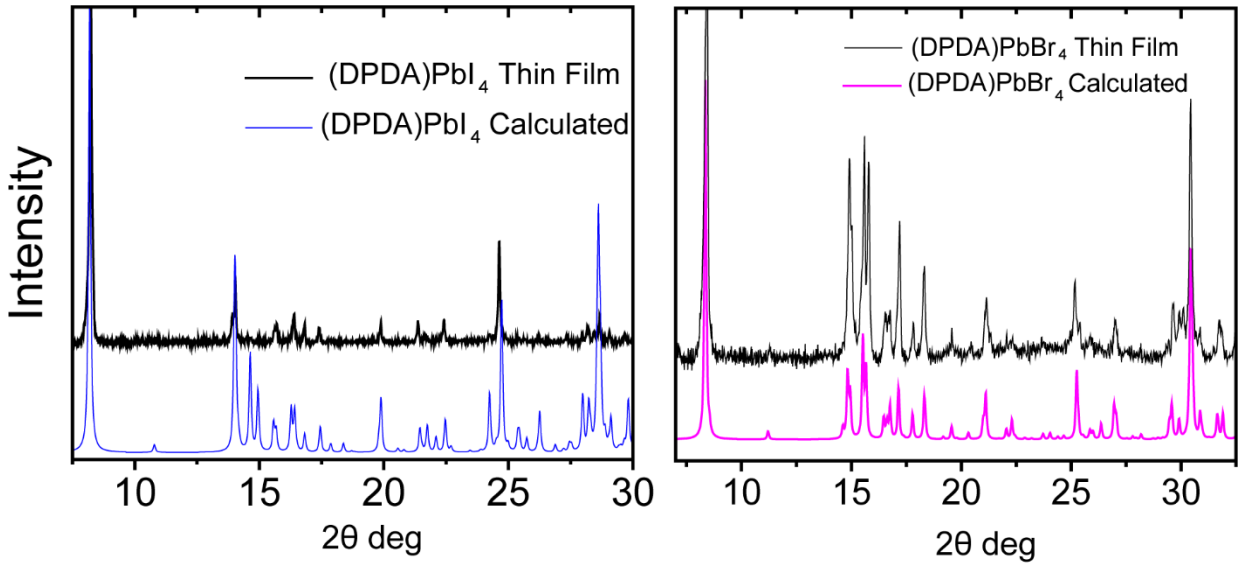

Figure A.4. PXRD patterns of the spin coated thin films of (A) (DPDA)PbI_4 and (B) (DPDA)$PbBr_4$ in comparison with their respective calculated patterns from single crystal structures.

Appendix A. References

1. Robinson, K.; Gibbs, G. V.; Ribbe, P. H., Quadratic elongation: a quantitative measure of distortion in coordination polyhedra. *Science* **1971,** *172*, 567.
2. Brese, N. E.; O'Keeffe, M., Bond-valence parameters for solids. *Acta Crystallogr., Sect. B* **1991,** *47*, 192-197.

Appendix B. Supporting Information for Chapter 3 Incorporating Large A-Cations into Lead Iodide Perovskite Cages: Relaxed Goldschmidt Tolerance Factor and Impact on Exciton-Phonon Interaction*

Table B.1. Experimental parameters for the synthesis of various $(HA)_2(A)Pb_2I_7$.

	Conc ($APbI_3$)	Vol ($APbI_3$)	Vol (HAI)	Vol ($CHCl_3$)
$(HA)_2(MA)Pb_2I_7$	0.5 M	10 μL	40 μL	0.6 mL
$(HA)_2(FA)Pb_2I_7$	0.5 M	10 μL	30 μL	0.3 mL
$(HA)_2(DMA)Pb_2I_7$	0.67 M	10 μL	40 μL	0.4 mL [a] + 0.15 mL
$(HA)_2(EA)Pb_2I_7$	0.5 M	10 μL	10 μL	0.3 mL
$(HA)_2(GA)Pb_2I_7$	1.0 M	10 μL	30 μL	0.6 mL
$(HA)_2(AA)Pb_2I_7$	0.5 M	10 μL	22.5 μL	0.3 mL[a] + 0.2 mL

Note, the concentration of HAI solution in DMF is 2 M. [a] The initial precipitate after adding the first portion of chloroform was isolated and discarded, as it also contains non-perovskite phase.

Table B.2. Experimental parameters for preparing suspended solutions of various $(HA)_2(A)Pb_2I_7$.

	Conc ($APbI_3$)	Vol ($APbI_3$)	Vol (HAI)	Vol ($CHCl_3$)
$(HA)_2(MA)Pb_2I_7$	0.5 M	10 μL	40 μL	0.4 mL

* This appendix was originally made available online as the Supporting Information for *ACS Cent. Sci.*, **2019**, 5, 8, 1377-1386 in collaboration with Y. Fu, Z. Luo, F. Wang, M.M. Aristov, D. Pan, I.A. Guzei, A. Pan, X-Y. Zhu, and S. Jin

$(HA)_2(FA)Pb_2I_7$	0.5 M	10 μL	30 μL	0.3 mL
$(HA)_2(DMA)Pb_2I_7$	0.67 M	10 μL	40 μL	0.2 mL
$(HA)_2(EA)Pb_2I_7$	0.5 M	10 μL	10 μL	0.3 mL
$(HA)_2(GA)Pb_2I_7$	1.0 M	10 μL	30 μL	0.6 mL
$(HA)_2(AA)Pb_2I_7$	0.5 M	10 μL	22.5 μL	0.3 mL

Note, after centrifugation, 10 μL of top clean solution was added into ~2 mL chloroform to obtain suspended solutions of $(HA)_2(A)Pb_2I_7$ for absorption measurement.

Equations used to calculate Quadratic Elongation ($\langle\lambda\rangle$) and Bond angle variance (σ^2).[1]

Equation B.1: Quadratic Elongation ($\langle\lambda\rangle$)

$$\langle\lambda\rangle = \frac{1}{6}\sum_{\{i=1\}}^{6}\left(\frac{d_i}{d_o}\right)^2$$

Where d_i is the Pb-I bond length, d_o is the Pb-I bond length from an ideal octahedron of the same volume, $\langle\lambda\rangle$ is dimensionless.

Equations B.2: Bond angle variance (σ^2)

$$\sigma^2 = \frac{1}{11}\sum_{\{i=1\}}^{12}(\alpha_i - 90)^2$$

Where α_i is the I-Pb-I bond angles of the octahedra.

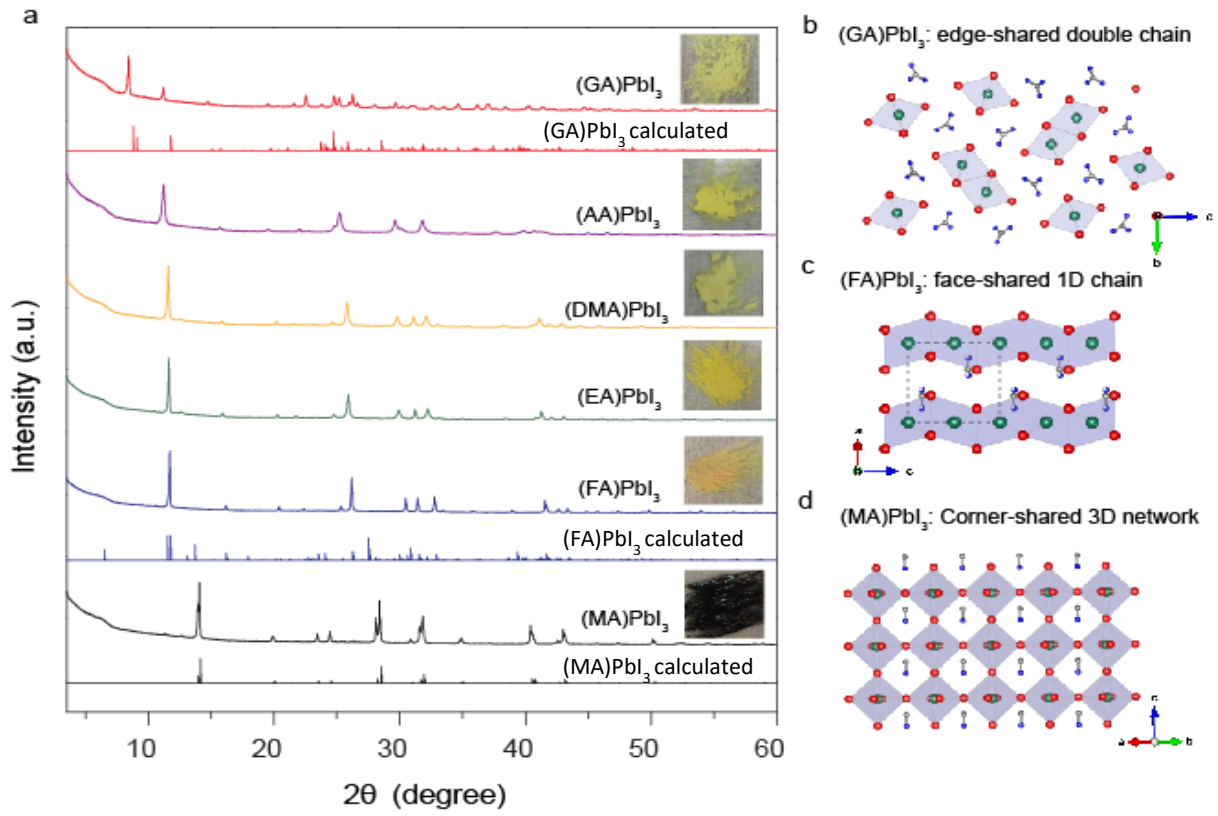

Figure B.1. (a) PXRD patterns of non-perovskites of $APbI_3$ with various A cations prepared by antisolvent growth, together with the standard PXRD patterns of $GAPbI_3$ (non-perovskite phase), hexagonal $FAPbI_3$ (non-perovskite phase), and tetragonal $MAPbI_3$ (perovskite phase). Insets are photographs of various $APbI_3$ powders on glass slides. The crystal packing diagrams of (b) $GAPbI_3$ with edge-shared connection (crystallographic data in Table B.6), (c) hexagonal $FAPbI_3$ with face-shared connection,[2] and (d) tetragonal $MAPbI_3$ perovskite[2] with corner-shared connection.

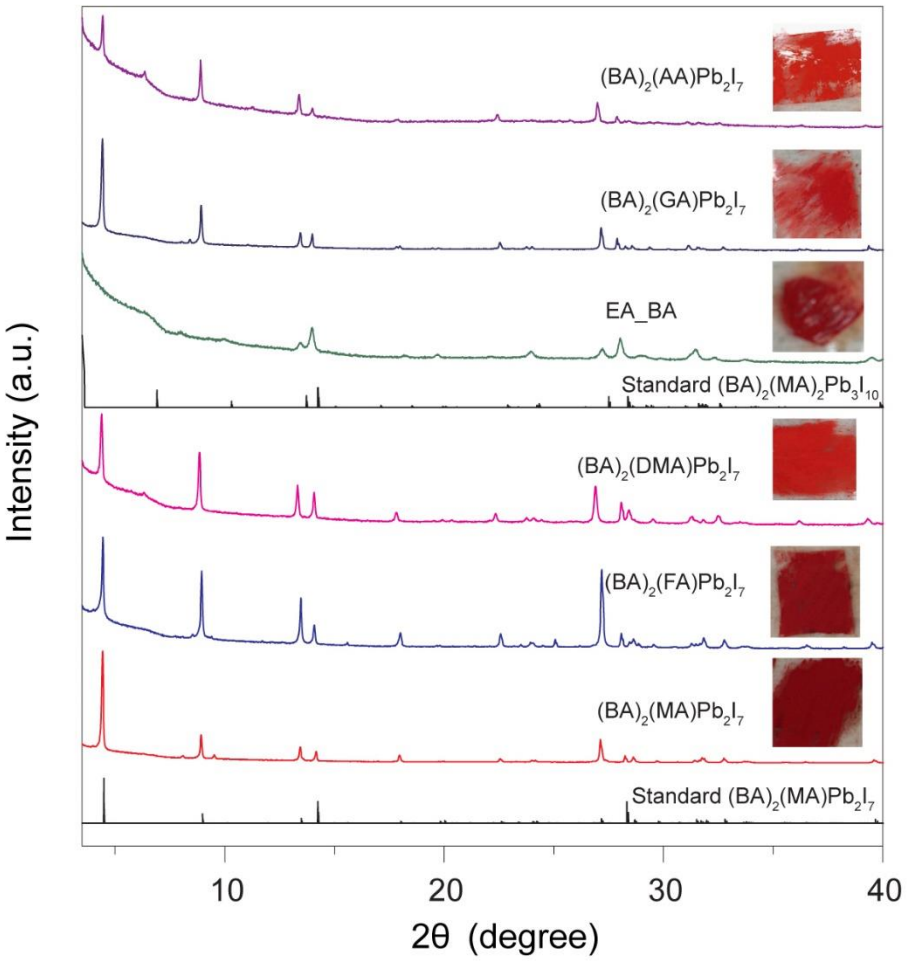

Figure B.2. PXRD patterns of the $(BA)_2(A)Pb_2I_7$ with the various A cations prepared by antisolvent growth of $APbI_3$ with excessive *n*-butylammonium iodide (BAI), in comparison with the standard PXRD of $(BA)_2(MA)Pb_2I_7$ and $(BA)_2(MA)_2Pb_3I_{10}$.[3] The results show that the Goldschmidt tolerance factor relaxation is general in 2D RP structures with different LA cations. The PXRD pattern for the case of EA and BA cations is very different from those of other A-site cations, which suggests this product is not a (pure) $n = 2$ perovskite structure. Instead, the pattern seems to be more similar to that of $(BA)_2(MA)_2Pb_3I_{10}$, and the diffraction peaks just slightly shift to lower angle. The color of the powder appears to be the darkest (suggesting the smallest bandgap). These suggest the possible formation of higher-*n* (i.e. $n > 2$) structures for the EA cation.

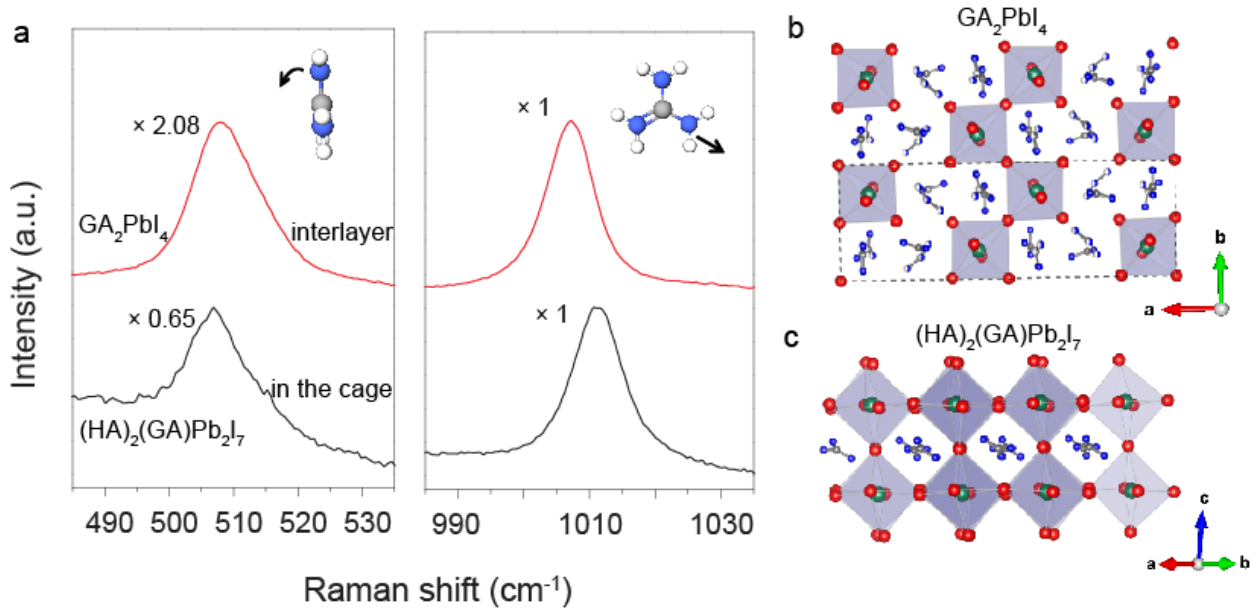

Figure B.3. (a) Raman spectra of $(HA)_2(GA)Pb_2I_7$ and $(GA)_2PbI_4$ single crystals, showing the different vibrational behaviors of GA cations in the cage and gallery. (b) The crystal structure of $(GA)_2PbI_4$ with GA cation in the gallery.[4] (c) The crystal structure of $(HA)_2(GA)Pb_2I_7$ with GA cation in the perovskite cage.

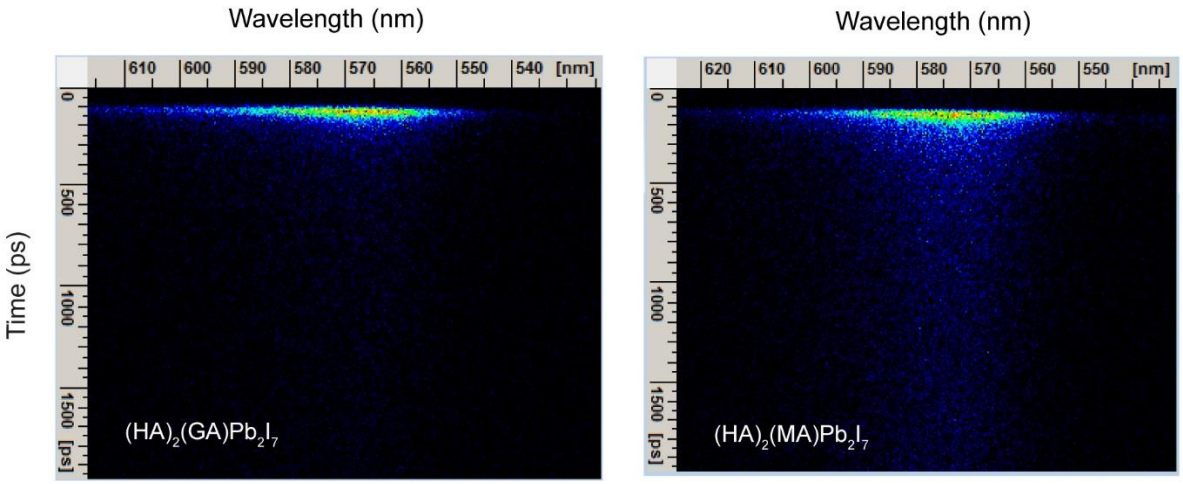

Figure B.4. 2D pseudo-colour plots of the TRPL spectra of $(HA)_2(GA)Pb_2I_7$ and $(HA)_2(MA)Pb_2I_7$ single crystals.

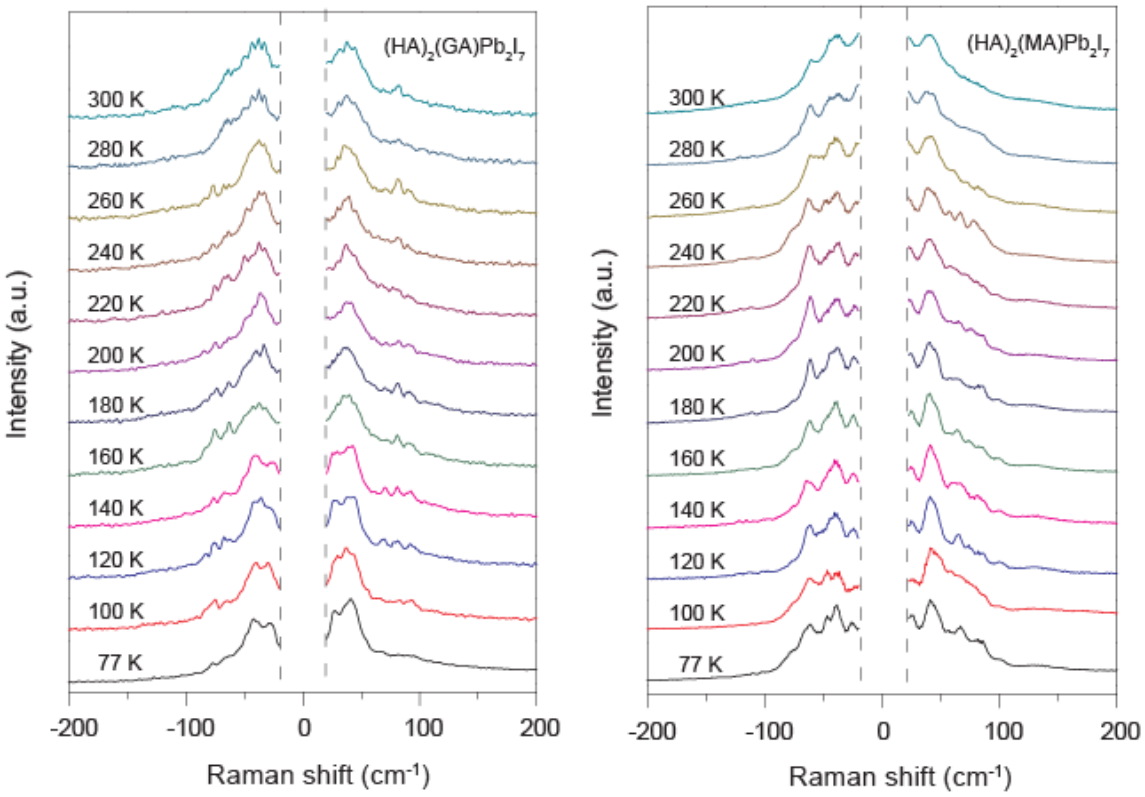

Figure B.5. Temperature-dependent low-frequency Raman spectra of $(HA)_2(GA)Pb_2I_7$ and $(HA)_2(MA)Pb_2I_7$ single crystals from 77 K to 300 K. Representative curves at 3 temperatures are highlighted in Figure 4a,b in the main text.

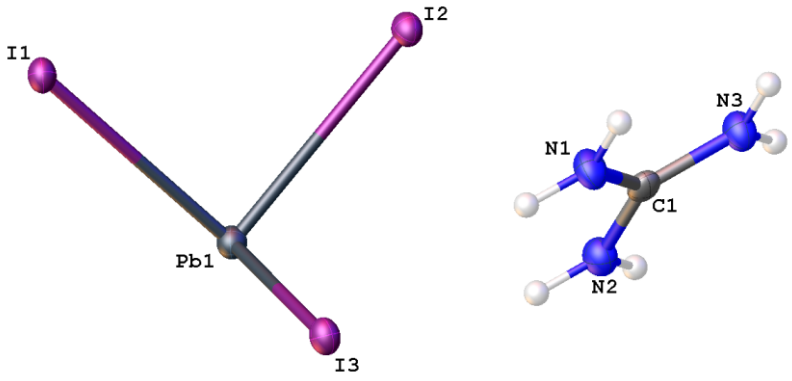

Figure B.6. A molecular drawing of the asymmetric unit of $GAPbI_3$ shown with 50% probability ellipsoids.

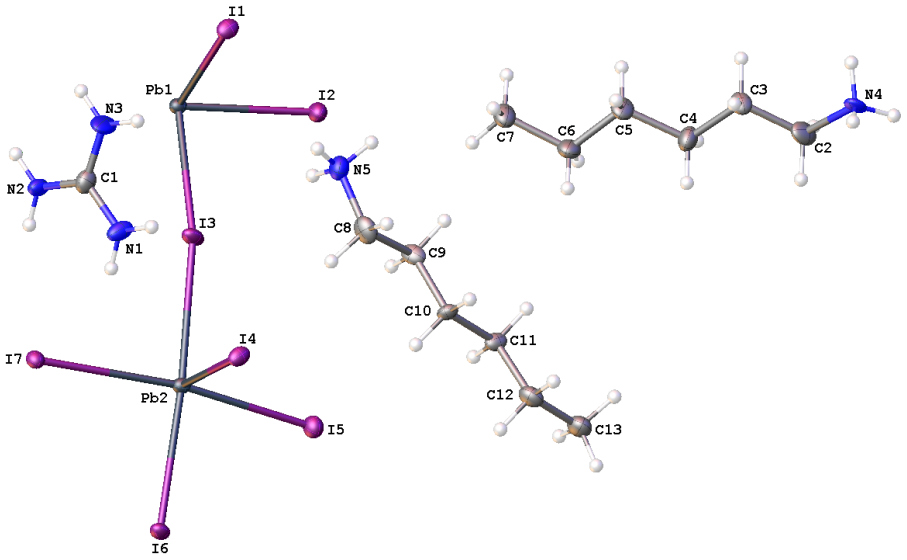

Figure B.7. A molecular drawing of the asymmetric unit of $(HA)_2(GA)Pb_2I_7$ shown with 50% probability ellipsoids. Only one disorder component at N5 is shown.

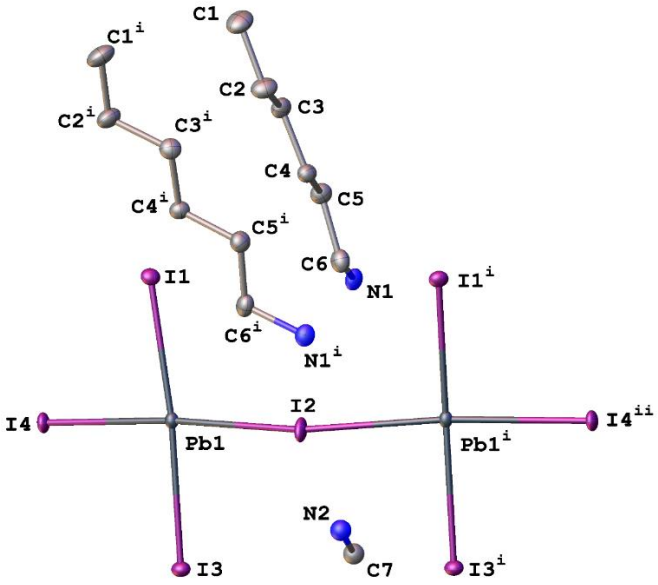

Figure B.8. A molecular drawing of the asymmetric unit of $(HA)_2(MA)Pb_2I_7$ shown with 50% probability ellipsoids except for the methylammonium. All H atoms are omitted.

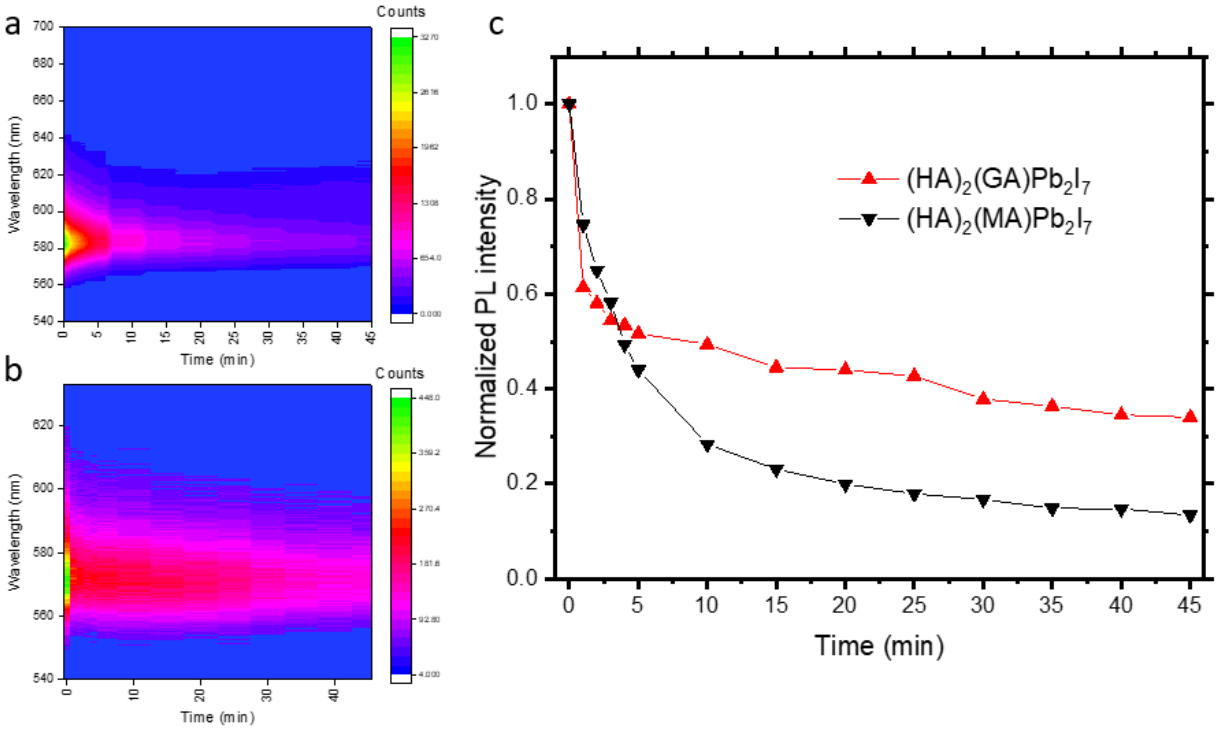

Figure B.9. Evolution of PL spectra of (a) $(HA)_2(GA)Pb_2I_7$ and (b) $(HA)_2(MA)Pb_2I_7$ single crystals collected under constant laser illumination ($\lambda_{ex} = 532\,nm$, 9 mW/cm^2) in ambient conditions. (c) Plot of PL intensity (at λ_{max}) vs. time, demonstrating that $(HA)_2(GA)Pb_2I_7$ is slightly more stable under illumination (34% initial intensity (GA) vs. 13% initial intensity (MA)).

Table B.3. Complete crystal data and structure refinement details of $(HA)_2(MA)Pb_2I_7$ and $(HA)_2(GA)Pb_2I_7$.

Compound name	$(HA)_2(MA)Pb_2I_7$	$(HA)_2(GA)Pb_2I_7$
Empirical formula	$(C_6H_{13}NH_3)_2(CH_3NH_3)Pb_2I_7$	$(C_6H_{13}NH_3)_2[C(NH_2)_3]Pb_2I_7$
Formula weight	665.04	1567.16
Crystal system	monoclinic	triclinic
Space group	*C*2/*c*	*P-1*
a/Å; α/°	45.146(16) ; 90	8.8195(14); 79.965(13)
b/Å; β/°	8.814(3); 100.030(5)	9.0300(15); 87.341(9)

c/Å; γ/°	8.695(3); 90	21.699(4); 89.986(10)
Volume/Å^3	3407(2) Å^3	1699.8(5)
Z	4	2
Temperature (K)	99.99	99.92
ρ_{calc}, g/cm^3	3.000	3.062
Absorption Coefficient μ/mm^{-1}	16.217	16.259
F(000)	2688	1372
2Θ range for data collection/°	3.664 to 55.148	1.908 to 53.004
Index ranges	$-58 \leq h \leq 58$, $-11 \leq k \leq 11$, $-11 \leq l \leq 11$	$-11 \leq h \leq 11$, $-11 \leq k \leq 10$, $-27 \leq l \leq 27$
Reflections collected	61721	28779
Independent reflections	3931 [R_{int} = 0.0456, R_{sigma} = 0.0170]	28779 [R_{int} = 0.0390, R_{sigma} = 0.0463]
Data/restraints/parameters	3931/2/125	28779/105/298
Goodness-of-fit on F^2	1.061	1.047
Final R indexes [I>=2σ (I)]	R_1 = 0.0211, wR_2 = 0.0497	R_1 = 0.0315, wR_2 = 0.0886
Final R indexes [all data]	R_1 = 0.0241, wR_2 = 0.0509	R_1 = 0.0335, wR_2 = 0.0928
Largest diff. peak/hole / e Å^{-3}	2.36/-1.32	2.40/-1.74

Table B.4. Comparison of the perovskite cage volume of $(HA)_2(GA)Pb_2I_7$ with all previously reported 2D RP lead iodide perovskites with $n = 2$.

Structure	Temp. (K)	Cage volume (Å^3)	Pb-I-Pb angle (a,b) (°)	Pb-I-Pb angle (c) (°)	Pb-plane to Pb-plane (cage)	
					(a,b axis)(Å)	(c-axis) (Å)
$(HA)_2(GA)PbI_7$ (this work)	100	**264.44**	162.62, 161.42	178.87	6.29, 6.31	6.66
$(HA)_2(MA)Pb_2I_7$ (this work)	100	250.25	155.73	179.23	6 6.20	6.52
$(HO_2C(CH_2)_3NH_3)_2(MA)Pb_2I_7$ [5]	293	256.94	160.22, 159.75	179.94	6.41, 6.33	6.49
$(CH_3C_6H_4CH_2NH_3)_2(MA)Pb_2I_7$ [6]	295	252.36	155.39, 158.86	178.28	6.22	6.52
$(C_5H_{11}NH_3)_2(MA)Pb_2I_7$ [7]	300	257.35	164.31	164.05	6.301724	6.48
$(CH_3(CH_2)_3NH_3)_2(MA)Pb_2I_7$ [3]	293	256.82	164.2, 173.1	165.64	6.30, 6.29	6.48
$(C_4H_3SCH_2NH_3)_2MAPb_2I_7$[8]	293	252.96	154.50, 157.97	178.37	6.24, 6.53	6.21

Table B.5. Comparison of the average PL lifetimes of $(HA)_2(GA)Pb_2I_7$ and $(HA)_2(MA)Pb_2I_7$.

GA #	$A_1\tau_1 + A_2\tau_2(ps)$	MA #	$A_1\tau_1 + A_2\tau_2(ps)$
1	41	1	124
2	57	2	119
3	58	3	111
4	52	4	109
5	49	5	109
6	62	6	111
7	60	7	104
Average	54 ± 7		114 ± 6

Table B.6. Complete crystal data and structure refinement details of $(GA)PbI_3$.

Compound name	$(GA)PbI_3$
Empirical formula	$[C(NH_2)_3]PbI_3$
Formula weight	647.98
Crystal system	monoclinic
Space group	$P2_1/n$
a/Å; α/°	4.5694(12); 90
b/Å; β/°	11.748(3); 94.147(14)
c/Å; γ/°	19.504(4); 90
Volume/Å^3	1044.2(4)
Z	4
Temperature (K)	100.0
ρ_{calc}, g/cm^3	4.122
Absorption Coefficient μ/mm^{-1}	24.961
F(000)	1096.0
2Θ range for data collection/°	4.05 to 55
Index ranges	$-5 \leq h \leq 5$, $-15 \leq k \leq 15$, $-25 \leq l \leq 25$
Reflections collected	31655
Independent reflections	2393 [R_{int} = 0.0357, R_{sigma} = 0.0141]
Data/restraints/parameters	2393/0/73
Goodness-of-fit on F^2	1.389
Final R indexes [I>=2σ (I)]	R_1 = 0.0233, wR_2 = 0.0523
Final R indexes [all data]	R_1 = 0.0234, wR_2 = 0.0523
Largest diff. peak/hole / e Å^{-3}	1.31/-1.04

Appendix B. References

1. Brese, N. E.; O'Keeffe, M. Bond-Valence Parameters for Solids. *Acta Cryst. B* **1991**, *47*,192-197.

2. Stoumpos, C. C.; Malliakas, C. D.; Kanatzidis, M. G. Semiconducting Tin and Lead Iodide Perovskites with Organic Cations: Phase Transitions, High Mobilities, and Near-Infrared Photoluminescent Properties. *Inorg. Chem.* **2013**, *52*, 9019-9038.

3. Stoumpos, C. C.; Cao, D. H.; Clark, D. J.; Young, J.; Rondinelli, J. M.; Jang, J. I.; Hupp, J. T.; Kanatzidis, M. G. Ruddlesden–Popper Hybrid Lead Iodide Perovskite 2D Homologous Semiconductors. *Chem. Mater.* **2016**, *28*, 2852-2867.

4. Michael, D.; Christoph, H.; Harald, H. Synthesis, Crystal Structures, Optical Properties, and Phase Transitions of the Layered Guanidinium-Based Hybrid Perovskites $[C(NH_2)_3]_2MI_4$; M = Sn, Pb. *Eur. J. Inorg. Chem.* **2017**, *2017*,1120-1126

5. Mercier, N. $(HO_2C(CH_2)_3NH_3)_2(CH_3NH_3)Pb_2I_7$: A Predicted Non-Centrosymmetrical Structure Built up from Carboxylic Acid Supramolecular Synthons and Bilayer Perovskite Sheets. *CrystEngComm* **2005**, *7,* 429-432.

6. Papavassiliou G. C.; C. P. Raptopouloub, G. A. M.; Terzis, A. Some New Luminescent Compounds Based on 4-MethyIbenzylamine and Lead Halides. *Zeitschrift für Naturforschung* **2000**, *55,* 536-540.

7. Han, S.; Wang, P.; Zhang, J.; Liu, X.; Sun, Z.; Huang, X.; Li, L.; Ji, C.; Zhang, W.; Teng, B.; Hu, W.; Hong, M.; Luo, J. Exploring a Polar Two-dimensional Multi-layered Hybrid Perovskite of $(C_5H_{11}NH_3)_2(CH_3NH_3)Pb_2I_7$ for Ultrafast-Responding Photodetection. *Laser Photonics Rev.* **2018,** *12,* 1800060.

8. Zhu, X-H.; Mercier, N.; Riou, A.; Blanchard, P.; Frere, P. $(C_4H_3SCH_2NH_3)_2(CH_3NH_3)Pb_2I_7$: non-centrosymmetrical crystal structure of a bilayer hybrid perovskite. *Chem. Comm.* **2002,** *18,* 2160-2161.

Appendix C. Supporting Information for Chapter 4

Band Edge Tuning of 2D Ruddlesden-Popper Perovskites by A Cation Size Revealed through Nanoplates*

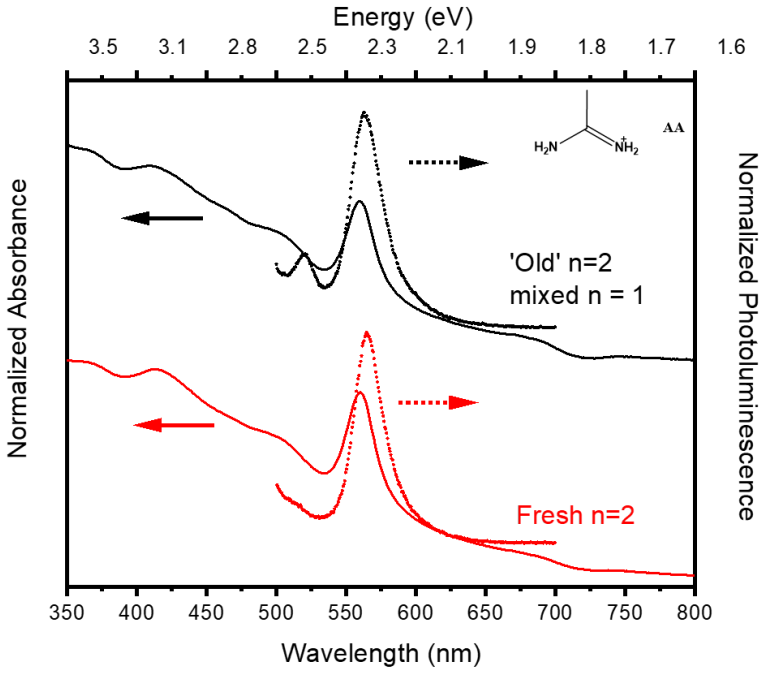

Figure C.1. Absorbance and photoluminescence of $(HA)_2(AA)Pb_2I_7$ nanoplates suspended in toluene showing the degradation with time. 'Old' is on a sample left in solution for 1 day, where a clear peak at 515 nm emerged in the PL, corresponding to the *n=1* $(HA)_2PbI_4$ perovskite.

* This appendix was originally made available online as the Supporting Information for *ACS Energy Lett.* **2020**, 5, 5, 1430-1437 in collaboration with D. Pan, A.K. Pigg, Y. Fu, D.J. Morrow, M. Leng, M. Kuo, N. Spitha, D.P. Lafayette II, D.D. Kohler, J.C. Wright, S. Jin

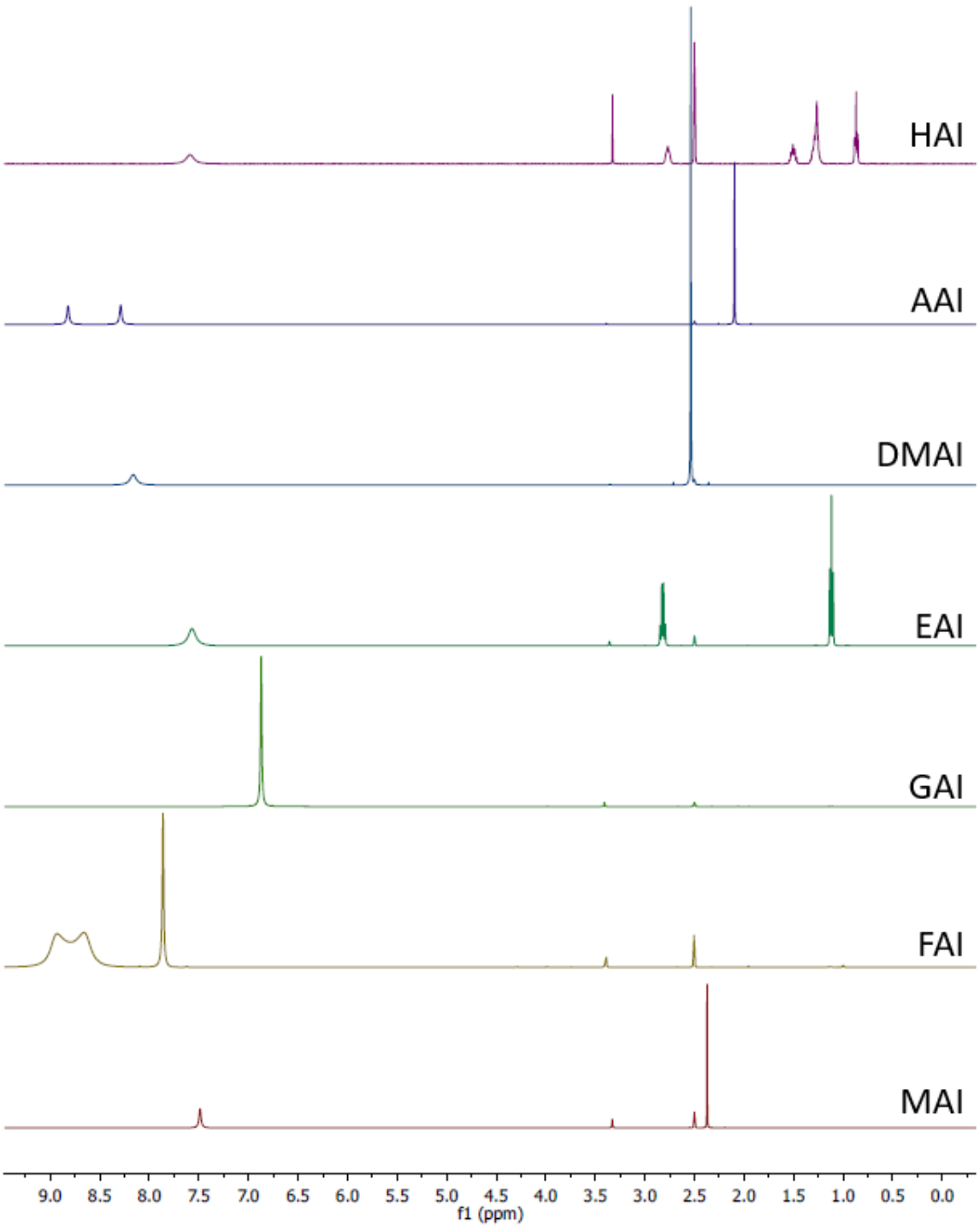

Figure C.2. ^{1}H NMR spectra of the individual A cation iodide salts used in the synthesis. These are used as the comparison spectra for the NMR spectra of RP perovskite samples shown in Figure C.3.

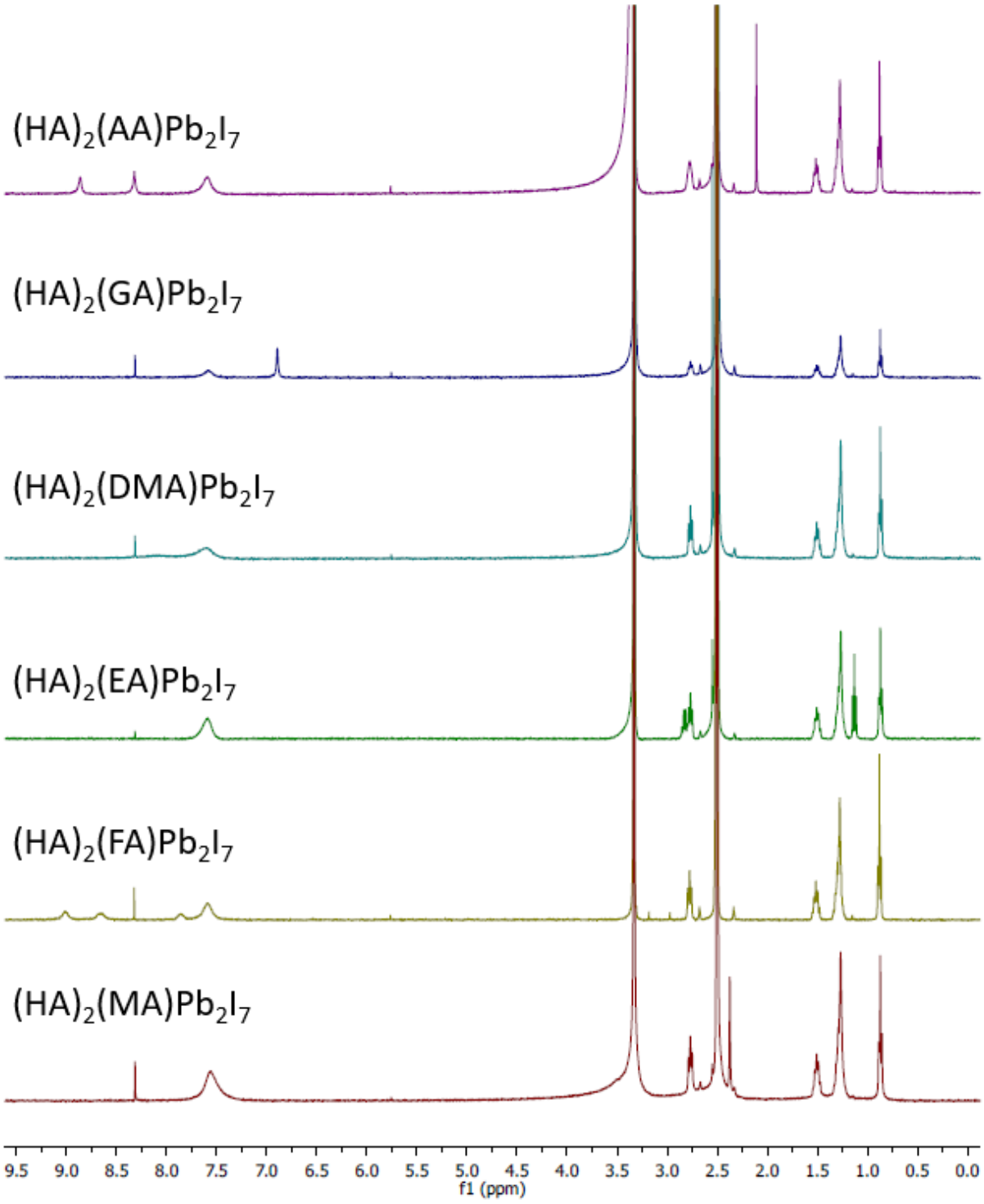

Figure C.3. ^{1}H NMR spectra of the various RP perovskite compounds dissolved in DMSO-d_6. The peak positions, peak areas, and the ratios of HA/A are tabulated in Table C.2

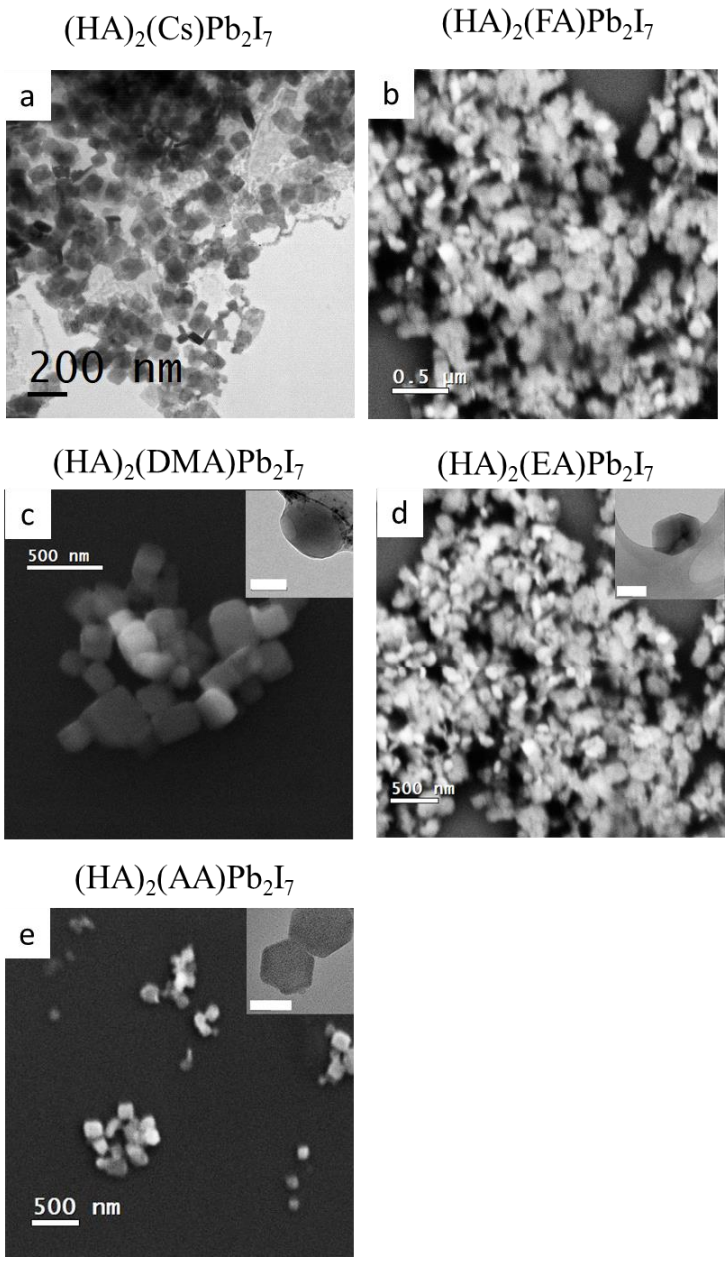

Figure C.4. Additional TEM and SEM images of the various nanoplates. (a) TEM of $(HA)_2(Cs)Pb_2I_7$. (b) SEM of $(HA)_2(FA)Pb_2I_7$. (c,d,e) SEM of $(HA)_2(A)Pb_2I_7$ with A = DMA, EA, AA, respectively, with insets of TEM images (inset scale bar is 100 nm).

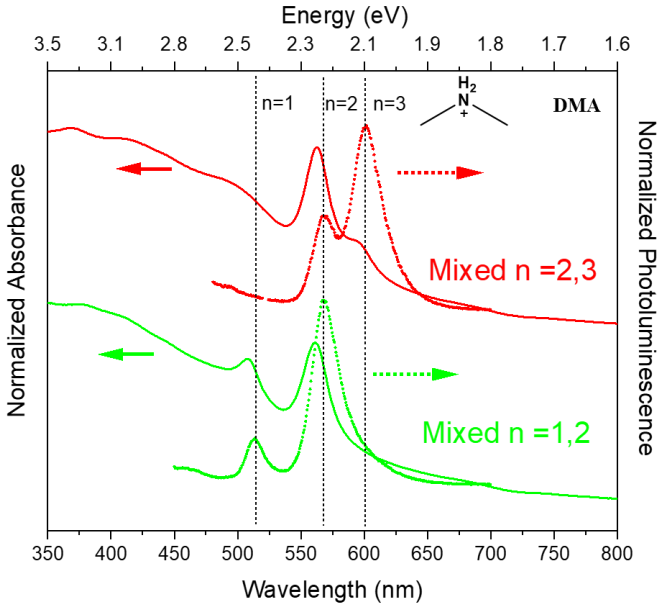

Figure C.5. Absorbance and photoluminescence spectra of $(HA)_2(DMA)_{n-1}Pb_nI_{3n+1}$ products, illustrating the precursor stoichiometry dependence. Mixed n = 2,3 RP perovskites were made by adding less HAI solution (50 μL), and mixed n= 1,2 RP perovskites were made by adding excess HAI (100 μL).

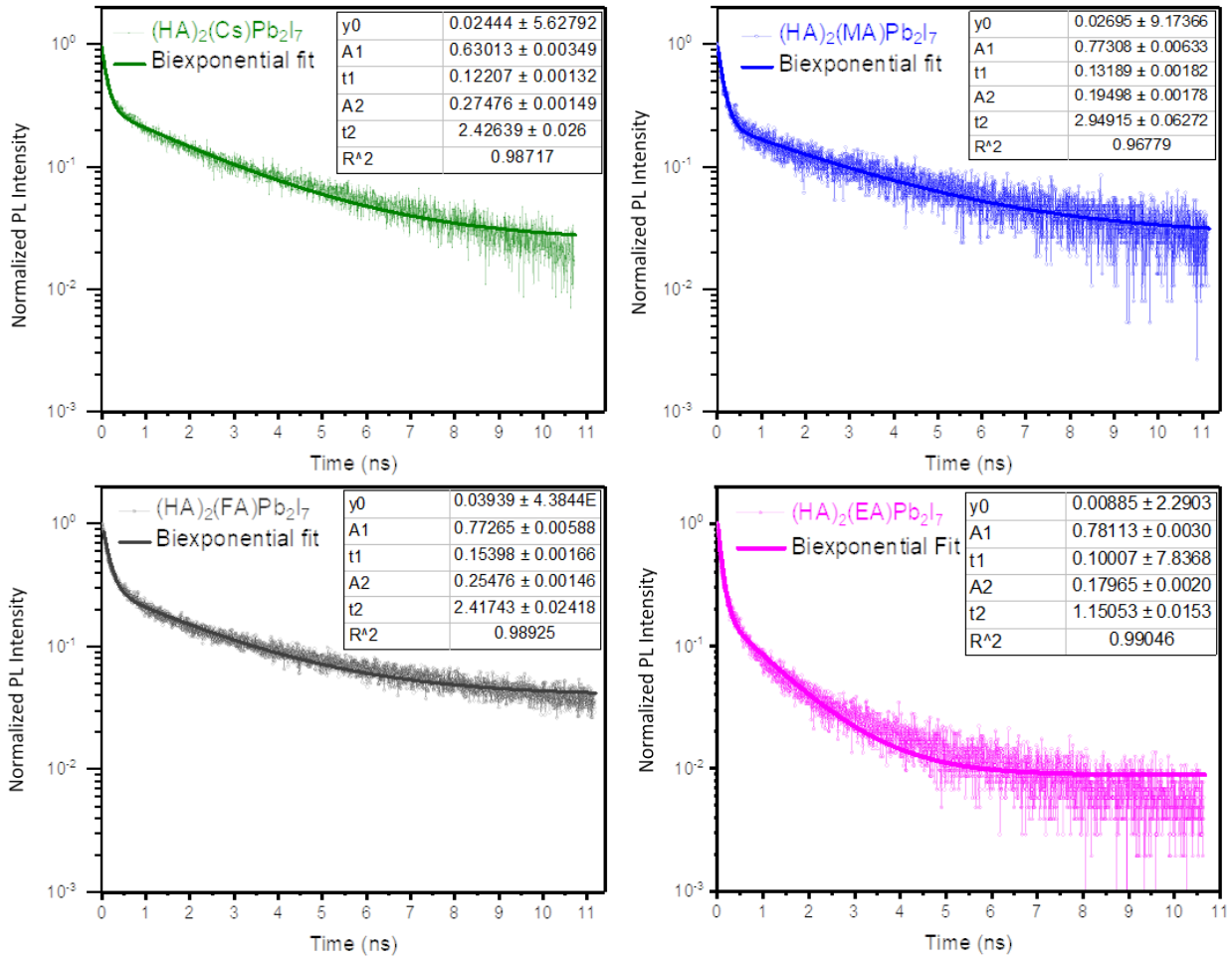
(HA)2(Cs)Pb2I7
Biexponential fit
y0 0.02444 ± 5.62792
A1 0.63013 ± 0.00349
t1 0.12207 ± 0.00132
A2 0.27476 ± 0.00149
t2 2.42639 ± 0.026
R^2 0.98717
(HA)2(MA)Pb2I7
Biexponential fit
y0 0.02695 ± 9.17366
A1 0.77308 ± 0.00633
t1 0.13189 ± 0.00182
A2 0.19498 ± 0.00178
t2 2.94915 ± 0.06272
R^2 0.96779
(HA)2(FA)Pb2I7
Biexponential fit
y0 0.03939 ± 4.3844E
A1 0.77265 ± 0.00588
t1 0.15398 ± 0.00166
A2 0.25476 ± 0.00146
t2 2.41743 ± 0.02418
R^2 0.98925
(HA)2(EA)Pb2I7
Biexponential Fit
y0 0.00885 ± 2.2903
A1 0.78113 ± 0.0030
t1 0.10007 ± 7.8368
A2 0.17965 ± 0.0020
t2 1.15053 ± 0.0153
R^2 0.99046
Normalized PL Intensity
Time (ns)

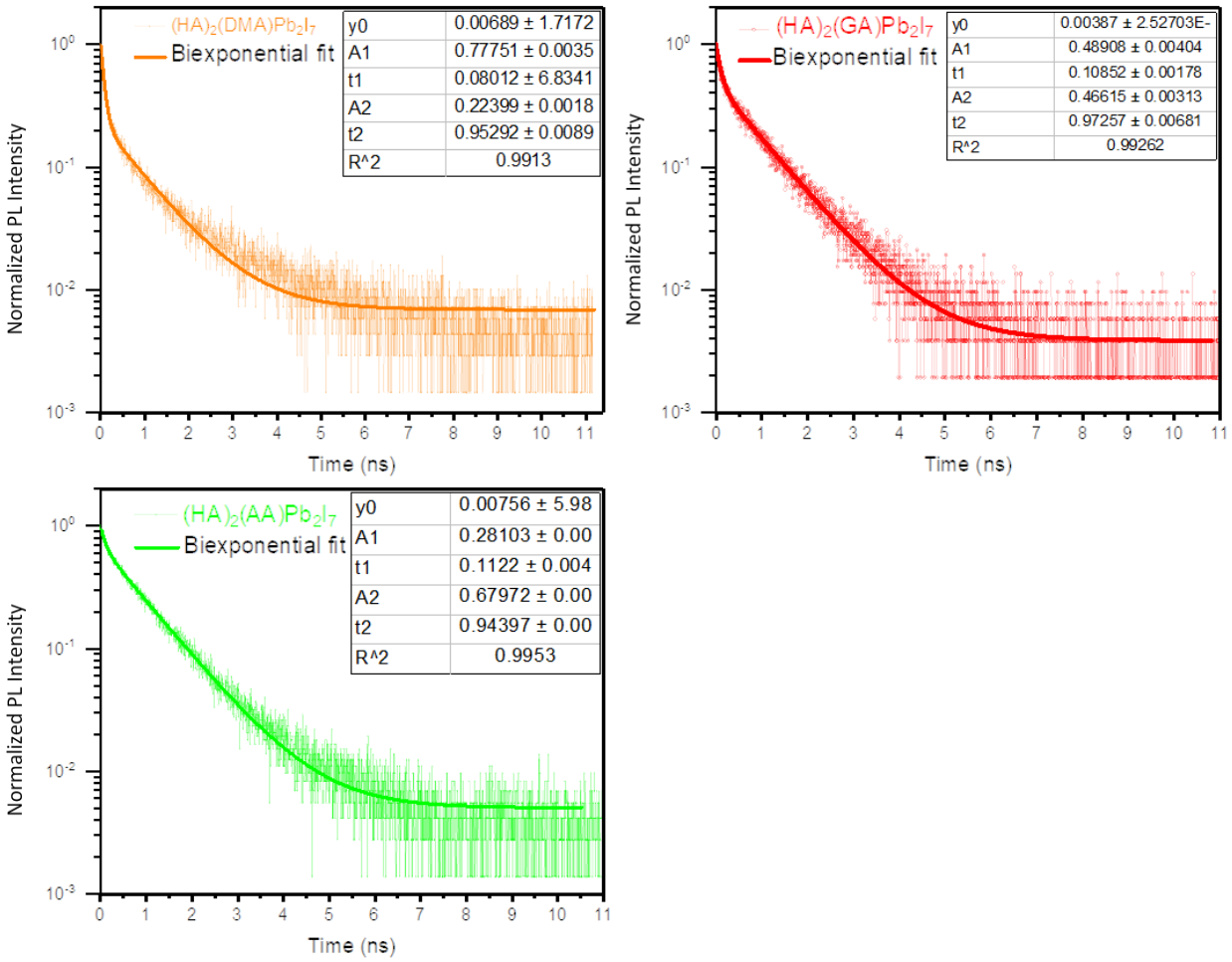

Figure C.6. Complete collection of the TRPL decay curves for each $(HA)_2(A)Pb_2I_7$ nanoplate sample (labeled on graph) and their corresponding biexponential fits (Equation C.2). Two representative examples were displayed in main text Figure 4.4a. The complete fitting results are displayed in Table 4.3.

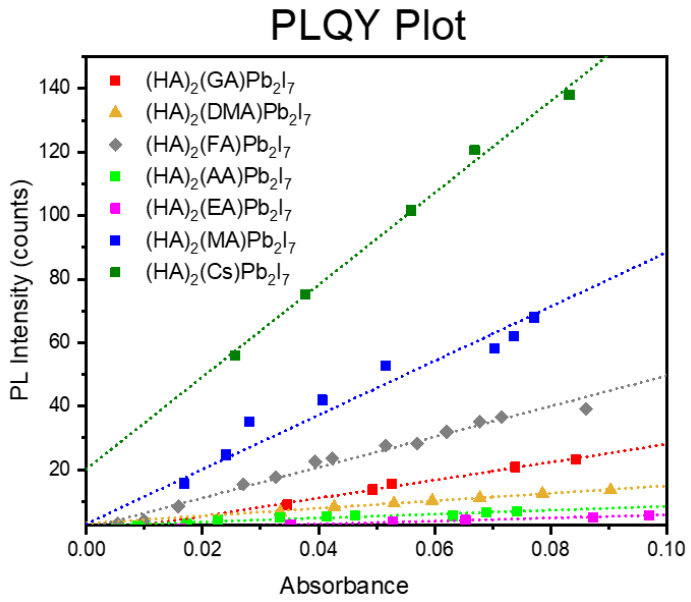

Figure C.7. Plot of the PLQY traces for each $(HA)_2(A)Pb_2I_7$ nanoplate sample. The slope was calculated and used in equation C.1.

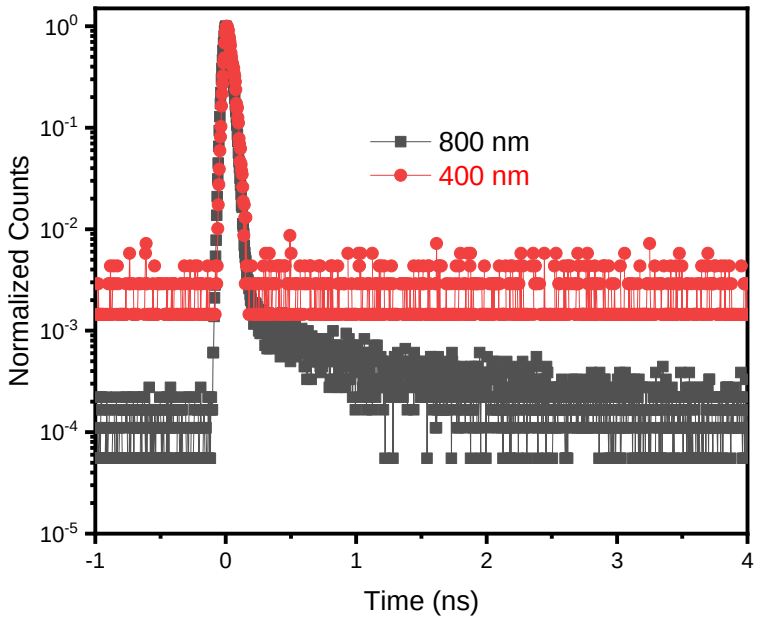

Figure C.8. Instrument response function (IRF) of our setup for the TRPL experiments (FWHM is 55 ps). The IRF is significantly faster than the TRPL decay of the nanoplate samples.

Table C.1. Structural parameters and selected crystallographic dimensions of RP lead iodide perovskite structures with large A site cations. The colored regions group the same RNH_3^+- *n* value combination.

Compound	A cation size	Average Pb-I distance (Å)	Average I-Pb-I angle (°)	Elongated axis distance (Å)	Unit cell volume/Z (A^3)
$(BA)_2(MA)Pb_3I_{10}$ [3]	217	3.163	170	52.0158	1029.5
$(BA)_2(EA)Pb_3I_{10}$ [3]	253	3.213	166	51.959	1047.2
$(HA)_2(MA)Pb_2I_7$ [4]	217	3.1792	163.56	45.146	851.8
$(HA)_2(GA)Pb_2I_7$ [4]	279	3.2081	167.63	43.398	849.90

Table C.2. Ratios of *n*-hexylammonium to A site cation determined from the NMR spectra taken for each RP perovskite compound in DMSO-d_6. Blue (HA) and yellow (A cation) cells highlight the NMR peaks used for determining the ratios of HA/A listed at the bottom.

	$(HA)_2(MA)Pb_2I_7$	$(HA)_2(FA)Pb_2I_7$	$(HA)_2(EA)Pb_2I_7$	$(HA)_2(DMA)Pb_2I_7$	$(HA)_2(GA)Pb_2I_7$	$(HA)_2(AA)Pb_2I_7$
1 (ppm)	0.87	0.87	0.87	0.87	0.87	0.87
Area	3.00	3.00	3	3	3.51	3
2 (ppm)	1.27	1.27	1.13	1.27	1.27	1.27
Area	6.01	6.06	1.57	6.09	7.29	5.12
3 (ppm)	1.51	1.51	1.27	1.51	1.51	1.51
Area	1.91	1.99	5.94	1.95	2.31	2.15
4 (ppm)	2.37	2.78	1.51	2.55	2.77	2.11
Area	1.52	2.02	1.89	3.05	2.77	1.49
5 (ppm)	2.77	7.59	2.55	2.77	6.89	2.77
Area	1.92	2.52	1.62	2.06	3.03	2.24
6 (ppm)	7.56	7.86	2.77	7.61	7.58	7.60
Area	3.82	0.55	1.76	2.45	3.00	2.99
7 (ppm)		8.67	2.82			8.86
Area		0.82	1.18			1.15
8 (ppm)		9.01	7.59			
Area		0.83	3.20			
Ratio HA/A	1.97	1.82	1.91	1.97	1.98	2.01

Table C.3. Complete fitting results of TRPL and τ_{avg} from equation C.2.

Compound	A_1	τ_1	A_2	τ_2	τ_{avg}
$(HA)_2CsPb_2I_7$	0.630	0.122	0.275	2.42	0.820
$(HA)_2(MA)Pb_2I_7$	0.773	0.132	0.194	2.95	0.699
$(HA)_2(FA)Pb_2I_7$	0.773	0.154	0.153	2.41	0.528
$(HA)_2(EA)Pb_2I_7$	0.781	0.100	0.179	1.15	0.296
$(HA)_2(DMA)Pb_2I_7$	0.777	0.080	0.223	0.953	0.275
$(HA)_2(GA)Pb_2I_7$	0.489	0.109	0.466	0.972	0.530
$(HA)_2(AA)Pb_2I_7$	0.281	0.112	0.679	0.943	0.700

Supporting Equations and Fitting:

Equation C.1. $QY = QY_{ref}\frac{\eta^2}{\eta_{ref}^2}\frac{I}{A}\frac{A_{ref}}{I_{ref}}$

$\eta -$ refractive index; $I -$ PL intensity; $A\ -$ Absorbance

The reference (ref) used was fluorescein in 0.1 M NaOH.

Equation C.2. $I(t) = y_0 + A_1 \exp\left(\frac{t}{\tau_1}\right) + A_2 \exp\left(\frac{t}{\tau_2}\right)$

Equation C.3. $\tau_{avg} = \frac{A_1\tau_1 + A_2\tau_2}{(A_1 + A_2)}$

Absorbance fitting. We model our absorption spectra using the 2D Elliott model.[5-7] This model is well known in the semiconductor literature and the 3D version of the model has been used fruitfully in the perovskite literature.[8] Our implementation of the model is written in Python and available on the Open Science Framework.[9]

Our implementation of the Elliott model assumes the existence of two non-degenerate, interband transitions. Each of these transitions has an optical susceptibility defined by bound exciton states and unbound continuum states, see Haug and Koch for a full treatment.[5]

The total, broadened susceptibility is given by the sum of broadened susceptibilities from individual bands indexed by *j*.

$$\chi_{\Gamma}[\hbar\omega] = \sum_{j} \chi_{\mathrm{j},\Gamma}[\hbar\omega]$$

The absorption coefficient is then given by

$$\alpha[\hbar\omega] \propto \hbar\omega \cdot \mathrm{Im}\left[\chi_{\Gamma}[\hbar\omega]\right]$$

The broadened susceptibility from the individual bands is given by an unbroadened susceptibility convolved with a complex, causal lineshape function; we choose to use a Lorentzian of width Γ.

$$\chi_{\mathrm{j},\Gamma}[\hbar\omega] = \chi_{j}[\hbar\omega] * \mathcal{L}\left[\hbar\omega; \Gamma_{\mathrm{j}}\right]$$

$$\mathcal{L}[\hbar\omega; \hbar\omega_0, \Gamma] \equiv \sqrt{\frac{\Gamma}{\pi}} \frac{1}{\hbar\omega_0 - \hbar\omega - i\Gamma}$$

The unbroadened interband transition susceptibility is given by

$$\chi_{j}[\hbar\omega] = A\left|d_{j,cv}\right|^2 \left(\zeta_{j,\mathrm{bound}}[\hbar\omega] + \zeta_{j,\mathrm{unbound}}[\hbar\omega]\right)$$

in which A is a proportionality constant and d_{cv} is the conduction to valence band transition dipole moment. The bound and unbound contributions are given by

$$\zeta_{j,\mathrm{bound}} = \sum_{\ell}^{\infty} \frac{4}{\left(\ell + \frac{1}{2}\right)^3} \delta\left[\Delta_{\mathrm{j}} + \frac{1}{\left(\ell + \frac{1}{2}\right)^2}\right]$$

$$\zeta_{j,\text{unbound}} = \frac{\exp\left[\frac{\pi}{\sqrt{\Delta_j}}\right]}{\cosh\left[\frac{\pi}{\sqrt{\Delta_j}}\right]}\Theta[\Delta_j]$$

$$\Delta_j \equiv \frac{\hbar\omega - E_{g,j}}{E_{0,j}}$$

In which E_g is the bandgap energy, E_0 is the exciton Rydberg energy, δ is the Dirac-delta distribution and Θ is the Heaviside step function. Note that the binding energy for a 2D exciton system is given by $4E_0$.

Appendix C References

1. Robinson, K.; Gibbs, G. V.; Ribbe, P. H., Quadratic Elongation: A Quantitative Measure of Distortion in Coordination Polyhedra. *Science* **1971,** *172* (3983), 567-570.
2. Brese, N. E.; O'Keeffe, M., Bond-valence parameters for solids. *Acta Crystallogr., Sect. B* **1991,** *47* (2), 192-197.
3. Fu, Y.; Jiang, X.; Li, X.; Traore, B.; Spanopoulos, I.; Katan, C.; Even, J.; Kanatzidis, M. G.; Harel, E., Cation Engineering in Two-Dimensional Ruddlesden–Popper Lead Iodide Perovskites with Mixed Large A-Site Cations in the Cages. *Journal of the American Chemical Society* **2020,** *142* (8), 4008-4021.
4. Fu, Y.; Hautzinger, M. P.; Luo, Z.; Wang, F.; Pan, D.; Aristov, M. M.; Guzei, I. A.; Pan, A.; Zhu, X.; Jin, S., Incorporating Large A Cations into Lead Iodide Perovskite Cages:Relaxed Goldschmidt Tolerance Factor and Impact on Exciton−Phonon Interaction. *ACS Cent. Sci.* **2019,** (5), 1377-1386.
5. Haug, H. A.; Koch, S. W., *Quantum Theory of the Optical and Electronic Properties of Semiconductors*. World Scientific Publishing Co. Pte. Ltd.: Singapore, 1994.
6. Shinada, M.; Sugano, S., Interband Optical Transitions in Extremely Anisotropic Semiconductors. I. Bound and Unbound Exciton Absorption. *Journal of the Physical Society of Japan* **1966,** *21* (10), 1936-1946.
7. Elliott, R. J., Intensity of Optical Absorption by Excitons. *Physical Review* **1957,** *108* (6), 1384-1389.
8. Yang, Y.; Ostrowski, D. P.; France, R. M.; Zhu, K.; van de Lagemaat, J.; Luther, J. M.; Beard, M. C., Observation of a hot-phonon bottleneck in lead-iodide perovskites. *Nature Photonics* **2015,** *10*, 53.
9. Morrow, D. J., Open Science Framework: **2020,** DOI: 10.17605/OSF.IO/M9DNW.

Appendix D. Supporting Information for Chapter 5

CVD Heterostructures*

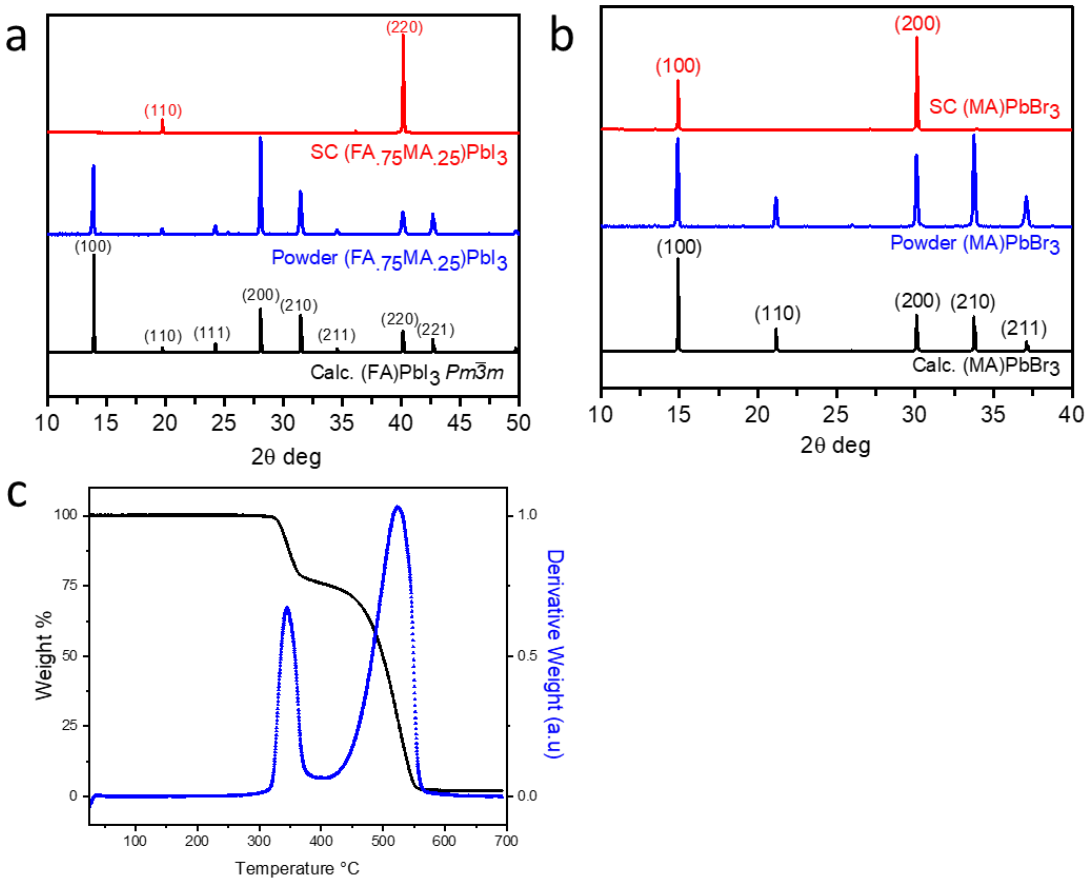

Figure D.1. Single crystal (SC) structure characterization. (a) $(FA_{.75}MA_{.25})PbI_3$ X-ray diffraction collected as an oriented SC and powder compared to the calculated $(FA)PbI_3$ pattern. (b)

* In collaboration with D. Lafayette II, J. Feng, Z. Luo, W. Zheng, M. Kuo, N. Spitha, J. Li, J. C. Wright, A. Pan, and S. Jin

(MA)$PbBr_3$ collected as an oriented SC and powder compared to the calculated (MA)$PbBr_3$ pattern. (c) Thermogravimetric analysis of $(FA_{.75}MA_{.25})PbI_3$ showing decomposition above 300°C.

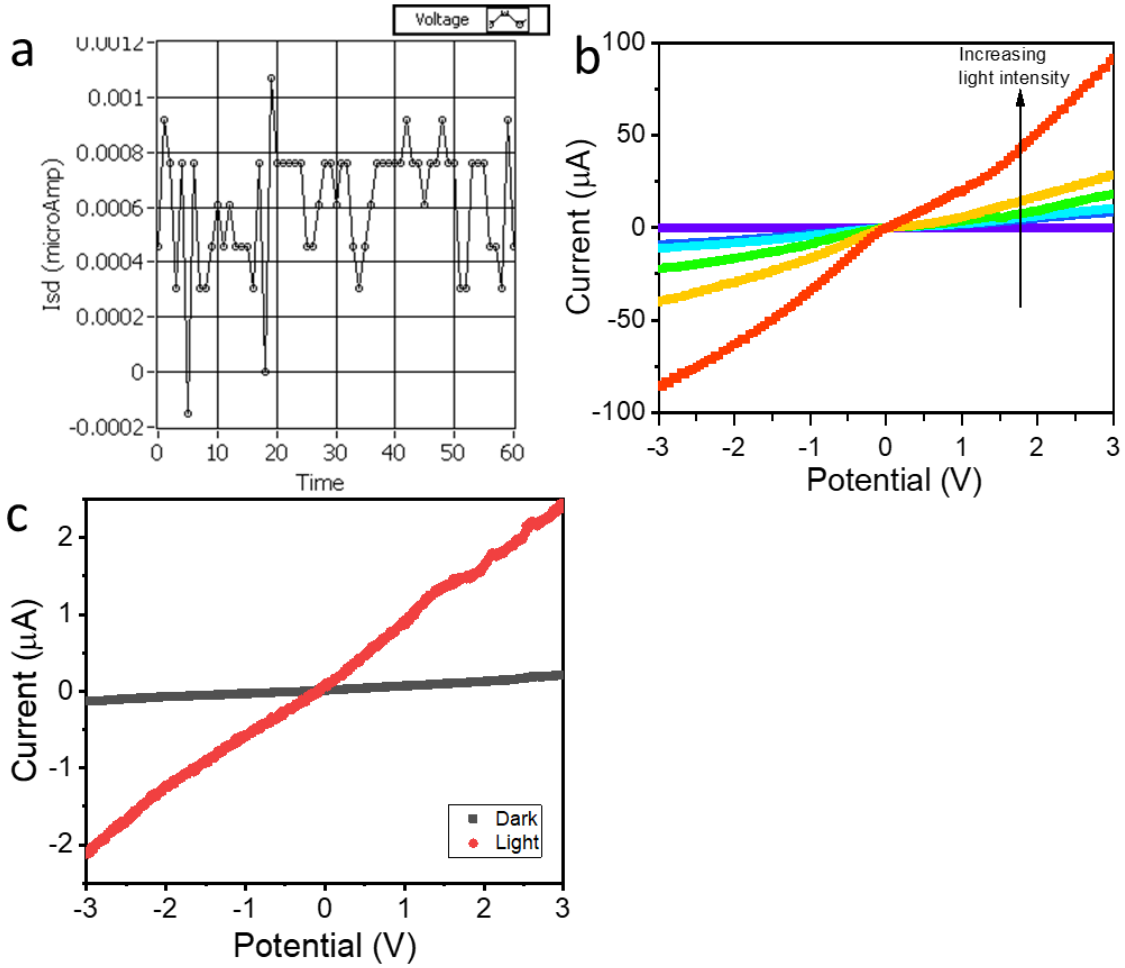

Figure D.2. Further electrical characterization. (a) Current vs. time measurement of $(BA)_2PbBr_4/(MA)PbBr_3$ showing the lack of photocurrent. I-V curve of (b) $(FA_{0.75}MA_{0.25})PbI_3$ single crystal and (c) $(BA)_2PbI_4$ thin-films under varying light intensity.

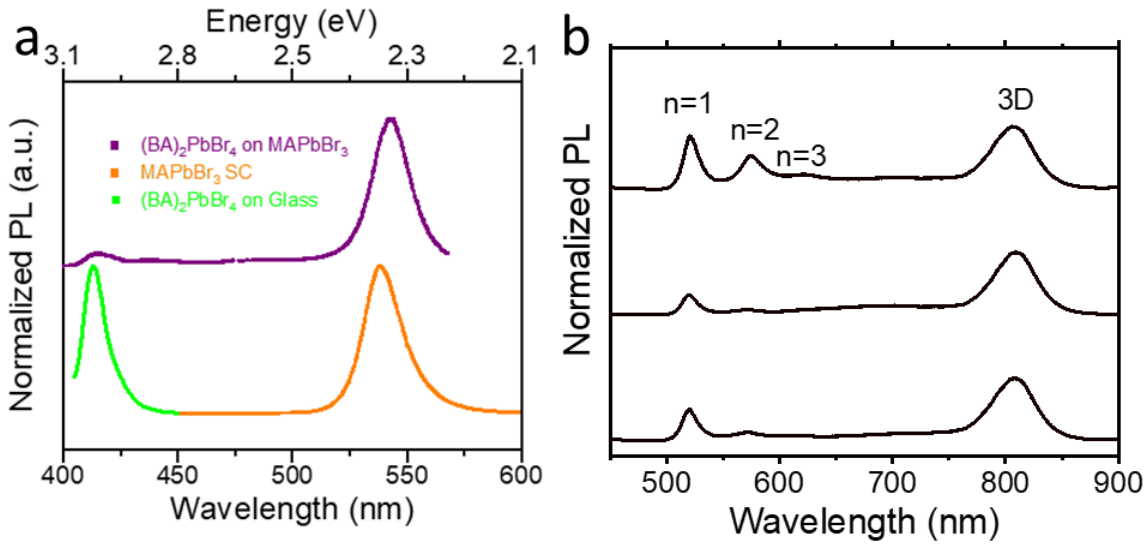

Figure D.3. Further PL spectra of 2D/3D heterostructures. (a) PL spectra of the $(BA)_2PbBr_4/(MA)PbBr_3$ heterostructure, pure $(BA)_2PbBr_4$, and pure $(MA)PbBr_3$. (b) PL at various position in the 2D/3D iodide heterostructure, showing select positions have higher *n* value impurities.

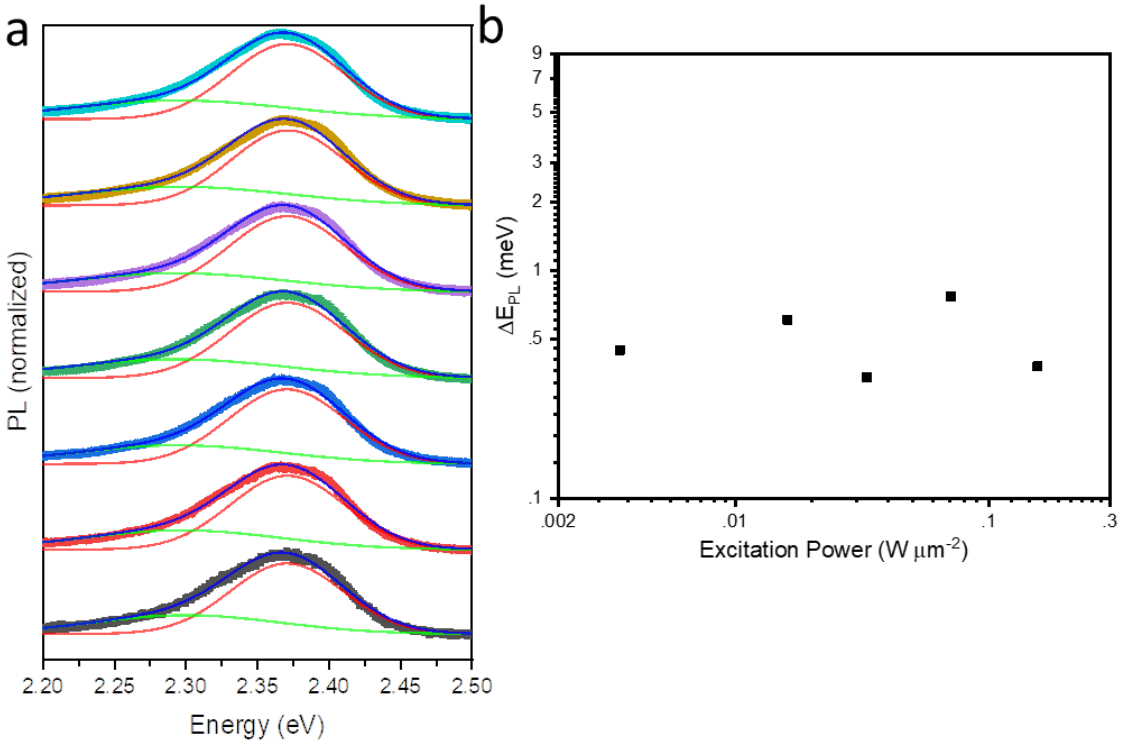

Figure D.4. Power dependent PL spectra of pure 2D $(BA)_2PbI_4$. (a) PL spectra at increasing excitation power with fittings shown. (b) Change in energy with respect to excitation power, showing no increase or major changes in peak position.

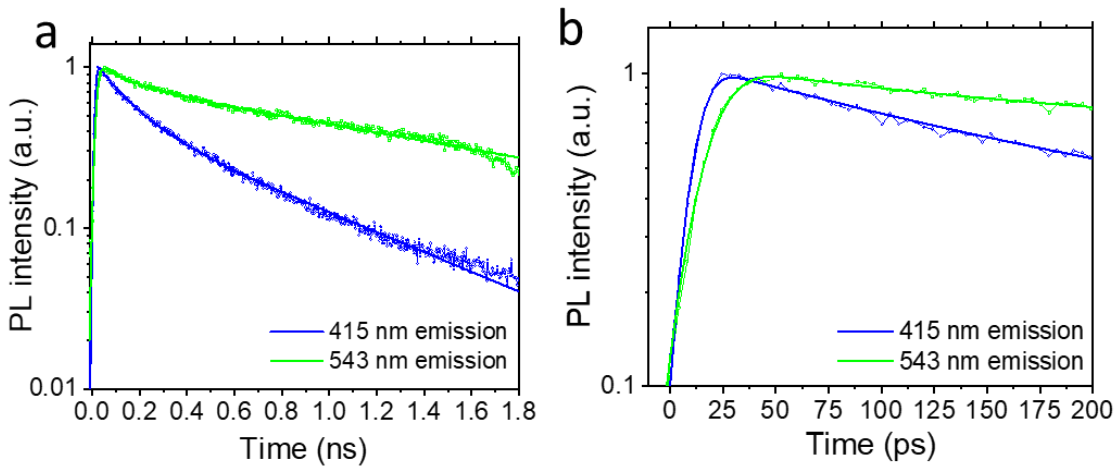

Figure D.5. TRPL of 2D/3D bromide heterostructures. (a) TRPL of $(BA)_2PbBr_4$ (415 nm emission) and $(MA)PbBr_3$ (543 nm emission). (b) TRPL of the same showing from 0 – 200 ps to highlight the slower rise of $(MA)PbBr_3$ relative to $(BA)_2PbBr_4$.

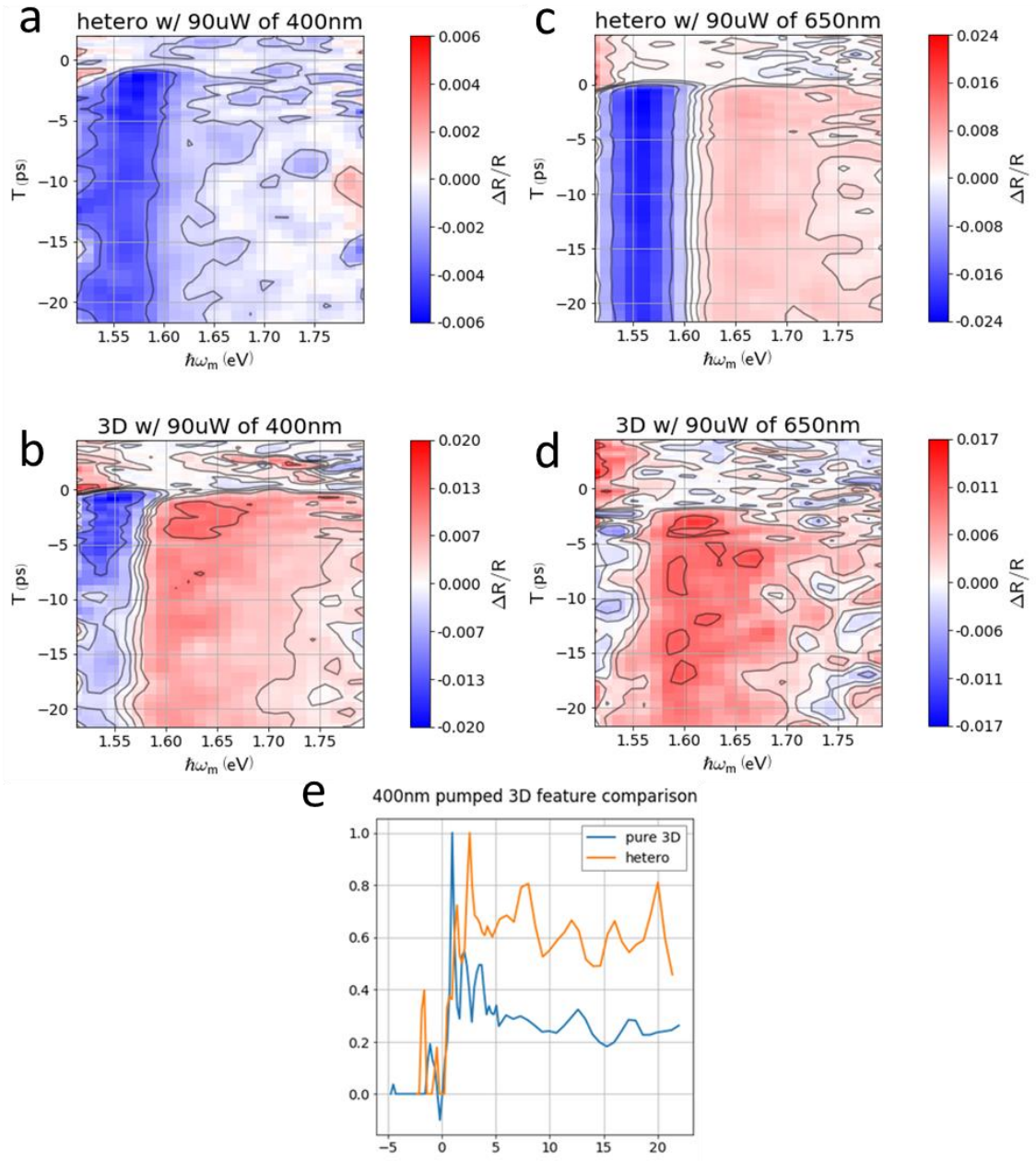

Figure D.6. Transient reflectance of 2D/3D iodide heterostructures with a white light probe. 400 nm pump of (a) heterostructure and (b) pure 3D. 650 nm pump of (c) heterostructure and (d) pure 3D perovskite. (e) Line plots of the pure material vs. the heterostructure showing a possible delay in the rise time.